AN ABSTRACT OF THE DISSERTATION OF

Christopher S. Loeb for the degree of Doctor of Philosophy in Chemical Engineering presented on May 17, 2013.

Title: Enhancement and Modeling of Cryogenic Solid-State Hydrogen Storage Systems with a Novel Microchannel Thermal Management Device

Abstract approved: _____
Goran N. Jovanovic

Compact storage systems demonstrating increased hydrogen storage capacity are the key to advancing the growth of the hydrogen economy throughout the world and reducing the global dependence on fossil fuels for transportation. The use of highly porous adsorbent materials for reversible hydrogen storage is a promising pathway towards achieving storage densities capable of reaching driving ranges comparable to gasoline automobiles without high-pressure compressed gas storage systems (>200 bars H_2).

The focus of this effort is the enhancement of solid-state hydrogen adsorption systems through the development and inclusion of a microchannel thermal management device for efficient heat removal and uniform gas distribution in compressed beds of activated carbon and metal organic framework. The stainless steel microchannel device utilizes 250 μm walls to remove heat from the contacting adsorbent bed with liquid nitrogen coolant flow through 250 μm channel. Cryogenic (<140 K) hydrogen adsorption experiments were completed with and without liquid nitrogen cooling at pressures between 50 and 55 bars.

The experiments demonstrate that the use of liquid nitrogen coolant effectively lowers the adsorbent bed temperature by removing the majority of the heat generated during the adsorption process, resulting in an 11% increase in stored H_2 gas with MOF-5 and a 3% increase with activated carbon compared to their respective non-cooled counterparts. The liquid cooled MOF-5 adsorbent bed increases average hydrogen storage throughout the experimental vessel by 14% compared to a cryo-compressed gas system at similar conditions (121 K and 55 bars).

A functional development tool representing the experimental adsorption system was developed in COMSOL Multiphysics and utilized derived conservation equations and the modified Dubinin-Astakhov equation to characterization the gas flow, energy transport, and physical adsorption of supercritical hydrogen on MOF-5 adsorbent. Simulated adsorption experiments, modeled with development tool, were validated against experimental data; the predicted temperature responses at embedded thermocouple locations show a strong correlation to experimental data. The development tool may assist in the design and development of future storage systems utilizing adsorbent materials with known physical, thermal, and adsorption parameters.

Enhancement and Modeling of Cryogenic Solid-State Hydrogen Storage Systems with a Novel Microchannel Thermal Management Device

By

Christopher S. Loeb

A DISSERTATION

Submitted to

Oregon State University

in partial fulfillment of

the requirements for the

degree of

Doctor of Philosophy

Presented May 17, 2013

Commencement June 2013

Doctor of Philosophy dissertation of Christopher S. Loeb presented on May 17, 2013

APPROVED:

Major Professor, representing Chemical Engineering

Head of the School of Chemical, Biological and Environmental Engineering

---

Dean of the Graduate School

I understand that my dissertation will become part of the permanent collection of Oregon State University libraries. My signature below authorizes release of my dissertation to any reader upon request.

Christopher S. Loeb, Author

ACKNOWLEDGEMENTS

I wish to express my appreciation and gratitude to everyone that has helped me throughout this process.

I wish to express my appreciation for the funding provided by the United States Department of Energy and the Hydrogen Storage Engineering Center of Excellence under Award Number: DE-FC36-08GO19005.

I would like to thank Dr. Goran Jovanovic for providing me with his continued support, guidance, and never-ending innovation. My ability to think well outside of the box has been greatly enhanced through his collaboration.

I would like to thank all of the members of the OSU Hydrogen Storage Group, the leadership of Dr. Kevin Drost and all of the guidance and collaboration I received from Dr. Vinod Narayanan, Dr. Brian Paul, and their great graduate students.

I would like to extend my gratitude to Dr. Keith Levien and Dr. Alexandre Yokochi for their help in expanding my knowledge and strengthening my engineering base.

Sincere thanks to everyone at the MBI that has helped me along the way, especially Kevin Harada and Dr. Jair Lizarazo-Adarme for their continued help and friendship.

Thank you to the rest of the Jovanovic lab group, for sharing many wonderful memories both in and outside of the lab.

I would like to thank my friends and family for all of their support and understanding of the opportunity that took Candi and me so far away. To my parents, thank you for the continuous love, guidance and wonderful examples that you have demonstrated throughout my life that have shaped me into the person I am today.

Finally, I would like to thank my wife, Candi, for her unconditional love, support, patience, and encouragement that has helped me every step of the way. I am eternally grateful to have had my best friend by my side throughout this journey and to share all the wonderful experiences we have encountered over the years.

TABLE OF CONTENTS

TABLE OF CONTENTS (Continued)

TABLE OF CONTENTS (Continued)

LIST OF FIGURES

Figure Page

LIST OF FIGURES (Continued)

Figure Page

LIST OF FIGURES (Continued)

Figure Page

LIST OF FIGURES (Continued)

Figure Page

LIST OF TABLES

LIST OF TABLES (Continued)

Table Page

Enhancement and Modeling of Cryogenic Solid-State Hydrogen Storage Systems with a Novel Microchannel Thermal Management Device

Chapter 1: Introduction, Motivation, Research Goals and Objectives

1.1 Introduction

1.1.1 Carbon dioxide and Fossil Fuel Reserves

As the global population continues to grow, the world's energy consumption continues to grow with it, and is expected to continue to by 1.1% per year until 2030. Recent energy consumption increase at approximately 2% per year [1]. Fossil fuels, including coal, natural gas, gasoline and diesel, account for approximately 81% of the total global energy consumed and 98% of that energy consumed is by the transportation sector alone [2]. In recent history, the transportation industry has demonstrated a greater increase in energy consumption compared to other sectors [3], and as carbonaceous fuels continue to dominate this rapidly expanding industry, the world bears witness to an increase in carbon dioxide (CO_2), nitrogen oxides (NO_x), and other greenhouse gas (GHG) emissions. The United States Environmental Protection Agency (EPA) estimated that the transportation sector was responsible for 28% of the total GHG emissions in 2006 [4]. The continued increase in transportation GHG emissions offsets the decrease in GHG emissions observed in other economic and energy sectors [5]. In addition, 98% of CO_2 currently present in throughout the world is dissolved in the global water supply, however, increasing ocean temperatures has led to a decrease in CO_2 solubility resulting in an average of 43% of the annual CO_2 emissions remaining in the atmosphere since 1959 [6 ,7]. This increasing atmospheric retention of CO_2 coupled with a 50% increase in emissions over the last three decades [8] has led to anthropologic climate change due to shifts in the atmosphere's ability to receive and re-radiate solar radiation [9].

In addition to the environmental and health effects of increased GHG emissions, the 18% increase in annual fuel consumption between 1996 and 2006 by mobile sources raises questions to the future stability and availability of fossil fuels for

transportation [10]. It has been estimated that 40% of the available conventional oil reserves have been depleted [3]. Some experts predict peak oil production could be reached as early as 2015 citing the lack of new major oil field discoveries and depletion of current oil fields as contributions [2]. The onset of peak oil production will have an immediate impact on global supply as countries throughout the world attempt to meet demands; this shift could lead to an increase in crude oil prices and influence all sectors of the global economy.

The United States, one of the world's biggest users of oil, imports over 50% of the oil it consumes [11] and will require an alternative form of energy to continue to meet demand following peak oil production. To solve this problem, transportation energy carriers such as gasoline, diesel, and jet fuel may be synthesized via chemical processes utilizing coal and natural gas feedstocks. Additionally, natural gas may be used to fuel automobiles and buses. Despite the abundance of coal and natural gas throughout the United States and the world [3], the use of synthesized transportation fuels does not help control or eliminate CO_2 emissions. In comparison to synthesized liquid fuels and natural gas, hydrogen possesses the ability to provide a carbon-free, renewable energy source for transportation. The use of hydrogen as an energy carrier is the unequivocal first step in the effort to minimize CO_2 emissions throughout the world and combat global climate change. Hydrogen is the responsible choice as the energy carrier of the future.

1.1.2 Hydrogen Production

Despite being the most abundant element on earth, the majority of hydrogen is bound in water, with less than 1% in molecular form [12]. Hydrogen production remains a key issue in the progress towards a hydrogen economy and zero emission transportation. Ninety-six percent of global hydrogen production is derived from fossil fuels and the remaining 4% via electrical processes that are primarily dependent on fossil fuels [13].

Of the three main hydrogen production methods, the two-step, high temperature steam reformation of hydrocarbons is the most widely used

$$C_mH_n + mH_2O \leftrightarrow mCO + \left(m + 0.5n\right)H_2 \tag{1.1}$$

$$CO + H_2O \leftrightarrow CO_2 + H_2 \tag{1.2}$$

The water-gas shift, (1.2), converts CO into CO_2 and additional H_2 gas. Because of its high carbon-to-oxygen ratio, natural gas is the preferred feedstock for steam reformation [13]. Another widely used reformation process for longer chained hydrocarbons is partial oxidation at high temperatures with or without a catalyst:

$$C_mH_n + \frac{m}{2}O_2 \leftrightarrow mCO + \frac{n}{2}H_2 \tag{1.3}$$

Again, the CO products of partial oxidation are subject to the water-gas shift reaction to produce carbon dioxide and additional hydrogen gas [14]. The third common production method is a process similar to steam reformation, known as coal gasification, is carried out using solid carbon to produce hydrogen gas from solid fossil fuel sources [13]. Although these methods succeed in producing the hydrogen necessary to power a hydrogen economy, they do not aid in the world's progress towards zero emission transportation and minimizing fossil fuel consumption.

In order to surpass fossil fuels as the world's premier energy carrier, the hydrogen economy requires an abundant, renewable, carbon-free, and inexpensive feedstock. With an atomic structure composed 66% of hydrogen, water is the ideal feedstock. Hydrogen gas is liberated from water by a number of processes, but the three most notable are electrolysis, indirect thermal decomposition, and photocatalytic decomposition; each process creates a mixture of hydrogen and oxygen that can be used directly with a fuel cell.

The direct decomposition of water by electricity (1.23V) is achieved on a commercial scale with efficiencies as high as 73% [14] by the following pathway:

$$2H_2O + Electricity \rightarrow 2H_2 + O_2 \tag{1.4}$$

Despite the energy requirements of hydrogen production, electrolysis can be a carbon-free source of hydrogen when electricity is provided from solar photovoltaic devices, wind farms, or hydropower sources. Of these three sources, wind farms are an ideal candidate for electrolytic production of hydrogen due to the intermittent nature of wind resulting in periods of over-production of electrical energy [15], creating an opportunity to harness electricity that could have potentially gone unused. A portion of produced hydrogen may be utilized for supplemental electricity production when renewable methods cannot support peak demands.

Hydrogen production achieved by pairing water with metal oxides and solar concentrator units provide high temperatures (as high as 2100 K) required for thermochemical decomposition of water. The two-step zinc/zinc oxide thermochemical cycle, requiring temperatures of 2073 K for zinc oxide decomposition (1.5), is a potential candidate for use with solar concentrators for hydrogen production [14]:

$$ZnO \rightarrow Zn + 0.5O_2 \tag{1.5}$$

$$Zn + H_2O \rightarrow ZnO(s) + H_2 \tag{1.6}$$

Attempting to learn from and replicate natural phenomena, sunlight is used to drive the photocatalytic decomposition of water. This is an example of "artificial photosynthesis," [16] used to produce H_2 and O_2 gases. As a proven purification agent, the photocatalytic process degrades organic materials in water, which could expand hydrogen production to wastewater treatment systems [17].

Photocatalytic materials capable of directly decomposing water utilize a partially metal-coated n-type semiconductor capable of absorbing UV and/or visible light. In a colloidal system, the photon absorption by the semiconductor material

results in band gap excitation and the formation of an electron-hole pair, e^- and h^+, respectively. The electron aligns itself with metal coating for catalytic H_2 evolution, while the hole catalytically forms O_2 [18]. This process is depicted in Figure 1.1 below; photon energy is represented by *hv*.

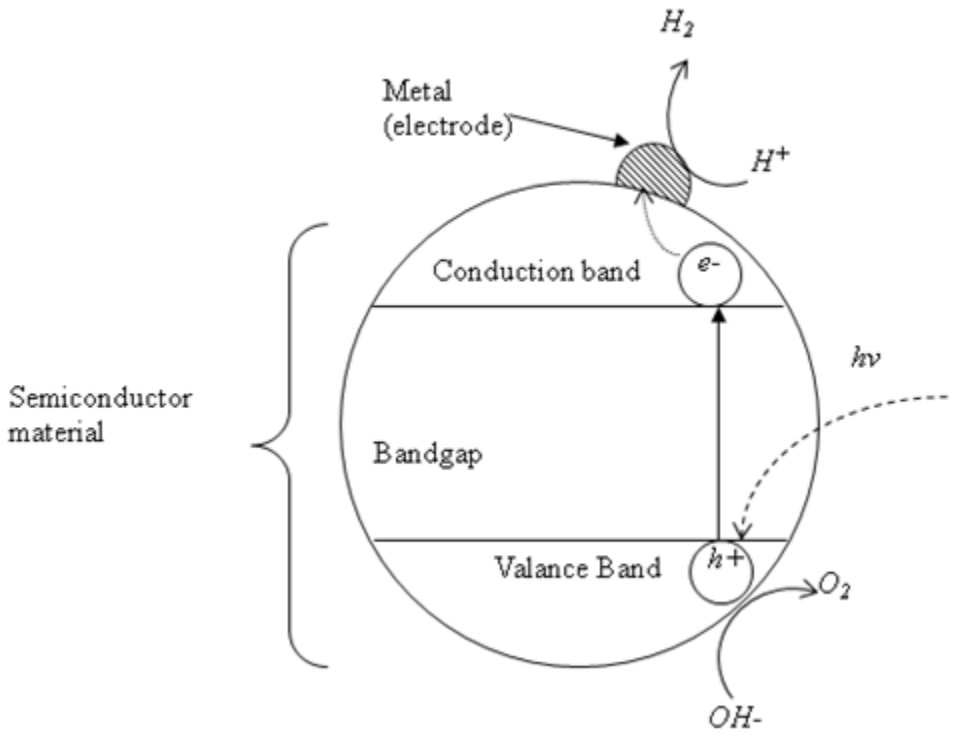

Figure 1.1 Representation of metal coated semiconducting particle for photocatalytic water splitting [18].

1.1.3 Hydrogen Transport

By establishing and employing carbon-free hydrogen production methods, the hydrogen economy can transition to a renewable, sustainable, zero-emissions industry capable of supporting a thriving hydrogen economy. Once produced, hydrogen can be transported between production, distribution, and end-user sites by a number of methods. Hydrogen can be shipped in storage tanks by road or rail in both compressed gas and liquid forms, or it can be transported through a network of pipelines similar to the current natural gas distribution infrastructure. Although for large scale distribution hydrogen pipelines can cost 1.5 to 1.8 times greater than those for natural gas, it is more economical than electricity transmission over distances of

1,000 km [15]. Furthermore, a solar photovoltaic water electrolysis system at distribution sites (i.e. vehicle refueling stations) for onsite hydrogen production negates the need for long distance hydrogen transport.

1.1.4 Energy Production by Hydrogen

Converting hydrogen gas to power in an automobile is accomplished with internal combustion engines (ICE) or fuel cell (FC) stacks, both of which provide a cleaner form of personal and public transportation. ICE vehicles using hydrogen gas benefit from a 20% increase in efficiency and FC automobiles perform nearly 2.4 times better than current gasoline powered ICE [4,15]. Additionally, FC and ICE vehicles operating with lean air:H_2 mixtures produce water as the major byproduct of energy production compared to CO_2 generated by gasoline and diesel engines.

1.1.5 Hydrogen Storage Methods

According to the 2007 "Overview of energy storage methods" conducted by Mora Associates, the specific energy (energy per mass) of hydrogen is three times that of gasoline and nearly 200 times greater than high-performance lithium-ion polymer batteries [19]. The difficulty for the hydrogen economy is the low energy density (energy per volume) exhibited by hydrogen in molecular forms, requiring large volume reservoirs to meet energy production requirements. In its liquid state, hydrogen's energy density is 3.5 times lower than that of gasoline and highly compressed hydrogen gas, 200 bar storage pressure, remains 15 times lower than the energy density of gasoline [15].

The "Hydrogen Fuel Initiative" was launched in 2003 to enhance and promote hydrogen technology research to accelerate and improve hydrogen production, fuel cell systems, and on-board hydrogen storage with driving ranges comparable to gasoline automobiles. In an effort to improve hydrogen storage capacity, the United States Department of Energy (DOE) has instituted parallel research tracks focused on on-board reversible storage and regenerable off-board storage systems [11]. The

technical targets established by the DOE provide a road map for the progression of technology focused on the realization of a hydrogen economy [20].

Table 1.1: DOE targets for hydrogen storage systems, new and old [20].

Target	2010 (New)	2010 (Old)	2015 (New)	2015 (Old)	Ultimate Full Fleet
System Gravimetric Density (%wt)	4.5	6	5.5	9	7.5
System Volumetric Density (g/L)	28	45	40	81	70
System Fill Time for 5-kg fill, min (Fueling rate, kg/min)	4.2 min (1.2 kg/min)	3 min (1.67 kg/min)	3.3 min (1.5 kg/min)	2.5 min (2.0 kg/min)	2.5 min (2.0 kg/min)

The use of regenerable off-board hydrogen sources could create a simplified concept for the transition from today's gasoline infrastructure, as many liquid chemicals could be dispensed using similar techniques. However, the need to unload and regenerate spent H_2 storage chemicals outside of the vehicle adds to the complexity of off-board storage solutions. A number of different systems are under investigation including on-vehicle reforming and dehydrogenation of carbon based feedstock such as methane or decalin-to-naphthalene reaction, (1.7), [11]:

$$C_{10}H_{18} \rightarrow C_{10}H_8 + 5H_2 \tag{1.7}$$

Non-reversible chemical hydrides, AlH_3 and NH_3BH for example, are also considered potential off-board regenerable hydrogen storage solutions, due to their high gravimetric capacity (10 wt% and 19.5wt% H_2, respectively) and low hydrogen liberation temperatures (near 100^{o}C). The low endothermic decomposition (7 kJ mol^{-1}

H_2) of aluminum hydrides can be initiated with waste heat from the fuel cell; however, their widespread use is hindered due to the difficult, energy intensive two-step regeneration process. Hydrogen liberation from ammonia borane is achieved by an on-board three-step thermal decomposition or a two-step hydrolysis process [21,22].

On-board reversible storage solutions operate by the direct addition of hydrogen into the storage tank at the refueling station [11]. Reversible systems include both the compressed gas and liquid hydrogen systems that have been discussed previously, as well as metal hydride systems and high surface area adsorbents. Metal hydrides dissociate atomic hydrogen to form strong chemical bonds with hydrogen ions within the host metal lattice via absorption. At increased hydrogen concentrations hydrogen-hydrogen interactions lead to nucleation and hydride formation. The formation of the hydride results in a 10-20% increase in the metal lattice volume. The absorption of hydrogen within the metal lattice is an exothermic process. The desorption of hydrogen from the hydride is a strongly endothermic process, requiring a large input of heat into the storage material to release hydrogen for consumption [23]. Metal hydride production typically yields dense powders, easily meeting the DOE's volumetric requirements for H_2 storage, but many are derived from heavy rare earth metals making it difficult to meet the gravimetric standards established by the DOE [24].

A large research focus has been placed on the development of high surface area adsorbents for gas storage, separations, and purification processes. Although there are a number of different materials that exhibit both high surface area and hydrogen storage capabilities, the two most talked about are activated carbons and metal organic frameworks. Unlike the formulation of chemical bonds observed in metal hydride formation, adsorbent materials physically store hydrogen on the material surfaces by physisorption caused by weak Van der Waals forces [23]. Due to the weak nature of physisorption, high capacity hydrogen storage is only reached at low temperatures (77 K) and moderate pressures (<60 bar H_2). Compared to metal

hydrides, adsorbents generate less heat during storage due to small heat of adsorption (<10kJ mol^{-1}) and display faster kinetics during H_2 charging and discharging of hydrogen [11]. The current storage capacities of adsorbent materials lie just short of the DOE's gravimetric targets; however, adsorbent materials are typically light powders making it difficult to reach volumetric targets. Continued materials research and densification techniques could make adsorbents the hydrogen storage material of the future.

Physical adsorption methods for hydrogen storage show tremendous potential to improve storage capacities. The hydrogen storage capacity of an adsorbent system increases faster with pressure compared to compressed gas systems at moderate pressures. As represented in Figure 1.2, for a given storage temperature, a breakeven pressure exists when higher system pressure no longer increases the storage capacity of an adsorbent system. However, the elevated breakeven pressure requires a structurally stronger tank that makes a low pressure adsorbent system easier to manage and incorporate into passenger vehicles [25].

If the hydrogen economy is to compete with, and eventually overtake the fossil fuel dominated transportation industry, vast improvements must be made in the development of the hydrogen storage systems. Despite great progress in tank development, hydrogen storage must move beyond molecular storage methods and embrace an alternative solid state such as metal hydride and physical adsorbents or regenerative solutions. No matter what path is chosen, a lightweight and compact thermal management system is needed to remove and/or supply the heat needed for the storage and liberation of hydrogen gas on demand. As the storage system develops, it becomes increasingly important to understand and predict the internal response of the storage process, the interactions of hydrogen gas, the storage media, and the thermal management system.

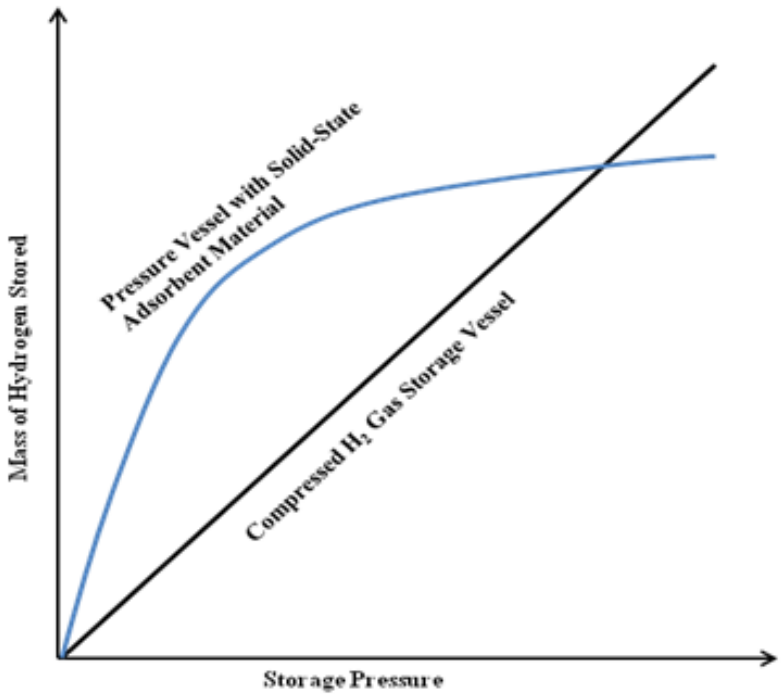

Figure 1.2: Storage capacity of adsorbent system compared to compressed gas tank with increasing pressure [25].

1.2 Research Goals

The first goal of this research is to contribute to the advancements and improvements in hydrogen storage systems through the development, manufacturing, and testing of a novel microchannel heat exchange and gas distribution system for reliable and efficient thermal management within a cryogenic hydrogen storage tank.

The second goal of this research is to further the understanding and characterization of reversible hydrogen storage on high surface area adsorbents through the development of an analytic tool to simulate the hydrogen adsorption process and system interactions.

1.3 Research Objectives

The investigation pertaining to this work is divided into four sections containing the key objectives necessary for the realization and fulfillment of the goals of this dissertation.

To begin, the design, manufacturing, and assembly of the microchannel heat exchanger and gas distribution system and cryogenic experimental system is required for the testing of the microchannel device and for the experimental investigation necessary for the validation of the analytic tool. This includes the complete design and manufacturing of the microchannel device and of the test facility, including gas delivery, delivery of heat transfer fluid, instrumentation, and safety equipment. A vital aspect of this objective is the procurement and machining of the adsorbent material required for the experimental investigations.

The design and fabrication process is accomplished in parallel with the development of a mathematical model and simulation tool of the adsorption process. The mathematical model, capturing the complex adsorption phenomena, is implemented using COMSOL Multiphysics to produce an analytic tool for the accurate simulation of the hydrogen charging process. This tool will allow for the extraction of vital characteristics and events taking place within the system. It is necessary that the model development reflect the experimental system and conditions as accurately as possible.

Next, the execution of the experimental investigations for the adsorption of nitrogen and hydrogen gases on the AC and MOF samples is conducted. This investigation will not only provide insight into the adsorption process but also to the effectiveness of the microchannel device to uniformly distribute gas into the adsorbent bed and remove the heat generated during gas adsorption.

Finally, it is necessary to validate the developed simulation package using the data obtained throughout the experimental investigation. The system validation is accomplished through the comparison of simulated and experimental temperature profiles in the adsorbent bed and the comparison of the predicted storage capacity to the observed mass of gas stored during the experimental investigations.

Chapter 2: Adsorption

Hydrogen storage on solid adsorbent materials is governed by the physical adsorption of gas molecules by a solid material. An understanding of the adsorption phenomena, theories, and their applications is vital for the successful completion of the system modeling and experimentation objectives required for this work. The following chapter provides an overview of adsorption fundamentals and theories governing hydrogen storage on highly porous materials.

2.1 Introduction to Adsorption

Adsorption phenomena results from the close proximity of gas molecules with a solid surface (adsorbent) that creates an interfacial region with an increased gas concentration compared to the bulk gas phase. Adsorbent molecules exert a force field upon the gas molecules that are in close proximity, aggregating to form an interfacial layer consisting of the solid surface and gas molecules that are retained within the exerted force field between the solid and the bulk gas phases. The gas molecules retained within the interfacial layer are known as the adsorbate [26].

The force field, acting upon the adsorbate molecules from the solid adsorbent (resulting in physical adsorption) is generated from perturbations and fluctuations in charge distributions caused by the relatively weak Van der Waals interactions between gas molecules and numerous surface atoms [6]. Van der Waals forces result from permanent and induced dipole interaction in molecules and are the sum of Keesom interactions, Debye interactions, and London forces. Keesom interactions create an attractive force between molecules interacting and oppositely oriented permanent dipoles. A molecule with a permanent dipole can temporarily induce a dipole in a non-polar molecule, which results in an attractive force, known as Debye interactions. London dispersion forces stem from the interaction between two molecules possessing instantaneous dipoles that are caused by the random motion of electrons [27]. The adsorption force field acting on gas molecules from a solid is much weaker than covalent and ionic bonds and, as a result, low storage capacities are observed at room

temperature. The attractive energy generated by the Van der Waals interactions are on the same order as the energy of thermal motion of the gas molecules at ambient conditions, making high storage capacities achievable at a lower magnitude of thermal motion, requiring low temperatures [28]. Once a monolayer of gas is adsorbed to the adsorbent surface, bulk gas molecules continue to interact with the adsorbate molecules present at the interfacial layer.

2.2 Excess and Absolute Adsorption

To fully evaluate and compare H_2 adsorption storage systems, it is necessary to quantify the supply of H_2 gas adsorbed by the adsorbent. This requires a distinction between adsorbed gas molecules and those remaining in the bulk gas phase. Gibbs', in an attempt to provide a solution, treated an adsorption system as two non-interacting bulk phases separated by a surface, known as the "Gibbs dividing surface" (GDS). Gibbs' proposed system treats the concentration of gas as constant up to the GDS at which point the concentration is that of the adsorbed molecules on the surface, and the gas concentration inside of the bulk solid is zero (depicted in Figure 2.1B) [29]. Therefore, total adsorbed gas decreases as the GDS approaches the solid surface.

The GDS model of the adsorption interface is in sharp contrast to the proposed "actual" interface of the adsorption system (Figure 2.1A) in which the bulk gas density remains constant up to the start of the interface and is followed by a subsequent increase in gas concentration within the adsorbed interface. The concentration of adsorbate within the interface increases to a maximum and subsequently decreases as the interfacial volume approaches the surface of the adsorbent. Similar to the GDS model, the concentration of gas inside of the bulk solid is zero at all locations [29].

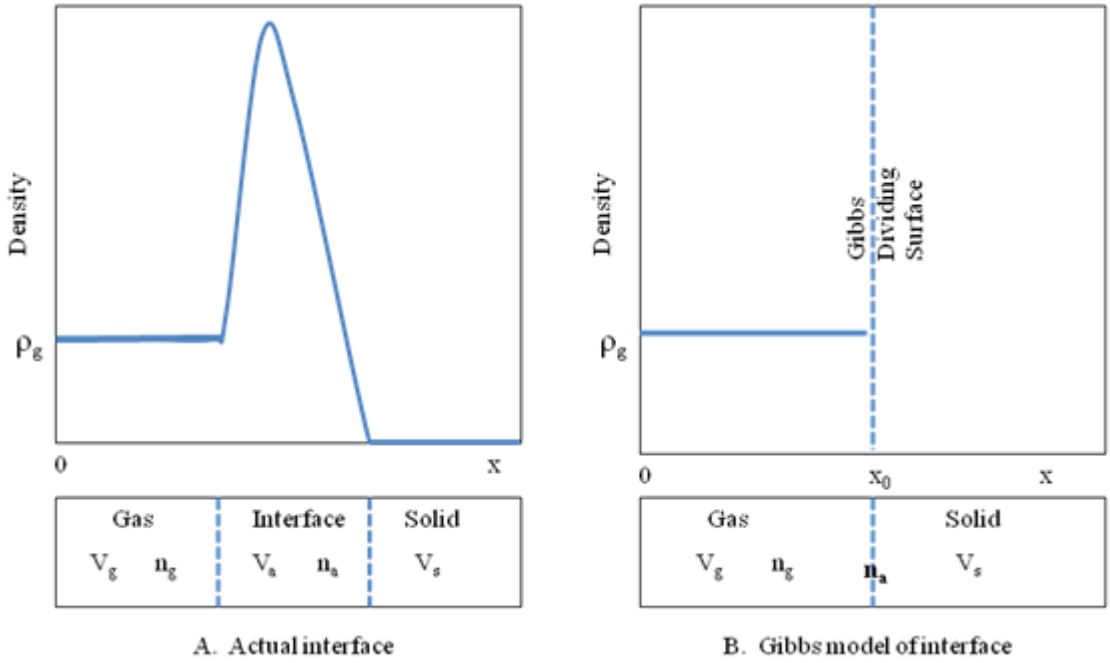

Figure 2. 1: Gas density profile near adsorbed interface (A) and the Gibbs' interpretation of the interface as a dividing surface (B) [29].

Thus the amount of gas adsorbed, n_a, is the difference between the total amount of gas present in the system, n_t, less the amount of gas occupying the bulk volume, n_g

$$n_a = n_t - n_g = n_t - V_g \rho_g \tag{2.1}$$

It is clear from (2.1) that it is necessary to obtain an accurate value for the volume occupied by the bulk gas phase to determine the amount of gas adsorbed. The gas volume is the difference in the total accessible void volume of the highly porous media, V_v, and the volume occupied by the adsorbed phase, V_a,

$$V_g = V_v - V_a \tag{2.2}$$

A known volume of helium gas, which is not known to be readily adsorbed ($n_a = V_a = 0$), is utilized in filling experiments to quantify the total accessible void volume of porous materials. With this convention, using He filling as a reference, the amount of gas adsorbed on the surface is known as the surface excess adsorption, n_{ex}, and is

defined as the total gas present in the system less the gas contained in the non-adsorbing volume

$$n_{ex} = n_t - \rho_g V_v \tag{2.3}$$

With the surface excess adsorption known, the absolute adsorption, n_a, is [30]

$$n_a = n_{ex} + \rho_g V_a = n_{ex} + \rho_g (V_v - V_g) \tag{2.4}$$

To illustrate, the absolute adsorption is equal to the gas adsorbed on the surface of the adsorbent, plus the gas located in the adsorption volume, V_a, at the bulk phase gas density, ρ_g, as depicted in Figure 2.2A below. The surface excess adsorption (Figure 2.2B) is defined as the amount of gas inside the pore less what would be present in the pore in the absence gas-solid interactions [31].

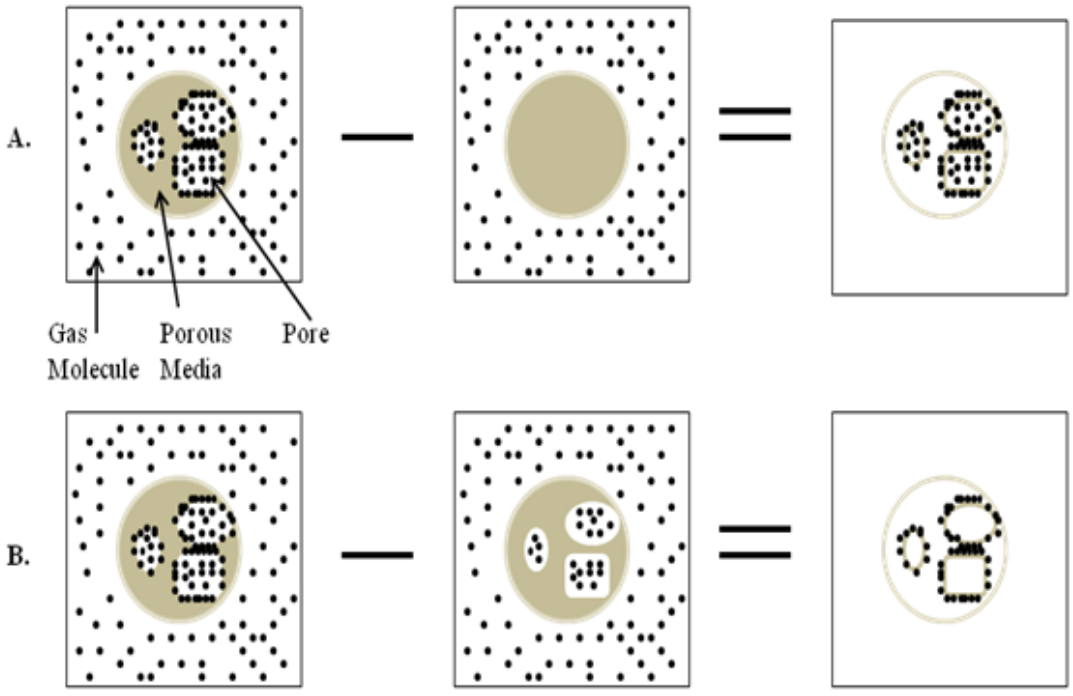

Figure 2. 2: Representation of absolute adsorption (A) and surface excess adsorption (B) [31].

Adsorption isotherms describe the adsorption system's capacity as a function of pressure at a constant temperature, which allows the effects of temperature to be

easily visualized by comparing multiple isotherms at once. Although the absolute and excess adsorption isotherms demonstrate an increase in adsorption capacity with decreasing temperature, their responses diverge at low temperatures and high pressures. At low temperatures (<125 K) the absolute adsorption isotherm demonstrates increased adsorption capacity with increasing pressure. However, the increase in adsorption capacity appears to near saturation and further pressure increases do not result in substantial increases in storage capacity.

The excess adsorption isotherms demonstrate an increase in adsorption capacity with increasing temperature until a maximum capacity is reached. At this point, further pressure increases result in a decreased adsorption capacity. The pressure at which the maximum adsorption is reached varies directly with storage temperature. The maximum excess adsorption capacity is observed when the pores begin to saturate with adsorbed gas molecules and increases in pressure result in a greater increase in bulk gas density than the corresponding increase in density of the adsorbed phase, resulting in a negative change in excess adsorption [31].

2.3 Adsorption Theories and Isotherms

Like many materials, adsorbents demonstrate a wide variety of material properties including: density, porosity, surface area, and pore volume. To distinguish between different classes of adsorbent materials, the International Union of Pure and Applied Chemistry (IUPAC) recommends the following pore size classifications of pore structure: micropores consist of pores with a width less than 2 nm, mesopores have pore widths between 2 nm and 50 nm, and pore widths greater than 50 nm are designated macropores [32]. Adsorption theory has developed to accommodate varying degrees of adsorbent-adsorbate interactions depending on the pore size designation and to include the various affects of adsorbent-adsorbate interactions within the porous adsorbent. As a result of differing adsorbent theories, a number of isotherms have been proposed to predict the quantity of gas adsorbed by the adsorbent as a function of the system pressure and temperature; this section will introduce the progression of both adsorption theory and the corresponding isotherms.

2.3.1 Langmuir Isotherm

The American scientist, Irving Langmuir, put forth a simplified and basic approach to describing gas-solid adsorption systems. The Langmuir model focuses solely on adsorbate-adsorbent interactions within the system while completely neglecting the affects of adsorbate-adsorbate interaction. By neglecting the interaction of gas molecules in the bulk phase with adsorbed gas molecules, only a monolayer of gas is capable of adsorbing on the surface of the adsorbent material, rendering the applicability of Langmuir's model to low pressure high temperature systems [33]. Langmuir's model assumes that an adsorbent contains a finite number of identical adsorption sites per unit area and that open sites, B_L, may reversibly interact with a bulk gas molecule, A_L, to create an adsorbed gas molecule, AB_L, such that

$$A_L + B_L \leftrightarrow AB_L \tag{2.5}$$

and, therefore, an equilibrium is established between open adsorption sites, the bulk gas molecules, and adsorbed phase

$$K_L = \frac{[AB_L]}{[A_L][B_L]} \tag{2.6}$$

K_L is the equilibrium constant and the brackets in (2.6) indicate the concentration of the species contained within. Therefore, the concentration of the bulk gas phase is proportional to the pressure of the bulk gas, p_L, and by defining the fraction of surface coverage as

$$\theta_L = \frac{[AB_L]}{[AB_L]+[B_L]} \tag{2.7}$$

it implies that the concentration of open sites, B_L, is proportional to $(1-\theta_L)$. Substituting the fractional surface coverage into (2.6) yields

$$K_L = \frac{\theta_L}{p(1-\theta_L)} \tag{2.8}$$

Finally, (2.8) is rearranged to solve for the fractional surface coverage

$$\theta_L = \frac{K_L p}{(1 + pK_L)} \tag{2.9}$$

The adsorbed monolayer surfaced coverage is predicted by (2.9), commonly referred to as the Langmuir isotherm [34]. Langmuir noted, following the derivation of (2.9), a proportionality between surface coverage and system pressure exists (at low temperature and pressures) that begins to diminish at higher system pressure as the surface nears saturation, complete monolayer coverage. A strong temperature dependency of the adsorption equilibrium constant was recognized by Langmuir's observation of a low but proportional increase in adsorbed concentration with pressure (even at high system pressures) at elevated system temperatures [35].

Following monolayer adsorption theory, Zuttel (2003) concludes that the minimum surface area required to achieve monolayer adsorbate coverage on an adsorbent surface, S_{ml}, is

$$S_{ml} = \frac{\sqrt{3}}{2}\left(\sqrt{2N_A}\frac{M_g}{\rho_{g,liq}}\right)^{\frac{2}{3}} \tag{2.10}$$

In (2.10), N_A is Avogadro's constant and M_g and $\rho_{g,liq}$ are the molar mass of the adsorbate and the liquid density of the adsorbate, respectively. From (2.10), Zuttel has calculated the monolayer surface area of hydrogen to be nearly 86,000 $m^2\,mol^{-1}$ [23].

2.3.2 BET Isotherm

Although the Langmuir isotherm has been implemented successfully in numerous adsorption systems, three scientists, Brunauer, Emmett, and Teller, expanded the Langmuir model to multi-layer adsorption of gas by including the interaction of adsorbed gas with bulk phase gas in an attempt to improve the accuracy of predicting the performance and storage capacity of an adsorption system. The aptly named BET isotherm was developed on the assumption that adsorbed molecules

possess the capability of inducing dipoles in molecules of the bulk gas to create the binding affinity needed to allow for multiple layers of molecules to adsorb. BET proceeded with Langmuir's assumption that each surface adsorption site could adsorb at most one gas molecule; however, their extension of the Langmuir model allows each adsorbed molecule to adsorb an additional molecule. Multi-layer adsorption must satisfy the requirement of maintaining an equilibrium between the bulk gas and the uppermost adsorbed layer [36].

The adsorption energy of additional layers of gas molecules is less than the adsorption energy required to adsorb on the surface of the bare solid and is equal to the heat of liquefaction of the gas at the specified temperature and equilibrium pressure. Additionally, it was proposed that the number of adsorbed layers would approach infinite when the adsorption system reaches the saturation pressure.

The BET isotherm developed to predict the volume of adsorbed gas at saturation pressure, i.e. infinite adsorbed layers, is [37]

$$a_{BET} = \frac{1}{(1-x)} \frac{a_{m,BET} c_{BET} x}{[1+(c_{BET}-1)(x)]}; x = \frac{p}{p_0} \tag{2.11}$$

And for a finite number of adsorbed layers, pressure less than saturation, is

$$a_{BET} = \frac{a_{m,BET} c_{BET} x}{(1-x)} \frac{[1-(n+1)x^n + nx^{n+1}]}{[1+(c_{BET}-1)x - c_{BET} x^{n+1}]} \tag{2.12}$$

In (2.11) and (2.12) a_{BET}, $a_{m,BET}$, p_0, and n are the amount of adsorbed gas, amount of adsorbate necessary for a complete surface monolayer, saturation pressure, and number adsorbed layers, respectively. The BET constant, c_{BET}, is found to be approximately [36]

$$c_{BET} = e^{\left(\frac{E_1 - E_L}{RT}\right)} \tag{2.13}$$

E_1, E_L, R and T are the heat of adsorption of the first surface layer, the heat of liquefaction, ideal gas constant, and the system temperature, respectively. The theory that additional adsorbed layers are formed by the condensation of gas molecules on the surface of previously adsorbed layers limits the application of the BET isotherm to adsorption systems at or below the boiling temperature of the pressurized gas.

The BET isotherm has proven an effective tool in describing the adsorption process of gas in macro and mesoporous materials, for which additional surface interactions with adsorbate through the surface layer would be minimal, due to the focus of adsorbate-adsorbate interactions leading to multi-layer formation. However, the BET method does not accurately describe the adsorption in microporous systems in which the binding affinity is greatly enhanced by the close proximity of gas to multiple surfaces [33].

Although the BET isotherm is most applicable to macro and mesoporous materials, it is still commonly used to determine the surface area of a variety of porous materials, including microporous materials, from N_2 gas adsorption at ~77 K. The BET surface area of an adsorbent is determined using a linearized form of (2.11)

$$\frac{x}{a_{BET}(1-x)} = \frac{1}{a_{m,BET}c_{BET}} + \frac{c_{BET}-1}{a_{m,BET}c_{BET}}x \tag{2.14}$$

and plotting the term on the left hand size of (2.14) versus x. The y-intercept of the resulting plot is equal to the first term in the right hand side of (2.14) and the slope of the line is equal to the second; therefore, the two values can be defined by the y-intercept, y_{BET}, and the slope, m_{BET}, as

$$a_{m,BET} = \frac{1}{y_{BET} + m_{BET}} \tag{2.15}$$

$$c_{BET} = 1 + \frac{m_{BET}}{y_{BET}} \tag{2.16}$$

Finally, the adsorbent surface is calculated from the amount of gas required for mono-layer coverage and the area occupied by a single adsorbate molecule at its normal boiling point, 0.162 nm^2 for nitrogen [37].

2.3.3 Theory of Volume Filling of Micropores

The treatment and characterization of microporous adsorbent systems extends beyond those developed for mesoporous materials and adsorption of gas on a flat surface. The development of additional theory to describe microporous adsorption systems stems from the increase in adsorption energy exerted on the adsorbate from overlapping adsorption fields of adsorption sites located on opposite walls, owing to the micropore being of similar dimensions as the interacting adsorbate molecule. Thus, Dubinin and co-workers formulated the theory of volume filling of micropores (TVFM) as an extension to the previously validated potential theory put forth by Polanyi [38].

TVFM is built on the assumption that the overlapping of temperature independent adsorption potentials arise from differences in inducing polarization of gas molecules by an adsorbent, defining the affinity coefficient, β, as the constant ratio of adsorption potentials required for two gases to have identical filling of the same adsorbent [38].

Dobruskin (1998) demonstrated that the presence of a monolayer of adsorbed gas on the surface of a micropore increases the adsorption affinity in the open region of the pore compared to the first layer. Therefore, as the micropore volume fills with increasing pressure, the overlapping adsorption potentials become numerous, further enhancing the adsorption potential of the adsorbate, leading to continued adsorption within the micropore volume. As the system pressure nears the saturation pressure, the adsorbate within the micropore is liquefied and the process continues as the micropore is filled. Additionally, according to TVFM, as filling of the micropore volume proceeds, the liquid adsorbate present becomes highly compressible as system temperature approaches the adsorbate's critical value. The increase in compressibility

of the liquid within the adsorption force field is of higher density than what would be observed for a liquid in free space [38, 39].

The most commonly used equation describing the adsorption of gas in homogeneous microporous solids is the Dubinin-Radushkevich (DR) model [40]

$$n_a = n_{\max} e^{\left(-\left[\frac{A}{\beta E_0}\right]^2\right)} \tag{2.17}$$

where n_a, n_{max}, and E_0 represent the absolute amount of gas adsorbed, limiting amount of adsorbed gas at saturation, and the characteristic adsorption energy of the reference adsorbate gas, respectively. The differential molar work, A, of adsorption is a function of the ratio of saturation pressure to system pressure

$$A = RT \ln\left(\frac{p_0}{p}\right) \tag{2.18}$$

The DR isotherm has been an effective tool in determining the equilibrium adsorption values of a variety of gases on homogeneous microporous adsorbents, typically at lower pressures and subcritical temperatures. However, its direct application to heterogeneous adsorbents has proven problematic and has led to a number of variations. One method investigated was the expansion of the DR model to be the summation of DR models, in which the right hand side of (2.17) is independently represented for each narrow microporous range, and the summation of all pore size ranges, therefore, satisfies the entire heterogeneous material. Each independent adsorption term exhibits independent parameters for the limiting adsorption amounts and adsorption energies. Thus for an adsorbent with two narrow ranges of micropores the DR model becomes [41]

$$n_a = n_{\max,1} e^{\left(-\left[\frac{A}{\beta E_{0,1}}\right]^2\right)} + n_{\max,2} e^{\left(-\left[\frac{A}{\beta E_{0,2}}\right]^2\right)} \tag{2.19}$$

Dubinin and Astakhov (DA) model only differs from the DR equation by the substitution of the exponent, 2, in (2.17) with the variable, *n*

$$n_a = n_{\max} e^{\left(-\left[\frac{A}{\beta E_0}\right]^n\right)} \tag{2.20}$$

This three-parameter DA model is assumed to describe a system of nonhomogeneous adsorbent materials for cases of *n* between one and two [40].

2.3.4 Extending Dubinin-Astakhov Model For Supercritical Gases

A common theme of the three adsorption theories outlined above is the occurrence of a phase change of the gaseous adsorbate to a liquid, or liquid-like, state as the system pressure approaches the saturation pressure of the bulk phase. However, as system temperatures exceed the critical temperature of the bulk phase, the laws of physics prevent a gas from liquefying at any exerted pressure [42]. The prevention of adsorbate condensation taking place would limit the adsorption of gas on any type of surface to a single monolayer.

Gas adsorption above the critical temperature is important for hydrogen storage in highly porous adsorbent materials due to hydrogen's extremely low critical temperature (~33 K). Despite surpassing the physical limitations of the parameters of the DA model above the critical temperature, saturation pressure and limiting capacity of adsorbed gas, researchers continue to utilize its form to characterize adsorption systems and expand TVFM theory to systems above the critical temperature and up to high pressures.

At supercritical temperatures and low pressures, the overlapping of adsorption potentials inside of micropores continues to enhance the effects of adsorbent-adsorbate interactions; however, the observed adsorption inside of the pore is limited. At higher system pressures, the adsorption limitations inside the micropore are overcome and the adsorbed volume approaches the total micropore volume [43, 44]. In the development of modified DA or DR models, these observations have led to the treatment of the

adsorbed state, referred to as a quasi-vapor [43] and over-heated liquid or quasi-liquid [45] as a function of a non-physical vapor, saturation, or limiting pressure.

The supercritical saturation pressure was first utilized by Dubinin and estimated by extrapolating the pressure-temperature relationship of a specific adsorption system [43]; others have obtained this supercritical value by extrapolating the log of vapor pressure data obtained from property handbooks [46]. Poirier *et al.* (2008) utilized a correction relation to calculate the pseudo-saturation pressure of a supercritical system based on a scaling parameter that is specific to the adsorbent-adsorbate pair investigated. The correction relation, (2.21), for the pseudo-saturation pressure, P_0, is a function of the scaling parameter, γ; the critical pressure of the adsorbate, P_c; and the ratio of the system temperature to the adsorbate critical temperature, T_c [47]

$$P_0 = \left(\frac{T}{T_c} \right)^{\gamma} P_c \tag{2.21}$$

The use of a limiting pressure of a supercritical adsorbent system is an alternative approach to corrections and correlations for the pseudo-saturations or supercritical saturation pressure. The limiting pressure corresponds to the maximum attainable adsorption capacity of an adsorbent-adsorbate system, i.e. the capacity will begin to decline above the limiting pressure [45]. The limiting pressure approach was formulated by the observation that the adsorption capacity of various linear isotherms (of a specific system) converge at a single pressure and subsequently diverge as the pressure continues to increase [42].

One of the original assumptions of the TVFM by Dubinin (1960) is that the characteristic adsorption energy of the gas, E_0, is independent of temperature (although he stated it was not mandatory but often observed [38]). As this was observed to be invalid for supercritical adsorption over a wide temperature and pressure range, the following temperature dependent relationship was proposed

$$E_0(T) = \alpha + \beta T \tag{2.22}$$

in which α is the enthalpic factor and β is the entropic factor of the adsorption energy term. The substitution of (2.22) into (2.20) yields the modified DA equation in terms of moles of adsorbed gas per unit mass of adsorbent

$$n_a = n_{\max} e^{\left(-\left[\frac{RT}{\alpha+\beta T}\right]^n \ln^n\left[\frac{P_0}{P}\right]\right)} \tag{2.23}$$

Equation (2.23) calculates the absolute adsorption, n_a, as a function of the limiting adsorption, n_{max}, and pseudo-saturation (or limiting) pressure, P_0 [48].

The DA, or modified DA, equation has proven to accurately predict the performance of supercritical gas adsorption on highly porous adsorbents when used with a pseudo-saturation (or limiting) pressure term when compared with experimental data [45 - 48]. The team of Clarkson *et al.* used a single adsorption data set to compare the performance of the Langmuir isotherm, BET isotherm, and the modified DA equation in predicting adsorption phenomena. The modified DA equations demonstrated only a 0.5% relative error compared to 5.0% and 2.1% relative error for the Langmuir and BET isotherm, respectively, for a supercritical system [46].

The success of the DA model in predicting supercritical gas adsorption has strengthened the argument that multi-layer adsorption and the TVFM are possible mechanisms for adsorption systems above the critical temperature of the adsorptive over a wide range of pressures. The supercritical adsorption phenomena is the result of an increase in adsorption potential acting on the adsorbate from overlapping force fields of surfaces in the confined space of a micropore.

Chapter 3: Adsorbent Materials

Numerous porous and non-porous materials have demonstrated the capability of storing diatomic hydrogen by physical adsorption, including graphite sheets, carbon nanotubes and fibers, zeolites, alumina, silica, activated carbons (AC), and metal-organic frameworks (MOF). Although all of these materials have a varying degree of surface area and pore volume, ACs and MOFs demonstrate increased hydrogen storage performance compared to many of the materials listed [49]. Consequently, ACs and MOFs have been chosen as the materials of interest for this investigation. A brief overview of both classes of materials and the materials used in this investigation will be provided in this chapter.

3.1 Activated Carbon

Activated carbon gained notoriety as a potential hydrogen storage material due to its highly porous structure, variety of starting materials, and the abundance of inexpensive materials utilized in its production and activation. One of the most common starting materials for activated carbon is bituminous coal because it is inexpensive, durable, and highly abundant throughout the world [50]. In addition, activated carbon is produced in a variety of regions and climates throughout the world; macadamia nutshells, coconut shells, olive stones, and even chicken feathers are being used as the starting material [51–53].

A physical or chemical activation pathway achieves the manufacturing of the highly porous adsorbent activated carbon material. Physical activation, a two-step process, begins with the production of char from the starting material by carbonization at elevated temperatures in an inert gas atmosphere. The subsequent activation of char product is achieved by oxidation at elevated temperatures using CO_2 or steam as the activating agent [50]. The oxidizing agent used in physical activation of char initiates the burning of interior material structure, leaving behind a porous framework. Different combinations of burn-off rate and activating agent result in a variety of porous structures within the activated carbon product. Rodriguez-Reinoso *et al.*

(1995) investigated the effect of the activation process on the pore structures of activated carbon and concluded that physical activation by steam produces a final product with higher percentage of meso and macropores due to the continuous widening of micropores throughout activation. Additionally, steam activation produces larger quantities of CO and H_2 gas, which inhibit the oxidation process, and the presence of inhibitors inside the porous structures results in the oxidation of the external surface, which diminishes surface pores. CO_2 activation leads to a higher percentage of micropores compared to meso and macropores within the structure compared to steam activation of carbon, corresponding to an increase in micropore volume [52].

Chemical activation is a single step process that includes the carbonization of raw material by a dehydrating agent at moderate temperatures; common activation agents include potassium hydroxide (KOH), phosphoric acid (H_3PO_4), and zinc chloride ($ZnCl_2$). Activation typically begins with the milling of raw material in the presence of an activating agent prior to heating [51]. Chemical activation results in higher yield of carbon structure and an increase in porous structure development compared to physical activation; however, chemical activating agents are more expensive and less environmentally friendly [54]. Activation by phosphoric acid and potassium hydroxide have demonstrated improved production of microporous structures, micropore volume and a narrower pore volume distribution compared to those produced by a physical activation [50, 54]. The team of Ahmadpour and Do (1997) observed a significant increase in total BET surface area and micropore volume in activated carbon samples prepared by zinc chloride compared to those activated by potassium hydroxide [51].

The activation process used in the production of activated carbon yields products with a variety of micropore volume and porous surface area. Texier-Mandoki *et al.* (2004) investigated a variety of activated carbons with a wide range of

porous surface areas and micropore volumes and observed a linear relationship between both properties and the hydrogen storage capacity of the material [55].

3.2 Metal-Organic Frameworks

Metal organic frameworks are the second class of materials used in this investigation. This up-and-coming porous material structure has been the focus of numerous research investigations for gas adsorption, gas purification/separation, catalysis, and materials development [56]. The synthesis of the crystalline material joins organic linkers to a secondary building unit (SBU), consisting of metal ions or metal clusters; the resulting three-dimensional structure is comprised of uniform, stable, and repeated cubic cavities and channels capable of hosting a variety of guest molecules [57, 58].

Multiple combinations of organic linkers and SBUs has resulted in the synthesis of a wide range of unique, highly porous materials exhibiting surface areas under 100 $m^2 g^{-1}$ to those exceeding 4500 $m^2 g^{-1}$. The hydrogen storage capability of MOF was first reported in 2003 and since then at least 60 different MOF composites demonstrating at some uptake of diatomic hydrogen have been identified. Wide ranges of atmospheric hydrogen adsorption at 77 K are reported in literature with capacities reaching as high 2.59wt%, and, similar to AC adsorbents, MOFs exhibit a near linear relationship between hydrogen adsorption capacity and adsorbent surface area [58].

Due to the large number of organic linker and SBU combinations available, MOFs are often described as a tunable porous structure because material properties, such as surface area and pore size, can be enhanced or suppressed depending on the combination of synthesis materials. The preparation of MOFs with a fine, uniform micropore structure has been sought through the use of smaller organic linkers to compose the rigid porous framework. The development of a MOF structure with a pore radius on the order of the dihydrogen molecule could lead to improved hydrogen adsorption resulting from an increase in overlapping adsorption potential of multiple

adsorbent surfaces in close proximity to the adsorbate molecule [59]. Collins *et al.* (2007) have produced an extensive list of synthesized MOFs with their characteristics and hydrogen adsorption capabilities [58].

Increasing the adsorption interactions between hydrogen and the adsorbent surface will increase the strength of the adsorption field, which would be identified by an increase in the heat of adsorption. Numerous investigations have focused on increasing the heat of adsorption, and thus the adsorbent-adsorbate interactions, of hydrogen on porous MOFs by methods other than tuning pore sizes, including the addition of dissociative catalyst particles, platinum and palladium, and the use of exposed metal sites inside of the SBU. It is believed that the successful synthesis of a MOF with a heat of adsorption of approximately 15 kJ mol^{-1} is necessary to obtain substantial room temperature hydrogen adsorption at pressures lower than 30 bar [59].

3.3 Materials for the Experimental Investigation

The adsorbent materials for the experimental investigation of this work are porous activated carbon and metal-organic framework 5, MOF-5. Both materials were procured from Oregon State University's partners in the DOE's Hydrogen Storage Engineering Center of Excellence (HSECoE). The activated carbon sample was obtained from Institut de recherche sur l'hydrogène at Université du Québec à Trois-Rivières in Québec, Canada and is believed to be similar to AX-21, however, no definitive identification of the material or adsorption properties have been provided. The MOF-5 samples were obtained from the production line of BASF through Ford Motor Company.

Figure 3.1 and Figure 3.2 compare the storage capacity of two solid-state storage materials, AC (represented by AX-21) and MOF-5, and a compressed H_2 tank at temperatures of 77 and 160 K over a pressure range of 1 to 60 bars. Although the additional storage capacity of a solid-state system diminishes with increasing temperature, both materials demonstrate an increase in storage capacity over a compressed gas system.

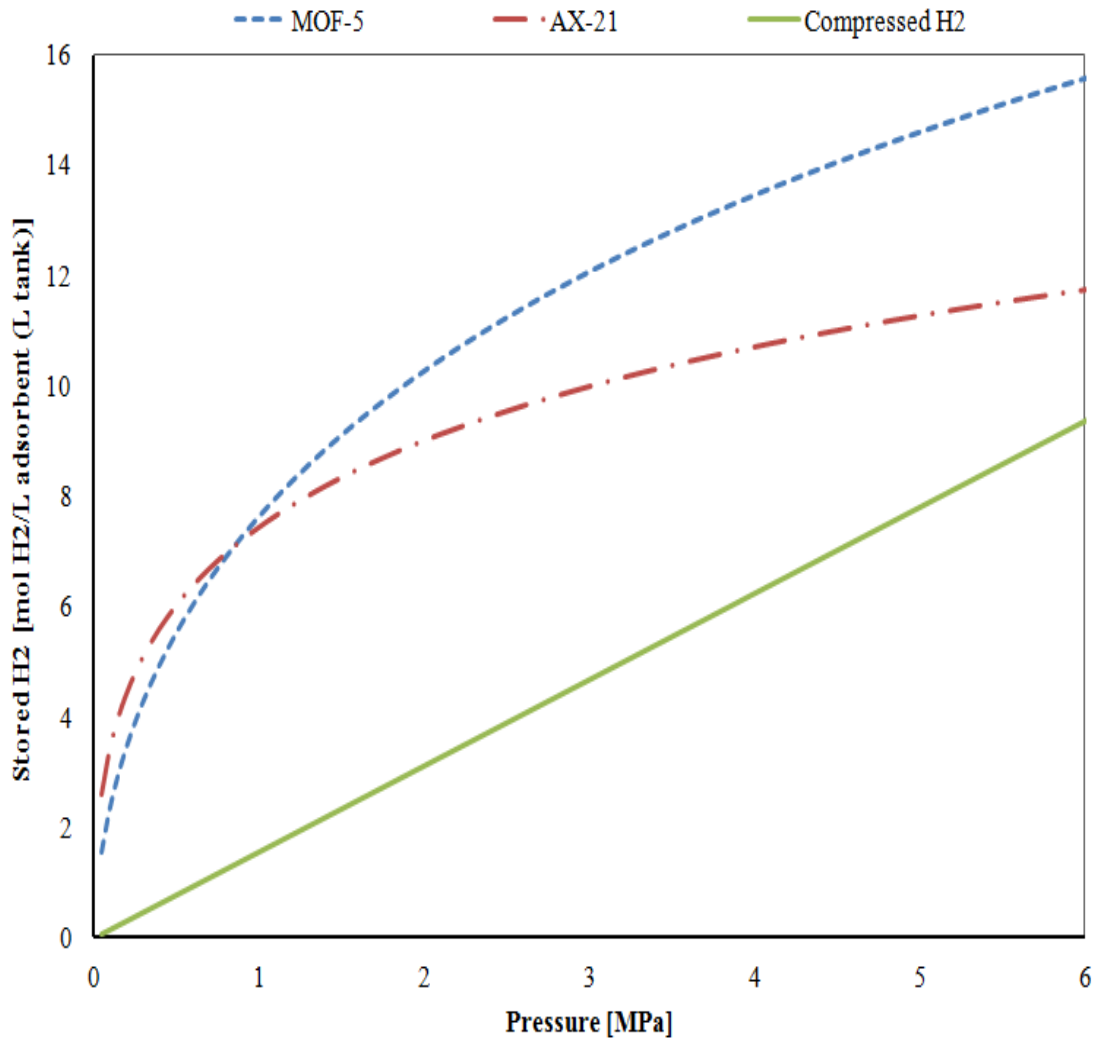

Figure 3.1: Comparison of stored H_2 gas at 77 K up to 6 MPa for MOF-5, AX-21, and Compressed gas systems.

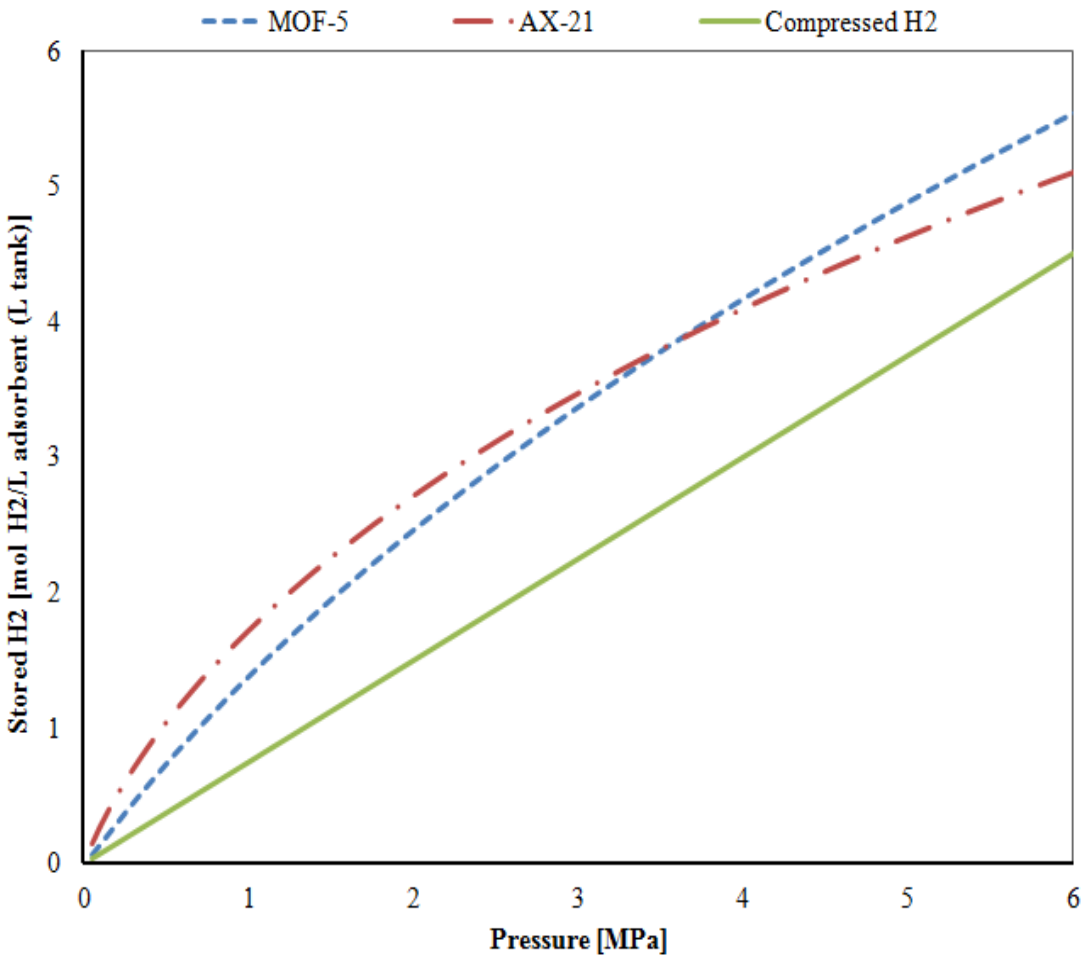

Figure 3.2: Comparison of stored H2 gas at 160 K up to 6 MPa for MOF-5, AX-21, and Compressed gas systems.

3.3.1 Activated Carbon

The activated carbon sample obtained for this investigation arrived as a compressed monolithic bed. Monolithic beds of AC have been used in research and system analysis since the early 1990s and were originally created for the storage of methane. The production of compressed monolithic beds increases the volumetric storage density of adsorbed gas in an activated carbon system by increasing the bulk density of the adsorbent material; thus increasing the number of adsorption sites per unit volume.

Monolithic compacts are produced by pressing a mixture of AC particles and a binding agent. Prior to the addition of the binder, AC particles are wetted with a solvent, to allow the solvent to enter inside the pores of the adsorbent material and prevent the binder from entering and clogging the pores. The wetted carbon is mixed with a small amount of binding agent, consisting of a thermoplastic such as polyvinyl alcohol, to create a slurry of particles in binder, approximately 10wt% binder. The adsorbent containing slurry is subsequently placed in a cylindrical dye and hydraulically pressed while slowly heating to a temperature just above the melting temperature of the binder.

Following compression, the compacted AC bed is heated above the boiling point of the solvent in a vacuum to open the pores previously filled with solvent solution. Additional heating of the compacted material pyrolyzes the binding agent to form a carbonized bed of adsorbent [60, 61].

The formation of a monolithic bed results in a decrease in the adsorbent surface area and minimal loss in micropore volume. The higher decrease in surface area compared to micropore volume stems from the loss of meso and macroporous structure during compression [62, 63]. The effects of the compaction process on the adsorption parameters can be seen below.

Table 3.1: Change in adsorption parameters in activated carbon following densification.

Skeleton Density [g cm^{-3}]	2.2	[64]
Tap Density [g cm^{-3}]	0.3	[33]
Pore Volume[cm^3 g^{-1}]	1.6	[64]
BET Surface are [m^2 g^{-1}]	2800	[33]
Pelletized Density [g cm^{-3}]	0.47	[33]
BET Surface are [m^2 g^{-1}]	2000	[33]

The activated carbon used in this experiment can be seen in Figure 3.3. Figure 3.3A is a sample of activated carbon powder received with the compressed packed

bed. Figure 3.3B is the sample of compressed AC prior to machining, 1.3" tall and 2.0" diameter with a bulk density of 0.7 g cm^{-3}, and Figure 3.3C is the machined compressed bed following the experimental investigation performed for this work. The machining process allows the bed to be placed over the headers of the novel microchannel heat exchanger developed for this investigation. Additionally, six holes are drilled into the bottom surface of the compressed bed to allow for the insertion of thermocouples at various depths and two radii to capture the temperature profile within the material during the experiments. The application of latex paint to the outer bed perimeter promotes gas to enter the bed through the bottom surface by minimizing the flow through the painted surface during experimental trials.

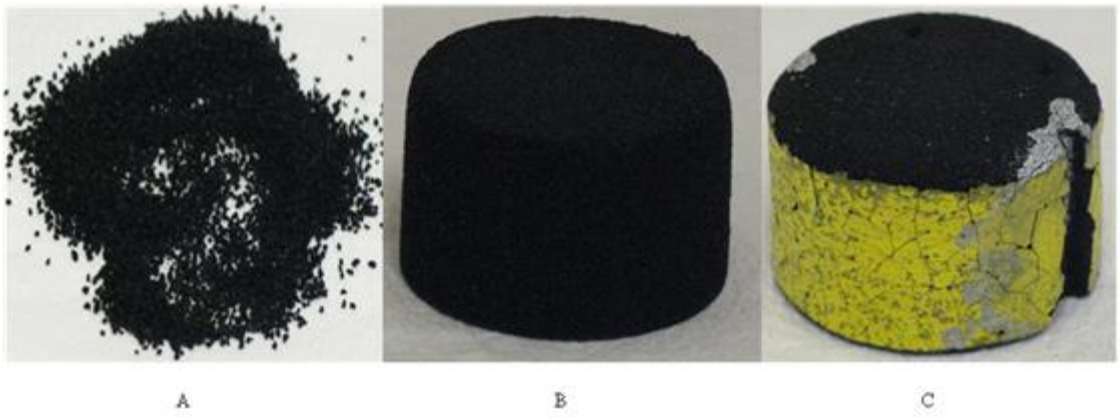

Figure 3.3: Pictures of AC powder particles (A), un-machined compressed AC bed (B), and the compressed bed following AC experimental trials of this work (C).

Although machining of the AC sample was performed in open air, the sample was quickly returned to a vacuum chamber for storage to minimize continued exposure to air.

3.3.2 Metal Organic Framework – 5

The MOF-5 sample bed used for this work arrived as a physically compressed bed without the addition of a binding agent. The physically compressed samples are prepared by hydraulically pressing MOF-5 powder loaded into a 2.0" diameter dye. A compressed MOF-5 sample with bed density 0.3 g cm^{-3} has demonstrated a slight reduction in BET surface area and adsorption volume of only 1.7 and 1.5%,

respectively, while increasing the maximum hydrogen adsorption by 2.1wt% compared to uncompressed MOF-5 powder samples with a density of 0.13 g cm^{-3}. Decreases in surface area and adsorption volume become much larger with increasing density of the compressed material; however, higher density materials also display a decrease in hydrogen adsorption, with respect to weight percent adsorbed [65]. Adsorption studies performed by Ford Motor Company have shown that densification of MOF-5, with density of approximately of 0.3 g cm^{-3}, has no impact on the gravimetric H_2 capacity while improving the volumetric storage capacity by a factor of two. The densification of MOF-5 at 0.5 g cm^{-3} exhibits a 20% drop in gravimetric capacity that is offset by a fourfold increase in volumetric capacity [66]. The minimal change in adsorption parameters observed in MOF-5 following densification to 0.3 g cm^{-3} are listed below.

Table 3.2: Change in adsorption parameters in MOF-5 following densification.

Skeleton Density [g cm^{-3}]	2.03	[67]
Tap Density [g cm^{-3}]	0.13	[67]
Pore Volume[cm^3 g^{-1}]	1.36	[65]
BET Surface are [m^2 g^{-1}]	2763	[65]
Pelletized Density [g cm^{-3}]	0.3	[65]
Pore Volume [cm^3 g^{-1}]	1.34	[65]
BET Surface are [m^2 g^{-1}]	2716	[65]

Table 3.3 shows the dimensions and packing density of the seven MOF-5 samples compressed in a 2.0" diameter dye and received from our partners at Ford Motor Company; sample #3 is used in the experimental investigation of this work. Figure 3.4, below, is a sample of powder MOF-5 (Figure 3.4A) and the compressed MOF-5 bed used in the experimental investigation of this work (Figure 3.4B).

Table 3.3: Samples of compressed MOF-5, provided by Ford Motor Company, for this investigation.

Sample #	Mass (g)	Height (cm)	Diameter (cm)	Density (g cm^{-3})
1	46.674	6.288	5.08	0.3662
2	46.641	6.232	5.08	0.3693
3	23.195	3.282	5.08	0.3487
4	23.420	3.203	5.08	0.3608
5	11.863	1.718	5.08	0.3407
6	11.648	1.636	5.08	0.3513
7	11.776	1.700	5.08	0.3418

Figure 3.4: MOF-5 powder sample (A) and compressed bed used in this investigation (B).

Chapter 4: Thermal Management of Solid-State Hydrogen Storage Systems

An efficient and reliable thermal management system is required for the proliferation of solid-state hydrogen storage systems in the automotive industry. The nature of solid-state hydrogen systems requires the removal of generated heat during the storage process and the addition of heat to release stored hydrogen for consumption and energy production. Removing generated heat from adsorbent materials becomes increasingly difficult at cryogenic temperatures, especially considering the low thermal conductivities exhibited by many virgin adsorbent materials [68].

A hydrogen storage system's ability to remove generated heat has a direct impact on the systems storage capacity and, therefore, system size and weight necessary to store the 5.6 kg of H_2 required by the DOE. Figure 4.1 below, is an illustration of the importance of proper thermal management due to the significant decreases of storage capacity with increasing temperature. The initial storage capacity of a system at the start of re-charging, 5 bars and 125 K, is approximately 7 moles of H_2 per kg of adsorbent material. A 50 bar storage system with insufficient or no cooling during charging could finish at 160 K, capable of storing 15.5 moles H_2 per kg, however, if enough cooling is provided to remove only the heat generated during the charging process, to finish charging at 125 K, an additional 6.5 moles of H_2 per kg could be stored. With additional cooling, the material is able to finish charging at a lower temperature than it started, 100 K, the adsorbent material has nearly doubled its H_2 storage capacity, 29 moles of H_2 per kg. Insufficient or no cooling results in a lost storage capacity of 6.5 moles H_2 compared to a 7 mole per kg gain realized with additional cooling, and every mole of storage capacity gained decreases the system size required for total H_2 storage.

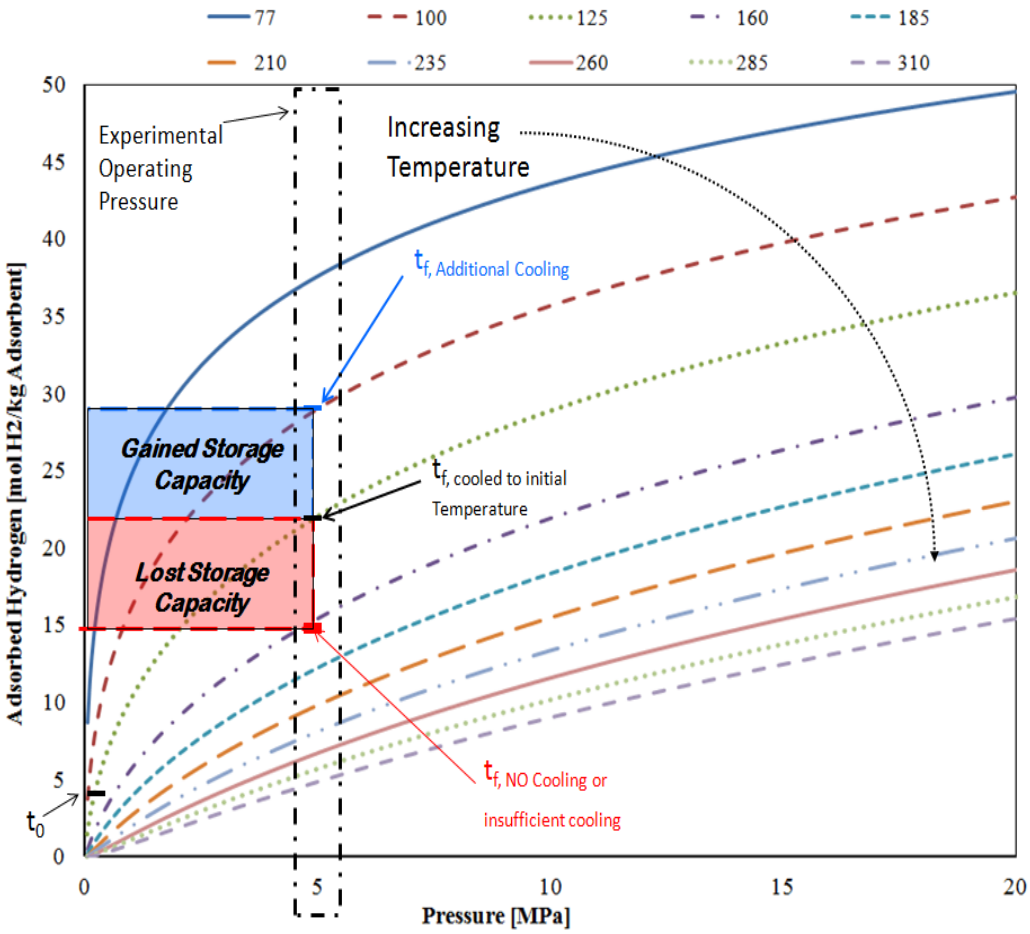

Figure 4. 1: Adsorption isotherms of AX-21 and the impact of cooling on storage capacity.

The remainder of this chapter will provide a review of the various thermal management systems proposed for solid-state hydrogen storage and introduce the thermal management system developed at Oregon State University for use in this dissertation work and future hydrogen vehicles.

4.1 Thermal Management Systems for Solid-State H_2 Storage

Although limited literature is available for thermal management systems for adsorbent hydrogen storage, there are a number of heat exchanger designs available for metal hydride storage that could be adapted for use in an adsorbent system.

Flow-through cooling is under investigation as a possible method of removing the generated heat in adsorbent systems. Cooling occurs by flowing excess quantities of cold hydrogen gas through the storage media during charging. While the material adsorbs a portion of the hydrogen sent into the tank, the remainder of the flowing gas convectively removes the generated heat and is recovered for later use. One benefit of flow-through cooling is the absence of any additional material needed inside of the tank for heat removal; however, a similar process cannot be used to add heat to the system to liberate stored hydrogen for consumption. The required heat for desorption is thus supplied by a helical coil resistance heater that reduces the storage volume in the tank for adsorbent material and consumes energy for operation [69]. The flow-through cooling method also requires materials that exhibit a high permeability capable of allowing high superficial velocity gas flow [70]. Adsorbent permeability will likely decrease with increasing bulk density of the adsorbent due to compaction and compression of materials. Further, it could potentially limit the application of flow-through cooling to loosely packed adsorbent beds, thus increasing the volume of adsorbent required to reach the 5.6 kg H_2 capacity.

In preliminary experiments, the flow-through system decreased the average adsorbent bed temperature from 300 K to 120 K in approximately 30 minutes using incoming hydrogen gas at 100 K. To illustrate the difficulty of removing heat at cryogenic temperatures, the flow-through device required approximately 19 minutes, nearly $^2/_3$ of the entire cooling time, to decrease the average bed temperature from 160 K to the final temperature of 120 [71].

Similar to adsorbent systems, metal hydride storage tanks require the removal of heat generated from hydride formation and an input of heat to liberate and reform H_2 gas for consumption, although metal hydrides operate at temperatures above ambient in contrast to the cryogenic temperatures necessary for adsorbent systems. This need has generated multiple investigations in the design and simulation of a variety of heat exchange systems for hydride storage tanks.

The group of Mellouli *et al*. (2007) utilized a spiral metal tube heat exchanger to circulate cooling fluid inside of lanthanum pentanickel ($LaNi_5$) packed bed. The group found that higher rates of heat transfer and lower cooling fluid temperatures increased the rate of hydrogen absorption but did not greatly influence the mass of absorbed hydrogen at equilibrium. The time required to reach 80% maximum hydrogen capacity dropped from 5,000 to 1,000 s using the spiral heat exchanger. Similarly, desorption rates increased with increasing fluid temperature and heat transfer coefficient [72].

Internal and external designs for improving heat transfer inside of a metal hydride system were investigated by Askri *et al.* (2009). The research concluded that the addition of fins to the external surface of the storage tank had no measurable increase in hydride bed cooling and that the thermal properties of material have a greater impact on cooling compared to the thermal mass of the storage tank, even for highly conductive tank materials. Additionally, the research group investigated the use of a fluid cooled tube-and-fin heat exchanger placed inside of the metal hydride tank. Similar to Mellouli's results, a significant improvement in storage time (80%) is observed with the use of an internal heat exchanger [73].

Other heat exchange designs have been investigated, including multiple fluid flow paths in the bed [74], and demonstrated the importance of material thickness and the distance between cooled surfaces on heat removal and charging time.

4.2 Additional Heat Transfer Improvements of Solid-State Materials

A significant challenge in thermal management of solid-state storage systems is the low thermal conductivity inherent in many adsorbent and hydride materials [68,75]. This has led researchers to investigate material additives aimed at increasing the thermal conductivity of the bulk storage material.

Thus far, one of the main additives of interest for increasing thermal conductivity of porous adsorbent materials is the use of expanded natural graphite (ENG) to varying degrees. The research team of Liu *et al.* (2012) created a series of

MOF-5 and ENG composites containing 1-10% ENG to investigate changes in thermal properties of the material as a function of ENG content. It was observed that neat MOF-5 samples exhibit an increase in thermal conductivity as a function of increased bulk density of the material and that the addition of 5-10% ENG increased the thermal conductivity of the sample significantly; larger increases were observed for higher density samples of the same composition. Adding ENG to MOF-5 results in slight increases to the heat capacity of the composite pellet for each density investigated and the largest increases were observed for the lowest density sample. Interestingly, small additions of ENG (less than 5%) resulted in higher BET surface area compared to neat MOF-5 samples of similar density; however, this demonstrated no improvement in H_2 storage capability as the maximum H_2 adsorption actually decreased [65].

A variety of materials and methods have been investigated for increasing the thermal conductivity of metal hydride materials, including metal foams, integrated copper net structures, packing material between fin-like structures, and encapsulation techniques [72]. Although the addition of thermal enhancement materials have demonstrated improved charging and discharging times, they have also resulted in a decrease in volumetric storage capacity due to the volume occupied by the additional material in the storage bed. Therefore, increasing the material required to improve thermal transport throughout the storage media continues to move the system performance away from the DOE's final storage targets.

4.3 Development of Novel Heat Exchanger and Gas Distribution Device

It is clear from the review presented above that quick and efficient heat exchange provides a tremendous advantage to the hydrogen storage system, especially for porous adsorbent materials such as ACs and MOFs, which demonstrate a strong temperature dependence on H_2 storage capacity. In addition to the importance of proper heat exchange, the size of the thermal management system is a critical aspect in ultimately meeting the DOE's system goals. Figure 4.2 illustrates the importance of

properly designing the thermal management system to minimize size and mass while providing high performance heat exchange.

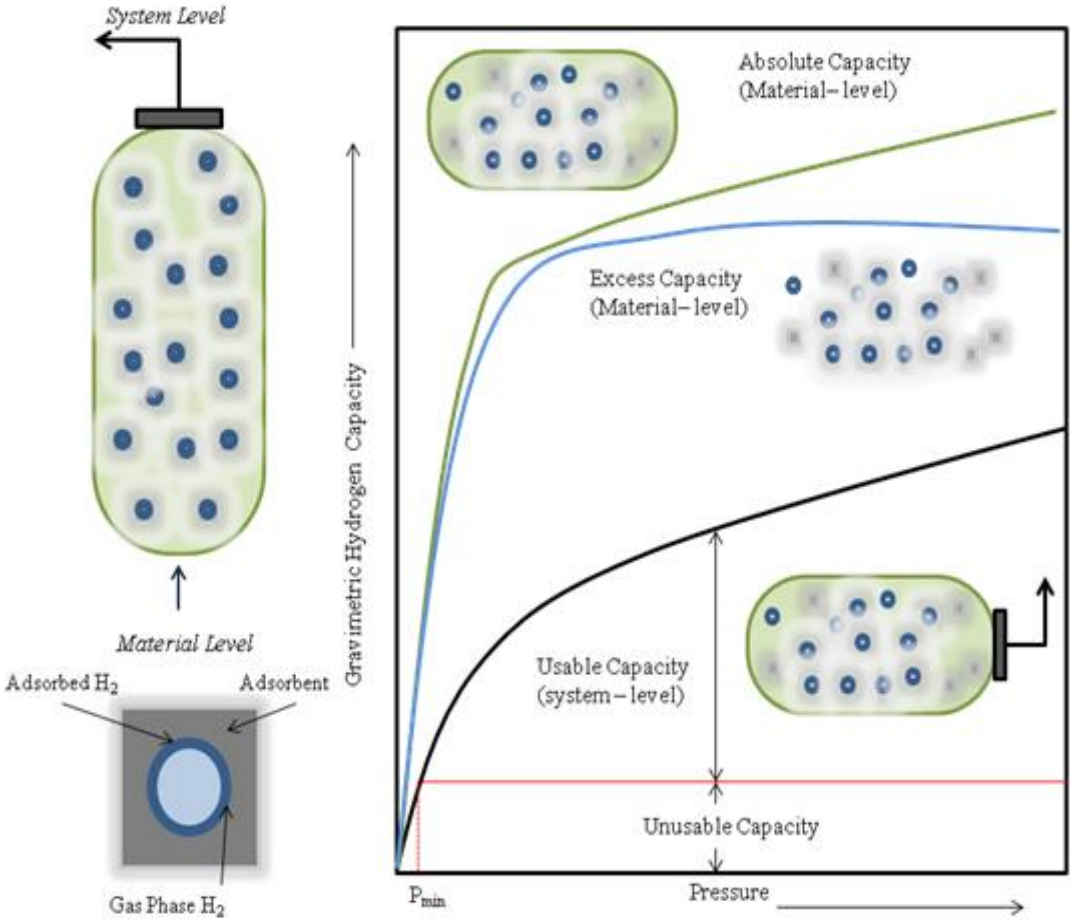

Figure 4.2: General representation of hydrogen storage capacity at material and system levels [75].

The hydrogen storage materials may exhibit high gravimetric capacities on their own; however, the fully constructed storage tank, with all required components, demonstrates a lower gravimetric capacity. The same trend exists for the volumetric capacity as well; therefore, a light, low-volume thermal management system will have a tremendous impact on maximizing the material capabilities while minimizing the size and weight of the entire storage system.

Microtechnology serves a number of industries by minimizing system size and weight while providing enhanced performance in heat exchange and mass transfer.

Minimizing diffusion distances and greatly enhancing the surface-to-volume ratio drives the increased efficiency exhibited by microchannel devices. The use of repeating identical units allows for quick transition from the laboratory to full-scale operations because of their inherent ability to “number-up” devices as opposed to scaling-up units to increase throughput or meet performance requirements [76]. For the considerations above, the thermal management and gas distribution system used in this work was designed as a microchannel device to provide quick and efficient removal of generated heat, uniform fluid distribution, uniformly distribute gas into the adsorbent bed, and occupy a small fraction of the system volume compared to the volume of the adsorbent material.

Stainless steel 304 was chosen as the fabrication material for this work due to its stability under cryogenic temperatures and high pressures and its ability to operate in a hydrogen rich environment. The dimensional constraint in the design of the microchannel device is 2.0" diameter to allow contact of the entire bottom surface of the adsorbent beds obtained for this investigation.

Prior to designing the microchannel device, a fabrication plan was established defining the characteristics necessary for successful production of the novel integrated thermal management and gas distribution prototype. The fabrication plan is:

1. Photochemical machining (PCM) to create all raised features
2. Laser cut all through-holes
3. Diffusion bond shims together
4. Machine slits into headers
5. Braze headers to microchannel thermal management unit

The Microproducts Breakthrough Institute (MBI), Corvallis, OR, is currently not equipped to perform the PCM process necessary for the production of the microchannel shims. Therefore, Great Lakes Engineering in Maple Grove, MN was contracted to complete the first two steps of the fabrication plan (PCM and laser

cutting). The final three steps in the production process were performed onsite at the MBI. The design of the integrated microchannel device must fit within the fabrication plan and meet the design requirements listed in Table 4. 1.

Table 4. 1: Design requirements for microchannel device.

	Design Requirements for Integrated Microchannel Device
1	Hermetically seal heat transfer fluid from adsorbent environment
2	Provide uniform flow of heat transfer fluid
3	Uniformly distribute hydrogen gas axially into adsorbent bed
4	Allow thermocouples to be passed through device into adsorbent bed

The integrated microchannel device, Figure 4.3 and Figure 4.4, utilizes liquid nitrogen coolant to remove heat generated during the adsorption process. A 250 μm thick flow path uses 250 μm tall features, resulting from PCM process, to uniformly distribute the cooling fluid throughout the entire device. The segmented inner wall and pillars aid in fluid distribution and provide the necessary surfaces required to diffusion bond the 500 μm thick liquid distribution plate (bottom of Figure 4.3) to the 250 μm thick sealing plate (top of Figure 4.3) creating a sealed fluid path. Laser-cut holes, seen in the medium and large pillars, distribute feed gas axially into the adsorbent bed and facilitate thermocouple passage into the bed via the large pillars. A cut view of the assembled device with headers demonstrates the complete formation of the internal liquid nitrogen flow path and depicts the hermetic seals created by the perimeter wall and pillars for the external gas distribution sites.

Figure 4.5, below, displays the microchannel device through the various stages of fabrication, Figure 4.5A and B are the liquid nitrogen distribution plate and sealing plate, respectively, as they were received from Great Lakes Engineering following the PCM and laser-cutting processes.

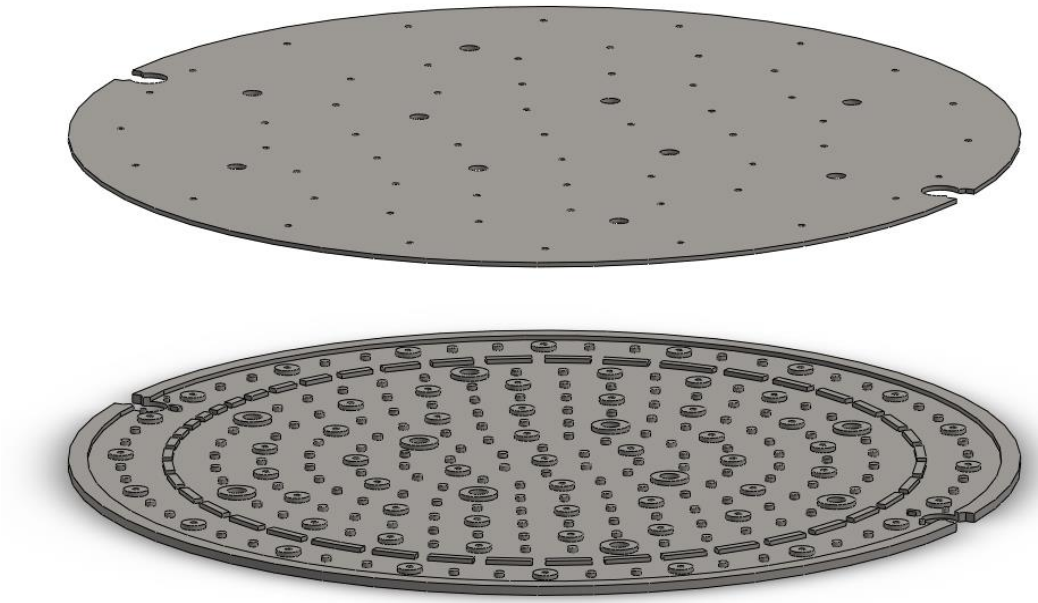

Figure 4.3: SolidWorks image of the fluid distribution plate (bottom) and sealing plate (top) of the microchannel device.

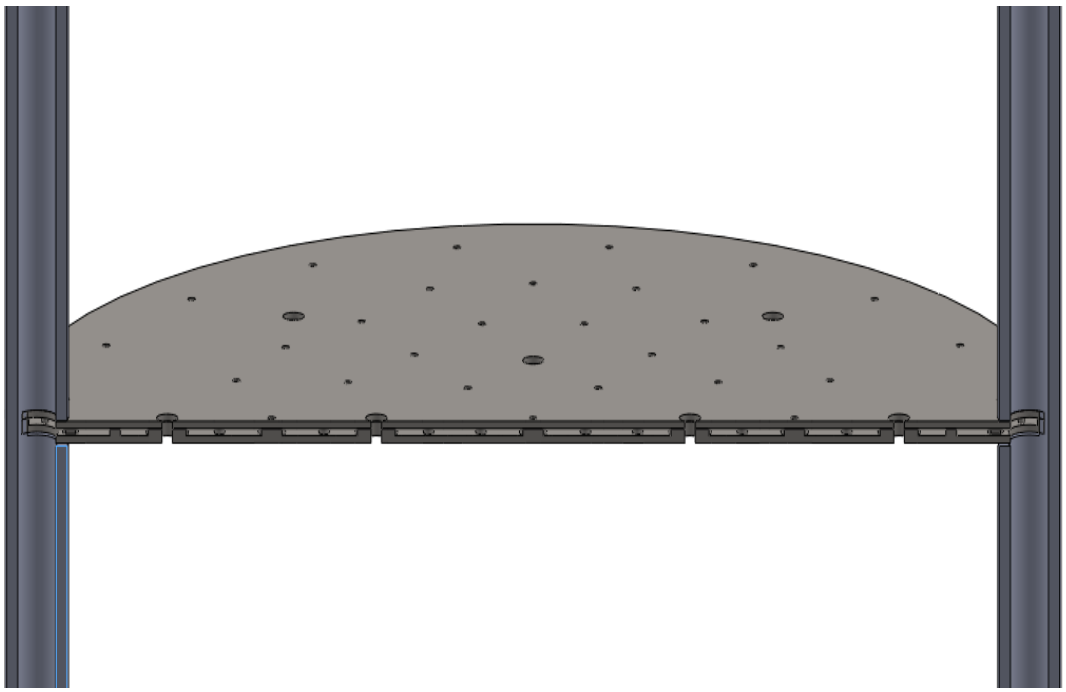

Figure 4.4: Cut view of assembled microchannel plate and headers.

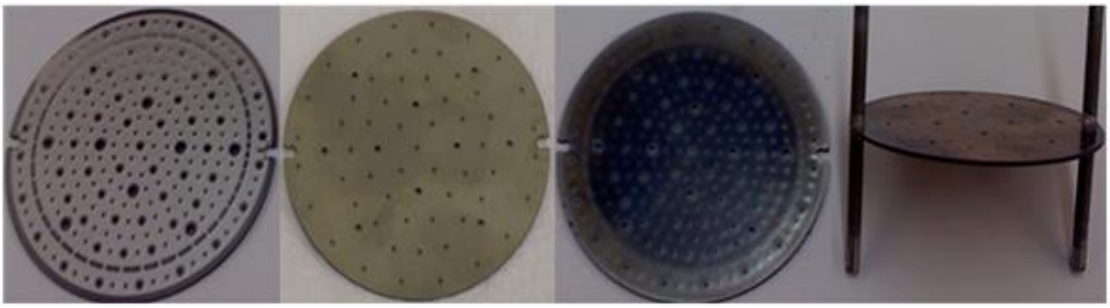

Figure 4. 5: Liquid nitrogen distribution plate (A) and sealing shim (B) received from Great Lakes Engineering, two shims diffusion bonded (C) and final assembly with brazed headers (D).

The two shims were diffusion bonded, Figure 4.5C, at the MBI using a vacuum hot press (VHP) at 975^{o}C with an applied bonding pressure of 2.0 MPa. Figure 4.5D is the fully assembled and operational microchannel thermal management and gas distribution device following the brazing of three-millimeter stainless steel headers to the bonded shims with Braze 820 (BNi-2) [77].

Only a single microchannel device is used in the experimental and mathematical investigations associated with this work. The development of the microchannel thermal management device is the first step in the production of a modular adsorption tank insert design (MATI) under investigation at OSU. The MATI utilizes the benefits of "numbering up" the small volume microchannel devices with separate heat exchange and gas distribution plates located between adsorbent beds to create a hydrogen storage concept in a progression towards meeting the DOE's storage goals. A complete system analysis of the MATI design including sizing, computational fluid dynamic modeling (CFD) of the fluid flow path, material analysis, information on the vacuum brazing technique, and a full cost analysis is found in the Master's thesis of Leif Steigleder [77].

Chapter 5: Experimental Apparatus and Methods

A description of the experimental apparatus necessary for the completion of this work, including an overview of the experimental equipment and materials, instrumentation, experimental methods, and general experimental procedures, are contained within this chapter.

5.1 Materials of Construction

The experimental conditions for this work consist of elevated pressures up to 60 bars and cryogenic temperatures as low as 77 K. Consequently, stainless steel was chosen as the material of construction for the pressure vessel, thermal management system, fittings, and the majority of tubing. As discussed in chapter 4, stainless steel exhibits high-pressure strength and low embrittlement at cryogenic temperatures, and satisfactory rating in hydrogen-rich environments make it well suited for this investigation.

To help isolate the adsorbent materials (MOF-5 and AC discussed in chapter 3) from the stainless steel vessel wall, a cylinder of polytetrafluoroethylene (PTFE) is placed concentrically inside the pressure vessel. PTFE was chosen for this work due to its low operating temperature, strength, and inert qualities with respect to the adsorbent materials and both H_2 and N_2 gases. Although PTFE is susceptible to hydrogen permeation, it is presumed that hydrogen permeation through the material will have a negligible impact on the performance of the experimental investigation because (1) it is located in a closed system and cannot permeate to the environment, and (2) the duration of the experimental trials is relatively short, less than 5 minutes, minimizing loss from the adsorbent or void regions to the PTFE. Two additional plugs of PTFE, one on the adsorbent bed surface furthest from the microchannel device and the second in contact with the pressure vessel, are used to minimize void space, help maintain contact between the bed and microchannel surface, and further isolate the adsorbent material from the pressure vessel body. Finally, thin-film PTFE

is used as the gasket material to provide a leak-proof gas seal between the body and cap of the pressure vessel.

5.2 Experimental Apparatus

The experimental system constructed in support of this work is composed of three sections: adsorption gas pre-cooling and analysis, liquid nitrogen coolant delivery and analysis, and the integrated adsorption environment. A general layout of the experimental system is depicted in Figure 5.1.

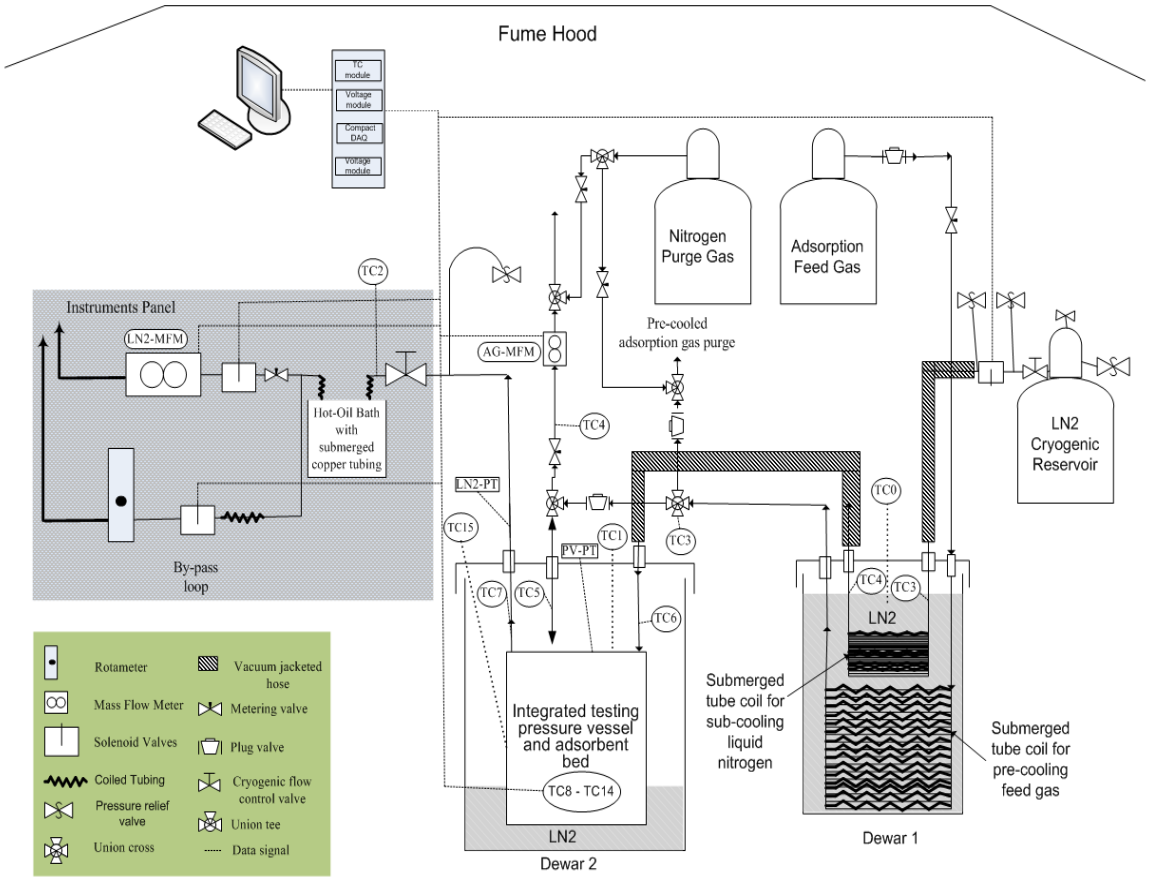

Figure 5.1: Flow diagram of the complete experimental system.

5.2.1 Adsorption Gas Cooling and Analysis

Ultra High Purity (UHP) Nitrogen and UHP Hydrogen gases were used to perform the adsorption experiments in this investigation; both gases are supplied by AirGas in high-pressure cylinders. Single stage regulators, Y11-N114G for nitrogen

gas and Y11-N115H for hydrogen, maintain the delivery pressure of the adsorption gas throughout an experimental trial, while the filling time and gas flow are controlled using a Swagelok stainless steel metering valve.

To minimize potential heat and mass transfer complications stemming from the direct feeding of room temperature adsorption gas into the cryogenic environment and in order to maintain the integrity of the system analysis it is essential to cool incoming gas prior to feeding into the pressure vessel. Gas pre-cooling is achieved by flowing adsorption gas through forty-five feet of stainless steel tubing submerged in atmospheric liquid nitrogen prior to entering the pressure vessel (Figure 5.2A). As shown in Figure 5.1 and Figure 5.2B, the adsorption gas passes through a purge valve until the desired inlet temperature is reached, at which point the purge valve is closed and the pressure vessel begins charging.

Following the completion of an experimental trial, the adsorption gas is slowly discharged from the pressure vessel using a second metering valve. The flow rate of the discharging gas is obtained from an electronic mass flow meter, AG-MFM. The collected flow rate data is numerically integrated over the discharge time to calculate the total mass of gas present inside of the pressure vessel at the end of the experimental trial.

5.2.2 Liquid Nitrogen Coolant Delivery and Analysis

The heat transfer fluid for this investigation is pressurized liquid nitrogen delivered from an HP Cryo-Cyl 80 vessel at saturation conditions. To maximize the liquid nitrogen coolant through the system and minimize boiling inside the microchannel device, liquid nitrogen is sub-cooled from its saturation temperature (approximately 98 K at 100 psi) as it passes through ten feet of coiled stainless steel tubing submerged in atmospheric liquid nitrogen before flowing through the microchannel device (inner steel coil depicted in Figure 5.2A).

After passing through the experimental apparatus, liquid nitrogen is vaporized as it flows through coiled tubing submerged in a hot-oil bath. The vaporized nitrogen

gas subsequently flows through a second electronic mass flow meter to obtain the mass of liquid nitrogen used during the experimental trial (Figure 5.3).

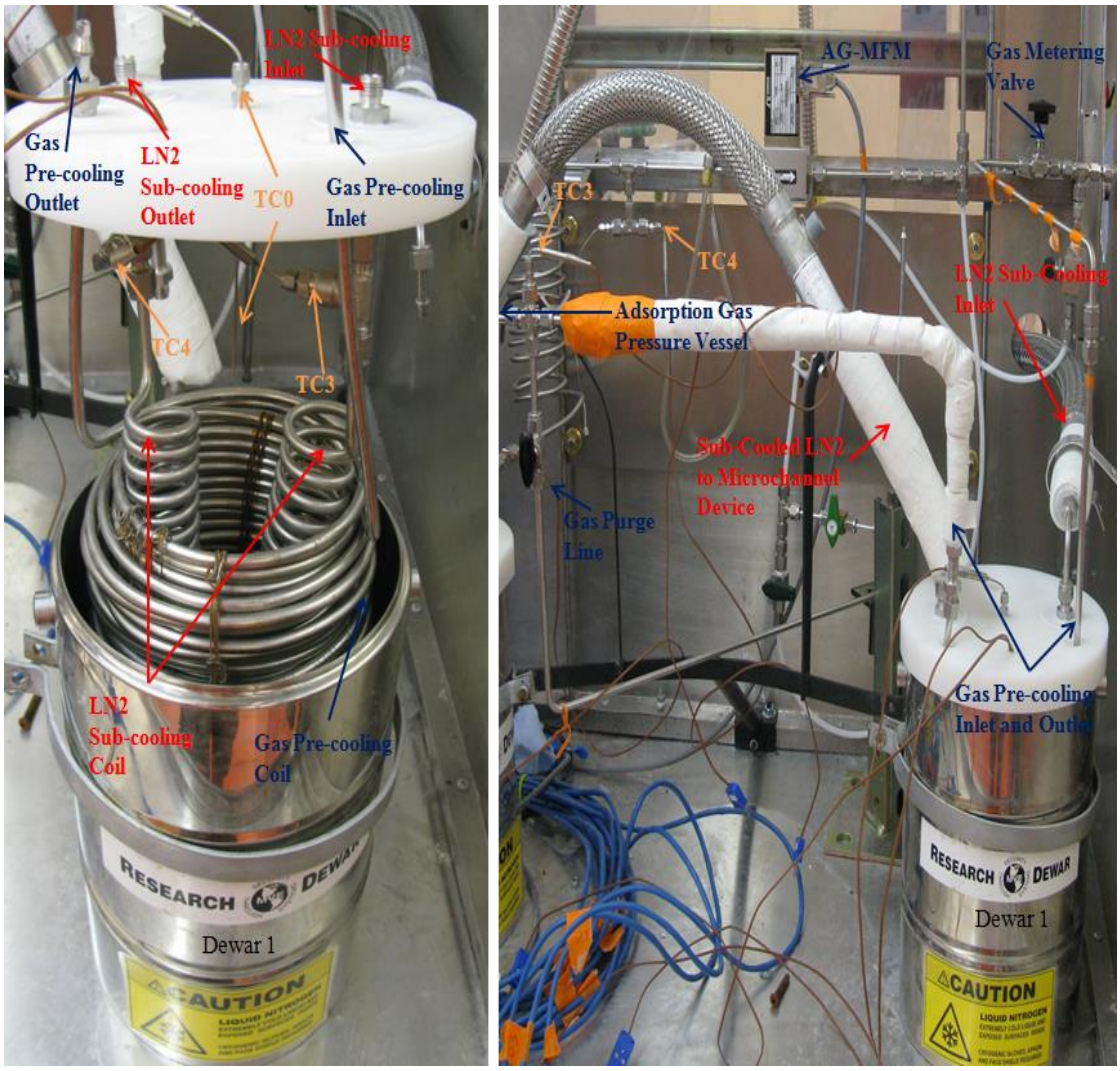

Figure 5. 2: Gas pre-cooling and liquid nitrogen sub-cooling coils (A) and the gas pre-cooling and analysis and liquid nitrogen sub-cooling system (B).

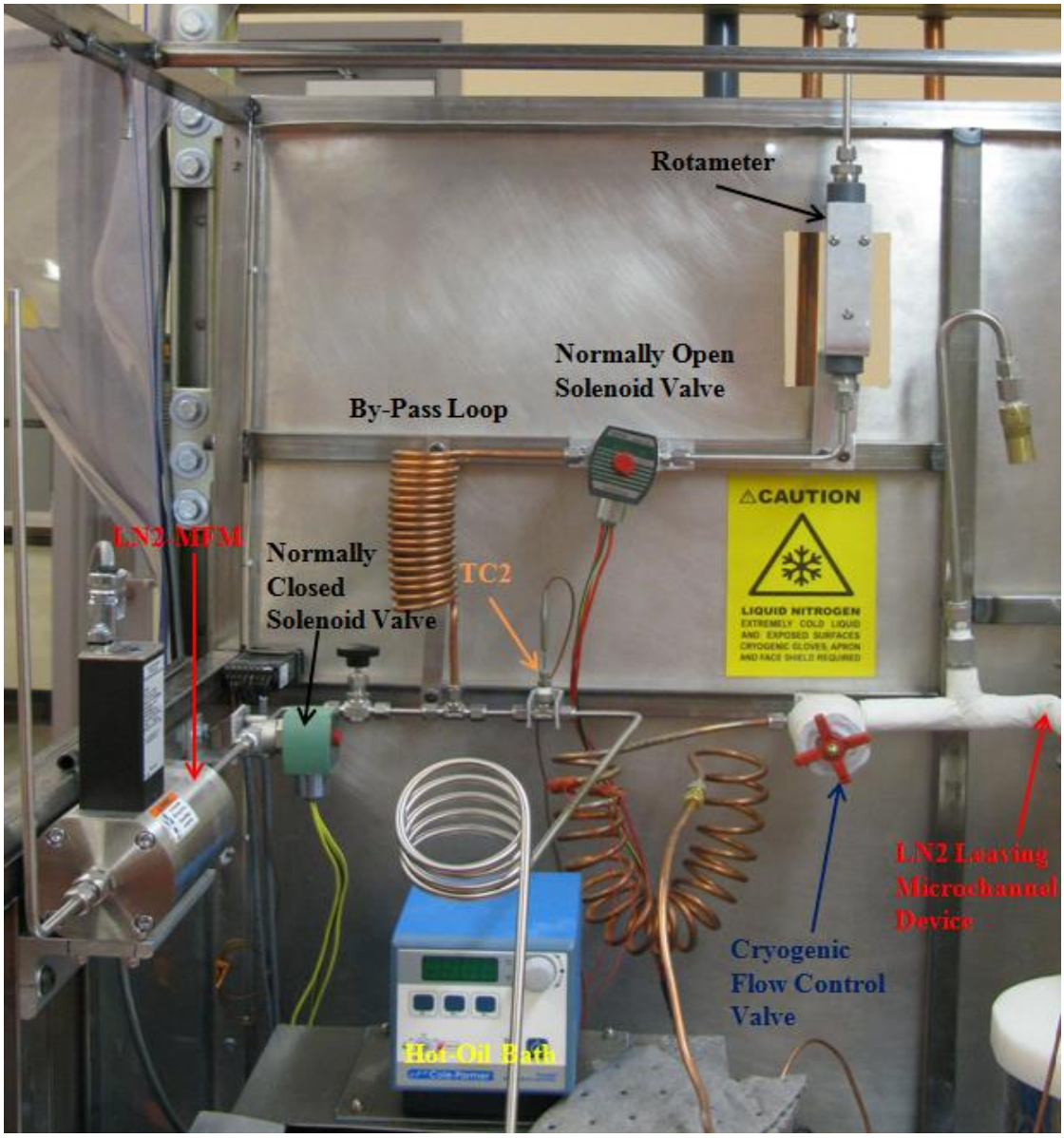

Figure 5.3: Liquid nitrogen vaporization and analysis system.

5.2.3 Integrated Adsorption Environment

All internal components of the integrated adsorption environment, and the order of installation of MOF-5 adsorbent are depicted in Figure 5.4. The same procedure is followed for AC investigation. The pressure vessel used in this work is fabricated from two steel pieces: a cup-like body constructed from a single piece of 304 stainless steel and a stainless steel cap that is integrated to allow for all fluidic connections, thermocouples ports, and pressure tap. A 0.010" thin-film PTFE gasket

placed between the vessel body and cap is used in conjunction with twelve perimeter bolts and 55 ft-lbs. of applied torque to create the high-pressure gas seal for the submergible vessel.

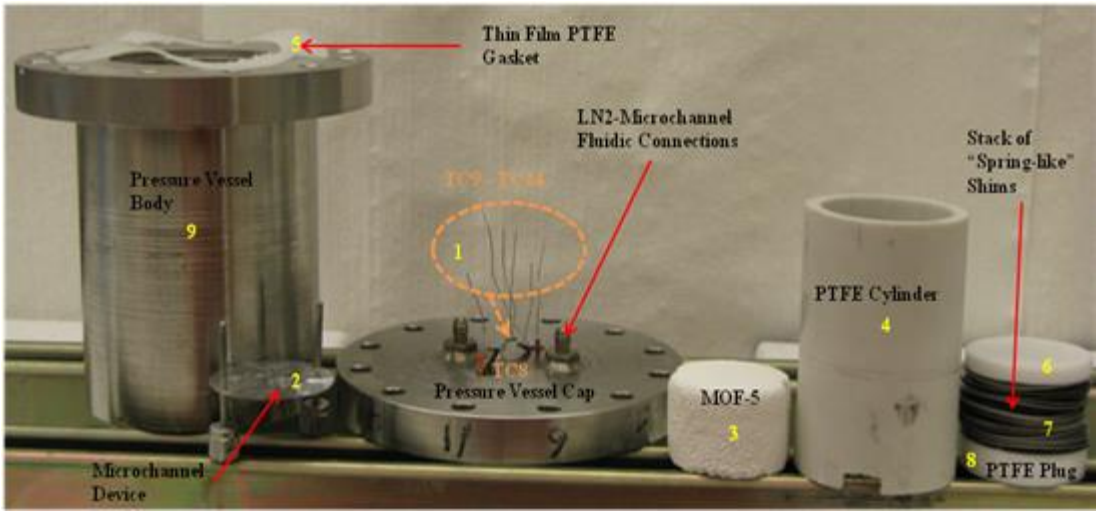

Figure 5.4: Internal components of integrated adsorption environment and the order of installation.

The integrated microchannel thermal management and gas distribution device is connected to the inside surface of the vessel cap via Swagelok fittings, and 0.020" thermocouples pass through the cap and the microchannel device (Figure 5.5A). A thin layer of silicone grease is placed at the thermocouples' base to minimize preferential gas flow. The adsorbent bed contacts the surface of the microchannel device after inserting the thermocouples inside (Figure 5.5A and Figure 5.5B). Figure 5.6 and Table 5.1 indicate the depth and location of the six thermocouples embedded in the adsorbent material in relation to the liquid nitrogen flow path through the microchannel device.

As seen in Figure 5.7, the PTFE cylinder (2.5" outer diameter by 2.0" inner diameter) is placed over the adsorbent bed, microchannel, and thermocouples to isolate the adsorbent material from the stainless steel walls and provide support and alignment for the remaining materials of construction. Subsequently, the thin-film

PTFE gasket is placed on the contacting surface of the vessel cap around the PTFE cylinder.

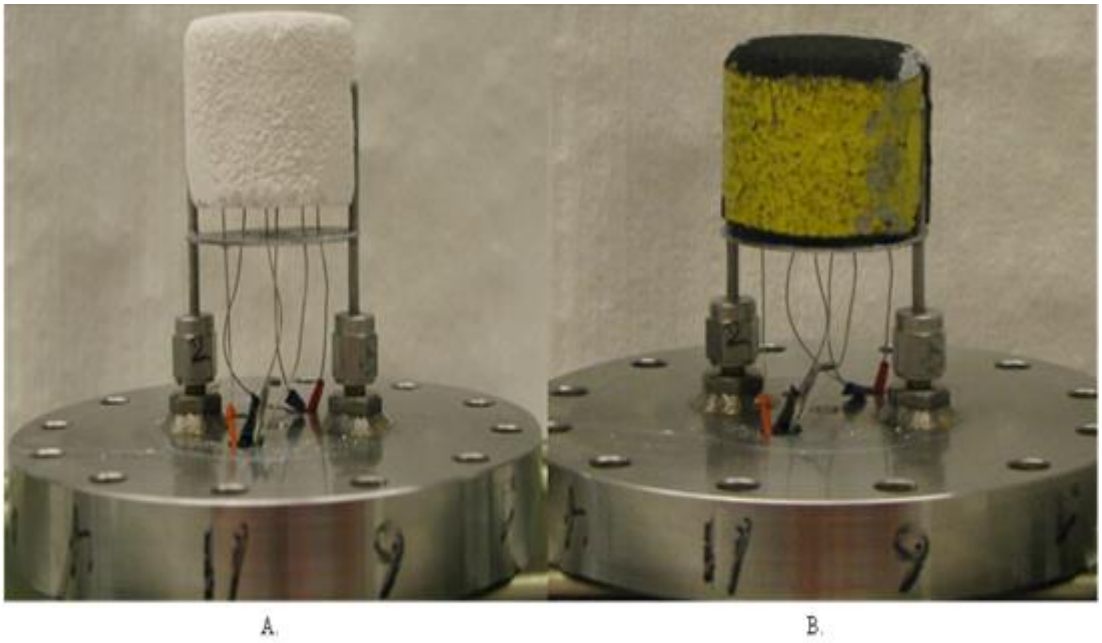

Figure 5.5: MOF-5 bed suspended over microchannel plate by thermocouples before contacting plate surface (A) and AC bed with thermocouples inserted in contact with microchannel plate (B).

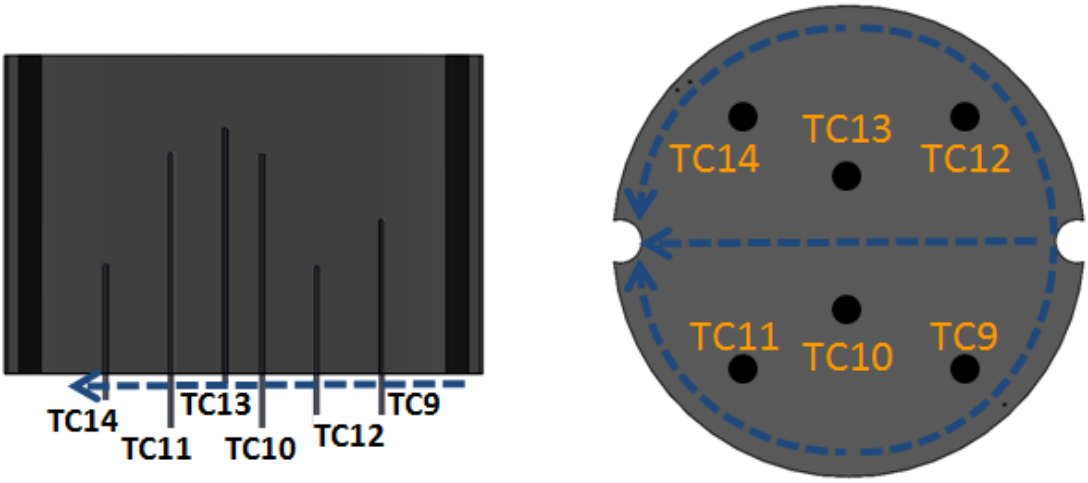

Figure 5.6: Thermocouple locations inside adsorbent bed and the direction of liquid nitrogen flow through microchannel device.

Table 5.1: Location and depth of thermocouple probes in adsorbent bed.

Thermocouple Name	Distance from Center [in]	Depth [in]
TC9	0.682	0.630
TC10	0.292	0.900
TC11	0.682	0.902
TC12	0.682	0.438
TC13	0.292	1.005
TC14	0.682	0.450

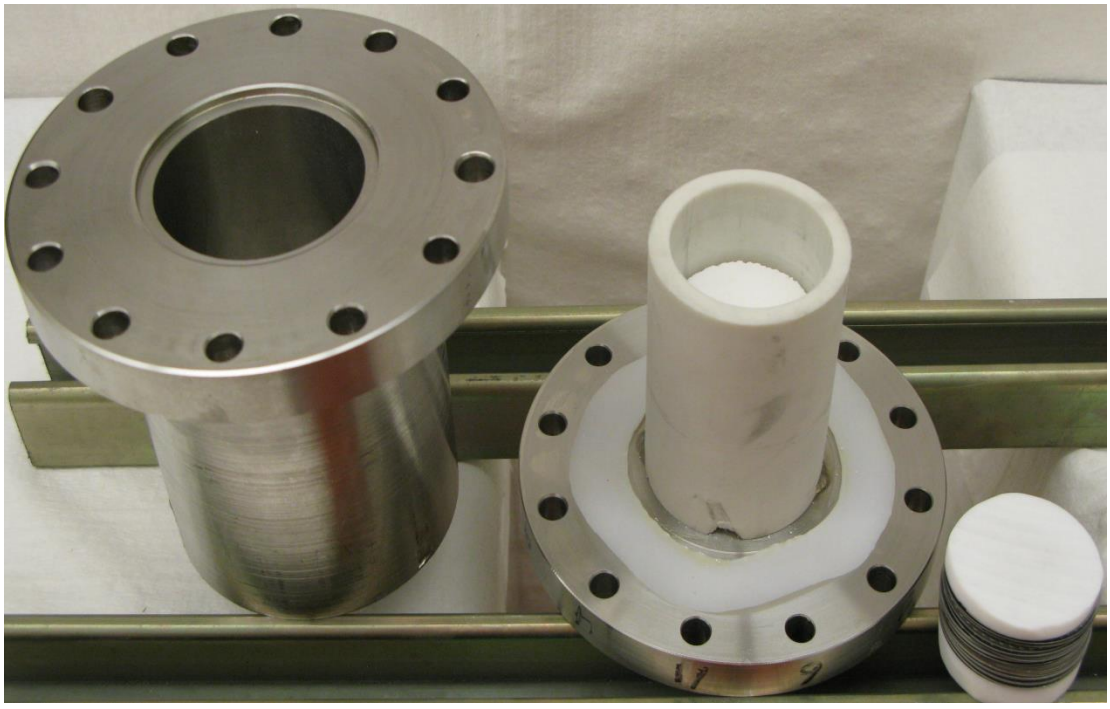

Figure 5.7: Placement of the PTFE cylinder over of the adsorbent bed followed by the thin-film PTFE gasket on the cap surface.

Next, a solid PTFE plug is placed in contact with the exposed surface of the adsorbent bed followed by a stack of 500 μm thick stainless steel shims and a second PTFE plug. The stack of shims between the two PTFE plugs act as a spring inside of the PTFE cylinder (by compressing up to 13 mm, ½") to maintain uniform contact between the adsorbent bed and the microchannel surface when the pressure vessel body is placed over the assembled internal components (Figure 5.8).

Following the assembly of the internal components and the securing of the pressure vessel, adsorption gas, liquid connections, and pressure tap are secured to the top surface of the vessel cap (Figure 5.9A) and placed inside the second research Dewar of the experimental system. Once inside the second Dewar, final assembly of the experimental systems includes securing the fluid connections of the pressure vessel to the pre-cooled gas, sub-cooled liquid nitrogen, gas analysis, and liquid nitrogen analysis lines as seen in Figure 5.9B and Figure 5.10.

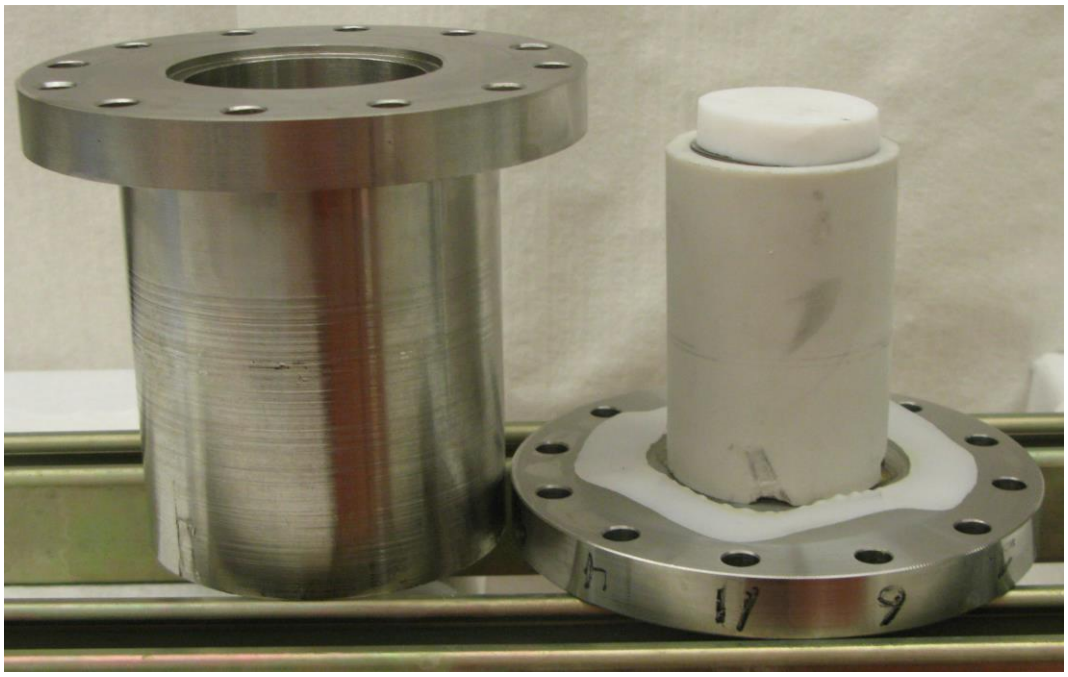

Figure 5. 8: Complete assembly of all internal components of the integrated adsorption environment.

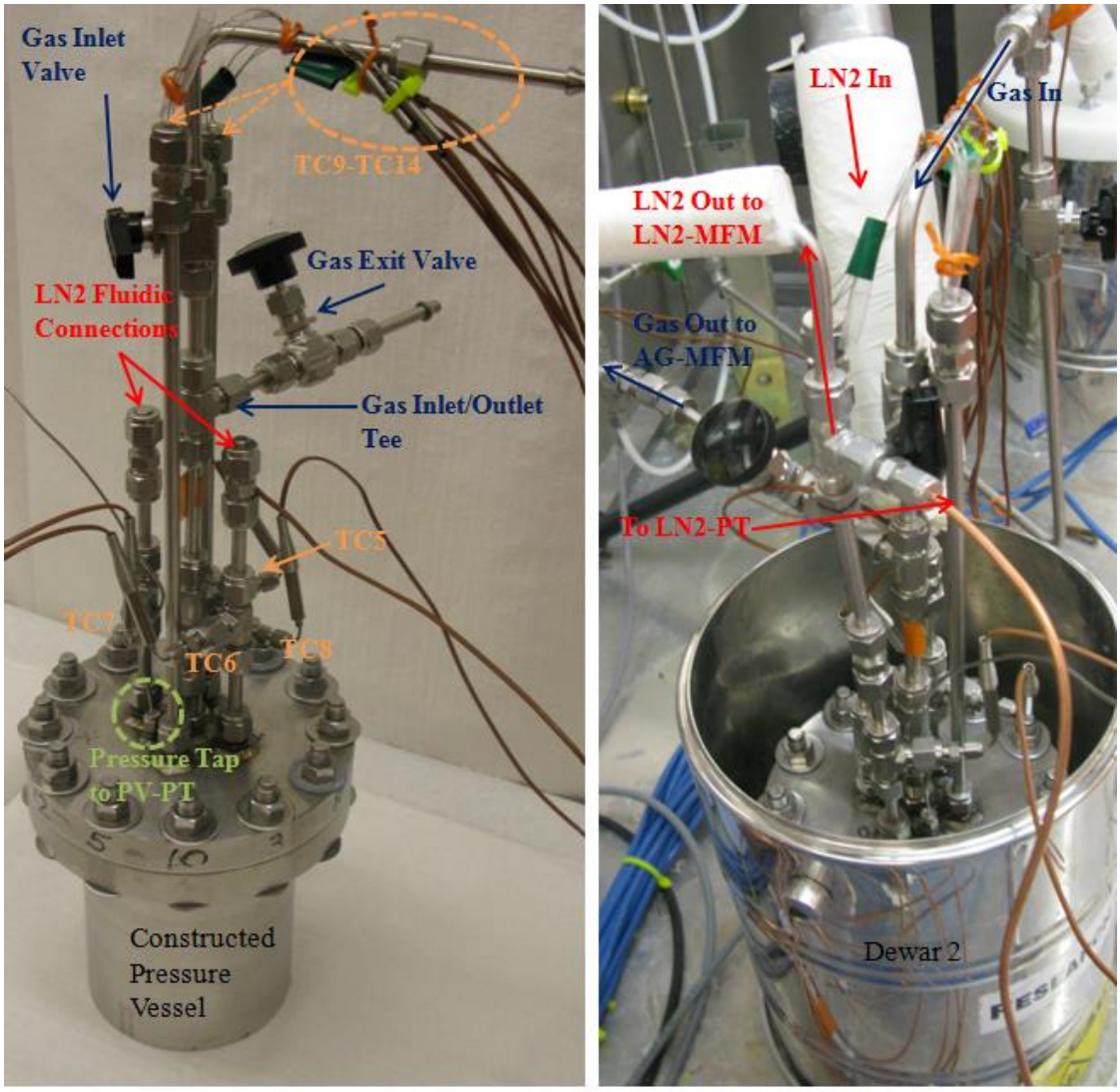

Figure 5.9: Fully constructed pressure vessel (A) with all fluidic connections attached to source and analysis lines (B).

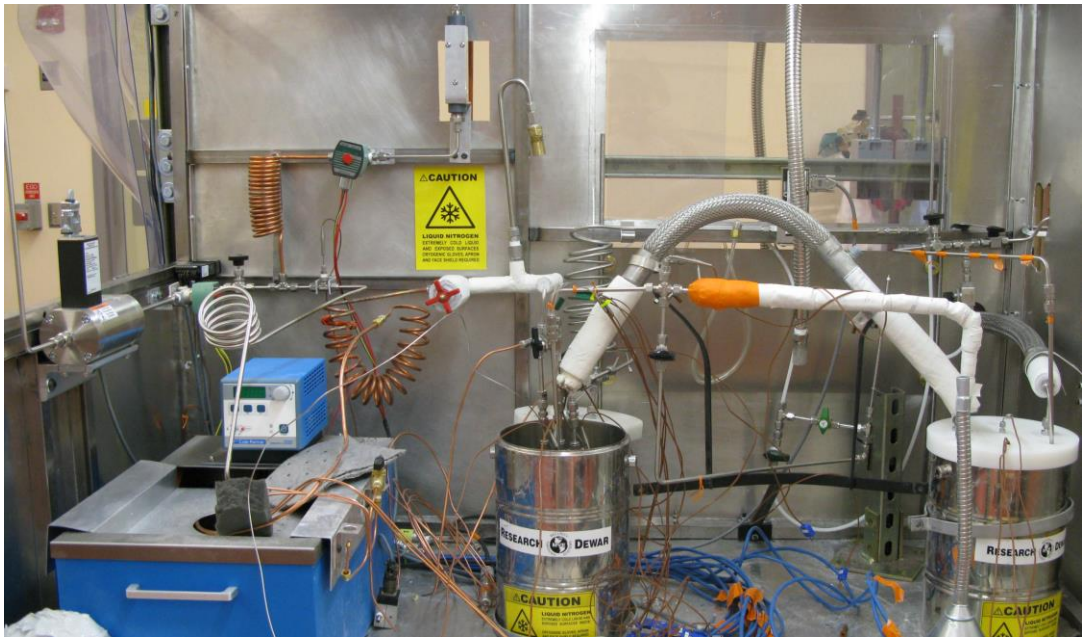

Figure 5.10: Fully constructed experimental adsorption system with liquid nitrogen coolant.

5.3 Methods

The experimental data generated during this investigation includes temperature, pressure, and flow rates; a list of the instruments and their location within the experimental system is located in Table 5.2. Data collection, real time plotting, and switching of solenoid valves are accomplished with National Instruments' LabView software. A Nation Instruments' compact data acquisition unit, NI cDAQ-9174, houses a thermocouple input module, NI 9214; analog input module, NI 9205, used to obtain temperature, pressure, and flow data; and a relay module, NI 9481, used to control the functionality of solenoid valves. The LabView program generated for this work continuously acquires data from all instruments at a rate of 4 Hz while providing continuous real time plotting and display of temperatures, pressures, and flow rates throughout the system. Integrated push-button controls operate three solenoid valves integral to the liquid nitrogen flow, analysis, and the creation and writing of data files.

Prior to performing experimental trials, the pressure transducers obtained for this work were calibrated using an Omega Engineering DPG4000 Series calibration

kit. Gauge pressure readings were obtained in 50-psi increments from 0 – 500 psig; 1,000 voltage samples were collected at each pressure increment using LabView software. The 1,000 collected voltage readings were averaged, with a standard deviation of 2 mV at each pressure increment, and plotted against the known pressure to create a calibration curve specific to each pressure transducer; a sample calibration curve is shown in Figure 5.11. Although the maximum experimental pressures for this investigation exceed the calibration range by 300 psi, it is believed that the linear trend can be accurately extrapolated to pressures beyond 500 psi with minimal additional error.

Table 5.2: Instrument names, locations, and models

Device Type [data type]	Device Name	Location	Model
Thermocouple [Temperature]	TC0	Sub-cooling Dewar - Level indicator	TJ36-CPSS-116U-6
	TC1	Second Dewar on vessel Surface	TJ36-CPSS-116U-6
	TC2	LN2-MFM in	TJ36-CPSS-116U-2
	TC3	LN2 sub-cooling in/Gas pre-cooling out	TJ36-CPSS-116U-2
	TC4	LN2 sub-cooling out/ AG-MFM in	TJ36-CPSS-116U-2
	TC5	Adsorption gas inlet/outlet	TJ36-CPSS-116U-2
	TC6	Liquid nitrogen inlet	TJ36-CPSS-116U-2
	TC7	Liquid nitrogen outlet	TJ36-CPSS-116U-2
	TC8	Void space of pressure vessel	TJ36-CPSS-116U-6
	TC9	Adsorbent bed - Hole 1	TJC36-CPSS-020U-18
	TC10	Adsorbent bed - Hole 2	TJC36-CPSS-020U-18
	TC11	Adsorbent bed - Hole 3	TJC36-CPSS-020U-18
	TC12	Adsorbent bed - Hole 4	TJC36-CPSS-020U-18
	TC13	Adsorbent bed - Hole 5	TJC36-CPSS-020U-18
	TC14	Adsorbent bed - Hole 6	TJC36-CPSS-020U-18
	TC15	Second Dewar – Outside wall	TJ36-CPss-116U-6
Pressure Transducer [Pressure]	LN2-PT	LN2 outlet	PX409-3.5KG10V
	PV-PT	Pressure tap of pressure vessel cap	PX409-3.5KG10V
Mass Flow Meter [Standard Gas Flow Rate]	LN2-MFM	LN2 exit - Following hot oil bath	FMA-874A-V
	AG-MFM	Pressure vessel outlet	Brooks Delta II: SLA5863S2CAA0B2A1

The type T thermocouples obtained from Omega Engineering were tested and guaranteed to meet or exceed special limits of error prior to shipment; therefore, the limits of error (the greater of 0.5^{o}C or 0.4%) are used without additional calibration. Ensuring that no significant error in temperature data is observed in the experimental system, an Omega Engineering CL540ZA Thermocouple Simulator was employed to create an electrical signal corresponding to specific temperature readings, in order to account for the second source of error from the thermocouple to the data acquisition unit. Three temperatures, 77.05 K, 273.15 K and 473.15 K, are simulated to test each of the sixteen thermocouples in the experimental system. The procedure used in the pressure transducer calibration is repeated to produce 1000 samples at each temperature tested. Samples were subsequently averaged and compared to the given setpoint. The highest standard deviation, 0.27 K, and combined error, 0.60% (Table 5.3) at any setpoint was observed at the lowest calibration temperature.

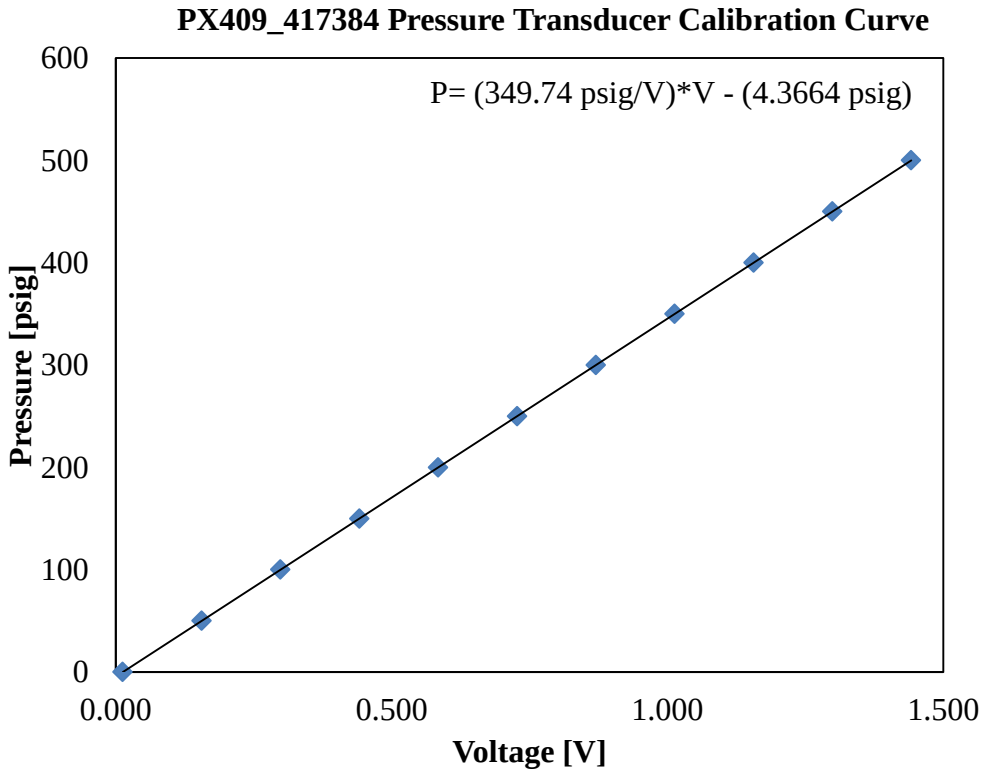

Figure 5.11: Sample pressure transducer calibration curve.

Liquid nitrogen flow rate data is generated by a Brooks Delta II electronic mass flow meter, ±1% flow rate accuracy, and the discharging adsorption gas flow rate is obtained by an Omega Engineering FMA-874A-V electronic mass flow meter, ±1% full scale accuracy. Both flow meters used in this investigation were received with a factory certified calibration curve converting the instruments' output voltage into standard gas flow rate reading.

Table 5.3: Temperature reading error at the three calibration temperatures.

	Type T Thermocouple [K]	Observed in Wire + DAQ Connection [K]	Total Error [K]	Maximum % Error
Limits of Error	Greater of 0.5°C or 0.4%	-	-	-
Error at 77.05 K (-196.1°C)	0.78	0.98	1.76	0.88
Error at 273.15 K (0°C)	0.50	0.46	0.96	0.48
Error at 473.15 K (200°C)	0.80	0.40	1.20	0.60

5.4 Experimental Procedures

Below is a summary of the procedures employed in the completion of the experimental investigation.

5.4.1 Safety considerations

Vaporizing liquid nitrogen poses a tremendous asphyxiate danger in a confined area; therefore, it is important that the provided oxygen monitor, located in close proximity to the experimental systems, indicates a safe oxygen content. To prevent damage to any component of the pressure vessel and delivery systems, assembling and disassembling of any component is only be performed at room temperature. Safety glasses must be worn at all times and, additionally, cryogenic gloves, face shield, and laboratory coat must be worn when working with liquid nitrogen and cryogenic

surfaces. To minimize the potential damage resulting from a bursting liquid nitrogen delivery line, a metal enclosure has been constructed to house the experimental system and limit any “spray” of liquid nitrogen to the surrounding environment.

5.4.2 Activation of adsorbent material

Additional activation of the AC sample was not recommended or provided with the material sample, the AC sample was removed from the vacuum storage chamber and placed quickly into the integrated system assembly. Prior to placing the MOF-5 adsorbent material in the system assembly, the activation procedure described in chapter 3 is performed to remove any traces of moisture and contamination from exposure to air. The adsorbent material is placed in the adsorption environment assembly as quickly as possible to minimize further exposure to air following activation.

5.4.3 Assembly of pressure vessel and experimental system

All electronic equipment should be powered “ON” and provided ample warm-up time for all sensors and devices prior to experimentation and liquid nitrogen flow. A solid ¼" Teflon ferrule is used to ensure complete sealing of 0.020" type “T” thermocouples by drilling three 0.020" holes in a triangular pattern on the top surface. Thermocouples are subsequently passed through ¼" steel tubing in the stainless steel cap.

Thermocouples are passed vertically through the thermocouple holes located in the microchannel heat exchanger and gas distributor plate. A thin layer of silicone grease is applied to the base of the six thermocouples inserted inside the pre-drilled holes located in the compressed adsorbent bed. The PTFE insulation cylinder is placed concentrically around the heat exchanger and adsorbent bed assembly, followed by the placement of the PTFE gasket in contact with the cap surface. The thin plug of PTFE is place on the exposed surface of the adsorbent bed and is followed by the stack of steel shims and second PTFE plug.

The pressure vessel body is subsequently lowered on top of the cap; covering the assembled internal components of the adsorbent system. Each perimeter bolt is applied with 55 ft-lbs. of torque to create the gas seal before securing all fluidic connections to the top-side interfaces of the cap and placing inside the second research Dewar.

The liquid nitrogen sub-cooling coil is secured to the tee fittings located on the Dewar cap and subsequently placed in the center of the gas pre-cooling coil prior to placing inside the first research Dewar. Feed and transfer lines are securely connected to the inlet and outlet of both coils before connecting to the pressure vessel inlets. The liquid nitrogen analysis line is connected to the exit of the microchannel device from the pressure vessel and all other fittings are inspected for secure fitting.

5.4.4 Initial startup and leak testing

Begin LabView program and connect a nitrogen gas cylinder to the inlet of the liquid nitrogen sub-cooling coiling and to the gas inlet line. Using low pressure, approximately 50 psi, flow nitrogen gas through the liquid nitrogen lines and check for any leaks using Snoop. It is important to trigger solenoid valves in the LabView program to confirm functionality. Next, begin to pressurize the feed gas line, with the inlet and purge valves closed, and check for any gas leaks between the gas cylinder and pressure vessel. Slowly open the inlet valve and allow the pressure vessel to fill to operating pressure, then close the inlet valve, again checking for leaks along the vessel perimeter and all fittings; finally, slowly evacuate the pressure vessel by opening the gas outlet valve. Connect the liquid nitrogen delivery vessel to the inlet of the sub-cooling coil and properly connect hydrogen gas cylinder, open purge line valve, and then close gas inlet and outlet valves to the pressure vessel. Begin auxiliary nitrogen flow lines to dilute hydrogen flow prior to discharging into fume hood; if nitrogen adsorption experiments are scheduled, auxiliary nitrogen flow is not needed and the same nitrogen cylinder is used for experimental trial and leak testing.

5.4.5 Experimental operation

Slowly fill the first research Dewar with liquid nitrogen through the stainless steel funnel, while monitoring the LabView program to determine when proper liquid nitrogen level has been reached inside the capped Dewar. Refill the research Dewar with liquid nitrogen as needed. Initiate liquid nitrogen flow by activating the normally-closed solenoid valve located on the delivery vessel and opening the liquid delivery valve. Allow liquid nitrogen to freely flow through the system until both liquid inlet and outlet temperatures are below saturation temperature (an approximate flow rate of liquid nitrogen may be gauged using the rotameter of the bypass loop). If the vaporized gas is consistently 21^{o}C, activate the outlet stream solenoid using LabView, rerouting vaporized liquid nitrogen from the bypass loop to the electronic mass flow meter. The small metering valve is used to adjust the flow rate of liquid nitrogen based on the accurate readings provided by the electronic mass flow meter.

Allow liquid nitrogen to flow through the microchannel device until the void temperature within the pressure vessel reads below 200 K before adding liquid nitrogen to the second research Dewar. Slowly add liquid nitrogen until thermocouples in second Dewar (TC1 and TC15) read below 160 K. Continue to flow liquid nitrogen through the system while adding liquid nitrogen to the second Dewar until the internal void space and bed are near the desired initial temperature.

Slowly begin to flow adsorption gas through the purging line and monitor feed gas temperature exiting the coiled tubing. When the desired inlet gas temperature is reached, begin collecting and writing data to the designated file. Next, simultaneously switch the purge valve to the closed position, open the gas inlet valve, and allow the pressure vessel to fill to the desired operating pressure and then close the gas inlet valve at the end of charging. Turn off the gas feed line to minimize free flowing gas and slowly open purge gas line to discharge compressed gas.

At the end of cooling time, terminate liquid nitrogen flow by deactivating solenoid valve on pressurized delivery tank and continue to monitor flow rate.

Continue to monitor system for at least two minutes after cooling has been terminated. Slowly open the pressure vessel outlet valve and evacuate contents through AG-MFM; monitor flow rate closely and adjust metering valve if necessary to allow for increased flow at lower vessel pressures.

At the end of the experiment, deactivate data writing button on LabView, redirect vaporized liquid nitrogen through by-pass loop, and verify all valves are in proper starting position. If additional experiments are scheduled, repeat the above procedure when the internal temperature reaches desired initial conditions. Only perform experiments in the absence of cooling after the prescribed procedure has been followed and a cooling experiment has been performed.

5.4.6 Normal shutdown procedure

Following the final experiment of the session, use LabView to verify deactivation of all three solenoid valves, that all vaporized liquid nitrogen flow is directed towards the by-pass loop, and that the cryogenic valve after the test section is fully open. Close liquid nitrogen feed valve located on the pressurized delivery tank and keep the purge valve and outlet valve of the pressure vessel open to prevent pressure buildup during warming. Close high pressure feed gas cylinder and allow entire system to return, undisturbed, to ambient conditions and all liquid nitrogen in research Dewars to evaporate.

At room temperature, disconnect the liquid nitrogen hose from the inlet of the sub-cooling coil, liquid inlet and outlet lines and the gas inlet from the pressure vessel. Place all components in designated location, properly terminate LabView program, and shut down computer.

5.4.7 Emergency shutdown procedure

In the unlikely event of an emergency, shut liquid nitrogen delivery valve, close delivery valves on gas cylinder, hit emergency power button to deactivate all solenoid valves and data acquisition, exit laboratory and contact safety officer.

Chapter 6: Experimental Results and Discussion

In fulfillment of the first research goal of this work, an experimental investigation was performed to observe the effect of incorporating the microchannel heat exchanger and gas distribution system inside of the storage tank on the temperature distribution throughout the adsorbent bed and the hydrogen storage capacity.

The impact of utilizing the microchannel device on the hydrogen storage capacity is determined through repeated adsorption experiments with and without the flow of liquid nitrogen coolant passing through the microchannel. As detailed in chapters 4 and 5, activated carbon and metal organic framework, MOF-5, adsorbents are used in the experimental investigation. Nitrogen adsorption experiments are initially performed on a packed bed of compressed AC prior to executing the hydrogen adsorption investigation. For consistency, nitrogen gas adsorption experiments preceded hydrogen adsorption in the subsequent MOF-5 investigation.

Tables of experimental parameters, conditions, and results of the experimental data obtained throughout the investigation (for both adsorbents, feed gases, and cooling states) are found in the Appendix. Representative nitrogen adsorption results are initially presented below for both adsorbent materials followed by representative results of the hydrogen adsorption investigations.

6.1 Nitrogen Adsorption

Due to the nature of the adsorption system and experimental apparatus, it is very difficult to repeat initial and operating conditions from one trial to another; therefore, a variety of initial and operating conditions are investigated. The range of experimental conditions experienced throughout the nitrogen adsorption investigations are summarized in Table 6.1.

Table 6.1: Ranges of initial and operating conditions observed throughout the nitrogen adsorption investigations.

Material	Activated Carbon		MOF-5	
Liquid Nitrogen Cooling	**Yes**	**NO**	**Yes**	**NO**
Final Charging Pressure [bar]	50 - 55	50 - 55	52 - 55	53 - 55
Pressurization Time to 50 bar[s]	40 - 130	30-120	30 - 133	22 - 52
Charging Time [s]	180	180	180	180
LN2 Cooling Time [s]	180	0	180; 300	0
LN2 Mass Flow Rate [g s^{-1}]	0.4 - 2.1	0	1.1 - 2.6	0
Average Initial Bed Temperature [K]	100 - 160	95 - 125	90 - 140	80 - 105
Number of Experiments Performed	7	7	7	4

The cryogenic nitrogen adsorption experiments conducted with both activated carbon and metal organic framework materials indicate an improved adsorption capacity in the presence of active heat removal with liquid nitrogen flow through the microchannel device. A sample temperature profile for the four combinations tested, material and cooling condition are presented in Figure 6.1 to Figure 6.4.

For nitrogen adsorption on activated carbon, the average temperature rise during the liquid cooled charging process is lower at all thermocouple locations, suggesting that the flow of liquid nitrogen helps to quickly remove generated heat due to adsorption and compression of gas within the bed. In addition, the gas penetrating the adsorbent bed experiences additional cooling as it flows through the gas distribution holes of the microchannel device, which is not achieved in the absence of coolant flow.

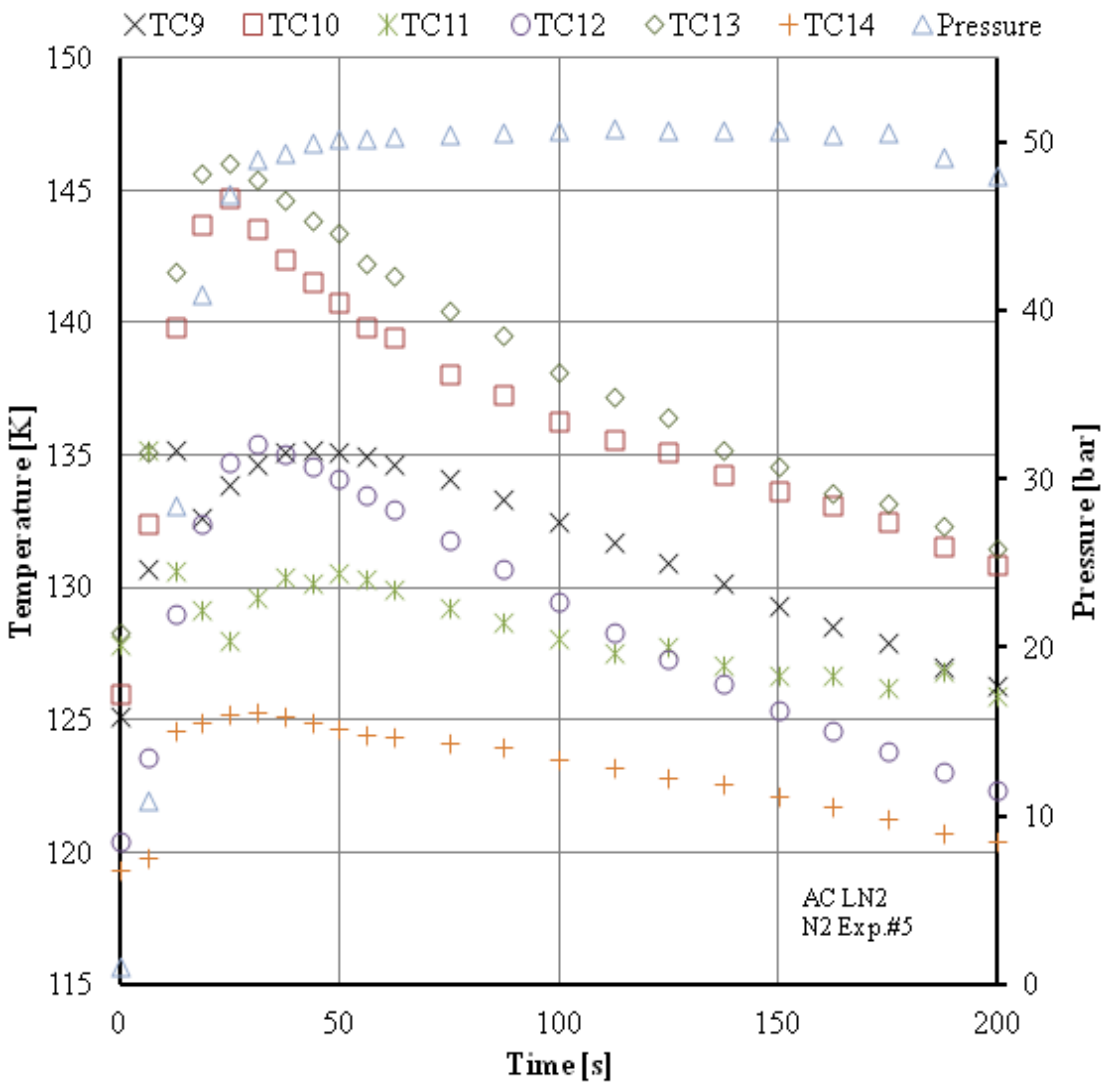

Figure 6.1: Temperature and pressure response in AC bed during N_2 adsorption with LN2 cooling.

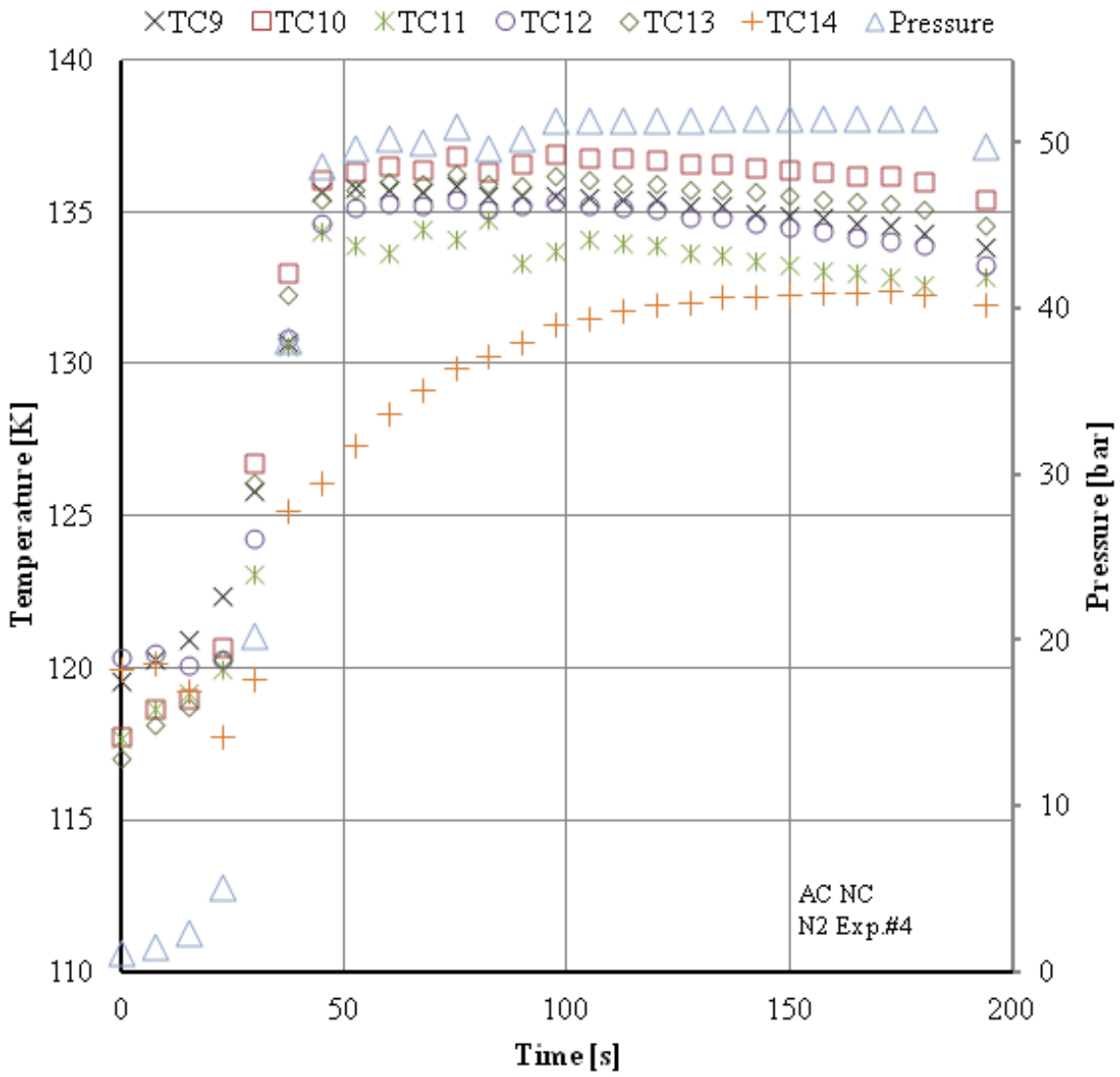

Figure 6.2: Temperature and pressure response in AC bed during N_2 adsorption without cooling.

Comparing Figure 6.1 and Figure 6.2 it is clear that the presence of liquid nitrogen flow through the microchannel device provides significant removal of heat from the activated carbon bed compared to the trial without cooling. Only 180 seconds of liquid nitrogen cooling flow was supplied in the nitrogen adsorption on activated carbon experiments; however, an additional 20 seconds of cryogenic vapor flow is observed as the liquid nitrogen delivery lines empty. It is clear that within 200 seconds all the thermocouple locations have nearly returned to their initial

temperatures; however, the trial without cooling demonstrates very little temperature drop from the maximum temperatures reached during charging.

The first performance metric used in this analysis to compare the cryogenic adsorption system operating with and without liquid nitrogen cooling is the amount of gas present inside the pressure vessel and contained within the adsorbent bed. The amount of gas present in the pressure vessel is calculated from numerical integration of mass flow meter data obtained during the evacuation of the vessel. The amount of gas inside the adsorbent material is determined by subtracting the mass present in the void space from the mass obtained by numerical integration. To analyze the effect of liquid nitrogen flow through the microchannel device on the energy transfer throughout the adsorbent system, the temperature profiles at each thermocouple and corresponding average temperature vales are compared to trials without cooling. In addition, the effective heat generation achieved during the experimental tri al is utilized as an additional performance metric for evaluation of the thermal management system. In this present analysis, the effective heat generation, Q_{eff}, is defined as

$$Q_{eff} = m_{ads}\left(\left[C_{p_{ads}}(\overline{T}_{final})\right]\overline{T}_{final} - \left[C_{p_{ads}}(\overline{T}_{initial})\right]\overline{T}_{initial}\right) \tag{6.1}$$

the over bar indicates the average temperature of at all six thermocouples located inside the bed. The results of the representative nitrogen adsorption on activated carbon experiments are located in Table 6.2.

It is clear from Table 6.2 that the presence of the coolant flow through the microchannel device successfully removes significantly more generated energy from the adsorption process than experiments performed without cooling fluid flow. This results in higher mass of gas inside the adsorbent bed stemming from a lower average bed temperature at the end of the experimental trial.

Table 6.2: Results of nitrogen adsorption on activated carbon with and without liquid nitrogen cooling.

Experimental Condition	Cooling	NO Cooling
Nitrogen in Vessel [g]	69.35	61.42
Nitrogen in Bed [g]	36.85	29.81
Initial Average Temperature [K]	124.5	118.7
Average Temperature Rise [K]	12.7	16.6
Final Average Temperature [K]	126.2	133.5
Effective Heat Generation 200s [J]	49.5	328.0
LN2 Mass Flow [g s^{-1}]	0.5	-
Outside Wall Temperature [K]	137	134.5

In the presence of heat removal, a larger temperature drop at the embedded thermocouple locations following gas compression and ongoing adsorption is observed with activated carbon. The MOF-5 bed did not experience a significant temperature drop following the initial temperature rise at the thermocouple locations in either mode of operation. However, with liquid nitrogen flow, a lower average temperature rise of 10 K and a two times higher average temperature drop, after 200 seconds, is demonstrated for the MOF-5 bed. A wider distribution of temperature readings at all thermocouple locations are recorded with the addition of liquid cooling.

In the absence of cooling, nearly three percent more nitrogen gas was present in the pressure vessel compared to the trial with liquid flow; however, an increase in nitrogen mass inside the adsorbent bed is observed in the liquid cooled experiment. The increase in total nitrogen results from the increased pressure observed in the non-cooled trial. As a result of increased pressure, a higher nitrogen density is present in the void space of the system. The larger system pressure drop is attributed to an increase in adsorption after terminating the gas feed of the liquid cooled system. The representative system results for nitrogen adsorption on MOF-5 are found in Table 6.3.

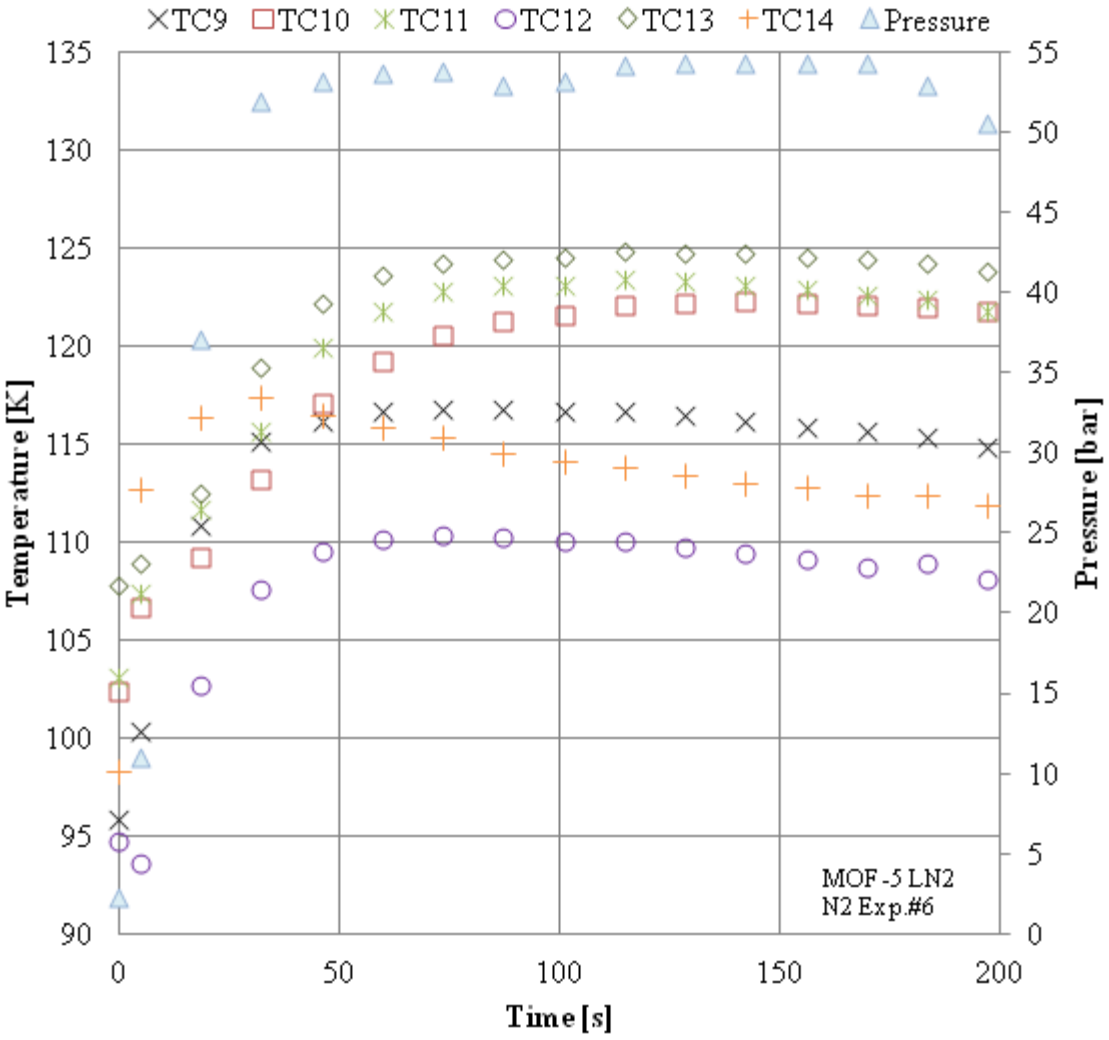

Figure 6.3: Temperature and pressure response in MOF-5 bed during N_2 adsorption with LN2 cooling.

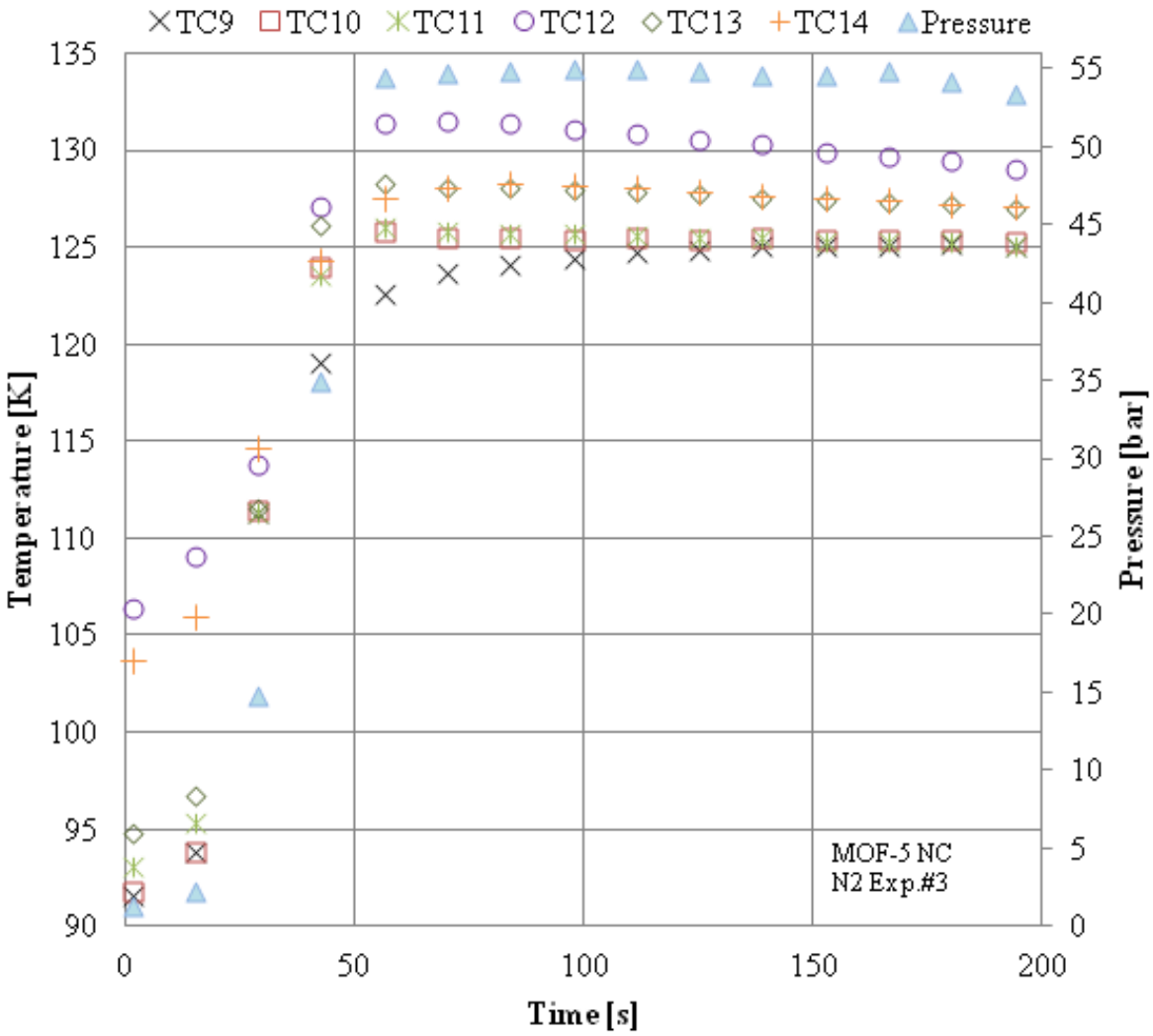

Figure 6.4: Temperature and pressure response in MOF-5 bed during N_2 adsorption without cooling.

Experiments conducted with liquid nitrogen cooling consistently exhibit a significantly lower effective heat generation through the course of the adsorption trials compared to those conducted without cooling. The increased temperature drop results in an slight increase of mass present in the packed bed but does not guarantee greater mass present inside of the pressure vessel.

Table 6.3: Results of nitrogen adsorption on MOF-5 with and without liquid nitrogen cooling.

Experimental Condition	Cooling	NO Cooling
Nitrogen in Vessel [g]	77.93	80.09
Nitrogen in Bed [g]	36.23	31.44
Initial Average Temperature [K]	99.3	96.9
Average Temperature Rise [K]	20.4	30.8
Final Average Temperature [K]	117.4	126.3
Effective Heat Generation 200s [J]	260.1	505.8
LN2 Mass Flow [g s^{-1}]	1.9	-
Outside Wall Temperature [K]	146.5	129.5

For trials with similar initial bed temperatures, the temperature rise of non-cooled experiments exceeds those of cooled trials by nearly 50%, although significantly higher temperature increase is observed with higher initial MOF-5 bed temperatures in the presence of cooling. The AC trials exhibited approximately half the temperature rise compared to MOF-5 experiments of the same cooling state. Similarly, MOF-5 resulted in an increase in N_2 stored in the bed by 12% for cooled systems and 22% for non-cooled systems compared to AC trials, however, the total N_2 mass in the system is higher for liquid cooled AC, on average, compared to cooled MOF-5. While the non-cooled MOF-5 system stored more total N_2 in the system compared to cooled trials, the non-cooled AC trials exhibited lower total storage capacity compared to cooled experiments. It should be noted that wide variations in storage capacity, both total and in bed, are observed throughout the nitrogen adsorption experiments.

6.2 Hydrogen Adsorption

As described in the previous section, a range of initial and experimental conditions are observed throughout the completion of the hydrogen adsorption investigations on packed beds of activated carbon and MOF-5 (Table 6.4).

Table 6.4: Ranges of initial and operating conditions observed throughout the hydrogen adsorption investigations.

Material	Activated Carbon		MOF-5	
Liquid nitrogen Cooling	Yes	NO Cooling	Yes	NO Cooling
Final Charging Pressure [bar]	50 - 53	50 - 53	51 - 55	52 - 55
Pressurization Time to 50 bars [s]	34 - 130	33 - 147	23 - 64	20 - 85
Charging Time [s]	180; 300	180; 300	180	180
LN2 cooling Time [s]	180; 300	0	300	0
LN2 Mass flow Rate [g s^{-1}]	0.8 - 3.1	0	0.3 - 3.2	0
Average Initial Bed Temperature [K]	106 - 116	106 - 117	110 - 136	110 - 136
Number of Experiments Performed	7	5	11	16

During the hydrogen investigation on activated carbon, the active cooling of liquid nitrogen and hydrogen feed were extended to 300 seconds for a single trial for each cooling scenario to determine if longer hydrogen exposure would result in an increase of stored hydrogen gas in the packed bed of activated carbon. The following is a summary of the hydrogen storage experimental trials; including temperature and pressure profiles, Figure 6.5 to Figure 6.12, and tables of results, Table 6.5 through Table 6.7, for representative experiments.

During the H_2 adsorption on activated carbon experiments, the majority of generated heat is removed in the presence of liquid nitrogen flow through the microchannel heat exchanger and gas distribution system. Hydrogen storage on activated carbon exhibits a much lower overall temperature rise during the experimental trials for both liquid cooled and non-cooled experiments compared to MOF-5; the liquid cooled trials display a lower average temperature rise for both adsorbent materials compared to their respective non-cooled counterparts.

Figure 6.5 depicts the temperature and pressure profile observed throughout an experimental trial with a hydrogen exposure and liquid cooling time of 180 seconds and is compared to temperature profiles obtained from an experiment with 300-second hydrogen exposure and liquid cooling time (Figure 6.6). Both experimental trials exhibit similar initial conditions, compressions times, and final pressure; however, the 180-second trial experiences a lower temperature rise during the charging process and lower final temperature in four of six thermocouples. At the end of the 180-second cooling cycle, a definitive change at TC12 and TC14 is observed as the thermocouples begin to exhibit a relatively constant profile for the remaining 120 seconds, while the remaining thermocouples maintain a stable temperature decline over the same time period. As seen in Figure 6.6, a continued temperature drop is maintained at all six thermocouples through 300 seconds of active liquid nitrogen flow. Both experimental trials exhibit a stable pressure over 300 seconds, with only a slight pressure decline following the closure of the gas entrance valve at 180 seconds.

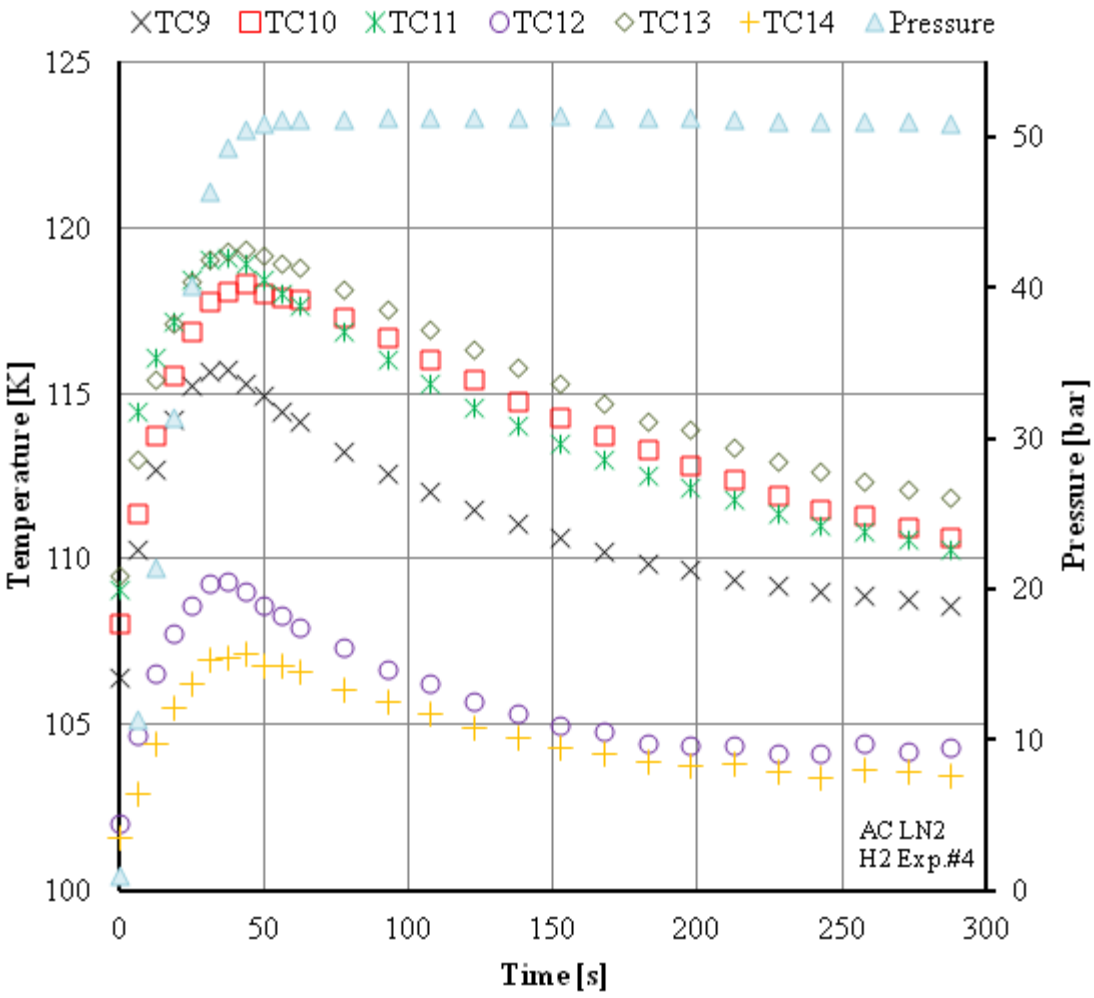

Figure 6.5: Temperature and pressure response in AC bed during 180 second H_2 exposure and 180-s of LN2 cooling.

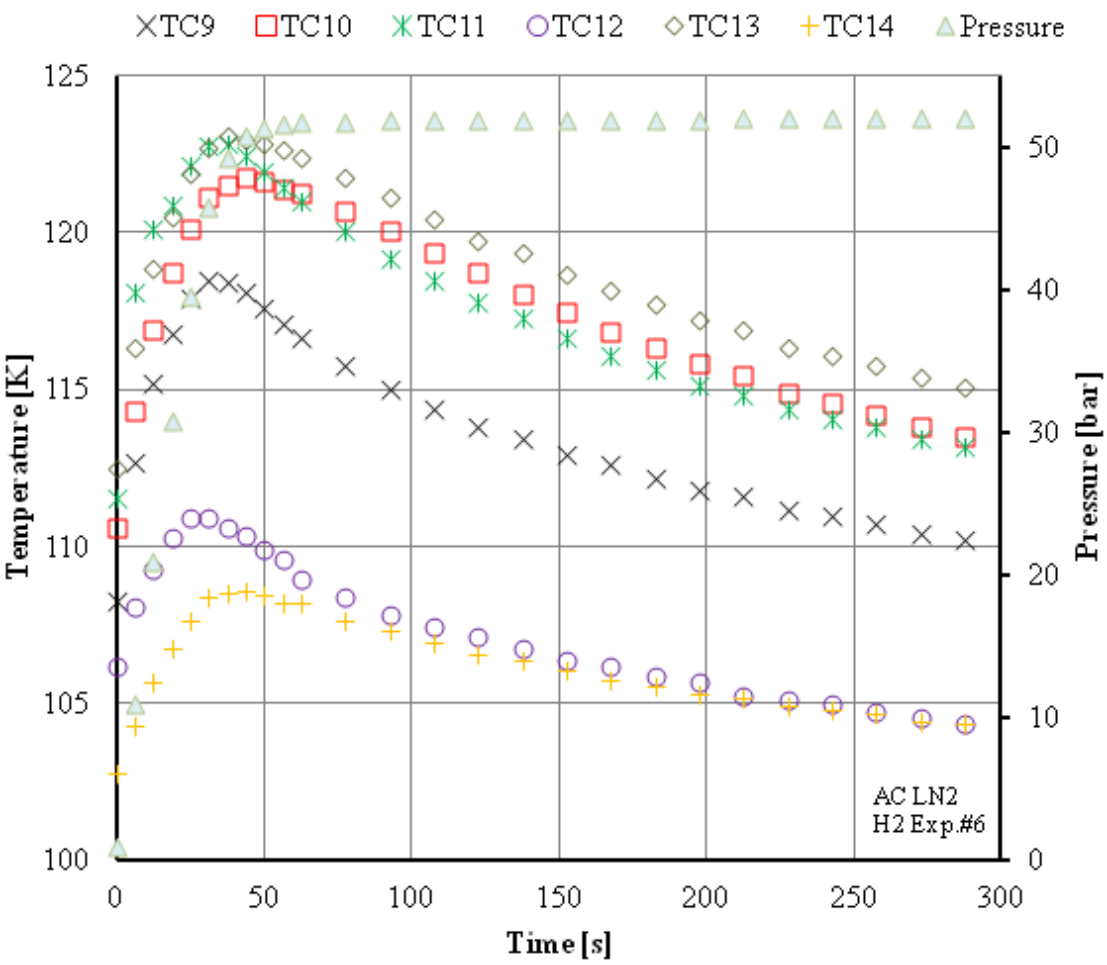

Figure 6.6: Temperature and pressure response in AC bed during 300 second H_2 exposure and 300-s of LN2 cooling.

Similar to the liquid cooled experiments, the 180-second non-cooled hydrogen exposure trial exhibits a slightly lower maximum temperature rise despite having very similar operating conditions as its 300-second exposure counterpart, however in both cooling states, the total charging time will not influence overall temperature rise during the pressurization process. In addition, a slightly more gradual temperature increase is observed at TC14 during the 300-second charging trial. Both trials exhibit minimal temperature decline after reaching maximum temperatures and appear to reach an equilibrium temperature towards the end of the 300-second trial; however, TC12 continues to display an increasing temperature in both trials as the experiment proceeds.

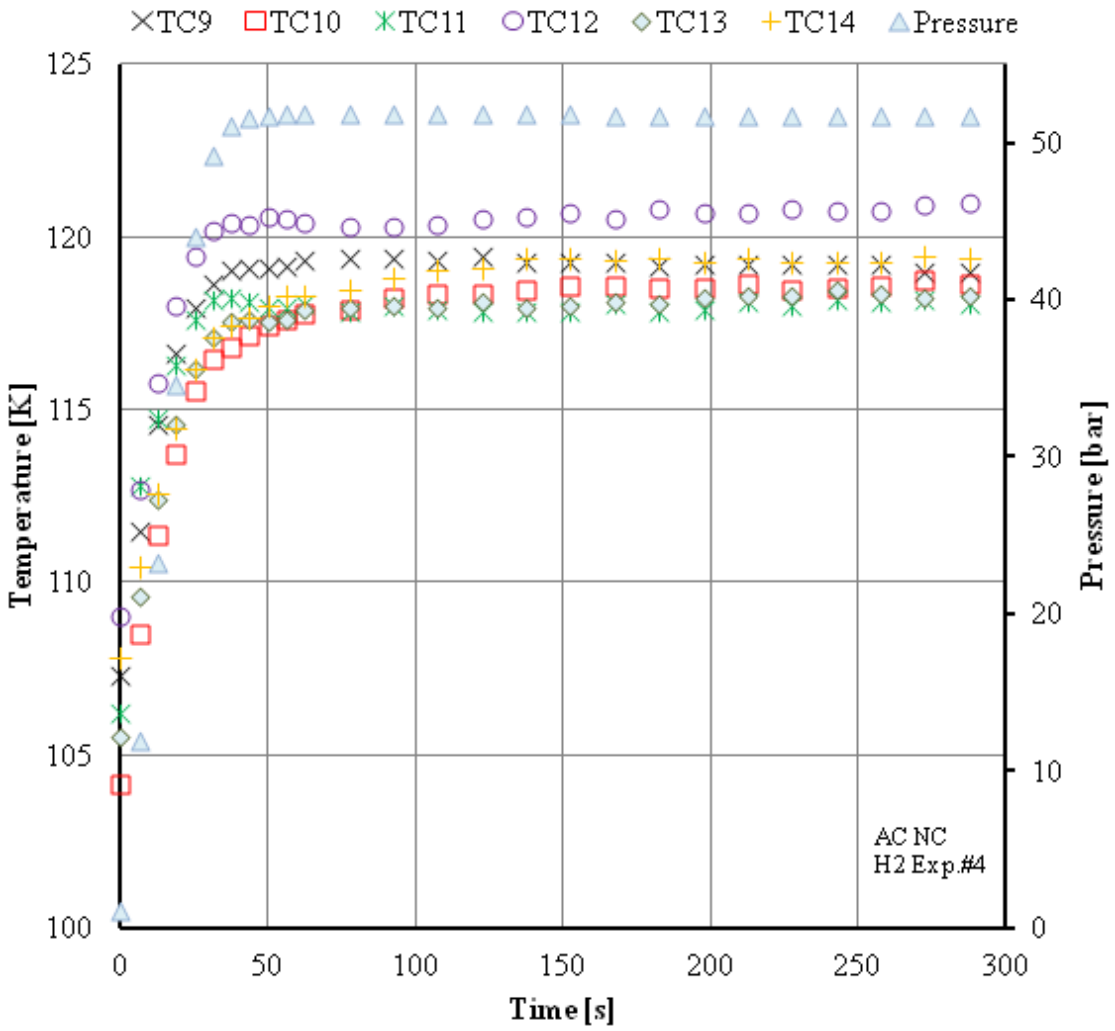

Figure 6.7: Temperature and pressure response in AC bed during 180 second H_2 exposure without cooling.

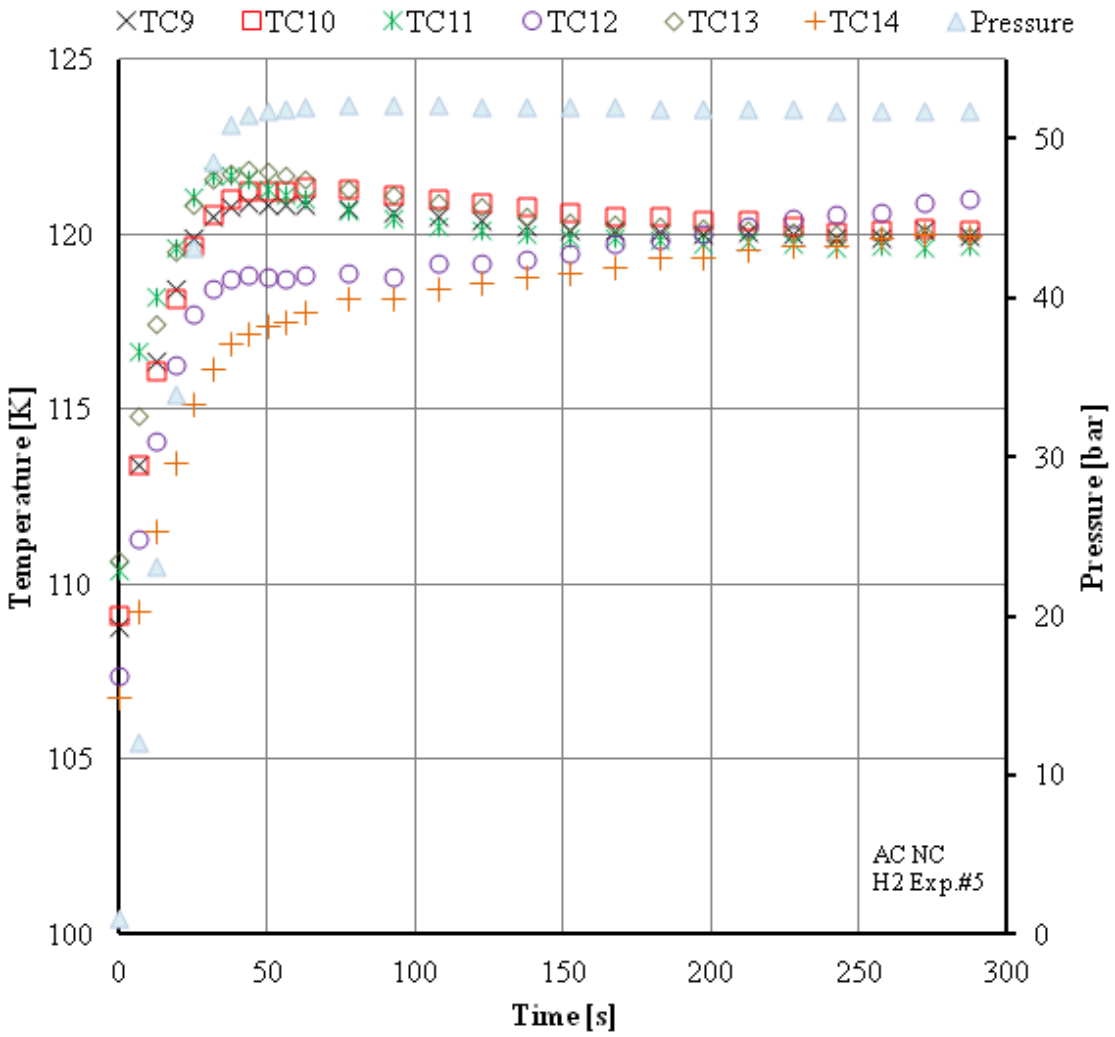

Figure 6.8: Temperature and pressure response in AC bed during 300 second H_2 exposure without cooling.

For both 180-second and 300-second exposure times, liquid nitrogen cooled systems demonstrate nearly 7% increase in the mass of hydrogen gas present in the pressure vessel and at least 5.5% increase in hydrogen mass contained within the adsorbent bed. The effective heat generation is at least 6.5 times smaller in both liquid cooled trials compared to the trials conducted in the absence of cooling.

Table 6.5: Results of hydrogen adsorption on activated carbon with and without liquid nitrogen cooling.

Experimental Condition	180 s H2 Charge & Cooling	180 s H2 Charge & NO Cooling	300 s H2 Charge & Cooling	300 s H2 Charge & NO Cooling
Hydrogen in Vessel [g]	1.69	1.57	1.69	1.56
Hydrogen in Bed [g]	0.73	0.69	0.72	0.67
Initial Average Temperature [K]	106.1	106.7	108.2	108.9
Average Temperature Rise [K]	8.8	12.6	9.5	12.0
Final Average Temperature [K]	108.0	119.0	110.0	120.1
Effective Heat Generation [J]	37.4	269.0	37.2	250.8
LN2 Mass Flow [g s^{-1}]	2.0	-	2.9	-
Outside Wall Temperature [K]	127.5	127.0	130.0	128.5

One of the primary focuses of the HSECoE is the development of a solid-state hydrogen storage system using MOF-5 adsorbent material and, therefore, is the main focus of the experimental investigation, as exhibited by the increase in experimental trials detailed in Table 6.4.

The highest temperature rise during the adsorption experiments was observed with hydrogen adsorption on MOF-5 with and without cooling, and a slightly larger temperature rise is observed in the absence of cooling. The average temperature rise was as much as five times larger than the observed temperature rise from hydrogen adsorption on activated carbon experiments performed. Two pairs of representative MOF-5 hydrogen adsorption trials will be presented; the first pair demonstrates lower and more widely distributed initial temperatures throughout the bed prior to hydrogen charging, while the second pair demonstrates a higher and more uniform initial temperature throughout the adsorbent bed.

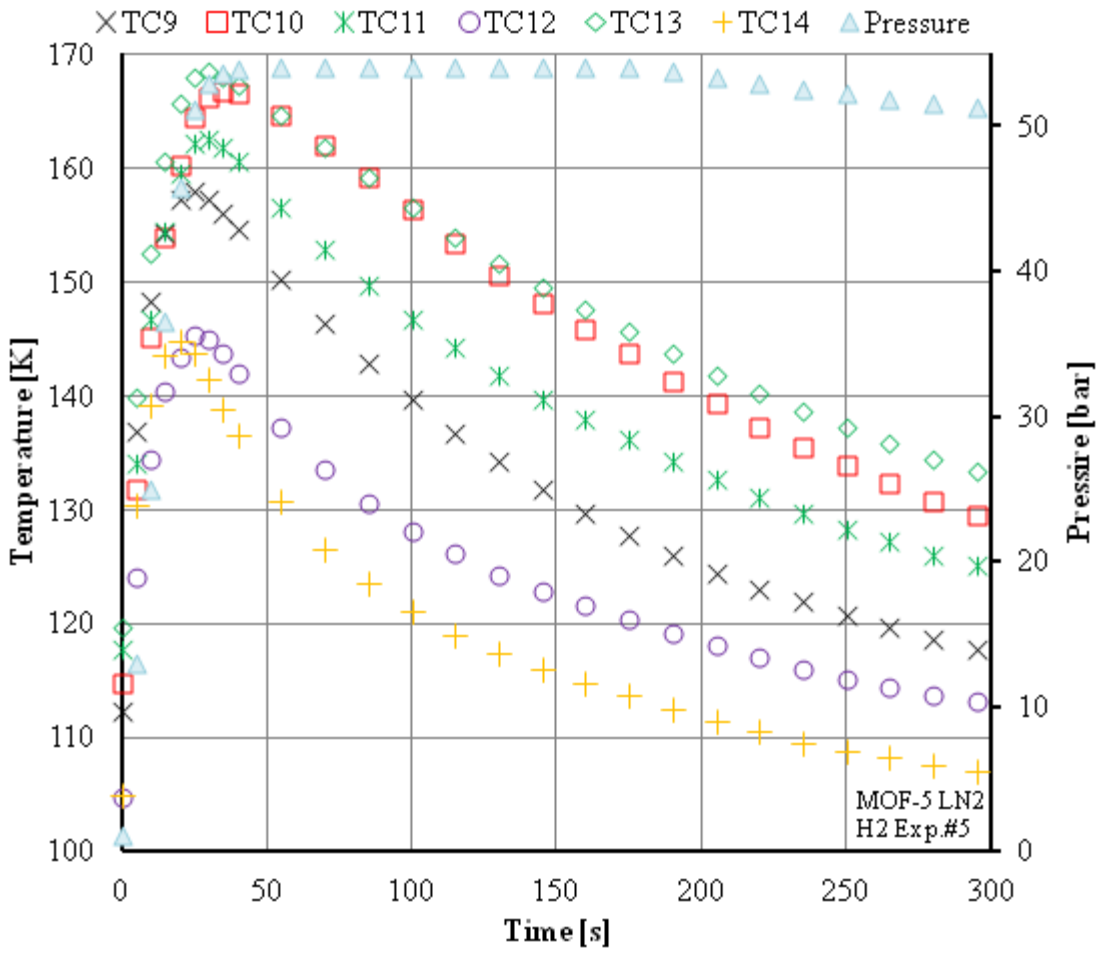

Figure 6.9: Temperature and pressure response in MOF-5 bed during H_2 adsorption with LN2 cooling.

In the widely distributed and lower initial temperature liquid cooled trial, the thermocouples return to within 10 K of their initial temperature following 300 seconds of cooling with exceptions to TC10 and TC14, which cooled to within 15 K of their initial temperatures (Figure 6.9). The temperatures readings of the non-cooled system finished greater than 19 K above the initial temperatures at all thermocouples locations at 300 seconds (Figure 6.10).

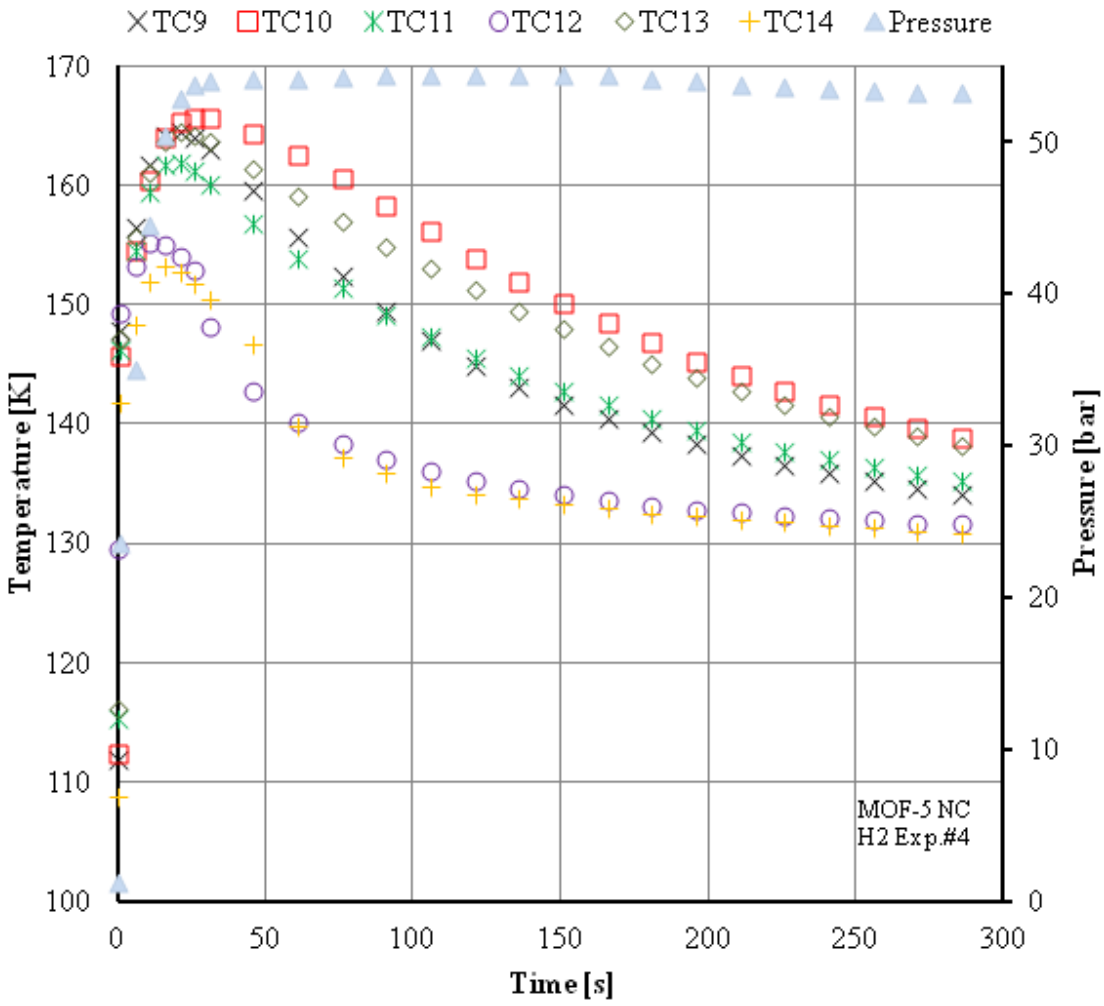

Figure 6.10: Temperature and pressure response in MOF-5 bed during H_2 adsorption without cooling.

In the lower initial temperature experiments, the liquid cooled trial exhibited an effective heat generation $^1/_3$ that observed by the non-cooled adsorption system, resulting in an 11 K increase in the temperature drop from maximum temperature. This coupled with a 3 K lower average temperature rise yielded a final temperature that was 14 K lower in the presence of liquid nitrogen flow. The increased heat removal by liquid nitrogen flow through the heat exchanger resulted in an increase of 5% hydrogen contained within both the pressure vessel and MOF-5 adsorbent bed. A

summary of the results for the lower initial temperature experiments is located in Table 6.6 below.

Table 6.6: Results of hydrogen adsorption on MOF-5 with and without liquid nitrogen cooling for lower average initial bed temperature experiments.

Experimental Condition	Cooling	NO Cooling
Hydrogen in Vessel [g]	2.05	1.95
Hydrogen in Bed [g]	1.15	1.09
Initial Average Temperature [K]	112.4	112.3
Average Temperature Rise [K]	45.3	48.6
Final Average Temperature [K]	120.6	134.7
Effective Heat Generation [J]	151.2	428.8
LN2 Mass Flow [g s^{-1}]	2.8	-
Outside Wall Temperature [K]	140.0	135.5

A more uniform temperature distribution at all thermocouple locations was achieved at slightly elevated initial temperatures and, for liquid cooled experiments, when initiating liquid nitrogen flow just prior to the start of hydrogen charging. Figure 6.11 and Figure 6.12 illustrate the temperature profiles obtained in cooled and non-cooled experimental trials with uniform and elevated average initial temperatures, respectively.

As depicted in Figure 6.11, in the presence of liquid flow through the heat exchanger, four of the six thermocouples located in the MOF-5 bed finished the 300-second hydrogen adsorption trial below their initial temperature readings; the remaining two thermocouples, TC10 and TC13, presented final readings within 3 and 6 K, respectively. The shallowest three thermocouples all finished at least 12 K lower than their initial temperature readings, while TC11 finished 2.5 K lower than its initial value.

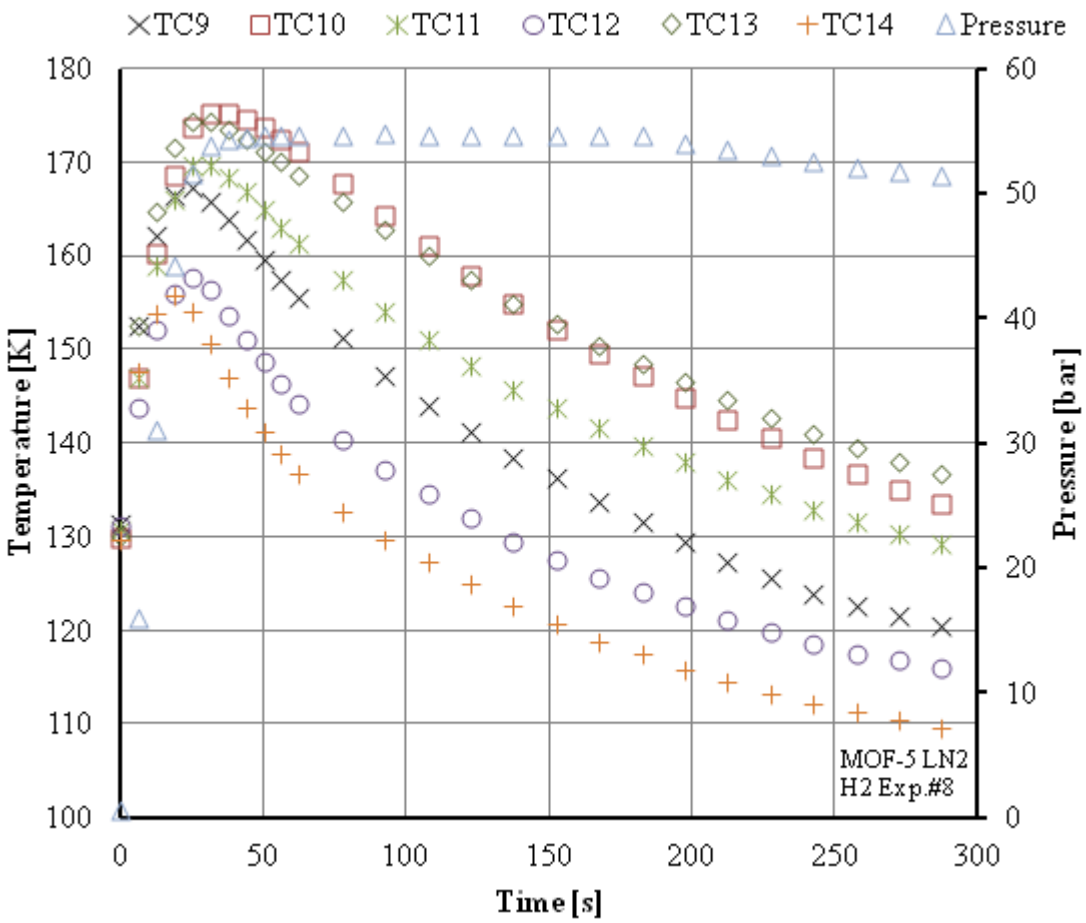

Figure 6.11: Temperature and pressure response in MOF-5 bed during H2 adsorption with LN2 cooling.

It is seen in Figure 6.12 that all six thermocouples inside the MOF-5 bed fail to return to their original temperature readings in the absence of cooling and only the two shallowest thermocouples reach within 10 K of their initial temperatures. At 300 seconds, all of the thermocouples read within 5 K of each other.

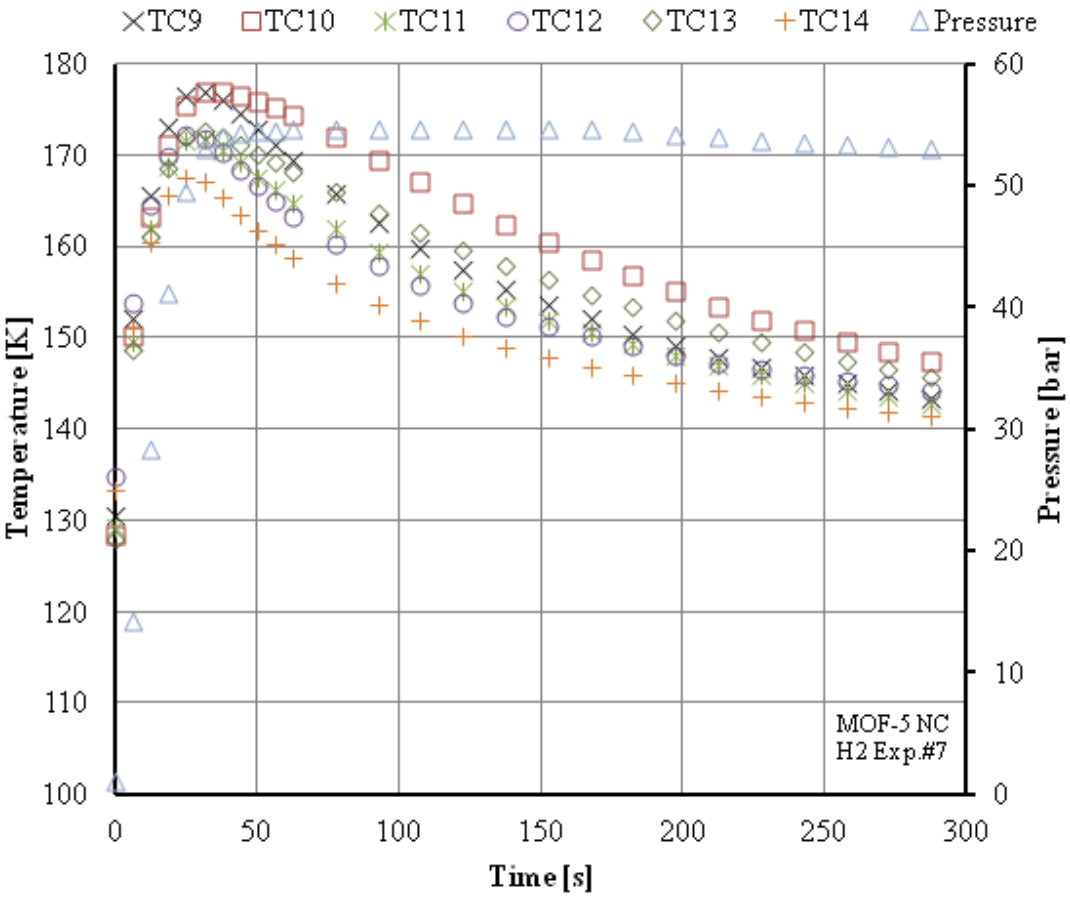

Figure 6.12: Temperature and pressure response in MOF-5 bed during H2 adsorption without cooling.

A smaller average temperature rise is observed during the hydrogen charging of the elevated initial temperature experiments compared to those performed at lower temperatures for both cooled and non-cooled operation. Although a 9 K lower average temperature rise is observed during hydrogen charging, the elevated initial temperature liquid cooled experiment displays 6 K of additional temperature reduction, from maximum temperature, compared to its lower temperature counterpart. The elevated initial temperature experiment reached a final average temperature within 3 K of the lower temperature experiment at 300 seconds.

The non-cooled adsorption experiment performed with an elevated initial temperature demonstrated a 6 K lower temperature rise but experienced a temperature drop, from maximum, 3 K larger than the lower temperature non-cooled trial;

however, the final average temperature is 9 K higher for the elevated temperature investigation.

The use of liquid nitrogen cooling resulted in a 14 K increase in the average temperature drop experienced throughout the MOF-5 adsorbent bed compared to the non-cooled hydrogen charging experiment at elevated temperatures. The microchannel heat exchanger reduced the effective heat generation by 291%, leading to a 7.5% increase in hydrogen inside the pressure vessel and nearly 6.5% more hydrogen in the adsorbent bed, as seen in Table 6.7.

Table 6.7: Results of hydrogen adsorption on MOF-5 with and without liquid nitrogen cooling for higher average initial bed temperature experiments.

Experimental Condition	Cooling	NO Cooling
Hydrogen in Vessel [g]	1.96	1.81
Hydrogen in Bed [g]	1.09	1.02
Initial Average Temperature [K]	130.6	130.7
Average Temperature Rise [K]	36.2	42.4
Final Average Temperature [K]	123.3	143.6
Effective Heat Generation [J]	-140.6	268.5
LN2 Mass Flow [g s^{-1}]	2.7	-
Outside Wall Temperature [K]	143.5	140.5

In addition to a significant increase in temperature rise in MOF-5 H_2 trials, higher storage capacities are reached with either cooling scenario. While MOF-5 increased the adsorbent bed N_2 storage capacity by 12% and 22% for cooled and non-cooled experiments compared to AC, respectively, a 54% and 45% increase in stored H_2 in the bed is observed for cooled and non-cooled MOF-5 trials over AC, respectively. The liquid cooled MOF-5 adsorption of N_2 demonstrated a total storage capacity increase compared to non-cooled AC only, however, for H_2 adsorption trials, liquid cooled MOF-5 resulted in the highest total storage capacity of any experiment, an improvement of 17% over AC and 8% increase over non-cooled MOF-5.

6.3 Discussion and Observations

For both adsorbent materials investigated, a higher molar storage of nitrogen gas is observed in the adsorbent bed with and without cooling compared to hydrogen gas. The additional storage density may be partially attributed to the higher density nitrogen compressed in the open void space of the adsorbent materials and, depending on the experimental temperature and pressures, compressed liquid nitrogen may potentially be present in material voids.

Of the six liquid cooled MOF-5 hydrogen adsorption experiments performed with an average initial bed temperature over 130 K, five demonstrated a negative effective heat generation over the 300-second cooling cycle; this indicates greater heat removal from the bed than is generated during charging, resulting in a lower average final temperature than it initially began with. The sixth trial, with an initial temperature greater than 130 K, achieved the lowest positive effective heat generation of the remaining MOF-5 experiments. The lowest effective heat generation for a non-cooled trial was found to be 192 J, approximately 40 J higher than the maximum generation observed with liquid nitrogen cooling.

Similar to the MOF-5 hydrogen adsorption trials, hydrogen adsorption on activated carbon trials demonstrated significantly lower effective heat generation using liquid nitrogen cooling compared to trials performed without cooling. Only a single activated carbon experiment demonstrated a negative effective heat generation, and the largest effective heat generation of the liquid cooled trials is 80 J compared to a minimum value of 155 J in the absence of cooling.

The majority of the nitrogen adsorption experiments, for both adsorbent materials, demonstrated lower effective heat generation with liquid nitrogen cooling compared to those conducted without cooling, with one exception: nitrogen adsorption on MOF-5 conducted at initial average bed temperatures below that of the liquid nitrogen coolant flowing through the heat exchange device.

In data analysis, it was uncovered that a lower limit appears on the final average bed temperature throughout the experimental investigations, which limited the microchannel heat exchanger's ability to remove additional heat from the system; this resulted in an upper storage limit on the adsorbent materials under investigation by preventing lower bed temperatures from being achieved. The low standard deviations of final average bed temperature and stored hydrogen in the adsorbent provides additional support of lower temperature limitation in the device (Table 6.8).

Table 6.8: Averages and standard deviations of experimental conditions and results for hydrogen adsorption (excluding outliers).

Material	**AC**	**AC**	**MOF-5**	**MOF-5**
Liquid Nitrogen Cooling	Yes	NO	Yes	NO
Average of Final Average Bed Temperatures [K]	111.7	120.3	125.2	140.5
Standard Deviation of Final Average Bed Temperatures [K]	3.7	1.6	5.1	4.7
Average Wall Temperature [K]	130.1	126.4	147.0	138.7
Standard Deviation of Wall Temperature [K]	4.2	1.9	11.4	6.3
Average Hydrogen Stored in bed [g]	0.71	0.69	1.09	0.98
Standard Deviation of Hydrogen Stored in bed [g]	0.05	0.01	0.06	0.06

Two insights into the experimental system and the transport phenomena governing the adsorption process support the presence of a performance limitation throughout the experimental investigation. A material's ability to withstand changes in temperature is described as thermal mass (the product of material's mass and specific heat capacity) and is an indication of the energy required per Kelvin of temperature change. The high average thermal mass (Table 6.9) exhibited by the pressure vessel and insulation materials illustrates the difficulty of substantially

cooling the experimental system with liquid nitrogen flow through a single microchannel heat exchanger. The inability to lower the temperature of the surrounding material, in addition to cooling the adsorbent bed and gas, results in the lower temperature limitation experienced by the adsorbent bed in the experiments.

Table 6.9: Average thermal mass, [J/K], of the experimental components and adsorbent beds over the experimental temperature range.

Stainless Steel Vessel	3435.8
PTFE Insulation	110.2
MOF-5	11.0
AC	9.8

Table 6.10:Ratio of the average thermal mass of the pressure vessel, and PTFE insulation, to the adsorbent beds used in the experimental investigation.

	MOF-5	**AC**
Stainless Steel Vessel	294.6	352.3
PTFE insulation	10.0	11.3

Thus, it is expected that a significantly lower vessel temperature will result in a lower average final bed temperature; however, comparing Figure 6.13 and Figure 6.14, if the vessel temperature is too low, the flow of pressurized liquid nitrogen results in the addition of heat to the adsorbent bed because higher temperature liquid nitrogen flows through the device. The liquid flow increases the final average bed temperature compared to the non-cooled system, which exhibits minimal change in temperature over the 300-second experiment.

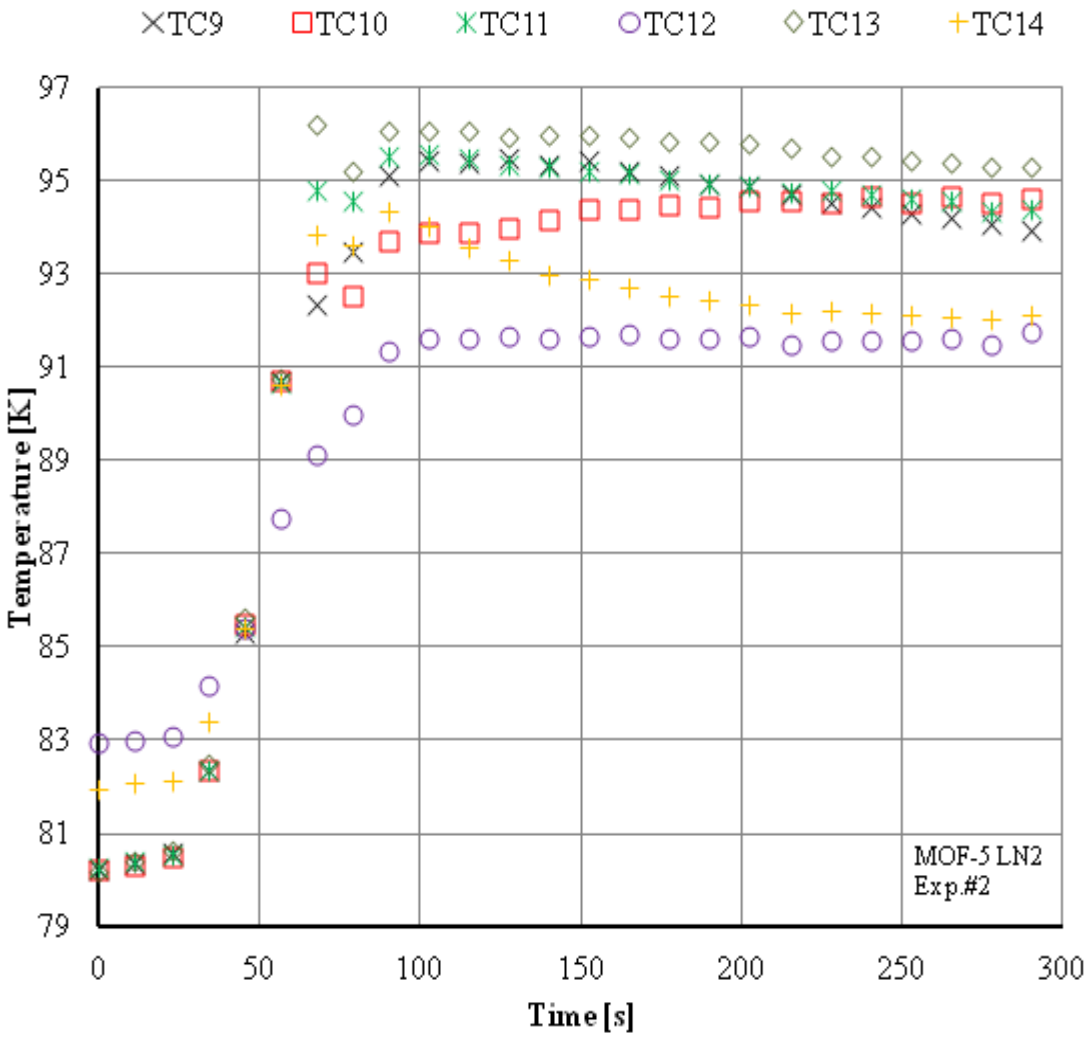

Figure 6.13: Nitrogen adsorption on MOF-5 with liquid nitrogen cooling, wall temperature 99.0 [K] and averaged initial bed temperature 81.0 [K].

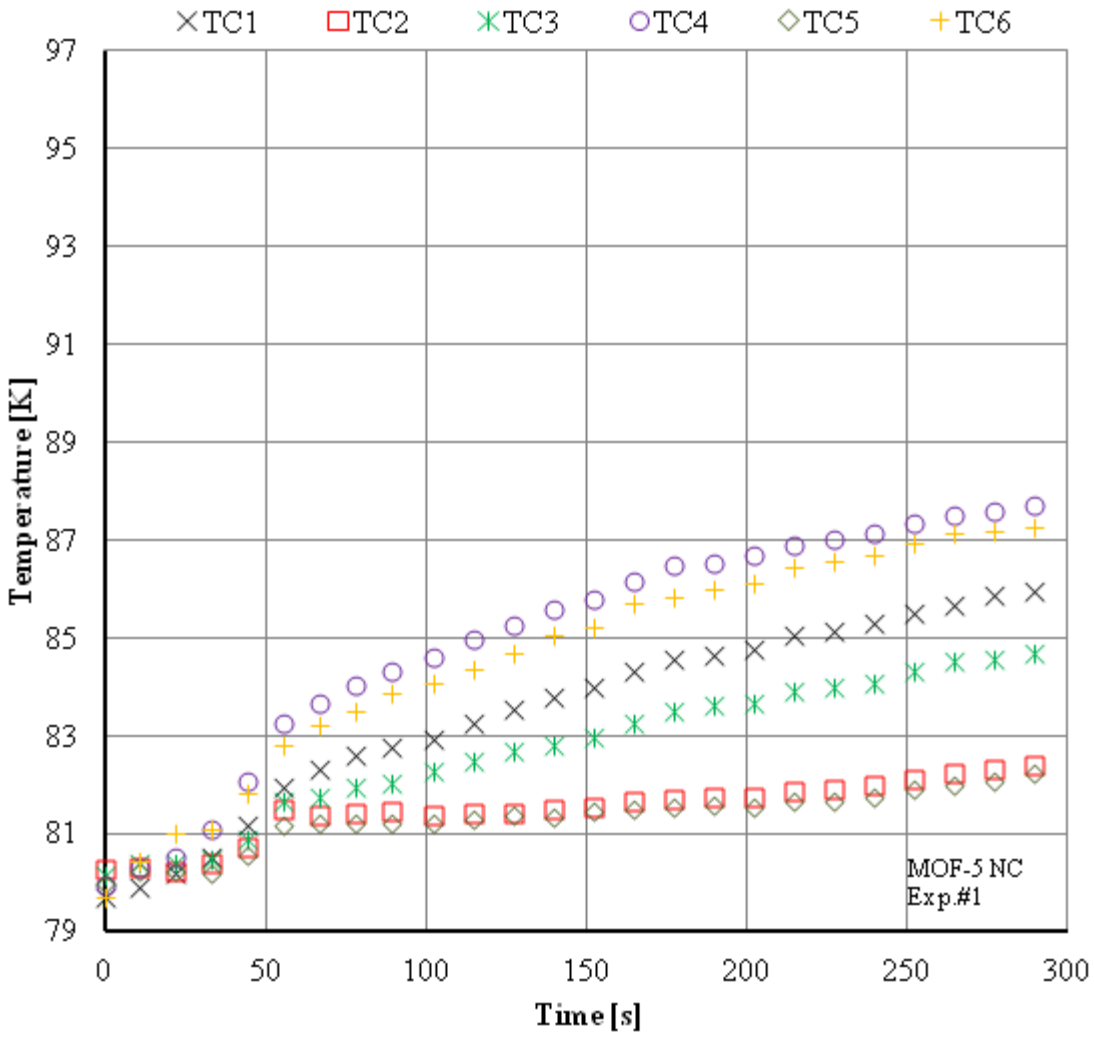

Figure 6.14: Nitrogen adsorption on MOF-5 without cooling, wall temperature 97.5 [K] and averaged initial bed temperature 80.0 [K].

Secondly, significant differences in the characteristic times of thermal transport within the system provide additional justification for the inability of a single microchannel heat exchanger to substantially lower the temperature of the adsorbent bed, PTFE insulation, and pressure vessel simultaneously.

Conductive transport through the solid PTFE insulation and stainless steel pressure vessel is the dominant form of energy transport. The characteristic time necessary for conductive transport is

$$\tau_{cond} = \frac{\rho C_p L^2}{k} \tag{6.2}$$

in which L is the characteristic length of conductive transport, defined by the material thickness in the system under investigation.

Energy transport throughout the adsorbent bed is achieved by conductive, convective, and reactive heat generation, yielding three independent characteristic times of energy transport. The conductive transport through the adsorbent bed is

$$\tau_{cond,ad} = \frac{\sum\left(\rho C_p\right) L^2}{k_{eff}} \tag{6.3}$$

The summation in (6.3) represents the contributions of gas, adsorbent, and adsorbed phases inside the adsorbent bed; k_{eff} represents the effective conductivity of the adsorbent bed and takes into account the contributions of solid adsorbent and gas present in the interparticle pores. The characteristic time of convective transport through the bed is

$$\tau_{cv,ad} = \frac{\sum\left(\rho C_p\right) L}{\rho_g C_{pg} \overrightarrow{u_A}} \tag{6.4}$$

Finally, the characteristic time of energy release due to adsorption is a function of a system reference temperature, T_R, the heat of adsorption, ΔH_{ads}, and the rate of gas adsorption

$$\tau_{ah,ad} = \frac{\sum\left(\rho C_p\right) T_R}{\Delta H_{ads} M_{Wg} \rho_b \dfrac{\partial n_a}{\partial t}} \tag{6.5}$$

The characteristic times for the pressure vessel, insulation and adsorbent bed are calculated using the COMSOL simulation tool (chapters 7 and 8) and are listed in Table 6.11, normalized with respect to the characteristic time of convective heat transfer. Although the characteristic transport times are dynamic quantities, it is clear

that the conductive heat transfer through the bed inhibits the removal of additional heat from the PTFE and stainless steel by liquid nitrogen flowing through a single microchannel device. This is true in the first 30 seconds, when convective heat transfer and adsorption heat generation are fastest, as well as throughout the entire 300-second simulation.

Table 6.11: Average characteristic times of thermal transport and generation

Material	**PTFE**	**Stainless Steel**	**MOF-5 Adsorbent, Gas & Adsorbed Phase**		
Form of Energy Transport	**Conductive**	**Conductive**	**Conductive**	**Convective**	**Generation**
First 30 Seconds of Simulation	2.50	1.24	24.38	1	0.48
300 Seconds of Simulation	1.26	0.56	25.12	1	20.39

Similarities were observed in final temperature and hydrogen storage capacity between the 180- and 300-second hydrogen exposure trials on activated carbon, despite an additional 120 seconds of liquid nitrogen cooling (at a higher flow rate) and pressurized hydrogen source, providing additional support of the presence of a lower temperature limit of the experimental system. In addition, a performance limitation would explain the similar final average bed temperatures and individual thermocouple temperatures observed throughout the adsorbent bed despite different liquid nitrogen flow rates and sub-cooled temperatures entering the heat exchanger.

With liquid nitrogen flow through the microchannel heat exchanger, the experimental results indicate increased heat removal from the adsorbent bed, resulting in an increase in hydrogen storage capacity. When compared to a cryo-compressed system of equal total volume, the presence of MOF-5 adsorbent provides a significant increase in the total H_2 stored in the system, at the final system pressure and temperature of the free space region, with and without liquid nitrogen cooling. The non-cooled AC experiments, however, produce only a small benefit over a cryo-

compressed system, while the liquid cooled AC system actually results in poorer H_2 storage performance.

Table 6.12: Storage capacity comparison of adsorbent system to cryo-compressed system (excluding outliers).

	MOF-5		AC	
	Cooled	**Non-cooled**	**Cooled**	**Non-cooled**
Average total H_2 stored using adsorbent [g]	1.91	1.78	1.64	1.56
H_2 stored in cryo-compressed system [g]	1.49	1.40	1.66	1.53
Relative Difference [%]	21.99	21.10	-0.97	1.30

Despite the imposed performance limitation of the experimental system, the observed temperature response during the liquid cooled adsorption experiments demonstrates a significant difference when compared with the response to non-cooled trials. This difference is evident through the comparison of the plotted thermocouple responses (Figure 6.15 to Figure 6.17) at each thermocouple location during the hydrogen adsorption experiments operated with and without liquid nitrogen flow.

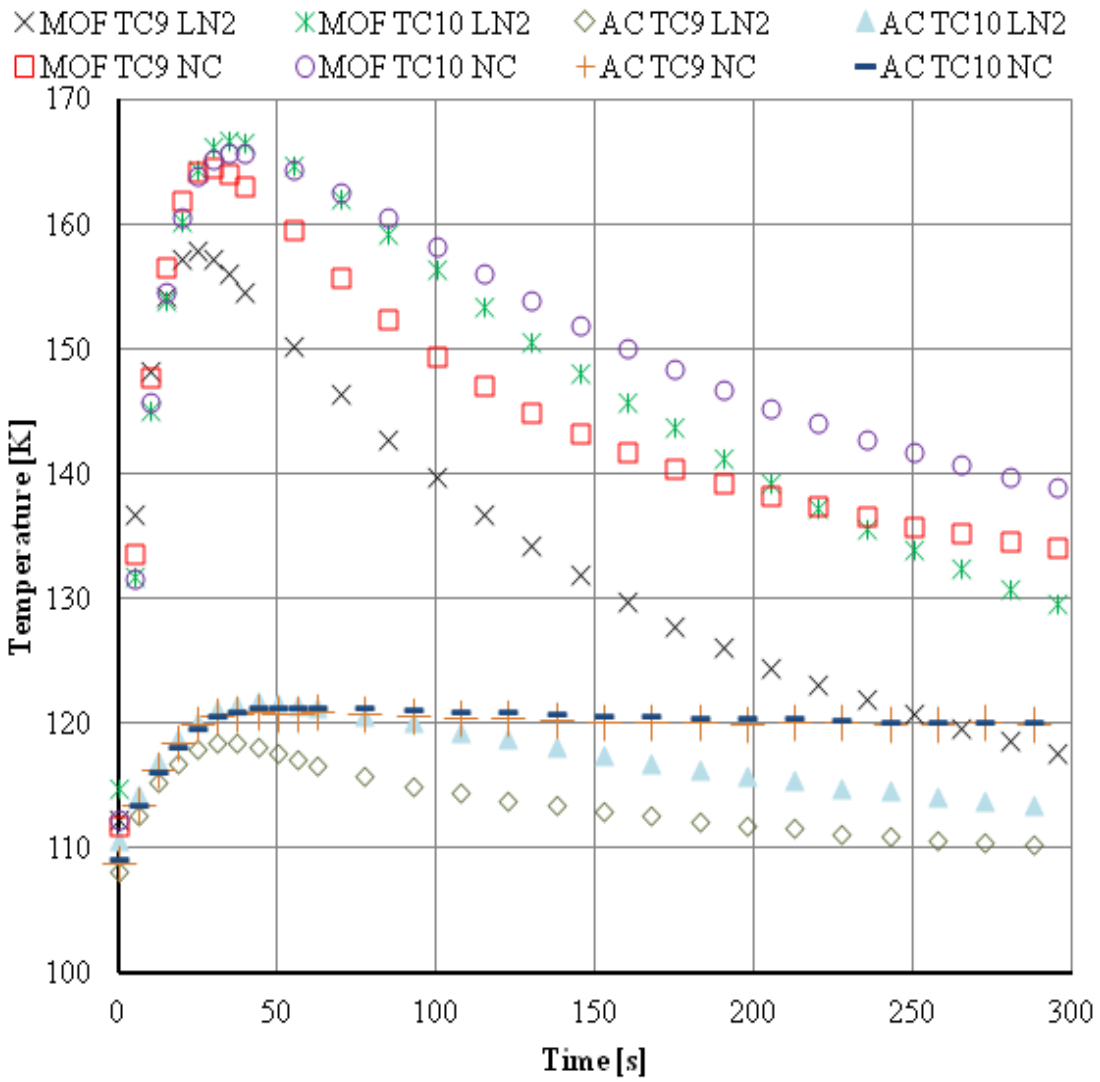

Figure 6.15: Comparison of the observed temperature responses with and without cooling at TC9 and TC10 in both MOF-5 and AX-21 (AC) adsorbent beds.

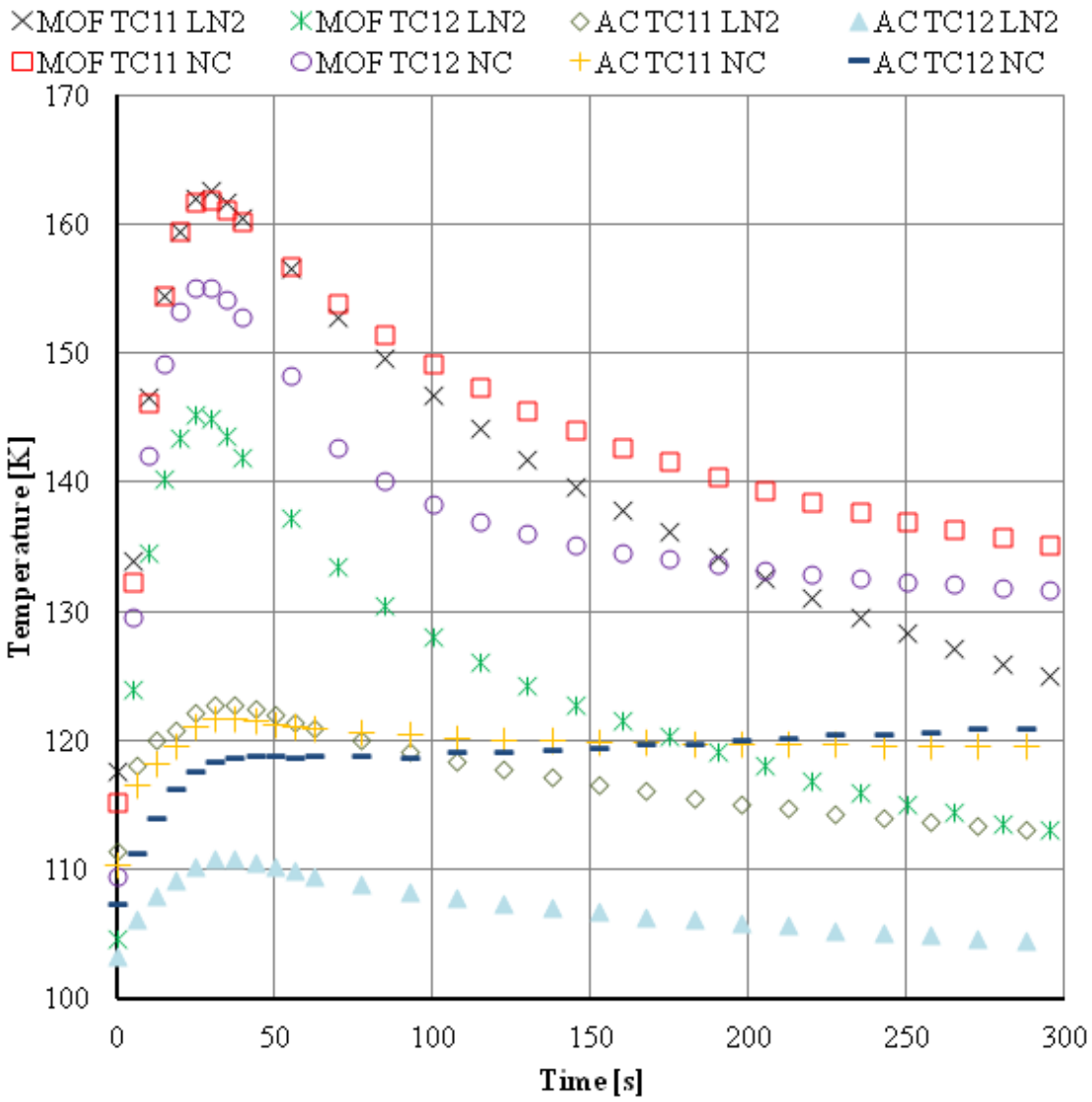

Figure 6.16: Comparison of the observed temperature responses with and without cooling at TC11 and TC12 in both MOF-5 and AX-21 (AC) adsorbent beds.

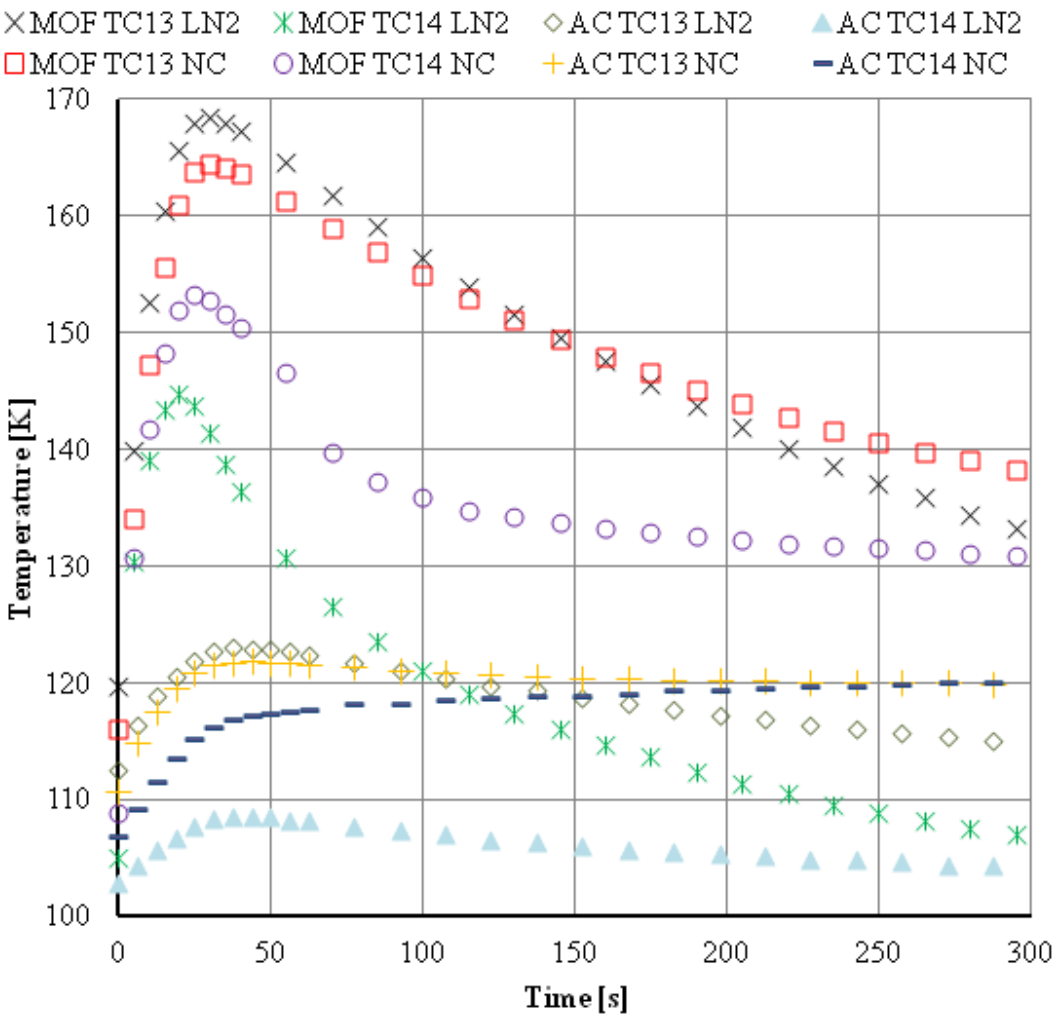

Figure 6.17: Comparison of the observed temperature responses with and without cooling at TC13 and TC14 in both MOF-5 and AX-21 (AC) adsorbent beds.

At greater insertion depth (TC10, TC11, TC13), the temperature observed during vessel charging is approximately equal with and without liquid nitrogen cooling; alternatively, at lower insertion depths, closer to the heat exchanger, the temperature rise is at least 4 K lower with cooling than is observed without. The combined effects of heat removal and lower gas temperature entering the bed would be responsible for this observation. However, at greater bed depths, charging gas continuously interacts with the adsorbent bed and regions of increased temperature (due to heat released because of adsorption) and does not possess the same cooling capacity exhibited at shallower depths. In addition, the penetration of conductive heat

transfer from the heat exchanger to the bed is insufficient to reduce the temperature rise deeper in the bed (during the brief period of pressurization) compared to a non-cooled system.

Based on thermocouple insertion depth and relation to the liquid nitrogen inlet, it is expected that TC12 (closer to cooling fluid inlet) records lower temperature readings than TC14 (located closer to fluid exit) if any difference is observed due the nearly identical vertical alignments. Of the eight experimental combinations of material, gas, and cooling state, TC12 demonstrated a higher temperature than TC14 except for liquid cooled nitrogen adsorption on MOF-5, which demonstrated an average of 5.5 K lower reading than TC14 at 300 seconds. In the remaining seven combinations tested, TC14 displayed a lower temperature, with an average ranging from 0.7 to 1.5 K; although liquid cooled hydrogen adsorption trials on MOF-5 trials demonstrated a 6.7 K lower temperature reading at TC14 compared to TC12. Based on the temperature difference between TC12 and TC14 for all of the non-cooled experimental trials, the two thermocouples are considered equal, with respect to the experimental error of the thermocouples. This similarity is, additionally, extended to the liquid cooled activated carbon experiments and is expected for all MOF-5 trials.

The significantly larger difference in both liquid cooled MOF-5 experiments indicates an alteration in the internal alignment of the thermocouples with respect to the cooling plate (contact between plate and thermocouple) that is not present in the activated carbon experiments. However, the change in affected thermocouple between experimental trials cannot be easily explained and could result from human error or from a rotation and shifting of the internal components during repeated assembling and disassembling of the pressure vessel with the bulk of the experimental system between investigations.

Table 6.13: Average differece of TC12 & TC14 and TC10 &TC13.

		Nitrogen		Hydrogen	
	Cooling	AX-21	MOF-5	AX-21	MOF-5
TC12-TC14	Yes	0.76	-5.45	0.69	6.65
	NO	0.82	0.74	1.14	1.44

Chapter 7: Mathematical Modeling and Production of Development Tool

The development and validation of mathematical models have aided in the design and optimization of a variety of laboratory and industrial equipment and processes. Validated models and simulation tools allow researchers to test a variety of experimental materials, designs, and operating conditions for improvements and optimization without needing to design and perform numerous experiments. This chapter provides a sampling of the modeling investigations focusing on solid-state hydrogen storage and describing the assumptions, boundary conditions, and equations used to develop the mathematical model and simulation tool in support of this work.

7.1 Modeling and Simulations of Solid-State Hydrogen Storage

Many research groups using various software packages, assumptions and theories to investigate both metal hydride and adsorbent storage systems have produced mathematical models and simulations.

In addition to investigating the importance of heat exchangers in a metal hydride system, the team of Visaria *et al.* (2010) used two-dimensional simulations to predict a maximum thickness of a $Ti_{1.1}CrMn$ metal hydride bed (10 mm) between cooling surfaces that would facilitate adequate heat transfer to charge in five minutes. Additionally, the investigation deduced the existence of a minimum coolant flow rate necessary to remove generated heat but that substantial performance enhancements were not observed with flow rates above the minimum [74].

Although system modeling plays an important role in design and optimization, validation of proposed modifications in the underlying mathematical models have a tremendous impact on the accuracy of the simulations performed. In a two-part investigation, Richard *et al*. (2009) proposed modifications to the classic Dubinin-Astakhov model, discussed in chapter 2, to enhance its capabilities in the characterization of the adsorption of supercritical fluids. The authors used adsorption data, over a wide range of temperatures and pressures, for three different

adsorbate/adsorbent pairs to validate their model and demonstrate a temperature dependence on the free energy of adsorption for supercritical fluids [48]. A subsequent study investigated the conservation of mass and energy with the modified DA equation and was found to accurately describe previously published data for the discharging of hydrogen, nitrogen, and methane storage systems [78].

A two-dimensional, axially symmetric simulation was produced by Momen *et al*. (2009) to investigate the hydrogen adsorption capacity of activated carbon as a function of energy release. Variations in adsorption capacity of the system allowed the authors to investigate multiple magnitudes of heat release and isolate the heat generated from the compression of gas during charging by setting the adsorption capacity to zero. As expected, a higher temperature increase is observed as storage capacity increases, and it was observed that the temperature rise during charging increases with increasing capacity: 5 K rise for 0.6% capacity versus 15 K rise for 6% capacity upon near doubling of flow rate. Finally it was found that the contribution of the heat generated by the compressing gas decreases with increasing storage capacity [79].

Paggiaro *et al.* (2010) and Hardy *et al.* (2012) investigated adsorption systems utilizing flow-through cooling to remove generated heat without adding an internal thermal management system or conductive enhancement materials by using two-dimensional axial symmetric simulations created in COMSOL Multiphysics. Paggiaro *et al*. concluded that a 30 bar storage system with recycled hydrogen gas flow was capable of removing the heat of adsorption; however, faster and more uniform cooling was achieved by providing an external flow of liquid nitrogen to the outer vessel wall [80]. Higher-pressure system investigations (200 bar flow-through) by Hardy *et al.* compared the performance and heat generation between MOF-5 and MaxSorb MSC-30 (similar to AX-21) storage systems. It was found that heat released by compression during a 20-second hydrogen charge, from five to 200 bars prior to onset of flow-through cooling, results in only 22% of the total heat generation in the MaxSorb

system. The higher bulk density MaxSorb system releases 2.25 times more heat during the adsorption process, yielding a 134% increase in adsorbed hydrogen compared to the MOF-5 system; however, 35% less hydrogen was available in the void volume of the MaxSorb system [70].

In a display of the versatility and robustness of mathematical modeling, a series of validated simulation tools, using multiple simulation packages, have been produced by the team of Xiao *et al*. (2010-2012). The group has produced simulations using COMSOL Multiphysics, Fluent, and Matlab/Simulink software platforms to simulate heat and mass transfer during charging and discharging processes. Other simulated investigations have focused on the effects of hydrogen mass flow rate on pressure and temperature evolution and adsorption capacity [81 - 85].

7.2 Mathematical Model

The mathematical model derived to characterize the experimental investigation of this work uses the Cartesian coordinate system. Although polar coordinates are often used to describe cylindrical systems (characteristic of the materials and apparatus in this work), COMSOL Multiphysics utilizes Cartesian coordinates to solve three-dimensional models and, therefore, were chosen for consistency with the simulation tool created. A detailed derivation of the conservation equations for mass, momentum, and energy of the system under investigation is located in the Appendix.

7.2.1 Conservation of mass

The continuity equation is used to describe the single component mass transfer of gas in both free space and the porous adsorbent materials. As a demonstration, the continuity equations, for both free and porous flow, will initially be presented in their fully expanded forms and subsequently condensed to vector notation to illustrate the similarities between them. The following balances for the porous media are derived based on the assumption that the adsorbent porosity,

$$\varepsilon = \frac{V_g}{V} = \frac{V - V_s}{V} = 1 - \frac{V_s}{V} \tag{7.1}$$

remains constant throughout the adsorption process, and therefore the continuity equation for the porous media is

$$\begin{aligned} &\varepsilon \frac{\partial \rho_g}{\partial t} + \varepsilon u_x \frac{\partial \left(\rho_g\right)}{\partial x} + \varepsilon u_y \frac{\partial \left(\rho_g\right)}{\partial y} + \varepsilon u_z \frac{\partial \left(\rho_g\right)}{\partial z} \\ &+ \rho_g \frac{\partial \left(\varepsilon u_x\right)}{\partial x} + \rho_g \frac{\partial \left(\varepsilon u_y\right)}{\partial y} + \rho_g \frac{\partial \left(\varepsilon u_z\right)}{\partial z} = -\gamma_m \end{aligned} \tag{7.2}$$

The term on the right-hand side of (7.2), γ_m, represents the mass sink associated with gas adsorption. Similarly, the continuity equation for free flow is

$$\begin{aligned} &\frac{\partial \rho_g}{\partial t} + u_x \frac{\partial \left(\rho_g\right)}{\partial x} + u_y \frac{\partial \left(\rho_g\right)}{\partial y} + u_z \frac{\partial \left(\rho_g\right)}{\partial z} \\ &+ \rho_g \frac{\partial \left(u_x\right)}{\partial x} + \rho_g \frac{\partial \left(u_y\right)}{\partial y} + \rho_g \frac{\partial \left(u_z\right)}{\partial z} = 0 \end{aligned} \tag{7.3}$$

Defining the superficial gas velocity in the porous media as

$$u_{i,A} = \varepsilon u_i \tag{7.4}$$

and is substituting into (7.2) yields

$$\begin{aligned} &\varepsilon \frac{\partial \rho_g}{\partial t} + u_{x,A} \frac{\partial \left(\rho_g\right)}{\partial x} + u_{y,A} \frac{\partial \left(\rho_g\right)}{\partial y} + u_{z,A} \frac{\partial \left(\rho_g\right)}{\partial z} \\ &+ \rho_g \frac{\partial \left(u_{x,A}\right)}{\partial x} + \rho_g \frac{\partial \left(u_{y,A}\right)}{\partial y} + \rho_g \frac{\partial \left(u_{z,A}\right)}{\partial z} = -\gamma_m \end{aligned} \tag{7.5}$$

Equations (7.5) and (7.3), respectively, can be rewritten as

$$\varepsilon \frac{\partial \rho_g}{\partial t} + \overrightarrow{u_A} \cdot \nabla \rho_g + \rho_g \nabla \cdot \overrightarrow{u_A} = -\gamma_m \tag{7.6}$$

$$\frac{\partial \rho_g}{\partial t} + \vec{u} \cdot \nabla \rho_g + \rho_g \nabla \cdot \vec{u} = 0 \tag{7.7}$$

Finally, the second and third terms on the left-hand side of (7.6) and (7.7) may be combined to yield

$$\varepsilon \frac{\partial \rho_g}{\partial t} + \nabla \cdot \left(\overrightarrow{u_A} \rho_g \right) = -\gamma_m \tag{7.8}$$

$$\frac{\partial \rho_g}{\partial t} + \nabla \cdot \left(\vec{u} \rho_g \right) = 0 \tag{7.9}$$

Therefore, it can be seen that the mass balance for free flow can be obtained from the porous media mass balance by setting the porosity to unity and the mass sink to zero.

It is assumed that throughout the adsorption process the mass of the solid adsorbent remains constant, and therefore, the mass balance for the solid is

$$\frac{\partial \left(m_{SA} \right)}{\partial t} = \frac{\partial \left(\dfrac{m_{SA}}{V_{SA}} \right)}{\partial t} = \left(1 - \varepsilon \right) V \frac{\partial \left(\dfrac{m_{SA}}{V_{SA}} \right)}{\partial t} = \left(1 - \varepsilon \right) V \frac{\partial \rho_{SA}}{\partial t} = 0 \tag{7.10}$$

On a per volume basis

$$\left(1 - \varepsilon \right) \frac{\partial \rho_{SA}}{\partial t} = 0 \tag{7.11}$$

Considering the bulk density of the packed bed to be

$$\rho_b = \frac{m_{SA} + m_g}{V} = \frac{\left(1 - \varepsilon \right) V \rho_{SA} + \varepsilon V \rho_g}{V} = \left(1 - \varepsilon \right) \rho_{SA} + \varepsilon \rho_g \tag{7.12}$$

Assuming the contribution of the mass of the gas phase is negligible compared to the solid adsorbent mass

$$\rho_b = (1-\varepsilon)\rho_{SA} \tag{7.13}$$

The change in density of the adsorbed gas phase is

$$\frac{\partial \rho_a}{\partial t} = \gamma_m \tag{7.14}$$

The mass source/sink due to the adsorption of gas on the adsorbent surface is expressed as

$$\gamma_m = M_g \rho_b \frac{\partial n_a}{\partial t} \tag{7.15}$$

Where M_g is the molecular mass of gas. The moles of adsorbed gas, n_a, is obtained by applying the modified Dubinin-Astakhov model, (7.16), described in chapter 2 [48].

$$n_a = n_{\max} \exp\left[-\left(\frac{RT}{\alpha + \beta T} \right)^2 \ln^2 \left(\frac{p_0}{p} \right) \right] \tag{7.16}$$

7.2.2 Conservation of Momentum

In deriving the conservation of momentum for free and porous flow, it was assumed that the change in momentum resulting from gravitational force acting on the gas is negligible. The conservation of momentum of gas flowing through the porous adsorbent is

$$\frac{\rho_g}{\varepsilon}\frac{\partial \overrightarrow{u_A}}{\partial t} + \frac{\overrightarrow{u_A}}{\varepsilon^2}\nabla\left(\rho_g \overrightarrow{u_A}\right) + \left[\frac{\mu}{\kappa} - \frac{\gamma_m}{\varepsilon^2}\right]\overrightarrow{u_A} = -\nabla p + \nabla \cdot \left[\frac{\mu}{\varepsilon}\left(\nabla \overrightarrow{u_A} + \nabla \overrightarrow{u_A}^T\right)\right] - \nabla \cdot \left[\frac{2\mu}{3\varepsilon}\nabla \cdot \overrightarrow{u_A} I\right] \tag{7.17}$$

The loss of momentum resulting from flow through the porous bed is captured in (7.17) by

$$\left[\frac{\mu}{\kappa}\right]\overrightarrow{u_A} \tag{7.18}$$

The permeability of the porous bed, κ, is obtained from the Blake-Kozeny equation [86]

$$\frac{1}{\kappa} = 150\frac{(1-\varepsilon)^2}{D_p^2\varepsilon^3} \tag{7.19}$$

The conservation of momentum for gas flowing in free space is obtained from (7.17) by setting the porosity to unity and mass and momentum sink terms to zero, yielding

$$\rho_g\frac{\partial\vec{u}}{\partial t} + \vec{u}\nabla\left(\rho_g\vec{u}\right) = -\nabla p + \nabla\cdot\left[\mu\left(\nabla\vec{u} + \nabla\vec{u}^T\right)\right] - \nabla\cdot\left[\frac{2\mu}{3}\nabla\cdot\vec{u}I\right] \tag{7.20}$$

7.2.3 Conservation of Energy

The presence of a local thermal equilibrium between the gas, solid, and adsorbed phases within the adsorption environment is assumed in this investigation, allowing a single conservation equation to characterize all three phases present in the adsorbent bed environment

$$\begin{aligned}\left(\rho_g C_{pg}\varepsilon + M_g\rho_b n_a C_{p,a} + \rho_b C_{p,SA}\right)\frac{\partial T}{\partial t} + \rho_g C_{pg}\overrightarrow{u_A}\nabla T = \\ \nabla k_{eff}\nabla T + \delta T\left(\varepsilon\frac{\partial p}{\partial t} + \overrightarrow{u_A}\nabla(p)\right) + \Phi_{Ag} + \gamma_T\end{aligned} \tag{7.21}$$

The first term on the left-hand side of (7.21) accounts for the transient temperature change in the adsorbent bed with respect to the effective heat capacity of the porous media. Above the critical temperature of a gas; the adsorbed phase behaves analogous to a highly compressed gas, therefore, the heat capacity of the adsorbed phase, $C_{p,a}$, is assumed to be equal to the heat capacity of the gas, C_{pg}. The effective thermal conductivity, k_{eff}, is a volumetric average that represents the influence of the gas and solid phase on conductive heat transfer and is computed as [81]

$$k_{eff} = \varepsilon k_g + (1-\varepsilon) k_{SA} \tag{7.22}$$

The second and fourth terms on the right-hand side of (7.21) represent the energy sources within the porous material resulting from the pressure work of the compressing gas and the heat generated by the exothermic adsorption process, respectively. The heat released due to adsorption is

$$\gamma_T = \Delta H_{ads} \gamma_m = \Delta H_{ads} M_{Wg} \rho_b \frac{\partial n_a}{\partial t} \tag{7.23}$$

The adsorption enthalpy decreases with increasing adsorption coverage according to [82]

$$\Delta H_{ads} = \frac{\alpha}{M_{Wg}} \sqrt{\ln\left(\frac{n_{\max}}{n_a}\right)} \tag{7.24}$$

The enthalpic parameter, α, is a constant parameter from the modified DA equation of adsorption. The heat released due to viscous dissipation of gas flow in the material is captured in (7.21) by the viscous dissipation term

$$\Phi_{g,A} = \left[\nabla \cdot \left[\frac{\mu}{\varepsilon}\left(\nabla \overrightarrow{u_A} + \nabla \overrightarrow{u_A}^T\right)\right] - \nabla \cdot \left[\frac{2\mu}{3\varepsilon} \nabla \cdot \overrightarrow{u_A} I\right]\right] \nabla \overrightarrow{u_A} \tag{7.25}$$

As demonstrated with the conservation of mass and momentum, the conservation equation derived for porous media can be transformed to characterize free flow of gas by setting porosity to unity and the mass sink to zero, to yield

$$\rho_g C_{pg} \left[\frac{\partial T}{\partial t} + \vec{u} \nabla T\right] = \nabla k_g \nabla T + \delta T \left(\frac{\partial p}{\partial t} + \vec{u} \nabla (p)\right) + \Phi_g \tag{7.26}$$

7.3 Production of Development Tool

The previous section outlined the conservation equations that must be implemented for the creation of an accurate and effective simulation tool; this section

presents the development of the three-dimensional simulation tool created in COMSOL Multiphysics v4.2a in support of this work. The simulation tool for this work is developed to represent and predict the performance and temperature profiles obtained from the experimental system with and without the cooling through the thermal management system and to better understand the adsorption process and performance metrics required for a highly functional storage system. Simulations are performed on a Dell Precision T7500 workstation running Red Hat Linux Enterprise operating system, 12 Intel Xeon X5690 CPUs, and 189 GB of Ram.

7.3.1 Model Geometry and Physics

The model geometry uses a series of contacting cylindrical volumes to represent the various characteristic regions of the experimental system (Figure 7.1); COMSOL automatically preserves continuity between shared boundaries of multiple domains utilizing a single module. During the formulation of the simulation tool, the major assumption used in building the model geometry is that the system is symmetric about the centerline of liquid nitrogen flow through the microchannel device, i.e. along the cut plan shown in Figure 4.4.

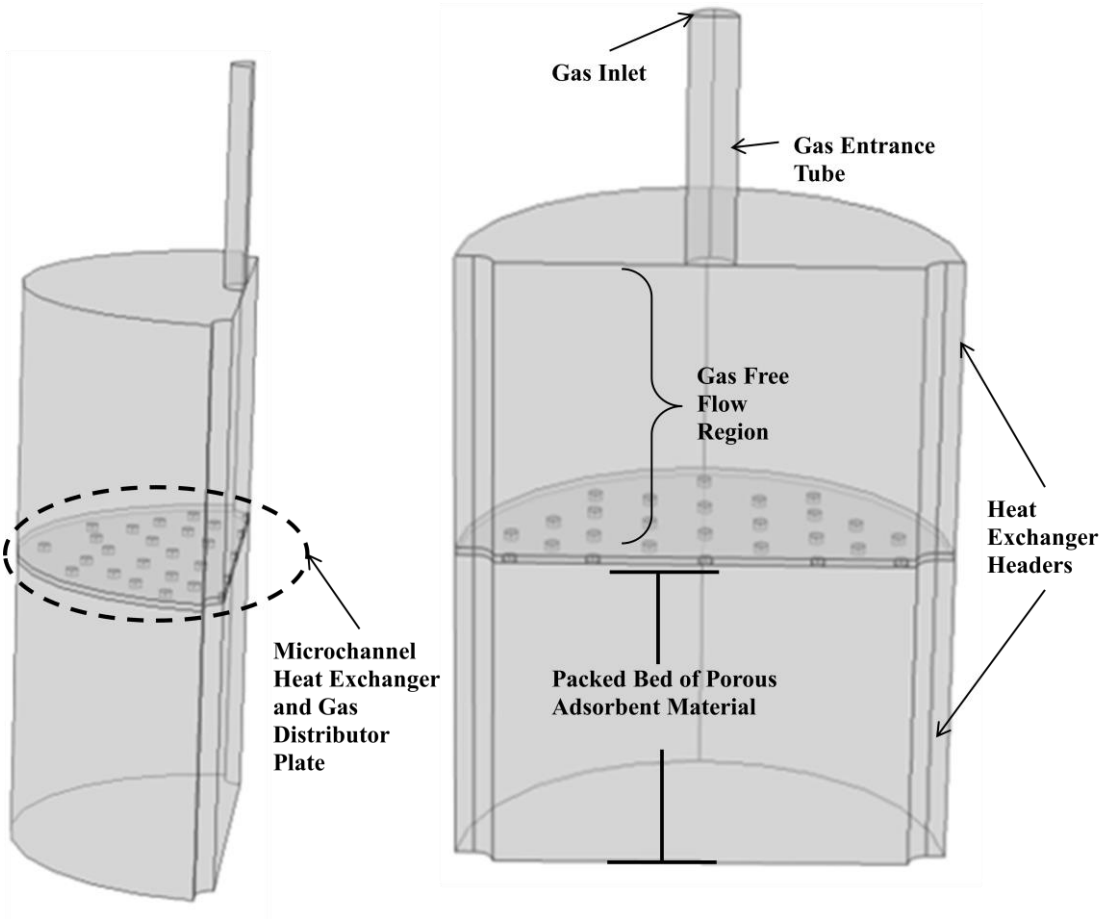

Figure 7.1: Generated model geometry.

7.3.1.1 Gas Inlet

In the experimental device, a four-inch length of tube exists between the gas temperature reading and the area gas actually enters inside the pressure vessel. It is assumed that the gas flowing through ¼" tubing does not change significantly between the temperature reading and vessel entrance and that only a small length of tube, one inch, is necessary to accurately simulate the gas flow into the vessel according to equations (7.9), (7.20) and (7.26).

7.3.1.2 Gas Free Flow Region

The open volume between the top of the vessel cap and the microchannel heat exchanger is solved according to equations (7.9), (7.20), and (7.26) which characterize the transport of gas and energy in free flow.

7.3.1.3 Thermal Management and Gas Distribution Device

The implementation of the imported microchannel device, using the original SolidWorks drawing file, proved difficult and time consuming for COMSOL to solve due to the size of the smaller gas distribution holes. To alleviate the increased meshing within the smaller hole dimensions, a simplified area-neutral design was generated in COMSOL to simulate the flow and distribution of gas from the void region into the adsorbent bed, as seen in Figure 7.2, below. Equations (7.9), (7.20), and (7.26) are utilized throughout the open spaces contained within the simplified domain. The region of the domain representing the solid heat exchanger does not contribute to mass and momentum transport of gas (except to provide wall boundary) and is not solved using the heat transfer equations derived for fluid flow. The solid domain is, instead solved by conductive heat transfer in solids.

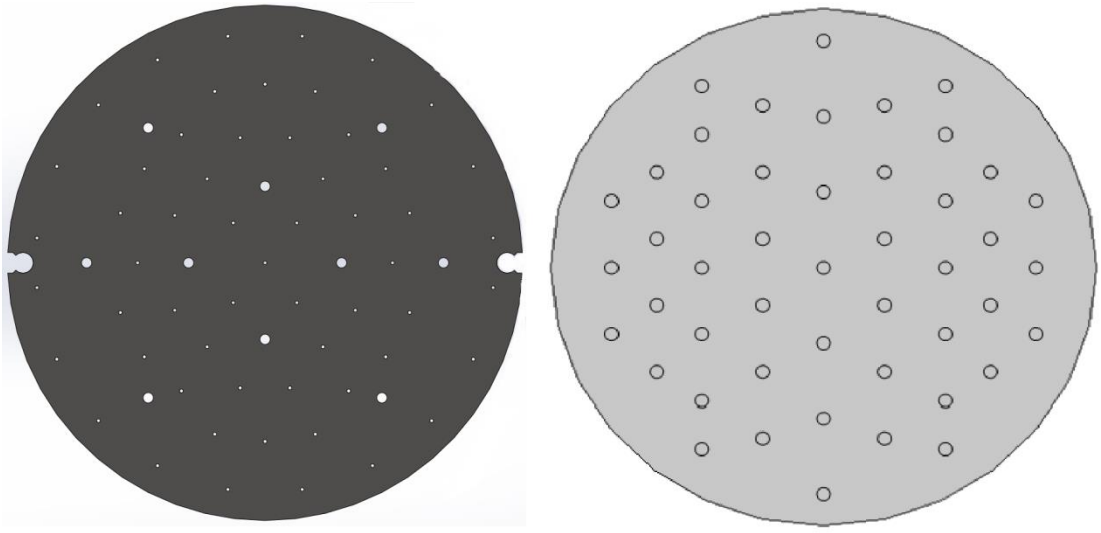

Figure 7.2: Comparison of original SolidWorks design of heat exchanger (left) and the area neutral domain created in COMSOL (right).

7.3.1.4 Packed Bed of Adsorbent Material

The packed bed of adsorbent material is positioned in contact with the heat exchange surface of the microchannel device. This domain utilizes the conservation equations derived for porous media in section 7.2; (7.8), (7.17), and (7.21).

In an effort to reduce the total number of numerical elements contained within the system mesh, the effects of the heat exchanger's headering tubes (only participating in heat transfer) are incorporated via boundary conditions and their occupied volume in the physical system is removed in the free space and adsorbent material domains using a Boolean difference. The Boolean difference results in an improved representation of the experimental bed used in this investigation and reduces the simulated volume taking part in the adsorption phenomena.

7.3.1.5 Physics Modules

Two physics modules are implemented in the simulation tool to characterization the experimental adsorption system. The conservation equations of mass and momentum are solved using the Free and Porous Media Flow physics module within COMSOL. As stated above, the microchannel heat exchanger domain device does not participate in the mass and momentum transport and is excluded from the solution within the flow module. The flow module is segregated to solve for the gas flow in open volume domains and the porous adsorbent bed domain; the porous bed properties are programmed within a sub-section of module.

The conservation of energy is solved using the Heat Transfer in Fluids physics module that allows for additional sub-physics of Heat Transfer in Solids and a second Heat Transfer in Fluids. The energy transport in open volume, porous bed, and heat exchanger are programmed in individual sub-physics that allow all of the required material properties to be designated in the proper domains to satisfy the mathematical model discussed in the previous section.

7.3.2 Initial and Boundary Conditions

Properly defined initial and boundary conditions are an important aspect in the development of the simulation tool and serve as the link between experimental trials and simulated experiments. This section details the initial and boundary conditions implemented in COMSOL to simulate the experimental adsorption system.

7.3.2.1 Initial Conditions

Initial conditions will be specified for gas velocity, pressure, temperature, adsorbent bed temperature, and heat exchanger temperature. To better resemble the experimental trials being simulated, different initial temperature conditions are applied to different domains within the model. A single velocity and pressure condition is set for all domains in the geometry. The densities of the gas and adsorbed phases are calculated as a function of temperature and pressure, and, therefore, initial density variations will be present throughout the system.

Pressure and Velocity

Throughout the entire model geometry, a zero initial velocity magnitude is applied along with an initial gas pressure of one bar.

Temperature

Experimental data is used to establish the initial conditions throughout the model geometry. TC5, the thermocouple located outside the pressure vessel but in the path of the incoming gas, is used to set the initial temperature inside the "Gas Entrance Tube." The initial condition of the free flow volume is obtained from the thermocouple located in the void region, TC8, approximately ½" below the gas entrance inside the pressure vessel.

The initial temperature of the liquid nitrogen headers are collected from the inlet and outlet thermocouples, TC6 and TC7, and are used to create a temperature distribution along the solid heat exchanger domain at the start of the adsorption process.

Throughout the experimental investigation a uniform initial temperature is not obtained at all thermocouple locations within the adsorbent bed; therefore, it is not appropriate to assign a uniform average initial temperature to the bed in the simulation tool. To account for the temperature changes with respect to vertical location, a linear temperature profile is calculated and used to describe the initial temperature of the

bed. The linear temperature profile is obtained by plotting the thermocouple penetration distance against its respective initial temperature using the average surface temperature of the heat exchanger as reference.

7.3.2.2 Boundary Conditions

The boundary conditions described below are applied in COMSOL to the model geometry to satisfy all three conservation equations. Boundary conditions are not required for internal boundaries due to the adherence of maintaining continuity between domains; however, a temperature boundary condition is applied to the microchannel device domain because liquid nitrogen flow is not simulated in this work.

Pressure

A pressure boundary condition is supplied to the top surface of the gas entrance tube; the pressure difference between the applied boundary condition and the simulated vessel pressure serve as the driving force for gas flow into system. The applied pressure boundary condition is

$$p\left(@H_{IN}\right) = P^0 + \left[(P^{feed} - P^0)\left[flc2hs\left(t - \frac{t^{p\max}}{2}, \frac{t^{p\max}}{2} \right) \right] \right]\left(t \le t^{p\max}\right) + (P^{feed} - P^0)\left(t > t^{p\max} \,\&\, t \le t^{ch}\right) + p^f\left(t > t^{ch}\right) \tag{7.27}$$

Superscripts are used in defining the boundary conditions to differentiate variables and parameters in the simulation from variables used in the derivation and presentation of the conservation equations.

The pressure at the boundary, (7.27), is a function of the initial vessel pressure, P^0; final charging pressure, P^{feed}; time required to reach the final charging pressure, t^{pmax}; and the total charging time, t^{ch}. The total charging time is the time the pressure vessel remains connected to the gas source.

The pressure ramping function, in brackets on the right-hand side of (7.27), *flc2hs*, is a smoothed Heaviside function used in COMSOL to define a discontinuous function that creates an increasing pressure condition at the gas inlet boundary of this work. Thus, the pressure boundary condition is broken into three segments: a pressure ramp from the initial pressure to the final charging pressure during the charging time, t^{pmax}; followed by a constant pressure condition until the end of the filling time, t^{ch}; and finally, the system pressure is modeled by fitting a second order polynomial to the pressure response of the experimental trial, p^f.

Velocity

To satisfy the conservation equations with respect to the gas velocity, a no-slip boundary condition is applied at all solid walls of the modeled geometry, stating that

$$\vec{u} = \overrightarrow{u_A} = 0 \tag{7.28}$$

The no slip condition is applied to simulated boundaries that contact the PTFE cylinder, PTFE plug, pressure vessel cap, header tubes, gas entrance tube, and the solid surface of the heat exchange device in the experimental system.

Temperature

The simulation tool developed in support of this work utilizes several boundary conditions within the model geometry to characterize the heat transfer within the pressure vessel. The following will describe the various conditions applied.

A constant temperature boundary condition is applied at the top surface of the gas entrance tube to specify the temperature of gas entering the pressure vessel. The value of inlet gas corresponds to the initial temperature reading of TC5 at the onset of the charging process.

The outside boundaries of the simulation environment are supplied with a conductive heat flux boundary condition, except along the upper header tubes, to

transport heat in and out of the system. The general form of the heat flux boundary used in this simulation follows Fourier's law of heat conduction

$$q^i = k^m \frac{(T - T^i)}{(\Delta x^m)} \tag{7.29}$$

and is a function of the simulated temperature, T, at the boundary location of interest; the surrounding temperature, T^i; the thickness, Δx; and thermal conductivity, k, of the contacting material, m.

A constant temperature profile is maintained along the solid surface opposite the adsorbent bed of the solid microchannel device domain. The temperature profile applied to the upper surface is a function of the inlet and outlet liquid nitrogen temperatures obtained from the experimental data and the radius of the heat exchange device, r^{HEX}, in the form of (7.30)

$$T(x,y) = T^{L\_IN} + \left(\frac{T^{L\_OUT} - T^{L\_IN}}{2r^{HEX}} \right) \sqrt{\left(x - r^{HEX} \right)^2 + y^2} \tag{7.30}$$

Equation (7.30) produces a symmetric temperature profile along the centerline of the fluid flow path. Figure 7.3 is an example of the temperature profile, and applied boundary, of the microchannel device.

Finally, a heat flux boundary condition is applied to the surface of the excess header tubes protruding into the adsorbent material volume. Because the temperature inside the header tubes is unknown, 10 K is added to the average liquid nitrogen temperature and used in the flux calculation, T^i in (7.29). The portions of the headers in the gas free flow domain are provided with a constant temperature boundary condition corresponding to their respective temperature (inlet or outlet).

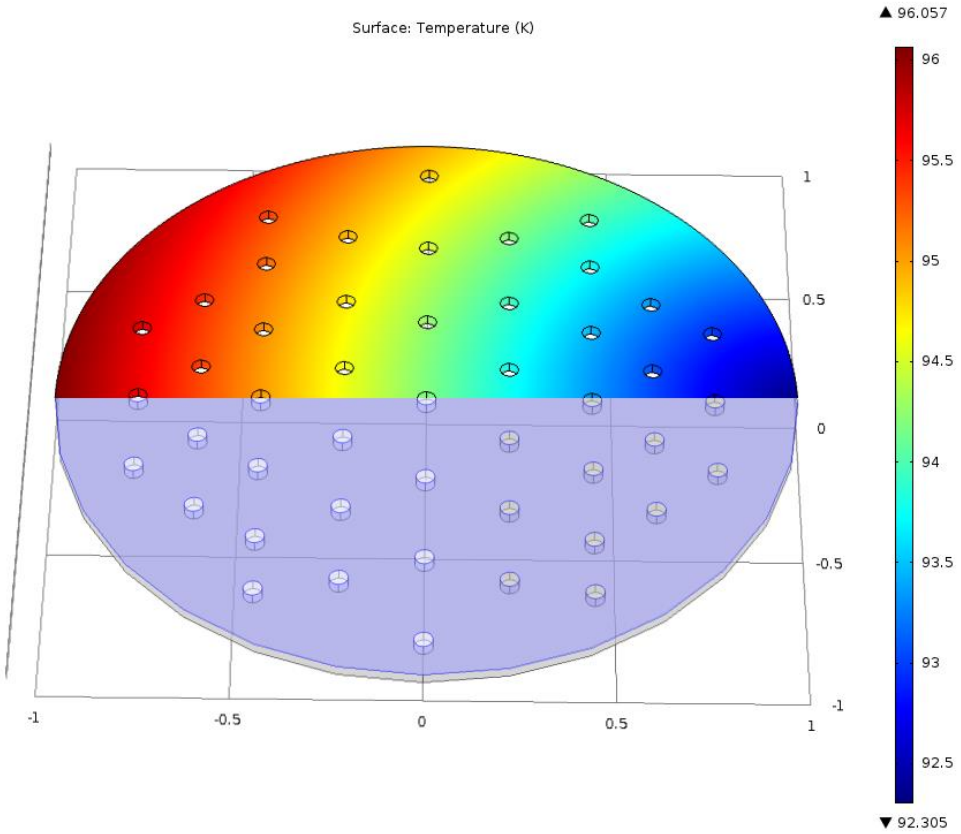

Figure 7.3: Example of temperature profile applied to surface of microchannel device.

Symmetry

In both the fluid flow and heat transfer physics modules employed in the simulation tool, a symmetry boundary condition is placed on all domains with respect to the *x*-*z* coordinate plane. COMSOL sets the normal flux across the symmetric boundary equal to zero to solve all transport equations.

7.3.2.3 Sources and Sinks

A mass sink and energy source are applied to the adsorbent material domain to account for the adsorption of gas, (7.15, 7.16), and the heat generated due to adsorption, (7.23, 7.24). In the bed domain, the energy source term also contains the heat generated during the compression of gas in the system. Similarly, an energy

source is applied to the free gas flow domains to account for the heat generated by gas compression in the open volume.

7.3.3 Material Properties

The ideal gas law has been successfully implemented in cryogenic hydrogen storage simulations produced by Xiao *et al.* using COMSOL and is used to calculate the gas phase density in this work [81 - 85]. Other gas phase properties, including thermal conductivity, viscosity and specific heat capacity, were obtained using the National Institute of Standards and Technology (NIST) Chemistry WebBook tool for thermophysical properties of fluid systems. Physical properties were collected in 1 K increments in the temperature range of 80 - 200 K at a single pressure. This process was repeated in the pressure range of 1 - 60 bars in 1 bar increments. A populated table containing all collected physical property values was uploaded into COMSOL and used with a two-dimension interpolation to retrieve the physical property value as a function of temperature and pressure. A sample of the property surface map generated in COMSOL is shown in Figure 7.4.

Thermal conductivity and specific heat capacity correlations for stainless steel and PTFE are obtained by plotting calculated values over a temperature range of 80 – 200 K using correlations provided by NIST Cryogenic Technologies Group and applying a curve fit to the data in Excel. The original correlations utilize a series of *log* functions that can be very computationally expensive to repeatedly evaluate and were easily fit using polynomial trendlines in Excel.

Physical and thermal properties and adsorption parameters of the adsorbent bed are obtained from literature and a series of reports and presentation from our partners in the HSECoE. A similar procedure was used to create a correlation for the heat capacity of MOF-5 as was applied to stainless steel and PTFE. The properties and parameters implemented in the simulation tool are listed in Table 7.1 to Table 7.3. Because the specific activated carbon material is unknown and a lack of literature

values pertaining to the adsorption of H_2 on a monolithic bed of adsorbent with binder was uncovered, the focus of modeling effort is on MOF-5.

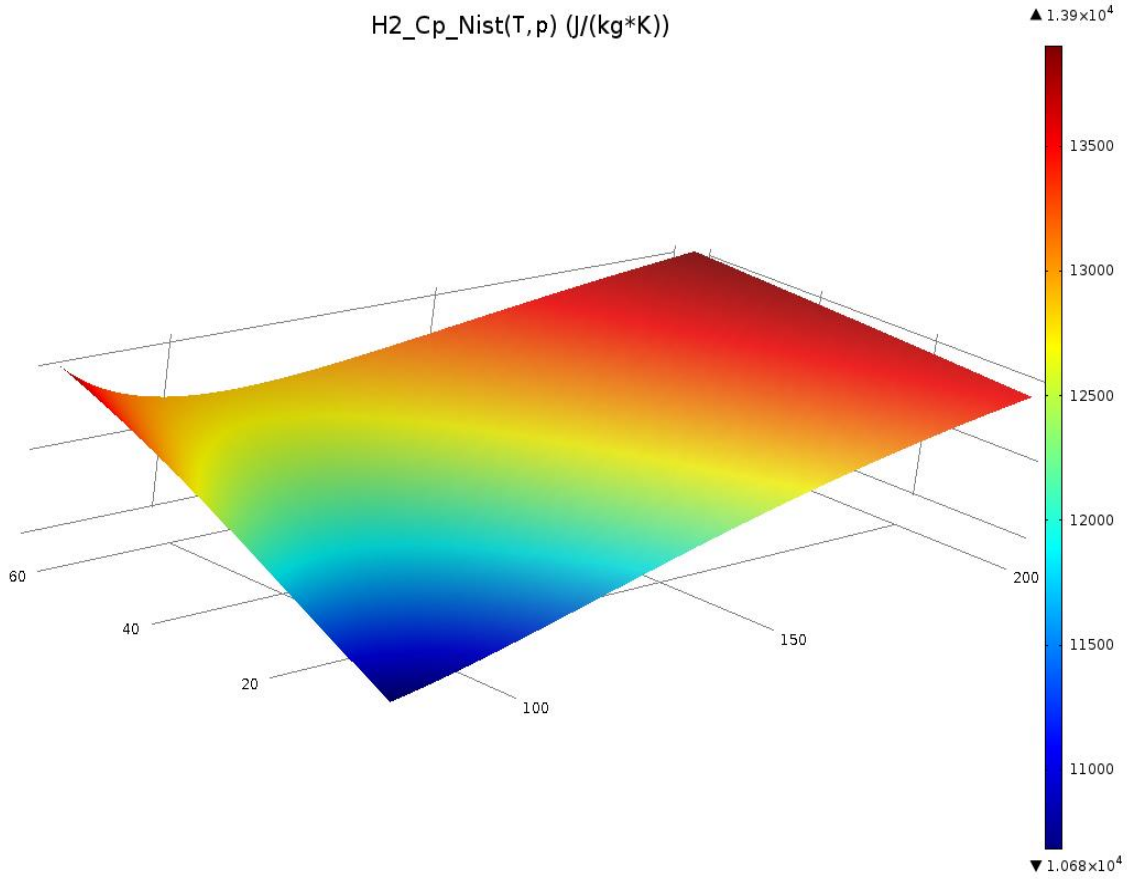

Figure 7.4: Hydrogen property surface generated by two-dimensional interpolation of NIST data in COMSOL.

Table 7.1: Physical and thermal properties of stainless steel and PTFE used in development tool.

	Stainless Steel 304	**PTFE**	**Reference**
Density [kg m^{-3}]	8027	2214	[87]
Specific Heat Capacity [W $m^{-1}K^{-1}$]	Fitting of Correlation	Fitting of Correlation	[88]
Thermal Conductivity [J kg^{-1} K^{-1}]	Fitting of Correlation	Fitting of Correlation	[88]

Table 7.2: Physical and thermal properties of adsorbent materials used in development tool.

Parameter	MOF-5	Reference
Bulk Bed Density [kg m^{-3}]	0.3487	
Porosity [%]	13	[89]
Mean Particle Diameter [μm]	108	[90]
Thermal Conductivity [W m^{-1} K^{-1}]	0.069	[69]
Specific Heat Capacity [J kg^{-1} K^{-1}]	Fitting of Correlation	[91]

Table 7.3: Dubinin-Astakhov parameters of MOF-5 adsorbent used in development tool.

Parameter	MOF-5	Reference
α [J mol^{-1}]	2123	[92]
β [J $mol^{-1}K^{-1}$]	19.6	[92]
P_0 [bar]	16049.5	[92]
n_{max} [mol_{H2} kg^{-1}_{Solid}]	139.6	[92]

7.3.4 Modeling Assumptions and Simplifications

Due to the rigorous computational sequences performed by COMSOL during the simulation, any simplifications applied to the model geometry can result in a decrease in processing time necessary to obtain a solution. In the development of the simulation tool, the inertial term is neglected for the porous media flow (second term on the left-hand side of (7.18)), because its effect on flow is negligible compared to the resistance caused by the porous solid [70].

As shown in (7.18), the momentum change due to gas adsorption is associated with an inverse square of the bed porosity

$$\left[-\frac{\gamma_m}{\varepsilon^2}\right]\overrightarrow{u_A} \tag{7.31}$$

However, COMSOL utilizes the term γ_m instead and it has been shown by Hardy *et al.* that the effect of this substitution is insignificant in calculating the pressure and velocity within the porous bed [70].

The coefficient of thermal expansion, δ, in (7.21) and (7.26) is defined as

$$\delta = -\frac{1}{\rho_g}\left(\frac{\partial \rho_g}{\partial T}\right)_p \tag{7.32}$$

this is equal to the inverse gas temperature of an ideal gas. Therefore, the δT term preceding the heat of compression (term in parenthesis on the right-hand side of (7.21)) will be replaced with a value of 1 to reduce the number of calculations required by the development tool [81].

It should be noted that the Dubinin-Astakhov parameters used in the simulation have been calculated from the experimental results of hydrogen adsorption on compacted MOF-5 beds (density ~0.3 g cm^{-3}), obtained from our partners in the HSECoE, and it is assumed that these parameters can be accurately applied to the compressed bed (density 0.349 g cm^{-3}) used in this work.

7.3.5 Meshing

The size, shape and quality of applied cell elements play a significant role in providing an accurate and stable numerical solution. Stability and accuracy tend to increase as element size decreases, resulting in a larger number of cells in the total mesh; however, the computational time required to reach a solution also increases with decreasing element size.

Narrow regions and domains necessitate small element cell sizes in order to allow multiple cells to span the applicable region, thus resulting in a higher overall mesh. The regions surrounding the microchannel device and gas distribution holes will require significantly smaller element sizes to produce a finer mesh in this work, thus increasing the overall mesh size.

A free tetrahedral mesh, for fluid dynamic simulations, is applied to the model geometry with different element size constraints applied to different regions and domains. The gas entrance tube, void free flow, and adsorbent bed domains utilize the same elemental constraints for a fluid dynamic simulation. The gas distribution holes of the microchannel device domain are given an extra fine mesh to ensure that at least two cells are generated to span the width of the domain. The solid region of the microchannel device, only participating in heat transfer, is given a fine mesh for a general physics domain, which is slightly larger than in the regions of free flowing gas. The final mesh applied to the model geometry is seen Figure 7.5; the darker regions indicate narrow features in the geometry that necessitate a larger number of smaller element cells as compared to other features.

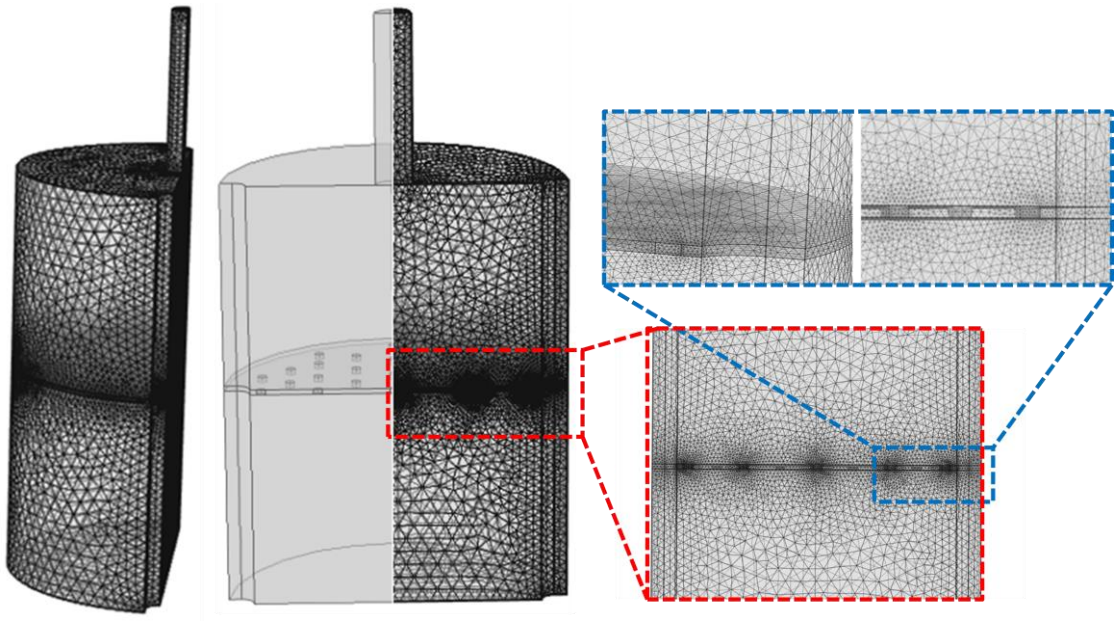

Figure 7.5 Final mesh applied to model geometry.

Chapter 8: Development Tool Validation and Investigation

In fulfillment of the second research goal of this work, the development tool, discussed throughout chapter 7, is validated against data obtained from the experimental investigation, chapters 5 and 6. As stated in chapter 1, comparisons of temperature profiles at the six thermocouple locations obtained from experimental trials and corresponding simulations will be used for the validation of the development tool created in COMSOL. Following the successful validation, an investigation is carried out to illustrate the effect that improvements of material properties and system conditions will have on the storage capacity and heat removal of adsorption system.

8.1 Validation of Development Tool

It is important that the temperature profiles obtained from simulations accurately represent the shape and key features of the experimental data in addition to the magnitude of the temperature readings. A number of the liquid nitrogen cooled and non-cooled MOF-5 hydrogen adsorption experiments are simulated as part of the tool validation effort. Representative simulation results are provided and discussed within this section and summary tables of the errors from the comparison of simulated data to its respective experimental investigation for both cooled and non-cooled MOF-5 hydrogen adsorption trials are listed in the Appendix.

The temperature profiles obtained from the initial simulation performed (Figure 8.1 and Figure 8.2) demonstrate a similar temperature response throughout the bed during the first 30 seconds, despite reaching higher maximum temperatures at all thermocouples during pressurization of the vessel. However, after 30 seconds, a significant departure between the experimental and simulated temperatures are witnessed at all thermocouples for the remainder of the experiment, an average absolute error of 9 K or greater at each thermocouple location. The significant difference between shape and magnitude of the experimental temperature profiles and those obtained from the simulation suggest additional heat transfer present in the experimental environment that is not present in the simulation. The additional heat

transfer is a result of (1) the thermocouples embedded in the adsorbent bed having a thermal conductivity at least 115 times higher than MOF-5, and (2) regions of preferential gas flow along the thermocouples that provide increased convective transport and delivery of H_2 gas to exposed adsorbent surfaces.

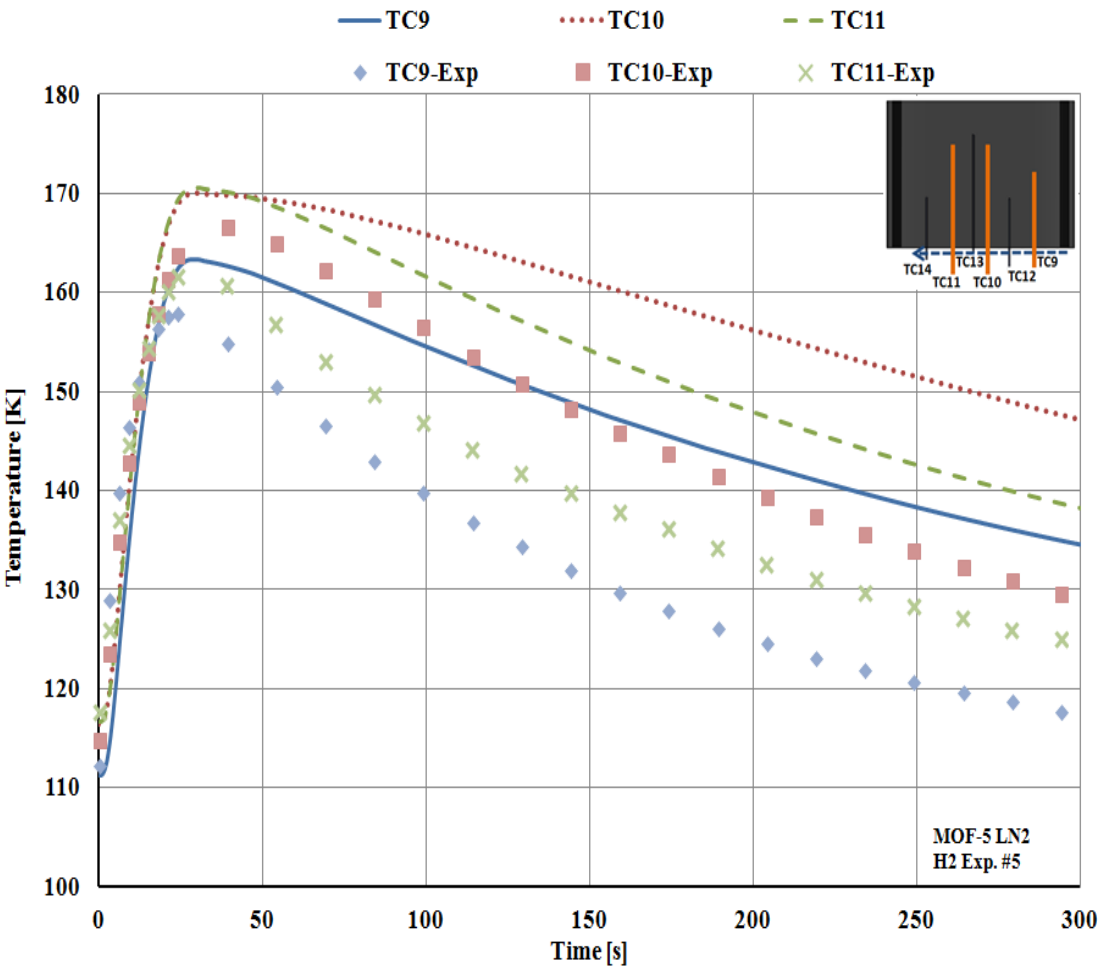

Figure 8.1: Comparison of liquid cooled data for the original simulation at TC9, TC10 and TC11.

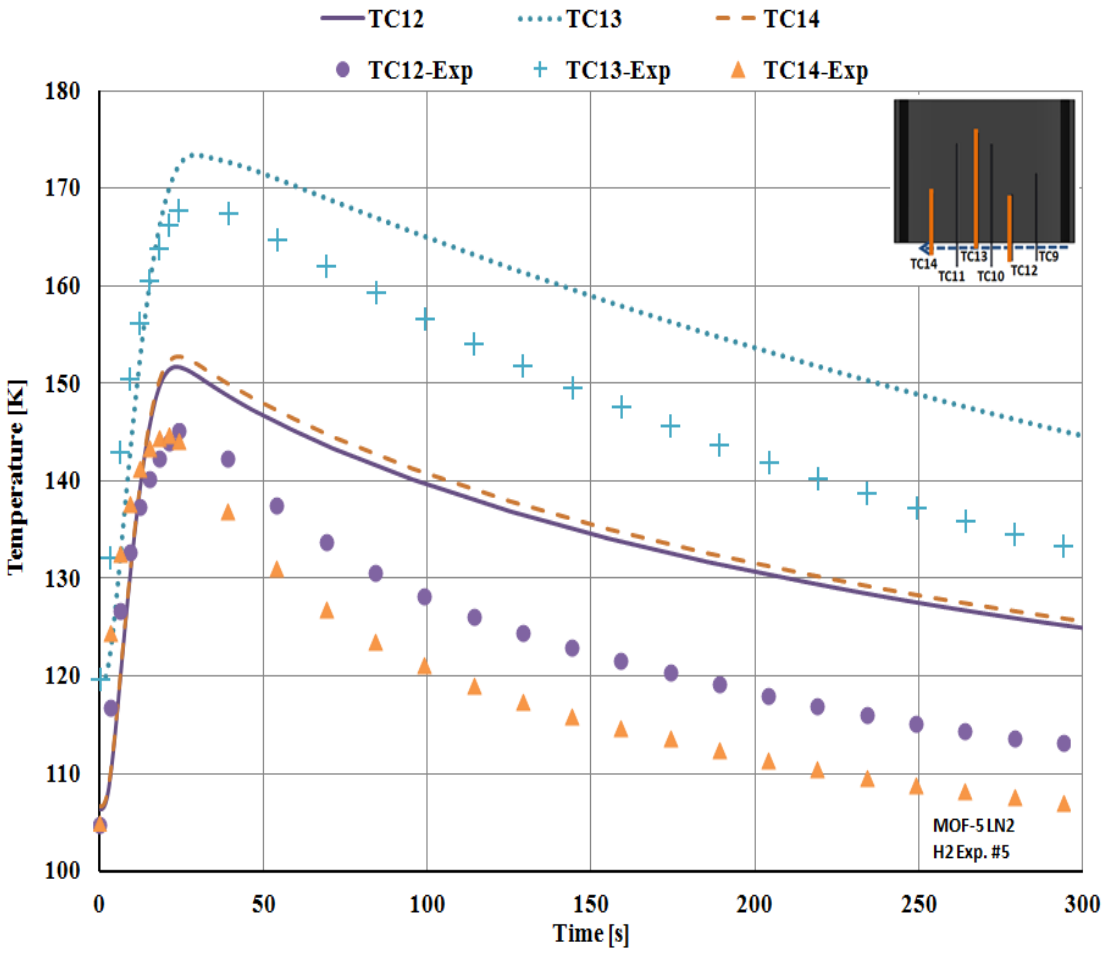

Figure 8.2: Comparison of liquid cooled data for the original simulation at TC12, TC13 and TC14.

It is clear that the additional cooling effects of the thermocouples must be included inside the adsorbent bed domain to improve the accuracy of the simulation volume with respect to the experimental system. Initially, two concentric cylindrical volumes are placed in the adsorbent bed domain according to the experimental thermocouple locations. The inner cylinder is treated as a solid stainless steel structure, only participating in heat transfer, while the outer cylinder represents the void region between the thermocouple and adsorbent bed and participates in mass, momentum, and heat transfer. Although the addition of two concentric domains creates a more realistic representation of the experimental bed in the simulated environment, it results in a significant increase in the number of cells generated in the

mesh, as seen in Figure 8.3. The increase in meshed cells (3.15 times more cells than the original mesh generated) would result in a significant increase in computational memory, time necessary to complete a single simulation, and the time required for data collection and analysis. The required memory and computational time increase per simulation are higher than could be justified for continued use.

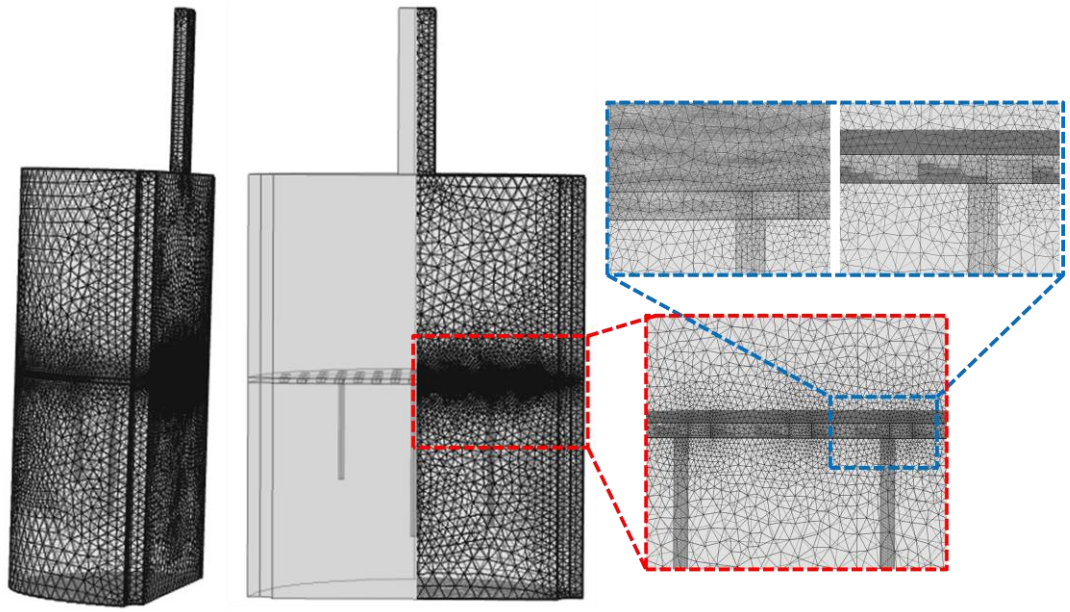

Figure 8.3: Resulting mesh using cylindrical domains to represent embedded thermocouples.

To maintain a manageable solution time and memory usage throughout the numerical investigation, an alternative to the explicit thermocouple and void domains is required to accurately model the adsorption phenomena. A geometric map of localized property compensation (LPC) parameters are created and imported into COMSOL to provide an alternative method to creating additional domains for increased heat transfer. The LPC parameters interpolate the magnitude of the adsorbent bed porosity, and a thermal conductivity multiplier as a function of x and y coordinates within the adsorbent bed domain. The LPC porosity map (Figure 8.4) provides a porosity value throughout the bed domain corresponding to Table 7.2, except in the locations of embedded thermocouples, which is increased to 0.61.

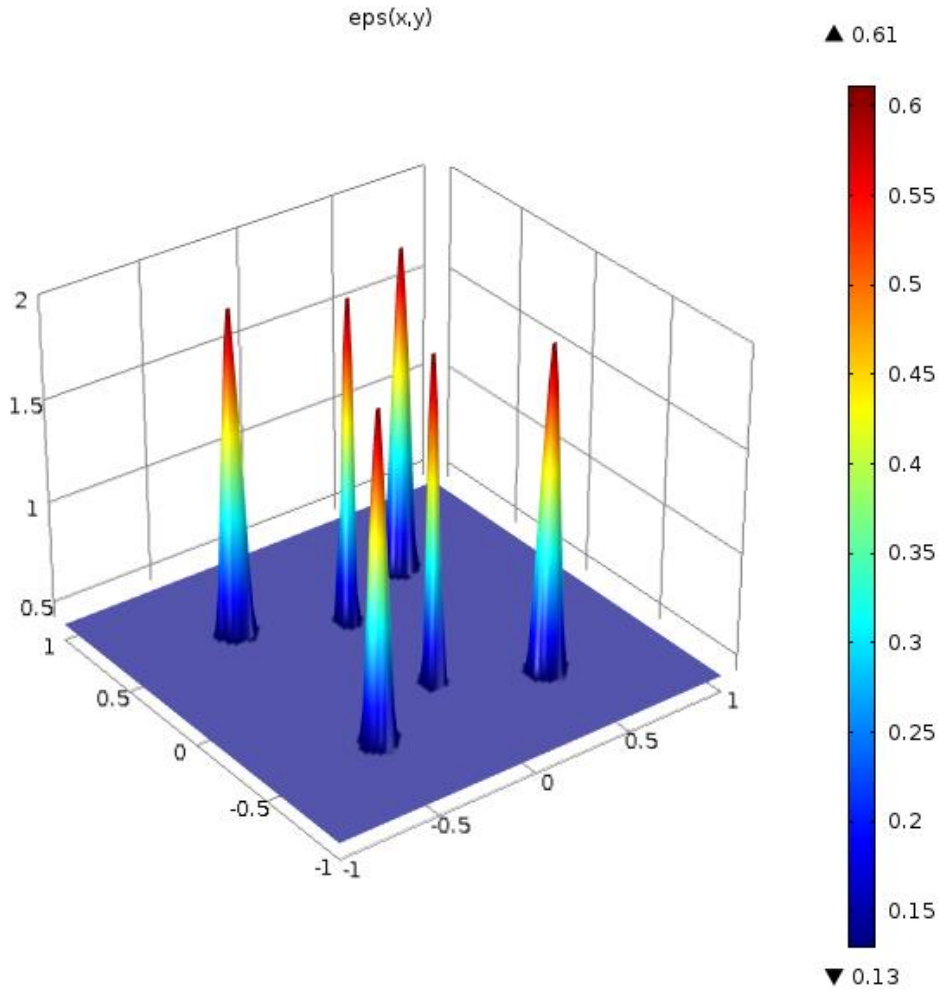

Figure 8.4: LPC porosity map used to interpolate porosity of the bed as a function of *x* and *y* coordinates.

The LPC thermal conductivity multiplier map (Figure 8.5) provides a multiplying factor to the effective thermal conductivity calculated throughout the bed, according to (8.1). A multiplier of 1 is input throughout the bed except in the locations of embedded thermocouples.

$$k_{eff}^{'} = k_{eff} \cdot k_{LPC\_mult} \tag{8.1}$$

Implementing the LPC as variable parameters within the adsorbent bed domain of the simulation allows the additional heat transfer effects from the thermocouples and preferential flow to be achieved with the original mesh generated in chapter 7.

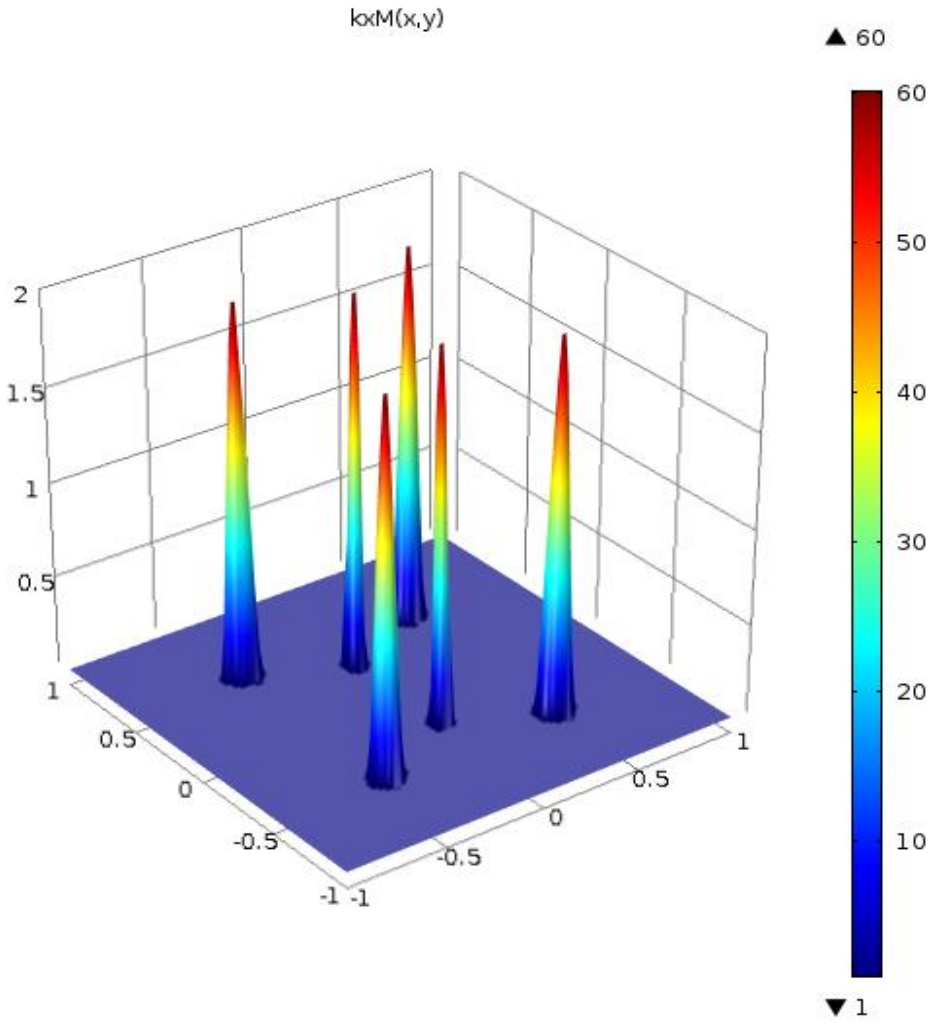

Figure 8.5: LPC thermal conductivity multiplier map used to interpolate multiplier value within the bed as a function of x and y coordinates.

The shape and magnitude of the simulated temperature profiles follows those of the experimental data with improved accuracy when the LPC parameters employed (Figure 8.6 and Figure 8.7). The simulated profile of TC10 demonstrates a slower and more linear temperature decline compared to the experimental data; however, the overall trend follows the experiment. The development tool is unable to replicate the additional cooling seen at TC14 in the liquid cooled experiments, discussed in chapter 6. The maximum temperature reached at TC14 corresponds with the experimental data, but a higher final temperature is simulated. As expected, the simulation predicts

similar temperatures at TC12 and TC14 with a slightly higher maximum temperature reached at TC14. The largest average absolute error observed between the liquid cooled representative experiment and simulation, calculated as $\left[\sum\left|(T_{EXP}-T_{SIM})\right|\right]/n$ (where n is the number of compared data points) is 8.4 K over the entire simulation time at TC14, which demonstrated a higher than expected rate of cooling during the experimental investigations.

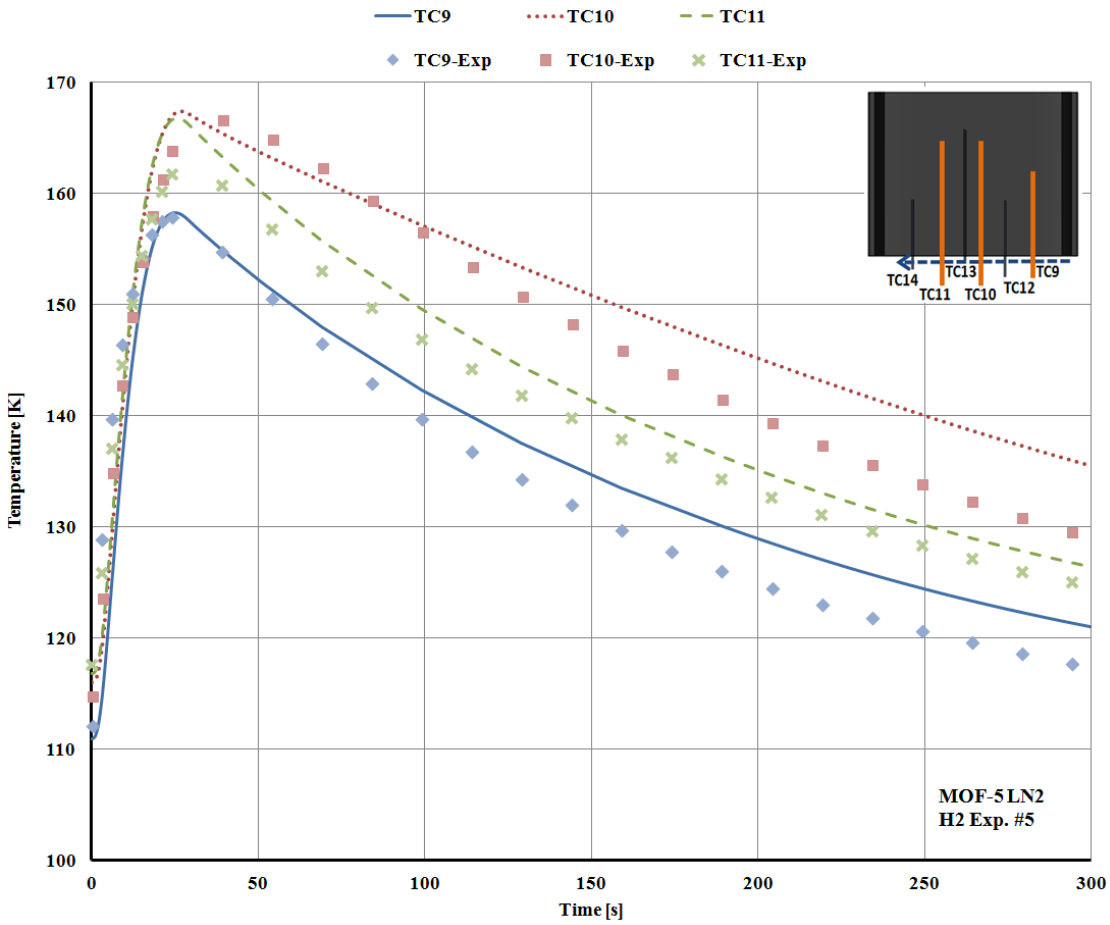

Figure 8.6: Comparison of liquid cooled data using LPC parameters for TC9, TC10 and TC11.

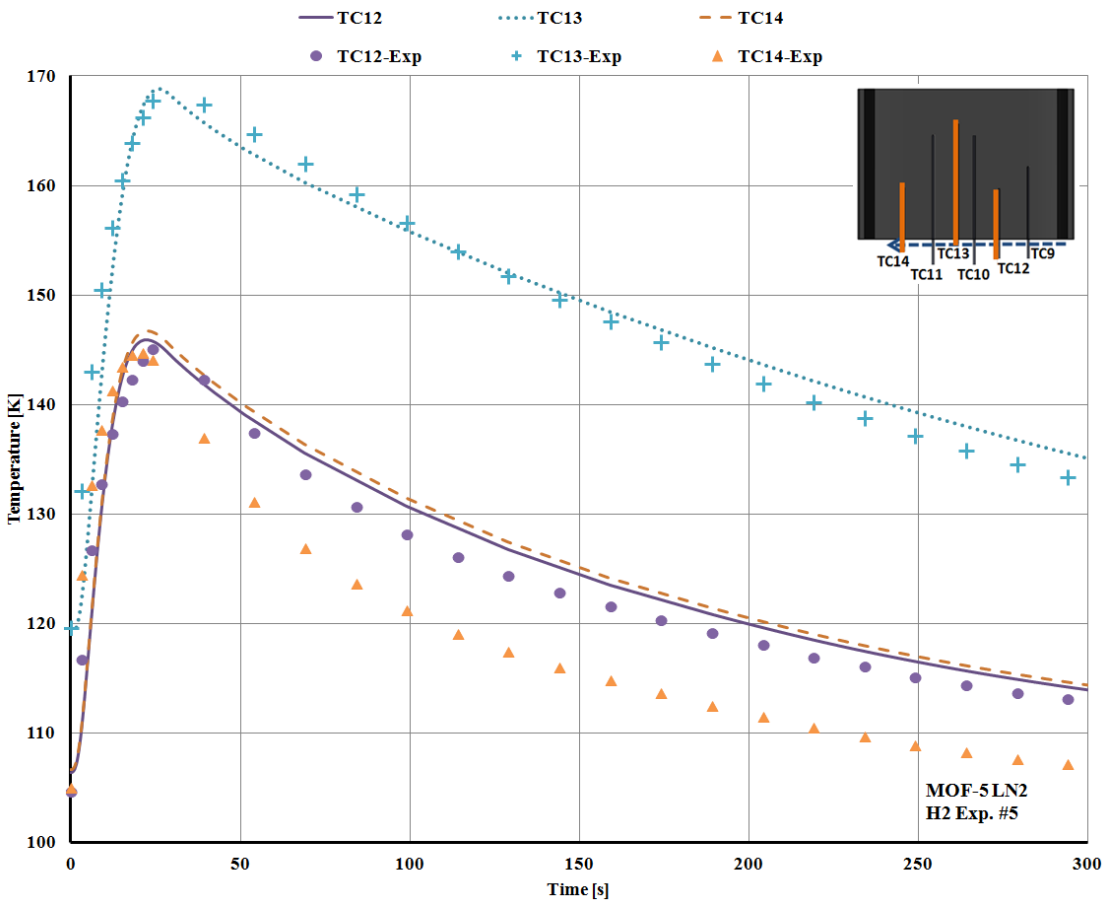

Figure 8.7: Comparison of liquid cooled data with LPC parameters for TC12, TC13 and TC14.

The shape of the simulated temperature trends throughout the adsorbent bed generally correspond to non-cooled experimental data (Figure 8.8 and Figure 8.9); however, the simulated profiles of TC10 and TC13 exhibit a slower and slightly more linear temperature decline than is observed in the experimental data – a trend that is also seen in the liquid cooled simulation. The simulation predicts a greater temperature distinction between TC9, TC10, and TC11 than is experimentally observed and is unable to predict a higher maximum temperature at TC9 versus TC11 that is observed in the experiment. A faster cooling rate directly following the maximum temperature is observed in the experiment for the shallowly embedded thermocouples; however, a similar temperature profile is maintained in the final 150 seconds of the simulation. All six thermocouples are within 2.5 K of the experimental

temperatures at the end of the simulation and TC9 and TC11 finish with 0.5 K of experimental data.

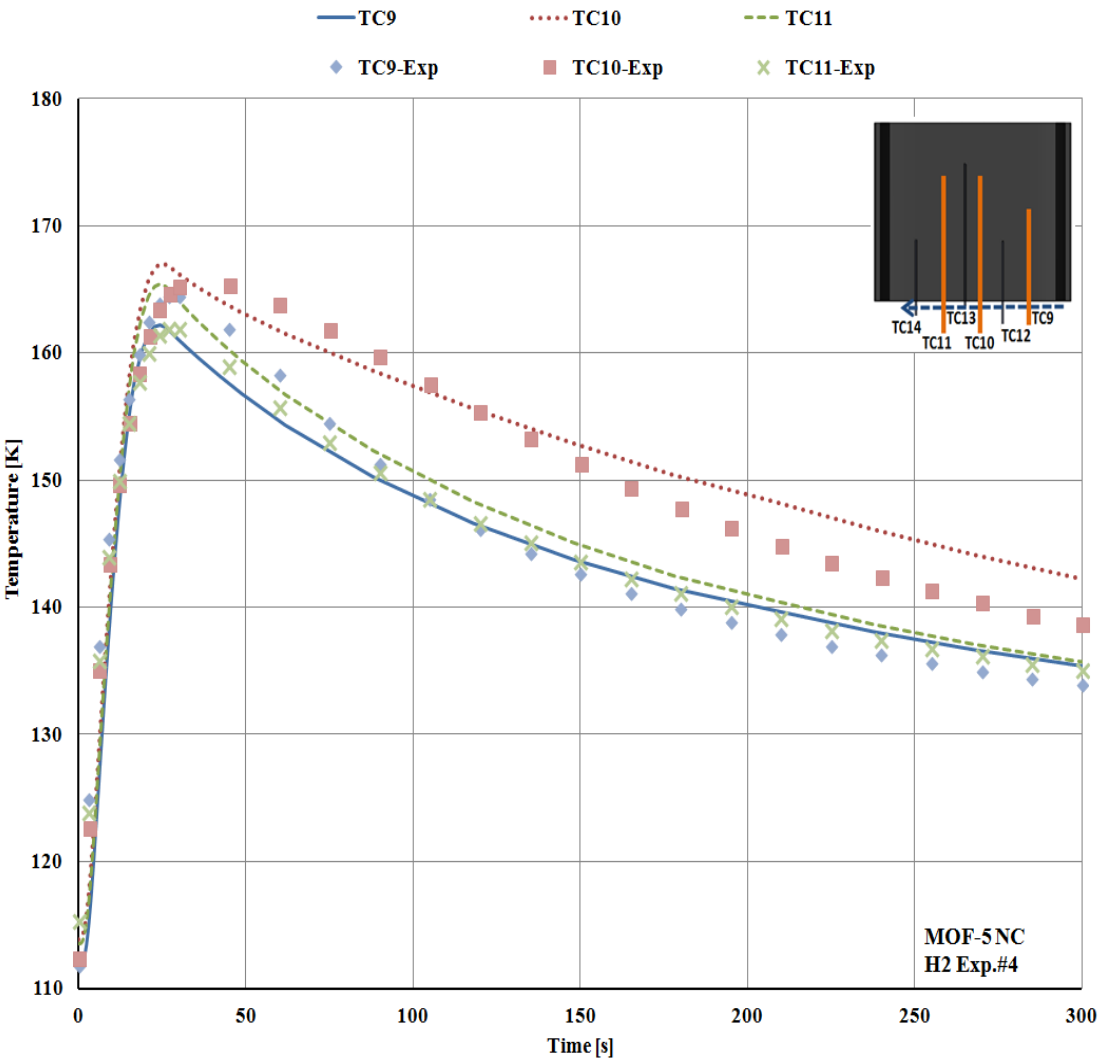

Figure 8.8: Comparison of non-cooled data using LPC parameters for TC9, TC10 and TC11.

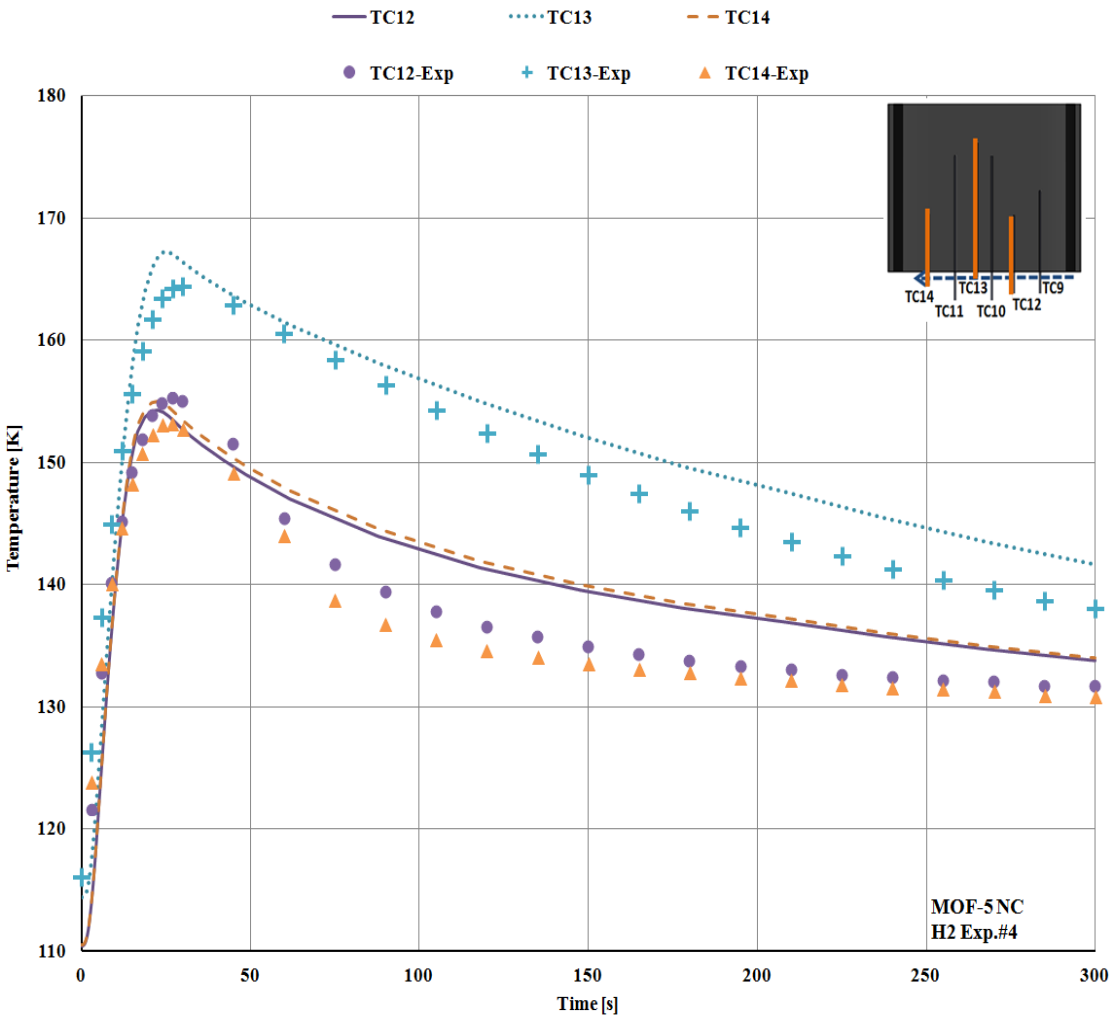

Figure 8.9: Comparison of non-cooled data using LPC parameters for TC12, TC13 and TC14.

The largest temperature differences are witnessed during the initial pressurization of the adsorption system, which arise from the imperfect representation of the experimental pressure increase in the development tool (Figure 8.10). Although the simulated system pressure strongly resembles the experimental system pressure over the majority of the simulation, the initial 19 seconds of pressurization produces large differences between the experiment and simulation. The result is an altered gas flow during the initial 19 seconds. Although the temperature errors can exceed 10% during this period, the remaining simulation demonstrates a strong resemblance to experimental data.

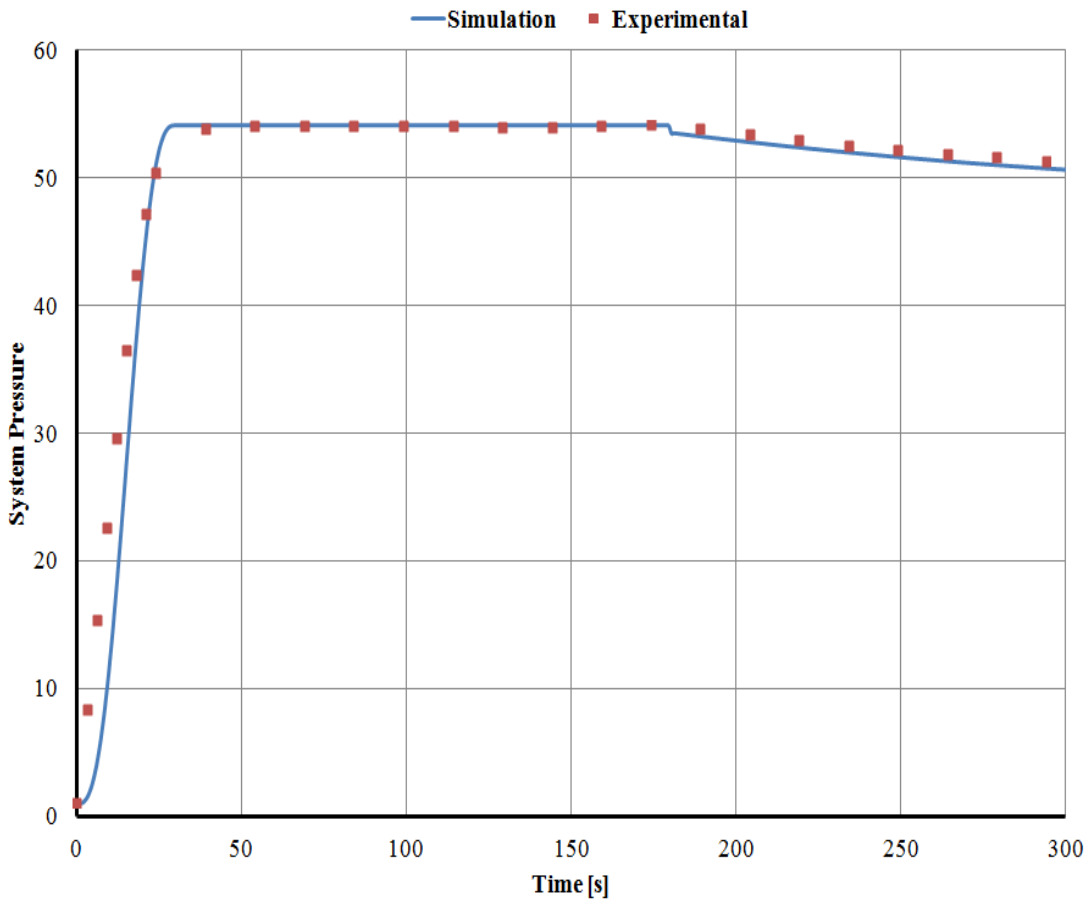

Figure 8.10: Comparison of simulated and experimental system pressure.

As seen in Table 8.1 for the representative simulations, the predicted storage capacity of the complete simulated environment (open void volume plus packed bed) maintains a larger error compared to the experimental data than observed in the temperature profiles.

Table 8.1: Comparison of experimental and simulated H_2 mass in the adsorption system.

Experiment	**MOF-5 LN2 H2 Exp. #5**			
Data Source	**Experimental**	**Simulation**	**Absolute Error [g]**	**Percent Error [%]**
Vessel Mass [g]	2.05	2.29	-0.24	-11.64
Bed Mass [g]	1.15	1.35	-0.20	-17.65
Void Mass [g]	0.90	0.94	-0.04	-3.99
Experiment	**MOF-5 NC H2 Exp.#4**			
Data Source	**Experimental**	**Simulation**	**Absolute Error [kg]**	**Percent Error [%]**
Vessel Mass [g]	1.95	1.99	-0.04	-1.95
Bed Mass [g]	1.09	1.12	-0.03	-2.43
Void Mass [g]	0.86	0.87	-0.01	-1.33

Multiple factors compound to produce the higher discrepancy in stored H_2 mass between experimental and simulation results, especially for liquid cooled systems. The amount of mass stored in the experimental system is obtained from the gas flow through the electronic mass flow meter during the discharging process. This initiates a pressure swing desorption of stored gas from the adsorbent bed; however, complete adsorbate discharging is unlikely in the absence of additional heat supply to the bed. Therefore, the mass obtained from discharging the tank is not the total mass of H_2 present in the tank at the end of an experiment. This runs counter to the simulation, which is a complete representation of the mass present in the adsorption environment. The smaller error contribution of the H_2 mass in the void space of the system supports incomplete desorption of the adsorbent bed.

In the experimental system, the embedded thermocouples may potentially contact the bed surface at multiple locations within pre-drilled hole and locally increase radial penetration of conductive heat transfer; however, it is not possible for the thermocouple to be in contact with the entire surface of adsorbent bed around it. The inclusion of the LPC parameters allows for the accurate prediction of the temperature response at the thermocouple locations while not requiring the addition of specific domains within the environment. Representation of the entire bed volume as

a porous domain results in a continuous region of increased conductive heat transfer that is not present throughout the entire pre-drilled hole of the experimental bed, allowing for increased radial penetration of conductive heat transfer. For liquid cooled trials, the increased penetration should yield a lower volume-averaged final bed temperature and increased absolute adsorption (calculated from the DA equation) compared to the experiments.

Finally, human error resulting from the use of a manually operated metering valve to initiate gas discharge at the end of the experimental trial contributes to the H_2 capacity discrepancy. The discharging process requires repeated manipulation of the metering valve as the internal system pressure diminishes and can result in a rapid rise of gas flow rate that is faster than the meter's response, yielding slightly lower storage capacity.

The Free and Porous Media flow module implemented in COMSOL solves the conservation of momentum based on the Navier-Stokes equations for laminar flow. Therefore, it is necessary to determine the Reynolds number in each domain to verify laminar gas flow throughout the charging process. The Reynolds number,

$$\mathrm{Re} = \frac{\rho_g U L}{\mu_g} \tag{8.2}$$

is a dimensionless representation of the ratio of inertial to viscous forces in a flow system as a function of fluid properties, fluid velocity (U), and characteristic length (L). Lower Reynolds values, less than 2000, are characteristic of laminar fluid flow and turbulent systems, in which perturbations in the flow are sustained and able to grow, possess Reynolds numbers greater than 2000. The volume-averaged velocity magnitude (superficial velocity in the porous bed) and cell Reynolds number, (8.3), for each domain pertinent to fluid flow are calculated in COMSOL and discussed below. The velocity magnitude (superficial velocity magnitude in bed), $|u|$, and element length, h, are used in the cell Reynolds calculation, $\mathrm{Re}^c = \left[\rho |u| h\right] / (2\mu)$ [93].

The volume-averaged velocity quickly reaches a maximum during the first few seconds of gas flow through the inlet tube. The velocity quickly diminishes as the system nears final pressure, within 30 seconds, and remains low for the remainder of the simulation, averaging 0.06 m s^{-1} over 300 seconds. Subsequently, the velocity in the open free flow region demonstrates a significantly lower velocity due to the expansion of the gas into the larger open volume. The small gas distribution holes of the microchannel device forces gas compression resulting in a higher velocity before reaching the adsorbent bed, where the superficial velocity is minimal throughout the simulation. While the highest volume-averaged velocity is nearly 2.4 m s^{-1}, the highest local velocity through the inlet tube is more than double, 5 m s^{-1}, during the first few seconds of gas flow into the system.

The cell Reynolds numbers calculated overwhelmingly indicate laminar flow throughout the system, maximum volume-averaged Re number of 71 and a local maximum of 155, despite the quick pressure ramp. A maximum local Reynolds number of 1890 is calculated using the physical inlet tube diameter and H_2 properties at the time of the local maximum velocity, although the instantaneous value approaches the limit of laminar flow, it satisfies the use of laminar flow equations to model gas flow in the adsorption environment.

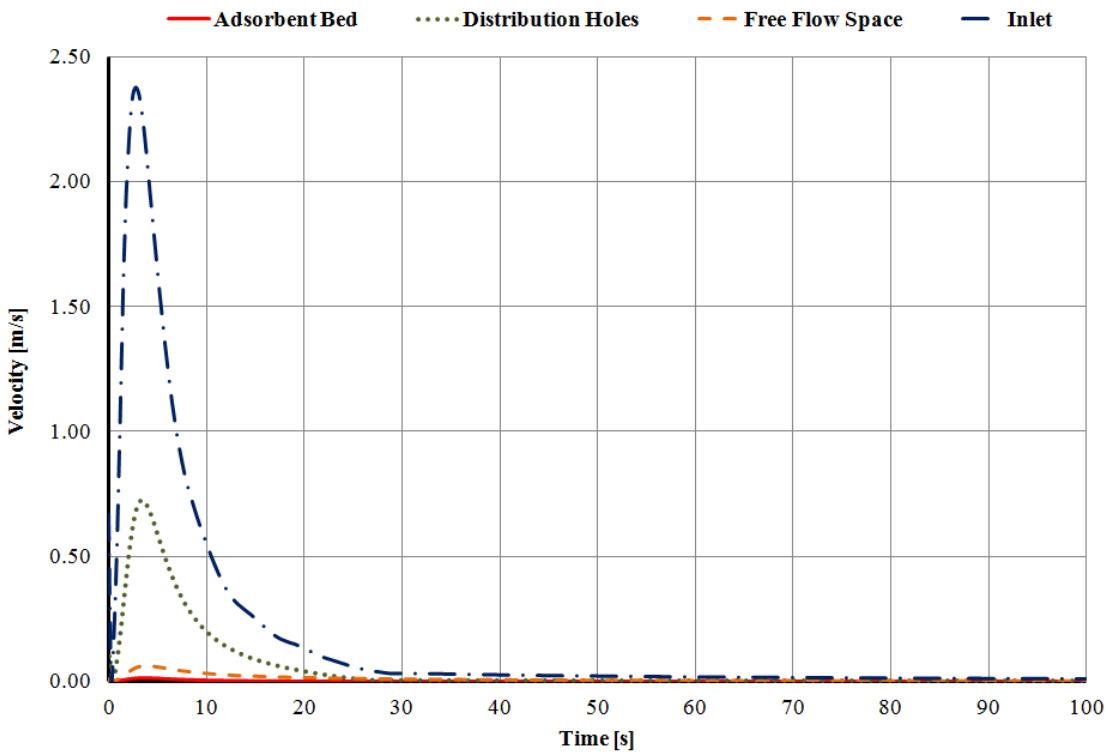

Figure 8.11:Volume-averaged velocity and superficial velocity magnitudes calculated for each domain of H2 adsorption simulation.

In addition to simulating realistic laminar flow conditions, it is important that the global energy balance of the system under investigation be satisfied throughout the simulation. This affirms that excess heat generation and/or removal during the adsorption process is not simulated and is an important step of model validation to ensure the reliability of the results produced. The rate of energy entering the simulated environment via hydrogen gas flow is determined by integrating the hydrogen enthalpy times the gas velocity across the inlet boundary surface. The rate of energy transferred across surfaces is determined through the surface integration of the total normal heat flux at all external surfaces (except inlet) and all surfaces of the microchannel heat exchanger. The energy generation rate throughout the environment is calculated through the volume integration of heat of adsorption (adsorbent bed domain) and pressure work terms (adsorbent bed domain and all free flow gas domains). Total energy values are obtained through numerical integration of the

collected data. The enthalpy changes of all species in the simulated system were, additionally, obtained via volume-integrated calculations.

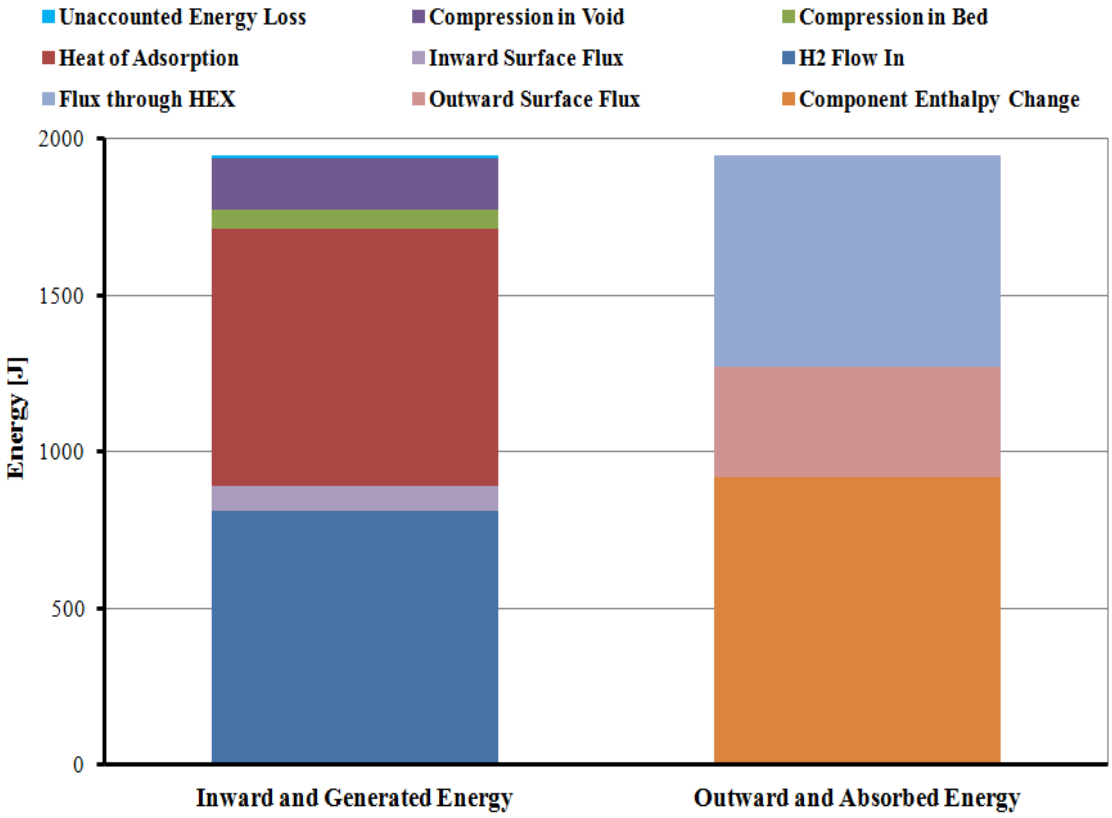

Figure 8. 12: Results of the energy balance calculations for the representative liquid cooled experiment.

H_2 gas flow into the system accounts for approximately 810 J of the total energy entering the system with an additional 80 J entering through the top surface of the gas free flow volume. The majority of energy generated throughout the simulation results from H_2 adsorption on MOF-5 (821 J) with an additional 224 J of energy produced from the compression of H_2 during the charging process. Sixty-five percent of the total energy generated (675 J) is removed through the microchannel heat exchanger with an additional 34% (352 J) of energy was removed through external surfaces of the simulated environment. After taking into account the 920 J of energy absorbed by the hydrogen gas, adsorbent bed, and adsorbed hydrogen (enthalpy

change of each component) only 12 J of additional heat loss (1.15% of incoming H_2 energy) is unaccounted for.

The development tool created for this work has demonstrated the ability to simulate the mass, momentum, and energy transport associated with cryogenic H_2 adsorption on MOF-5 while maintaining laminar gas flow during the pressure ramp and satisfying the global energy balance with minimal error. In addition, the tool possesses the capability to consistently represent the experimental data, for both liquid cooled and non-cooled investigations, with low relative error over the 300-second simulation; thus fulfilling the requirements of validation stated previously. The validated tool may be used to provide information related to the development and design of adsorbent-based H_2 storage systems for materials with known physical, thermal, and adsorption (DA parameters) properties.

8.2 Performance Investigation

A performance investigation is conducted with the validated development tool to determine the impact of enhancing material properties and operating conditions have on the heat transfer, storage capacity, and system requirements of an adsorbent-based hydrogen storage tank. To focus the performance investigation on an adsorption system more representative of an end-user device, the LPC parameters that were initially incorporated to enhance the representation of additional heat transfer associated to the embedded thermocouples, are disabled within the development tool.

The results of the system performance investigation are compared against the base case (BC) simulation for evaluation (Figure 8.1 and Figure 8.2). The BC simulation represents the expected response within the experimental system in the absence of increased heat transfer due to embedded thermocouples and preferential gas flow. The nine performance investigation simulations (PI-1 through PI-9) performed are outlined in Table 8.2, below, and detail the properties and operating conditions implemented.

Table 8.2: Properties and conditions implemented in the performance investigations.

	MOF-5 Properties		Initial and Operating Conditions			
	Thermal Conductivity	**Max Storage Capacity (n_{max})**	**LN2 Temperature**	**Flux Boundary Sink**	**Gas Inlet Temperature**	**Initial Conditions**
	[$Wm^{-1}K^{-1}$]	**[mol-H2 (kg-MOF)$^{-1}$]**	**[K]**	**[K]**	**[K]**	
PI-1	LTV*5	LTV	Exp.	Exp.	Exp.	Exp.
PI-2	LTV*10	LTV	Exp.	Exp.	Exp.	Exp.
PI-3	3	LTV	Exp.	Exp.	Exp.	Exp.
PI-4	LTV	LTV*1.5	Exp.	Exp.	Exp.	Exp.
PI-5	LTV	LTV*2	Exp.	Exp.	Exp.	Exp.
PI-6	LTV	LTV	77	77	77	Exp.
PI-7	3	LTV	77	77	77	Exp.
PI-8	LTV	LTV*2	77	77	77	Exp.
PI-9	3	LTV*2	77	77	77	Exp.

LTV = Literature Value EXP. = Experimental values corresponding to MOF-5 LN2 H2 Exp.#5

Enhanced Adsorbent Thermal Conductivity

As previously stated, the low thermal conductivity of MOF-5 and other adsorbent materials has driven numerous investigations in improving the overall, or effective, thermal conductivity of adsorbents. Three adsorption simulations are conducted to illustrate the increase in storage capacity that could be achieved with improved MOF-5 thermal conductivity under identical operating conditions. The three different thermal conductivities investigated are five and ten times higher than the literature value (Table 7.2) and 3 $Wm^{-1}K^{-1}$, respectively (PI-1 through PI-3). A material thermal conductivity 3 $Wm^{-1}K^{-1}$ was found to provide sufficient heat removal from an adsorbent system using microchannel heat exchanger and is used as the upper limit for this investigation [90]. The average temperature profile of the six thermocouple locations for each of the three investigated conductivities and storage capacities are compared to the BC simulation and experimental data in Figure 8.13, below.

As expected, significant improvements in cooling of the adsorbent bed and storage capacity are observed with an increase in the thermal conductivity. A MOF-5 adsorbent bed with a thermal conductivity five times the literature value closely

resembles the average experimental bed temperature with increased cooling from thermocouples and preferential gas flow.

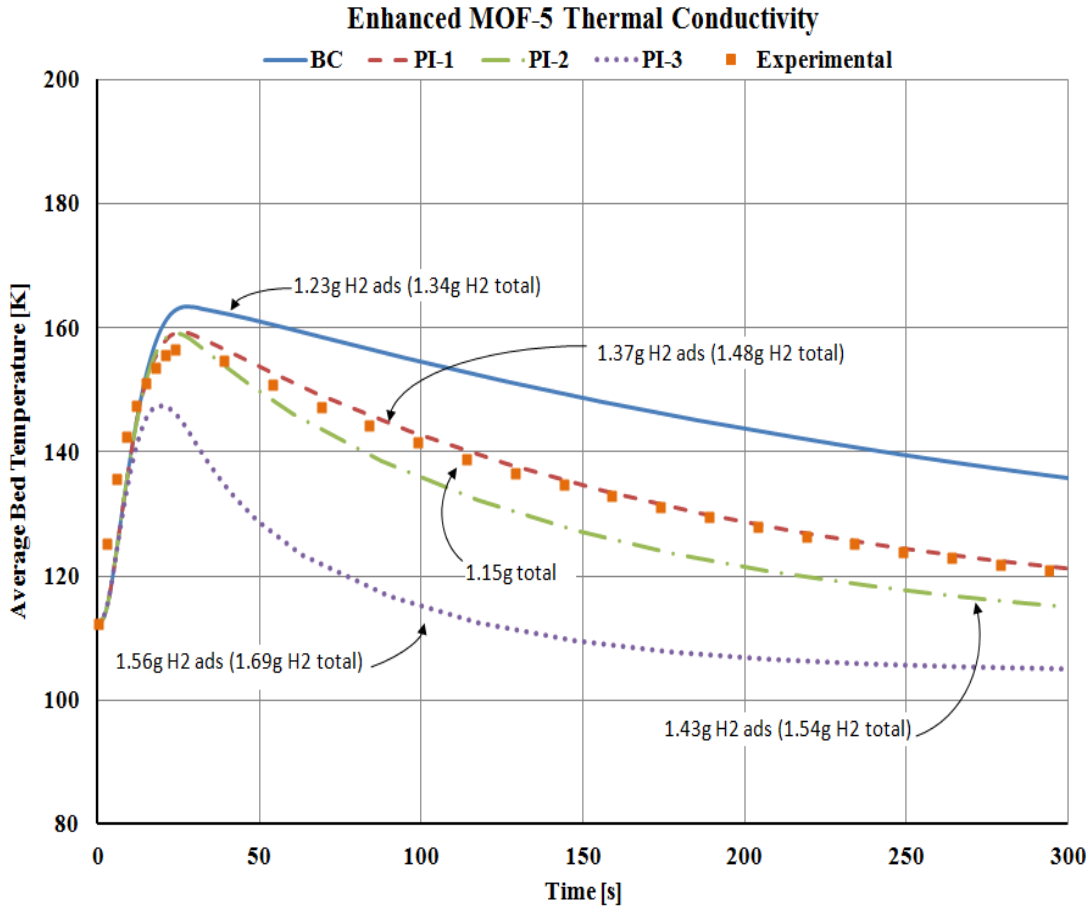

Figure 8.13: Average bed temperature and hydrogen storage capacity for simulations of the thermal conductivity performance investigation.

Enhanced Maximum Adsorption Capacity

Smaller storage systems can be fulfilled with increases in an adsorbent materials maximum storage capacity, or saturation capacity (n_{max}), that would allow for increased hydrogen storage in the same adsorbent mass. Increasing the maximum storage capacity of the material, with all other adsorption kinetic parameters held constant, results in additional heat release due to adsorption, (7.24). Two simulations are performed; PI-4 and PI-5, with increased n_{max} values; the average temperature profiles and storage capacities of the two simulations are compared to the BC simulation and experimental data in Figure 8.14. As expected, increasing the value of

n_{max} does not result in changes to the shape of the temperature profile, but does cause the final bed temperature to be increased beyond to the BC simulation, as a result of increases in heat release from additional gas adsorption. Despite the elevated final temperature, more hydrogen is present in the adsorbent system.

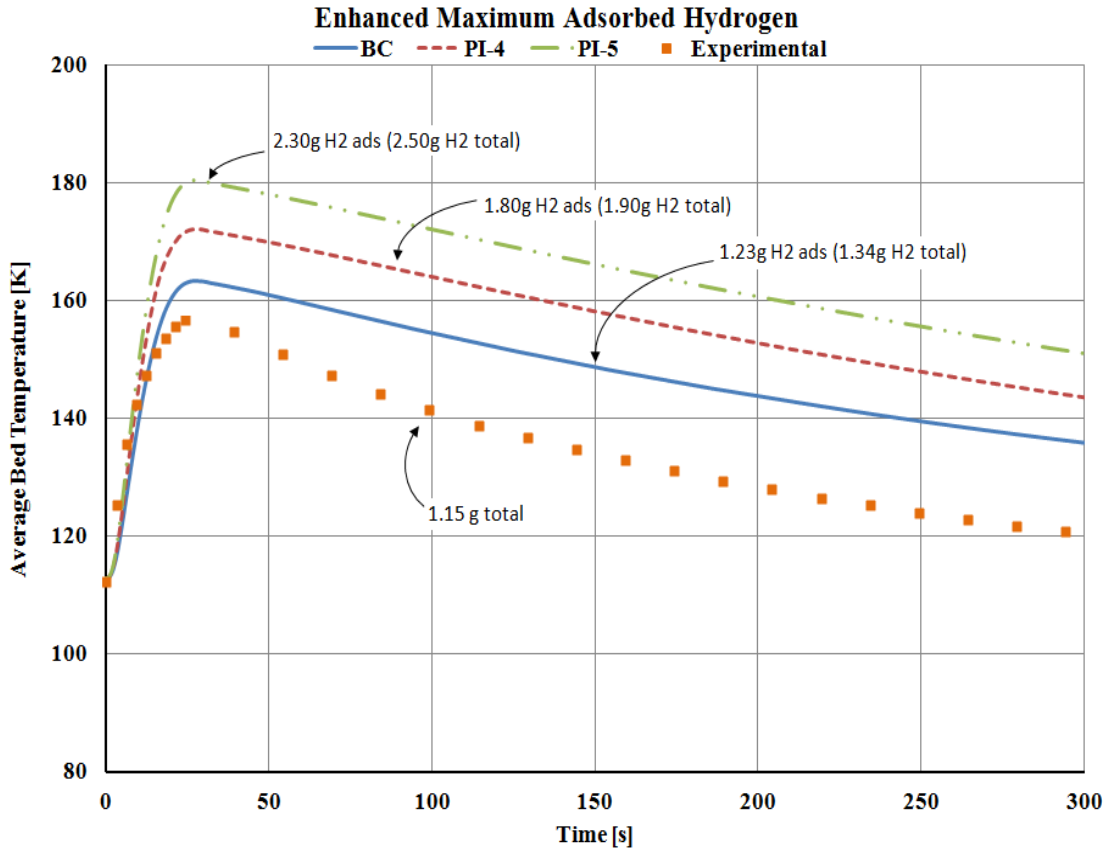

Figure 8.14: Average bed temperature and hydrogen storage capacity for simulations of enhanced MOF storage capacity performance investigation.

Improved Operating Conditions

Elevated operating conditions, liquid nitrogen coolant and vessel body temperatures, limited the performance of the experimental adsorption system used in this investigation. Ideally, liquid nitrogen coolant would flow through the microchannel heat exchanger at atmospheric temperature (77 K) and provide an isothermal contacting surface with the adsorbent bed, conditions that were unattained in the experimental investigations performed.

The vision for an end-user H_2 storage tank utilizing the microchannel device developed in this work uses repeated units of compressed adsorbent beds in contact with the heat exchanger surface. As each successive unit is "numbered-up," until the required system capacity is reached, the adsorbent bed contacts two cooling surface (top and bottom) to further enhance the rate of heat removal from the storage media (Figure 8.15). Fabrication of the storage tank to include liquid cooled tank walls, similar to the system modeled by Paggiaro [80], will further enhance heat transfer throughout the storage process.

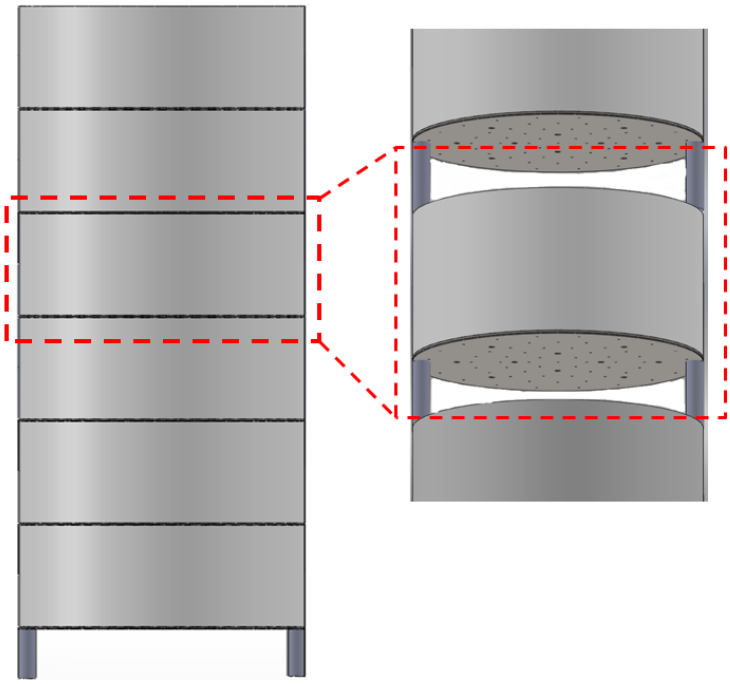

Figure 8.15: Representation of H_2 storage system creating by "numbering up" unit cells to reach desire system capacity.

As seen in Figure 8.16, a 36% improvement in H_2 capacity is observed when ideal isothermal cooling surfaces are applied to the "numbered-up" adsorbent bed and a heat flux to a liquid nitrogen sink is applied to the outside surface of the BC experiment (PI-6). Additional gains in the H_2 storage capacity are realized in PI-7 and PI-8 when ideal operating conditions are applied to the previous simulation conditions of PI-3 and PI-5, respectively, and in a final investigation combining higher thermal conductivity and increased maximum storage capacity (PI-9).

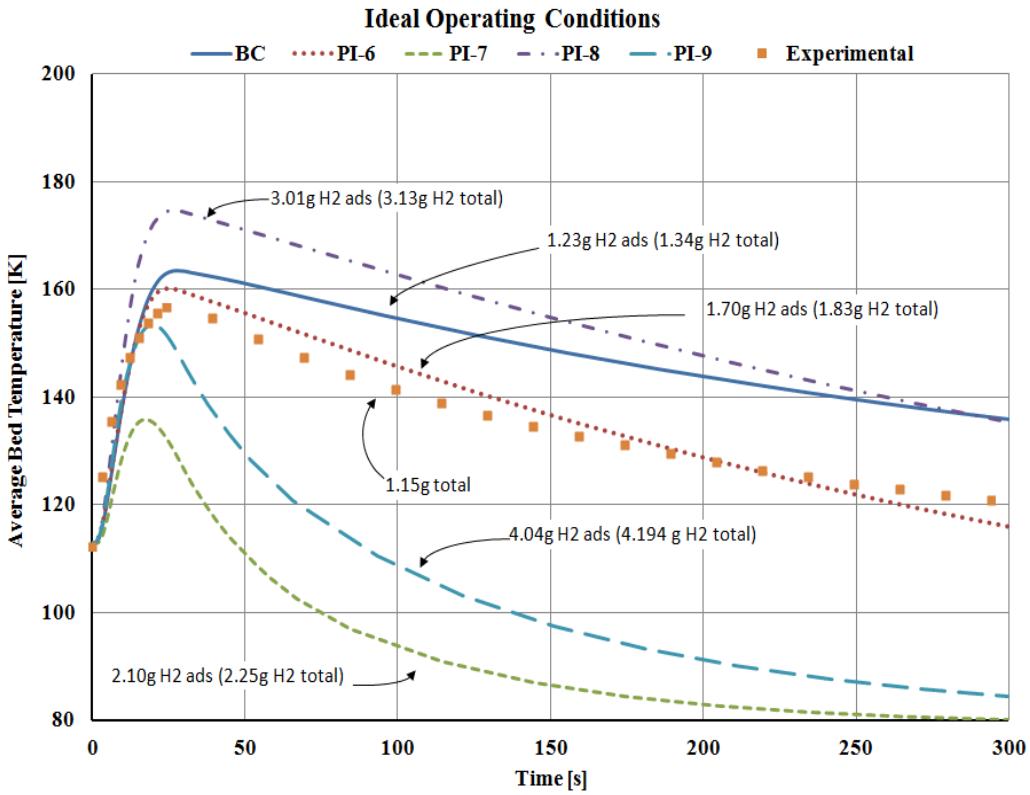

Figure 8.16: Average bed temperature and hydrogen storage capacity for simulations of the improved operating conditions performance investigation.

Hydrogen Storage System Development

An important application of the development tool is supporting and enhancing the design of the overall adsorbent-based hydrogen storage system. The effects of property and operational enhancements on the storage capacity, volume and mass of an adsorbent-based H_2 storage system with a 5.6 kg-H_2 capacity, are seen in Figure 8.17, Figure 8.18 and Table 8.3. The results produced for a single unit cell, discussed above, with a 1.3" tall and 2" diameter adsorbent bed is used for the system analysis.

Comparing a non-cooled trial (NC-BC), solved without LPC parameters, to the liquid cooled BC, a reduction in the required volume and mass of adsorbent is realized with the addition of liquid nitrogen cooling through the heat exchange device, even at the elevated operating conditions of the experiments; and greater reductions are realized with enhanced thermal properties and maximum storage capacities. A 26%

reduction in the number of required unit cells, compared to the BC, is achieved with improved operating conditions in the absence of property enhancements (PI-6). Further system reductions (as high as 68%) are accomplished with the application of ideal operating conditions to the enhanced property trials.

The production of new adsorbent materials with improved storage capacity and thermal conductivity are required to reduce the footprint of a H_2 storage tank. The benefit of the microchannel thermal management system developed is evident by the minimal additional volume required for integration within the complete storage system. Although the microchannel device accounts for $^1/_3$ of the total internal system mass, its contribution can be reduced using aluminum instead of stainless steel for production. The combination of improved adsorbent materials and the microchannel heat exchanger creates a pathway towards meeting DOEs goal of increasing the performance of H_2 systems and decreasing their volume towards the volume of today's automobile gasoline fuel tanks.

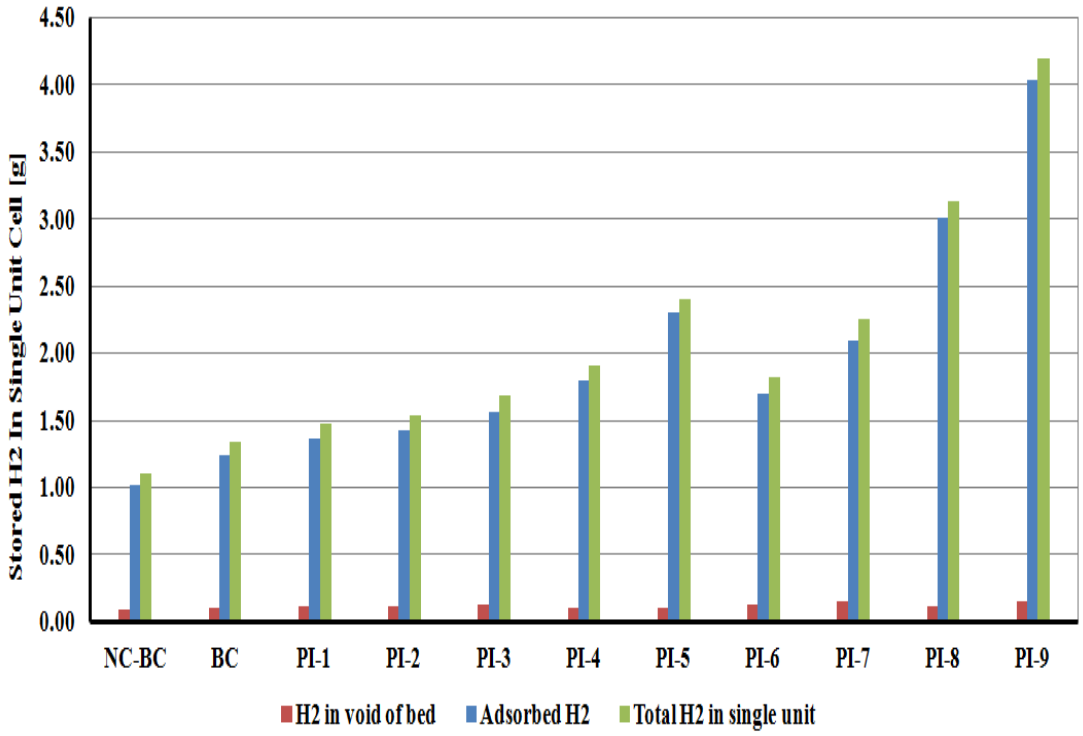

Figure 8.17: Single unit cell H_2 storage capacity.

Table 8.3: Results of system analysis based on the performance investigation, for internal system requirements.

	Adsorbed H2 [g]	H2 in void of bed [g]	Total H2 in Single Unit [g]	Units Needed to Store 5.6 kg H2	Total Volume MOF [L]	Total Mass of MOF-5 [kg]	Total System Volume [L]	Total System Mass [kg]
NC-BC	1.01	0.09	1.10	5084	333.67	116.35	340.64	172.27
BC	1.23	0.10	1.34	4187	274.80	95.82	280.54	141.88
PI-1	1.37	0.11	1.48	3793	248.94	86.81	254.14	128.53
PI-2	1.43	0.11	1.54	3630	238.24	83.07	243.22	123.00
PI-3	1.56	0.12	1.69	3323	218.09	76.05	222.65	112.60
PI-4	1.80	0.10	1.90	2944	193.22	67.38	197.25	99.76
PI-5	2.30	0.10	2.40	2335	153.25	53.44	156.45	79.12
PI-6	1.70	0.13	1.83	3067	201.29	70.19	205.49	103.93
PI-7	2.10	0.16	2.25	2485	163.09	56.87	166.50	84.21
PI-8	3.01	0.12	3.13	1787	117.28	40.90	119.73	60.55
PI-9	4.04	0.15	4.19	1337	87.75	30.60	89.58	45.31

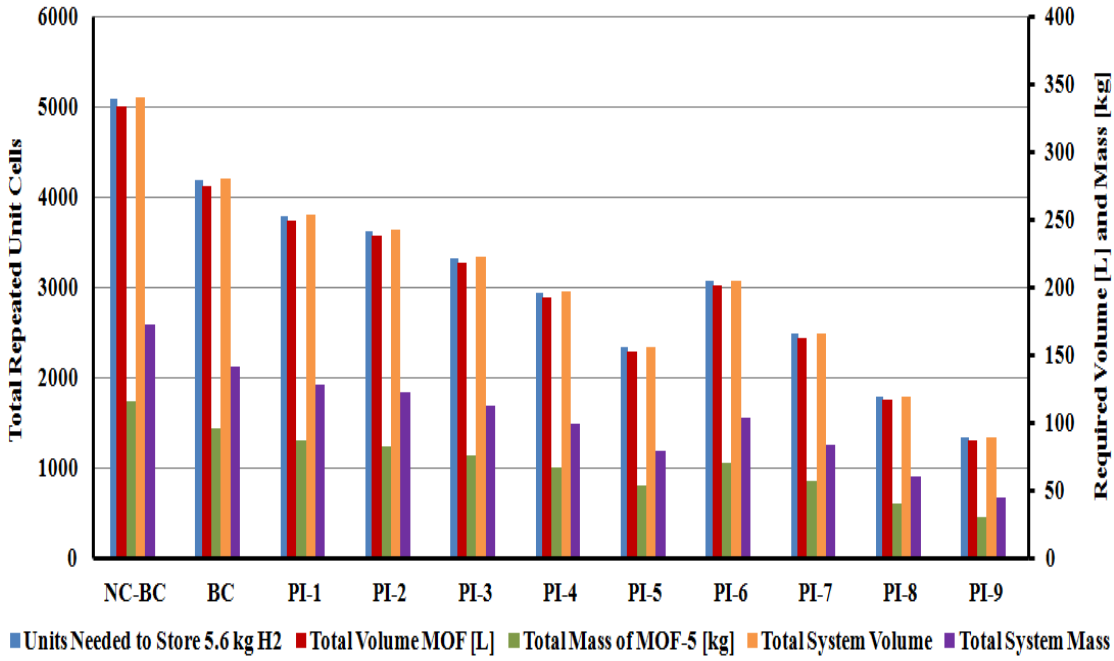

Figure 8.18: Results of the system analysis based on the performance investigation, for internal system requirements.

Chapter 9: Conclusion and Recommendations

9.1 Conclusion

The development and testing of a novel microchannel heat exchange and gas distribution device for the enhancement of solid-state hydrogen storage systems is investigated in this work. Packed beds of activated carbon and metal organic framework (MOF-5) are used to store hydrogen and nitrogen at cryogenic temperatures (<160 K) and elevated pressure (>50 bars). Physical adsorption serves as the underlying mechanism of hydrogen storage on the materials in question and additional capacity is attained from the presence of compressed gas in the interparticle voids of the packed beds.

An experimental investigation was performed to assess the impact of liquid nitrogen flow through a novel microchannel heat exchanger on heat removal and storage capacity compared to non-cooled adsorption trials. Liquid cooled H_2 adsorption experiments demonstrated a significantly lower effective heat generation compared to non-cooled trials. Increased heat removal resulted in an average increase of 11% and 3% stored H_2 in the MOF-5 and activated carbon beds, respectively. H_2 adsorption on MOF-5 demonstrates an increased heat release during the charging process and an additional 35% stored hydrogen for liquid cooled trials (30% increase in non-cooled trials), compared to activated carbon experiments. Improved N_2 storage capacity is also demonstrated by both adsorbents with liquid nitrogen cooling.

A detailed mathematical model is derived to characterize the H_2 adsorption process in addition to the mass, momentum, and heat transfer in both open and packed bed regions of the experimental system. The modified Dubinin-Astakhov adsorption kinetic parameters employed in the mathematical model are obtained from literature and our partners in the HSECoE. Successful simulations of experimental trials were achieved when the mathematical model is implemented through COMSOL Multiphysics 4.2a. The predicted temperature profiles and storage capacities for H_2

storage on MOF-5 are in good agreement with experimental data obtained throughout this work under a variety of operating conditions.

The experimentally validated model may be used as a tool to enhance the Oregon State University Hydrogen Storage program's ability to investigate and design future adsorbent-based hydrogen storage systems. Using the analytical development tool, a performance investigation was conducted to demonstrate the potential increases in storage capacity, yielding decreased system size, that can be realized with improvements in thermal conductivity and maximum storage capacity of future adsorbent materials. Further system reductions are realized by applying improved operating conditions to the various systems investigated.

9.2 Recommendations for Future Work

Modifications and enhancements in the experimental system will result in improved operation and experimental data to allow a broader parametric investigation to be performed in the future. Future adsorption system (pressure vessel, thermal management, and adsorbent beds) designs must yield a more favorable ratio of vessel mass to internal mass (adsorbent bed and thermal management system) in order to reduce or eliminate the lower temperature limit observed throughout this investigation. This may be accomplished by utilizing a numbered-up thermal management system to provide H_2 gas and liquid nitrogen cooling to multiple adsorbent beds in a single vessel. A series arrangement of microchannel devices will enable the verification of uniform flow distribution through each successive device and validate the concept of numbering-up to achieve an increased system capacity.

In addition to more uniform apparatus design, achieving a lower liquid nitrogen temperature at the inlet of the microchannel device will improve the performance of the experimental adsorption system by providing a greater temperature difference between the adsorbent bed and cooling fluid. Lower liquid nitrogen temperatures may be achieved by increasing the length of tubing used in the sub-cooling coil, moving the sub-cooling coil closer to the inlet of the microchannel

device, and increasing the insulation on all liquid lines before and directly after the adsorption vessel.

Future experimental vessels should allow thermocouples to enter adsorbent beds from the opposite surface of penetrating hydrogen gas flow. This will reduce the preferential gas flow along the thermocouples that provides additional convective cooling during vessel pressurization. Additional isolation of the thermocouples from the adsorbent bed should be achieved, except at the desired contact point, to reduce additional conductive heat removal provided from the increased conductivity of the stainless steel device and further reduce void regions for gas flow.

Further, future experimental investigations should include discharging experiments to ensure the microchannel device's ability to heat the adsorbent bed, using warm gas flow, and drive the desorption of stored H_2 from the system.

Finally, the expansion and validation of the COMSOL model to include both charging and discharging operation will improve the overall system design capabilities by allowing the optimization of both processes in one package. The additional inclusion of fluid flow through the microchannel heat exchanger and headers will further enhance the representation of the experimental system; however, a 2-D axisymmetric geometry may be required to reduce the simulation size and solution time to a manageable level.

References

[1] S. Shafiee and E. Topal, “When will fossil fuel reserves be diminished?,” *Energy Policy*, vol. 37, no. 1, pp. 181–189, Jan. 2009.

[2] P. de Almeida and P. D. Silva, “The peak of oil production—Timings and market recognition,” *Energy Policy*, vol. 37, no. 4, pp. 1267–1276, Apr. 2009.

[3] S. Davis, S. Diegel, and R. Boundy, *Transportation Energy Data Book 30th Edition*. Oak Ridge, Tennesse, Oak Ridge National Laboratory: Oak Ridge National Laboratory, 2011.

[4] P. Jaramillo, C. Samaras, H. Wakeley, and K. Meisterling, “Greenhouse gas implications of using coal for transportation: Life cycle assessment of coal-to-liquids, plug-in hybrids, and hydrogen pathways,” *Energy Policy*, vol. 37, no. 7, pp. 2689–2695, Jul. 2009.

[5] S. Clerides and T. Zachariadis, “The effect of standards and fuel prices on automobile fuel economy: An international analysis,” *Energy Economics*, vol. 30, no. 5, pp. 2657–2672, Sep. 2008.

[6] A. Züttel, “Hydrogen storage methods,” *Naturwissenschaften*, vol. 91, no. 4, pp. 157–172, Apr. 2004.

[7] C. Le Quéré, M. R. Raupach, J. G. Canadell, G. Marland et al., C. Le Quéré et al., C. Le Quéré et al., M. R. Raupach, J. G. Canadell, G. Marland, L. Bopp, P. Ciais, T. J. Conway, S. C. Doney, R. A. Feely, P. Foster, P. Friedlingstein, K. Gurney, R. A. Houghton, J. I. House, C. Huntingford, P. E. Levy, M. R. Lomas, J. Majkut, N. Metzl, J. P. Ometto, G. P. Peters, I. C. Prentice, J. T. Randerson, S. W. Running, J. L. Sarmiento, U. Schuster, S. Sitch, T. Takahashi, N. Viovy, G. R. van der Werf, and F. I. Woodward, “Trends in the sources and sinks of carbon dioxide,” *Nature Geoscience*, vol. 2, no. 12, pp. 831–836, Nov. 2009.

[8] R. Feely, S. Doney, and S. Cooley, “Ocean Acidification: Present Conditions and Future Changes in a High-CO2 World,” *Oceanography*, vol. 22, no. 4, pp. 36–47, Dec. 2009.

[9] A. Midilli and I. Dincer, “Hydrogen as a renewable and sustainable solution in reducing global fossil fuel consumption,” *International Journal of Hydrogen Energy*, vol. 33, no. 16, pp. 4209–4222, Aug. 2008.

[10] T. R. Dallmann and R. A. Harley, “Evaluation of mobile source emission trends in the United States,” *Journal of Geophysical Research*, vol. 115, no. D14, Jul. 2010.

[11] S. Satyapal, J. Petrovic, C. Read, G. Thomas, and G. Ordaz, “The U.S. Department of Energy’s National Hydrogen Storage Project: Progress towards

meeting hydrogen-powered vehicle requirements," *Catalysis Today*, vol. 120, no. 3–4, pp. 246–256, Feb. 2007.

[12] L. Schlapbach and A. Züttel, "Hydrogen-storage materials for mobile applications," *Nature*, vol. 414, Nov. 2001.

[13] R. Kothari, D. Buddhi, and R. L. Sawhney, "Comparison of environmental and economic aspects of various hydrogen production methods," *Renewable and Sustainable Energy Reviews*, vol. 12, no. 2, pp. 553–563, Feb. 2008.

[14] J. D. Holladay, J. Hu, D. L. King, and Y. Wang, "An overview of hydrogen production technologies," *Catalysis Today*, vol. 139, no. 4, pp. 244–260, Jan. 2009.

[15] S. A. Sherif, F. Barbir, and T. N. Veziroglu, "Wind energy and the hydrogen economy—review of the technology," *Solar Energy*, vol. 78, no. 5, pp. 647–660, May 2005.

[16] M. Matsuoka, M. Kitano, M. Takeuchi, K. Tsujimaru, M. Anpo, and J. M. Thomas, "Photocatalysis for new energy production," *Catalysis Today*, vol. 122, no. 1–2, pp. 51–61, Apr. 2007.

[17] S. U. M. Khan, "Efficient Photochemical Water Splitting by a Chemically Modified n-TiO2," *Science*, vol. 297, no. 5590, pp. 2243–2245, Sep. 2002.

[18] M. Graetzel, "Artificial photosynthesis: water cleavage into hydrogen and oxygen by visible light," *Accounts of Chemical Research*, vol. 14, no. 12, pp. 376–384, Dec. 1981.

[19] L. Wagner, "Overview of energy storage methods." MORA Associates, Dec-2007.

[20] Office of Energy Efficiency and Renewable Energy and the FreedomCAR and Fuel Partnership, "Targets for Onboard Hydrogen Storage Systems for Light-Duty Vehicles." US Department of Energy, Sep-2009.

[21] J. Graetz, "New approaches to hydrogen storage," *Chemical Society Reviews*, vol. 38, no. 1, p. 73, 2009.

[22] U. B. Demirci and P. Miele, "Sodium borohydride versus ammonia borane, in hydrogen storage and direct fuel cell applications," *Energy & Environmental Science*, vol. 2, no. 6, p. 627, 2009.

[23] A. Züttel, "Materials for hydrogen storage," *Materials Today*, vol. 6, no. 9, pp. 24–33, Sep. 2003.

[24] C. W. Hamilton, R. T. Baker, A. Staubitz, and I. Manners, "B–N compounds for chemical hydrogen storage," *Chemical Society Reviews*, vol. 38, no. 1, p. 279, 2009.

[25] S. Hynek, W. Fuller, and J. Bentley, “Hydrogen storage by carbon sorption,” *International Journal of Hydrogen Energy*, vol. 22, no. 6, pp. 601–610, Jun. 1997.

[26] A. Dabrowski, “Adsorption--from theory to practice,” *Adv Colloid Interface Sci*, vol. 93, no. 1–3, pp. 135–224, Oct. 2001.

[27] V. A. Parsegian, *Van der Waals forces : a handbook for biologists, chemists, engineers, and physicists*. New York: Cambridge University Press, 2006.

[28] B. Panella, M. Hirscher, and S. Roth, “Hydrogen adsorption in different carbon nanostructures,” *Carbon*, vol. 43, no. 10, pp. 2209–2214, Aug. 2005.

[29] A. L. Myers, “Thermodynamics of adsorption in porous materials,” *AIChE Journal*, vol. 48, no. 1, pp. 145–160, Jan. 2002.

[30] M.-A. Richard, D. Cossement, P.-A. Chandonia, R. Chahine, D. Mori, and K. Hirose, “Preliminary evaluation of the performance of an adsorption-based hydrogen storage system,” *AIChE Journal*, vol. 55, no. 11, pp. 2985–2996, Nov. 2009.

[31] W. Zhou, H. Wu, M. R. Hartman, and T. Yildirim, “Hydrogen and Methane Adsorption in Metal-Organic Frameworks: A High-Pressure Volumetric Study,” *Journal of Physical Chemistry C*, vol. 111, no. 44, pp. 16131–16137, Nov. 2007.

[32] R. L. BURWELL JR, “Manual of Symbols and Terminology for Physicochemical Quantities and Units—-Appendix ll: Part II: Advances in Catalysis,” *International Union of Pure and Applied Chemistry*, vol. 26, p. 351, 1977.

[33] P. Bénard and R. Chahine, “Determination of the Adsorption Isotherms of Hydrogen on Activated Carbons above the Critical Temperature of the Adsorbate over Wide Temperature and Pressure Ranges,” *Langmuir*, vol. 17, no. 6, pp. 1950–1955, Mar. 2001.

[34] J. Tóth, *Adsorption : theory, modeling, and analysis*. New York: Marcel Dekker, 2002.

[35] I. Langmuir, “THE CONSTITUTION AND FUNDAMENTAL PROPERTIES OF SOLIDS AND LIQUIDS. PART I. SOLIDS.,” *Journal of the American Chemical Society*, vol. 38, no. 11, pp. 2221–2295, 1916.

[36] S. Brunauer, P. H. Emmett, and E. Teller, “Adsorption of gases in multimolecular layers,” *Journal of the American Chemical Society*, vol. 60, no. 2, pp. 309–319, 1938.

[37] P. Schneider, “Adsorption isotherms of microporous-mesoporous solids revisited,” *Applied Catalysis A: General*, vol. 129, no. 2, pp. 157–165, Aug. 1995.

[38] M. M. Dubinin, “The Potential Theory of Adsorption of Gases and Vapors for Adsorbents with Energetically Nonuniform Surfaces.,” *Chemical Reviews*, vol. 60, no. 2, pp. 235–241, Apr. 1960.

[39] V. K. Dobruskin, “Physical Adsorption in Micropores: A Condensation Approximation Approach,” *Langmuir*, vol. 14, no. 14, pp. 3847–3857, Jul. 1998.

[40] M. M. Dubinin, “Fundamentals of the theory of adsorption in micropores of carbon adsorbents: characteristics of their adsorption properties and microporous structures,” *Pure & Applied Chemistry*, vol. 61, no. 11, pp. 1841–1843, 1989.

[41] N. S. Polyakov and G. A. Petukhova, “Extension of the Theory of Volume Filling of Micropores to Adsorption in Supermicropores,” *Adsorption*, vol. 11, no. 3–4, pp. 357–362, Jul. 2005.

[42] L. Zhou, “Progress and problems in hydrogen storage methods,” *Renewable and Sustainable Energy Reviews*, vol. 9, no. 4, pp. 395–408, Aug. 2005.

[43] K. Kaneko and K. Murata, “An analytical method of micropore filling of a supercritical gas,” *Adsorption*, vol. 3, no. 3, pp. 197–208, Sep. 1997.

[44] D. . Do and H. . Do, “Adsorption of supercritical fluids in non-porous and porous carbons: analysis of adsorbed phase volume and density,” *Carbon*, vol. 41, no. 9, pp. 1777–1791, Jan. 2003.

[45] G. Hermosillalara, G. Momen, P. Marty, B. Leneindre, and K. Hassouni, “Hydrogen storage by adsorption on activated carbon: Investigation of the thermal effects during the charging process,” *International Journal of Hydrogen Energy*, vol. 32, no. 10–11, pp. 1542–1553, Jul. 2007.

[46] C. R. Clarkson, R. M. Bustin, and J. H. Levy, “Application of the mono/multilayer and adsorption potential theories to coal methane adsorption isotherms at elevated temperature and pressure,” *Carbon*, vol. 35, no. 12, pp. 1689–1705, Jan. 1997.

[47] E. Poirier and A. Dailly, “Investigation of the Hydrogen State in IRMOF-1 from Measurements and Modeling of Adsorption Isotherms at High Gas Densities,” *Journal of Physical Chemistry C*, vol. 112, no. 33, pp. 13047–13052, Aug. 2008.

[48] M.-A. Richard, P. Bénard, and R. Chahine, “Gas adsorption process in activated carbon over a wide temperature range above the critical point. Part 1: modified Dubinin-Astakhov model,” *Adsorption*, vol. 15, no. 1, pp. 43–51, Feb. 2009.

[49] M. G. Nijkamp, J. E. M. J. Raaymakers, A. J. van Dillen, and K. P. de Jong, “Hydrogen storage using physisorption – materials demands,” *Applied Physics A Materials Science & Processing*, vol. 72, no. 5, pp. 619–623, May 2001.

[50] H. Teng, T.-S. Yeh, and L.-Y. Hsu, “Preparation of activated carbon from bituminous coal with phosphoric acid activation,” *Carbon*, vol. 36, no. 9, pp. 1387–1395, Sep. 1998.

[51] A. Ahmadpour and D. D. Do, “The preparation of activated carbon from macadamia nutshell by chemical activation,” *Carbon*, vol. 35, no. 12, pp. 1723–1732, Jan. 1997.

[52] F. Rodríguez-Reinoso, M. Molina-Sabio, and M. T. González, “The use of steam and CO2 as activating agents in the preparation of activated carbons,” *Carbon*, vol. 33, no. 1, pp. 15–23, Jan. 1995.

[53] E. Senoz and R. P. Wool, “Hydrogen storage on pyrolyzed chicken feather fibers,” *International Journal of Hydrogen Energy*, vol. 36, no. 12, pp. 7122–7127, Jun. 2011.

[54] J. A. Maciá-Agulló, B. C. Moore, D. Cazorla-Amorós, and A. Linares-Solano, “Activation of coal tar pitch carbon fibres: Physical activation vs. chemical activation,” *Carbon*, vol. 42, no. 7, pp. 1367–1370, Jan. 2004.

[55] N. Texier-Mandoki, J. Dentzer, T. Piquero, S. Saadallah, P. David, and C. Vix-Guterl, “Hydrogen storage in activated carbon materials: Role of the nanoporous texture,” *Carbon*, vol. 42, no. 12–13, pp. 2744–2747, Jan. 2004.

[56] H. Li, M. Eddaoudi, M. O’Keeffe, and O. M. Yaghi, “Design and synthesis of an exceptionally stable and highly porous metal-organic framework,” *Nature*, vol. 402, 1999.

[57] N. L. Rosi, “Hydrogen Storage in Microporous Metal-Organic Frameworks,” *Science*, vol. 300, no. 5622, pp. 1127–1129, May 2003.

[58] D. J. Collins and H.-C. Zhou, “Hydrogen storage in metal–organic frameworks,” *Journal of Materials Chemistry*, vol. 17, no. 30, p. 3154, 2007.

[59] T. K. Mandal and D. H. Gregory, “Hydrogen storage materials: present scenarios and future directions,” *Annual Reports Section “A” (Inorganic Chemistry)*, vol. 105, p. 21, 2009.

[60] T. K. Bose, R. Chahine, and J. M. St-Arnaud, “High-density adsorbent and method of producing same,” 4,999,33012-Mar-1991.

[61] J. A. F. MacDonald and D. F. Quinn, “Carbon absorbents for natural gas storage,” *Fuel*, vol. 77, no. 1–2, pp. 61–64, Jan. 1998.

[62] J. Sun, T. D. Jarvi, L. F. Conopask, S. Satyapal, M. J. Rood, and M. Rostam-Abadi, “Direct Measurements of Volumetric Gas Storage Capacity and Some New Insight into Adsorbed Natural Gas Storage,” *Energy & Fuels*, vol. 15, no. 5, pp. 1241–1246, Sep. 2001.

[63] X. Chen and B. McEnaney, “MONOLITHIC MICROPOROUS CARBON FOR GAS STORAGE,” *Poster*.

[64] R. Chahine, “Sorption Storage Technology Summary,” presented at the DOE H2 Storage Workshop - Compressed & Cryo-Compressed Hydrogen Storage Workshop, Washington DC, 14-Feb-2011.

[65] D. Liu, J. J. Purewal, J. Yang, A. Sudik, S. Maurer, U. Mueller, J. Ni, and D. J. Siegel, “MOF-5 composites exhibiting improved thermal conductivity,” *International Journal of Hydrogen Energy*, vol. 37, no. 7, pp. 6109–6117, Apr. 2012.

[66] A. Sudik, M. Veenstra, J. Purewal, D. Siegel, D. Liu, S. Maurer, U. Muller, and J. Yang, “Ford/BASF-SE/UM Activities in Support of the Hydrogen Storage Engineering Center of Excellence.” 2012.

[67] J. Purewal, D. Liu, A. Sudik, M. Veenstra, J. Yang, S. Maurer, U. Müller, and D. J. Siegel, “Improved Hydrogen Storage and Thermal Conductivity in High-Density MOF-5 Composites,” *The Journal of Physical Chemistry C*, vol. 116, no. 38, pp. 20199–20212, Sep. 2012.

[68] R. K. Ahluwalia and J. K. Peng, “Automotive hydrogen storage system using cryo-adsorption on activated carbon,” *International Journal of Hydrogen Energy*, vol. 34, no. 13, pp. 5476–5487, Jul. 2009.

[69] D. Kumar, M. Cai, A. Chakraborty, N. Kaisare, J. Ortmann, M. Sulic, and S. Kumar, “Thermal Management of On-Board Cryogenic Hydrogen Storage Systems,” presented at the Hydrogen Storage Engineering Center of Excellence, Washington DC, May-2012.

[70] B. Hardy, C. Corgnale, R. Chahine, M.-A. Richard, S. Garrison, D. Tamburello, D. Cossement, and D. Anton, “Modeling of adsorbent based hydrogen storage systems,” *International Journal of Hydrogen Energy*, vol. 37, no. 7, pp. 5691–5705, Apr. 2012.

[71] D. Tamburello, T. Motyka, R. Chahine, B. Hardy, M. Kesterson, and C. Corgnale, “SRNL Technical Work Scope for the Hydrogen Storage Engineering Center of Excellence: Design and Testing of Metal Hydride and Adsorbent Systems,” presented at the Hydrogen Storage Engineering Center of Excellence, Washington DC, May-2012.

[72] S. Mellouli, F. Askri, H. Dhaou, A. Jemni, and S. Ben Nasrallah, “A novel design of a heat exchanger for a metal-hydrogen reactor,” *International Journal of Hydrogen Energy*, vol. 32, no. 15, pp. 3501–3507, Oct. 2007.

[73] F. Askri, M. Bensalah, A. Jemni, and S. Bennasrallah, “Optimization of hydrogen storage in metal-hydride tanks,” *International Journal of Hydrogen Energy*, vol. 34, no. 2, pp. 897–905, Jan. 2009.

[74] M. Visaria, I. Mudawar, T. Pourpoint, and S. Kumar, “Study of heat transfer and kinetics parameters influencing the design of heat exchangers for hydrogen storage in high-pressure metal hydrides,” *International Journal of Heat and Mass Transfer*, vol. 53, no. 9–10, pp. 2229–2239, Apr. 2010.

[75] J. Yang, A. Sudik, C. Wolverton, and D. J. Siegel, “High capacity hydrogen storage materials: attributes for automotive applications and techniques for materials discovery,” *Chemical Society Reviews*, vol. 39, no. 2, p. 656, 2010.

[76] M. Janicke, “The Controlled Oxidation of Hydrogen from an Explosive Mixture of Gases Using a Microstructured Reactor/Heat Exchanger and Pt/Al2O3 Catalyst,” *Journal of Catalysis*, vol. 191, no. 2, pp. 282–293, Apr. 2000.

[77] L. Steigleder, “A Microchannel-Based Thermal Management System for Hydrogen Storage Adsorbent Beds,” Masters Thesis, Oregon State University, Corvallis, OR USA, 2012.

[78] M.-A. Richard, P. Bénard, and R. Chahine, “Gas adsorption process in activated carbon over a wide temperature range above the critical point. Part 2: conservation of mass and energy,” *Adsorption*, vol. 15, no. 1, pp. 53–63, Feb. 2009.

[79] G. Momen, G. Hermosilla, A. Michau, M. Pons, M. Firdaouss, and K. Hassouni, “Hydrogen storage in an activated carbon bed: Effect of energy release on storage capacity of the tank,” *International Journal of Hydrogen Energy*, vol. 34, no. 9, pp. 3799–3809, May 2009.

[80] R. Paggiaro, F. Michl, P. Bénard, and W. Polifke, “Cryo-adsorptive hydrogen storage on activated carbon. II: Investigation of the thermal effects during filling at cryogenic temperatures,” *International Journal of Hydrogen Energy*, vol. 35, no. 2, pp. 648–659, Jan. 2010.

[81] J. Xiao, Y. Liu, J. Wang, P. Bénard, and R. Chahine, “Finite element simulation of heat and mass transfer in activated carbon hydrogen storage tank,” *International Journal of Heat and Mass Transfer*, vol. 55, no. 23–24, pp. 6864–6872, Nov. 2012.

[82] J. Xiao, M. Hu, D. Cossement, P. Bénard, and R. Chahine, “Finite element simulation for charge–discharge cycle of cryo-adsorptive hydrogen storage on activated carbon,” *International Journal of Hydrogen Energy*, vol. 37, no. 17, pp. 12947–12959, Sep. 2012.

[83] J. Xiao, L. Tong, C. Deng, P. Bénard, and R. Chahine, “Simulation of heat and mass transfer in activated carbon tank for hydrogen storage,” *International Journal of Hydrogen Energy*, vol. 35, no. 15, pp. 8106–8116, Aug. 2010.

[84] J. Xiao, L. Tong, D. Cossement, P. Bénard, and R. Chahine, “CFD simulation for charge–discharge cycle of cryo-adsorptive hydrogen storage on activated

carbon," *International Journal of Hydrogen Energy*, vol. 37, no. 17, pp. 12893–12904, Sep. 2012.

[85] J. Xiao, Q. Li, D. Cossement, P. Bénard, and R. Chahine, "Lumped parameter simulation for charge–discharge cycle of cryo-adsorptive hydrogen storage system," *International Journal of Hydrogen Energy*, vol. 37, no. 18, pp. 13400–13408, Sep. 2012.

[86] R. B. Bird, W. E. Stewart, and E. N. Lightfoot, *Transport phenomena*. New York: J. Wiley, 2002.

[87] "McMASTER-CARR," *http://www.mcmaster.com/#*. [Online]. Available: http://www.mcmaster.com/#8984kac/=jq10ox, http://www.mcmaster.com/#8574kac/=jq0gt3.

[88] National Institute of Standards and Technology, "Cryogenics Technologies Group - Material Properties," *Material Properties*. [Online]. Available: http://cryogenics.nist.gov/MPropsMAY/material%20properties.htm. [Accessed: 16-Mar-2012].

[89] D. Siegel, "Personal Communication discussing MOF-5 properties, activation, and handling at World Hydrogen Energy Conference, Toronto, ON, Canada," 04-Jun-2012.

[90] K. Drost, "Microscale Enhancement of Heat and Mass Transfer for Hydrogen Energy Storage," Oregon State University, Quarterly Progress Report Award Number DE-FC36-08GO19005, Jan. 2012.

[91] V. S. Kumar and S. Kumar, "Generalized model development for a cryo-adsorber and 1-D results for the isobaric refueling period," *International Journal of Hydrogen Energy*, vol. 35, no. 8, pp. 3598–3609, Apr. 2010.

[92] M. Veenstra, "Ford/BASF-SE/UM Activities in Support of the Hydrogen Storage Engineering Center of Excellence," presented at the 2012 DOE Annual Merit Review Meeting.

[93] "COMSOL Multiphysics User's Guide v4.2a." COMSOL Multiphysics, Oct-2011.

[94] A. Bejan, *Convection heat transfer*. New York: Wiley, 1984.

Appendices

Appendix A: Experimental Results
Liquid Cooled Nitrogen Adsorption on Activated Carbon

Experiment Name	AC LN2 N2 Exp.#1	AC LN2 N2 Exp.#2	AC LN2 N2 Exp.#3	AC LN2 N2 Exp.#4
Charging time to 50 bar [s]	53.50	66.75	141.50	73.00
Charging Pressure [bar]	54.36	51.76	50.19	50.51
Avg. Initial Bed Temperature [K]	105.16	117.18	159.06	142.47
Avg. Bed Temperature Rise [K]	18.06	9.97	14.90	12.16
Avg. Max Bed Temperature [K]	119.69	127.16	173.96	154.62
Avg. Final Bed Temperature [K]	110.93	118.76	146.56	131.78
LN2 Flow Rate [g s^{-1}]	1.88	1.83	2.03	1.18
Avg. LN2 Temperature [K]	93.57	97.23	97.52	98.36
Dewar Temperature [K]	115.00	136.50	147.00	155.00
Effective Heat Generation [J]	41.14	-85.40	-162.38	-114.38
Mass of N2 in Vessel [g]	68.90	66.53	24.40	50.38
Mass N2 in AC Bed [g]	27.75	23.16	18.72	40.05

Experiment Name	AC LN2 N2 Exp.#5	AC LN2 N2 Exp.#6	AC LN2 N2 Exp.#7
Charging time to 50 bar [s]	43.75	52.75	128.25
Charging Pressure [bar]	50.99	51.76	50.91
Avg. Initial Bed Temperature [K]	124.48	106.76	112.87
Avg. Bed Temperature Rise [K]	12.74	15.01	12.24
Avg. Max Bed Temperature [K]	137.22	121.77	125.11
Avg. Final Bed Temperature [K]	126.21	114.05	118.68
LN2 Flow Rate [g s^{-1}]	0.45	2.03	0.67
Avg. LN2 Temperature [K]	104.52	94.80	102.14
Dewar Temperature [K]	137.00	139.00	114.00
Effective Heat Generation [J]	49.53	83.15	63.45
Mass of N2 in Vessel [g]	69.35	80.11	67.98
Mass N2 in AC Bed [g]	36.85	33.15	24.95

Non-cooled Nitrogen Adsorption on Activated Carbon

Experiment Name	AC NC N2 Exp.#1	AC NC N2 Exp.#2	AC NC N2 Exp.#3	AC NC N2 Exp.#4
Charging time to 50 bar [s]	119.25	51.25	92.25	57.25
Charging Pressure [bar]	52.50	60.26	54.13	51.51
Avg. Initial Bed Temperature [K]	123.72	86.79	94.57	118.71
Avg. Bed Temperature Rise [K]	11.87	17.74	24.02	16.62
Avg. Max Bed Temperature [K]	135.59	104.53	118.60	135.33
Avg. Final Bed Temperature [K]	134.34	103.74	117.70	133.46
LN2 Flow Rate [g s^{-1}]	-	-	-	-
Avg. LN2 Temperature [K]	-	-	-	-
Dewar Temperature [K]	108.50	106.50	122.00	134.50
Effective Heat Generation [J]	181.58	266.75	434.51	327.97
Mass of N2 in Vessel [g]	38.33	66.32	26.89	61.42
Mass N2 in AC Bed [g]	22.48	7.34	11.04	29.18

Experiment Name	AC NC N2 Exp.#5	AC NC N2 Exp.#6	AC NC N2 Exp.#7
Charging time to 50 bar [s]	30.25	32.50	35.00
Charging Pressure [bar]	53.95	51.31	51.90
Avg. Initial Bed Temperature [K]	124.18	106.52	114.23
Avg. Bed Temperature Rise [K]	18.53	24.63	20.71
Avg. Max Bed Temperature [K]	142.71	131.15	134.95
Avg. Final Bed Temperature [K]	142.45	129.35	133.77
LN2 Flow Rate [g s^{-1}]	-	-	-
Avg. LN2 Temperature [K]	-	-	-
Dewar Temperature [K]	152.50	133.50	137.50
Effective Heat Generation [J]	559.38	515.64	464.05
Mass of N2 in Vessel [g]	36.23	72.65	64.86
Mass N2 in AC Bed [g]	20.37	33.20	30.78

Liquid Cooled Nitrogen Adsorption on MOF-5

Experiment Name	MOF-5 LN2 N2 Exp.#1	MOF-5 LN2 N2 Exp.#2	MOF-5 LN2 N2 Exp.#3	MOF-5 LN2 N2 Exp.#4
Charging time to 50 bar [s]	133	84.75	39.25	38.75
Charging Pressure [bar]	52.47	53.26	53.67	54.20
Avg. Initial Bed Temperature [K]	113.12	80.97	151.79	108.12
Avg. Bed Temperature Rise [K]	20.21	14.35	53.62	26.15
Avg. Max Bed Temperature [K]	133.33	95.31	205.41	134.28
Avg. Final Bed Temperature [K]	131.96	94.06	175.92	130.09
LN2 Flow Rate [g s^{-1}]	1.84	1.86	1.08	2.11
Avg. LN2 Temperature [K]	93.09	92.24	96.10	95.18
Dewar Temperature [K]	108.50	99.00	149.00	150.50
Effective Heat Generation [J]	185.89	183.41	8.00	320.78
Mass of N2 in Vessel [g]	62.61	55.46	41.29	54.81
Mass N2 in MOF-5 Bed [g]	11.01	2.74	31.20	33.93

Experiment Name	MOF-5 LN2 N2 Exp.#5	MOF-5 LN2 N2 Exp.#6	MOF-5 LN2 N2 Exp.#7	MOF-5 LN2 N2 Exp.#8
Charging time to 50 bar [s]	31.25	37.25	45.5	46.5
Charging Pressure [bar]	54.92	54.36	54.87	53.67
Avg. Initial Bed Temperature [K]	140.93	99.30	96.47	90.13
Avg. Bed Temperature Rise [K]	42.27	20.39	21.37	24.72
Avg. Max Bed Temperature [K]	183.20	119.69	117.84	114.86
Avg. Final Bed Temperature [K]	161.60	117.39	115.34	112.18
LN2 Flow Rate [g s^{-1}]	1.86	1.94	2.65	2.58
Avg. LN2 Temperature [K]	93.59	93.72	94.40	95.25
Dewar Temperature [K]	149.50	146.50	142.00	135.50
Effective Heat Generation [J]	71.84	260.10	274.79	324.24
Mass of N2 in Vessel [g]	53.47	77.93	81.26	81.57
Mass N2 in MOF-5 Bed [g]	40.30	36.23	33.41	33.97

Non-cooled Nitrogen Adsorption on MOF-5

Experiment Name	MOF-5 NC N2 Exp.#1	MOF-5 NC N2 Exp.#2	MOF-5 NC N2 Exp.#3	MOF-5 NC N2 Exp.#4
Charging time to 50 bar [s]	51.75	22.00	46.25	42.25
Charging Pressure [bar]	53.79	54.68	54.98	54.55
Avg. Initial Bed Temperature [K]	80.03	102.50	96.89	94.91
Avg. Bed Temperature Rise [K]	4.33	34.30	30.80	29.53
Avg. Max Bed Temperature [K]	84.36	136.80	127.69	124.44
Avg. Final Bed Temperature [K]	84.03	133.43	126.31	122.42
LN2 Flow Rate [g s^{-1}]	-	-	-	-
Avg. LN2 Temperature [K]	-	-	-	-
Dewar Temperature [K]	97.50	146.00	129.50	132.00
Effective Heat Generation [J]	71.04	437.68	505.85	478.58
Mass of N2 in Vessel [g]	61.25	52.40	80.09	78.81
Mass N2 in MOF-5 Bed [g]	6.08	26.87	31.44	31.58

Liquid Cooled Hydrogen Adsorption on Activated Carbon

Experiment Name	AC LN2 H2 Exp.#1	AC LN2 H2 Exp.#2	AC LN2 H2 Exp.#3	AC LN2 H2 Exp.#4
Charging time to 50 bar [s]	128.50	34.75	107.75	40.00
Charging Pressure [bar]	50.34	51.11	51.17	51.44
Average Initial Bed Temperature [K]	115.85	111.81	112.98	106.13
Average Bed Temperature Rise [K]	8.14	7.97	5.61	8.79
Average Max Bed Temperature [K]	123.99	119.78	118.59	114.91
Average Final Bed Temperature [K]	118.43	112.86	111.24	108.00
LN2 Flow Rate [g s^{-1}]	1.89	1.96	1.89	2.01
Average LN2 Temperature [K]	94.45	94.17	95.31	93.99
Dewar Temperature [K]	136.00	134.50	123.50	127.50
Effective Heat Generation [J]	59.50	22.70	-37.22	37.36
Mass of H2 in Vessel [g]	1.48	1.31	1.65	1.69
Mass H2 in AC Bed [g]	0.61	0.39	0.74	0.73
Cryo-Compressed H2 storage system [g]	1.53	1.63	1.60	1.70
Percent change due to adsorbent [%]	-3.55	-24.54	2.79	-0.41

Experiment Name	AC LN2 H2 Exp.#5	AC LN2 H2 Exp.#6	AC LN2 H2 Exp.#7
Charging time to 50 bar [s]	40.50	40.00	37.25
Charging Pressure [bar]	51.60	52.02	52.21
Average Initial Bed Temperature [K]	106.38	108.16	109.45
Average Bed Temperature Rise [K]	9.19	9.51	9.33
Average Max Bed Temperature [K]	115.57	117.66	118.78
Average Final Bed Temperature [K]	107.91	109.97	113.18
LN2 Flow Rate [g s^{-1}]	3.11	2.93	0.77
Average LN2 Temperature [K]	93.18	94.20	97.94
Dewar Temperature [K]	129.50	130.00	130.00
Effective Heat Generation [J]	30.50	37.22	79.36
Mass of H2 in Vessel [g]	1.67	1.69	1.69
Mass H2 in AC Bed [g]	0.71	0.72	0.73
Cryo-Compressed H2 storage system [g]	1.71	1.73	1.70
Percent change due to adsorbent [%]	-2.12	-2.10	-0.44

Non-cooled Hydrogen Adsorption on Activated Carbon

Experiment Name	AC NC H2 Exp.#1	AC NC H2 Exp.#2	AC NC H2 Exp.#3
Charging time to 50 bar [s]	46.25	147.00	35.75
Charging Pressure [bar]	51.22	50.99	51.66
Avg. Initial Bed Temperature [K]	116.59	112.42	110.33
Avg. Bed Temperature Rise [K]	8.48	8.45	11.09
Avg. Max Bed Temperature [K]	125.07	120.87	121.42
Avg. Final Bed Temperature [K]	123.10	119.38	120.05
LN2 Flow Rate [g s^{-1}]	-	-	-
Avg. LN2 Temperature [K]	-	-	-
Dewar Temperature [K]	125.00	124.00	127.50
Effective Heat Generation [J]	155.97	157.98	218.63
Mass of H2 in Vessel [g]	0.89	1.54	1.56
Mass H2 in AC Bed [g]	0.05	0.69	0.70
Cryo-Compressed H2 storage system [g]	1.49	1.49	1.53
Percent change due to adsorbent [%]	-67.88	2.81	2.16

Experiment Name	AC NC H2 Exp.#4	AC NC H2 Exp.#5
Charging time to 50 bar [s]	33.25	34.25
Charging Pressure [bar]	51.92	52.12
Avg. Initial Bed Temperature [K]	106.68	108.86
Avg. Bed Temperature Rise [K]	12.56	12.14
Avg. Max Bed Temperature [K]	119.23	121.01
Avg. Final Bed Temperature [K]	119.04	120.13
LN2 Flow Rate [g s^{-1}]	-	-
Avg. LN2 Temperature [K]	-	-
Dewar Temperature [K]	127.00	128.50
Effective Heat Generation [J]	268.99	250.79
Mass of H2 in Vessel [g]	1.57	1.56
Mass H2 in AC Bed [g]	0.69	0.67
Cryo-Compressed H2 storage system [g]	1.56	1.57
Percent change due to adsorbent [%]	0.78	-0.53

Liquid Cooled Hydrogen Adsorption on MOF-5

Experiment Name	MOF-5 LN2 H2 Exp.#1	MOF-5 LN2 H2 Exp.#2	MOF-5 LN2 H2 Exp.#3	MOF-5 LN2 H2 Exp.#4
Charging time to 50 bar [s]	63.50	25.75	25.75	24.00
Charging Pressure [bar]	52.99	53.23	53.61	53.87
Avg. Initial Bed Temperature [K]	134.46	125.94	119.98	115.15
Avg. Bed Temperature Rise [K]	33.42	41.83	43.54	45.44
Avg. Max Bed Temperature [K]	167.88	167.77	163.52	160.58
Avg. Final Bed Temperature [K]	137.30	131.23	126.99	122.88
LN2 Flow Rate [g s^{-1}]	2.61	2.58	2.41	3.21
Avg. LN2 Temperature [K]	97.15	96.50	96.32	94.18
Dewar Temperature [K]	173.00	163.50	150.50	144.00
Effective Heat Generation [J]	58.65	104.58	134.27	143.68
Mass of H2 in Vessel [g]	1.73	1.78	1.90	1.73
Mass H2 in MOF-5 Bed [g]	1.03	1.00	1.06	0.85
Cryo-Compressed H2 storage system [g]	1.24	1.38	1.48	1.55
Percent change due to adsorbent [%]	28.40	22.72	21.88	10.53

Experiment Name	MOF-5 LN2 H2 Exp.#5	MOF-5 LN2 H2 Exp.#6	MOF-5 LN2 H2 Exp.#7	MOF-5 LN2 H2 Exp.#8
Charging time to 50 bar [s]	23.75	27.00	23.25	23.25
Charging Pressure [bar]	54.17	54.60	55.11	54.77
Avg. Initial Bed Temperature [K]	112.36	111.10	133.17	130.60
Avg. Bed Temperature Rise [K]	45.32	45.13	37.80	36.21
Avg. Max Bed Temperature [K]	157.68	156.22	170.98	166.81
Avg. Final Bed Temperature [K]	120.64	118.71	123.73	123.28
LN2 Flow Rate [g s^{-1}]	2.80	2.81	2.13	2.73
Avg. LN2 Temperature [K]	95.44	94.17	100.57	97.29
Dewar Temperature [K]	140.00	134.50	143.00	143.50
Effective Heat Generation [J]	151.22	137.65	-186.61	-140.63
Mass of H2 in Vessel [g]	2.05	2.17	1.96	1.96
Mass H2 in MOF-5 Bed [g]	1.15	1.24	1.09	1.09
Cryo-Compressed H2 storage system [g]	1.60	1.66	1.53	1.54
Percent change due to adsorbent [%]	22.11	23.72	21.51	21.56

Liquid Cooled Hydrogen Adsorption on MOF-5 (Continued)

Experiment Name	MOF-5 LN2 H2 Exp.#9	MOF-5 LN2 H2 Exp.#10	MOF-5 LN2 H2 Exp.#11
Charging time to 50 bar [s]	23.75	26.75	35.00
Charging Pressure [bar]	54.03	52.28	51.74
Avg. Initial Bed Temperature [K]	133.63	136.03	131.65
Avg. Bed Temperature Rise [K]	35.40	33.67	38.22
Avg. Max Bed Temperature [K]	169.03	169.70	169.88
Avg. Final Bed Temperature [K]	124.14	124.49	123.37
LN2 Flow Rate [g s^{-1}]	2.46	2.32	0.29
Avg. LN2 Temperature [K]	99.98	98.50	125.80
Dewar Temperature [K]	144.00	143.50	138.00
Effective Heat Generation [J]	-187.88	-230.56	-162.63
Mass of H2 in Vessel [g]	1.93	1.92	1.88
Mass H2 in MOF-5 Bed [g]	1.08	1.09	1.07
Cryo-Compressed H2 storage system [g]	1.51	1.46	1.43
Percent change due to adsorbent [%]	21.85	24.01	23.61

Non-cooled Hydrogen Adsorption on MOF-5

Experiment Name	MOF-5 NC H2 Exp.#1	MOF-5 NC H2 Exp.#2	MOF-5 NC H2 Exp.#3	MOF-5 NC H2 Exp.#4
Charging time to 50 bar [s]	23.75	22.25	21.75	24.50
Charging Pressure [bar]	53.41	53.77	54.04	54.42
Avg. Initial Bed Temperature [K]	126.37	119.36	113.96	112.32
Avg. Bed Temperature Rise [K]	47.25	48.97	48.62	48.57
Avg. Max Bed Temperature [K]	173.62	168.34	162.59	160.90
Avg. Final Bed Temperature [K]	148.27	141.24	136.61	134.72
LN2 Flow Rate [g s^{-1}]	-	-	-	-
Avg. LN2 Temperature [K]	-	-	-	-
Dewar Temperature [K]	154.50	145.00	139.00	135.50
Effective Heat Generation [J]	455.86	436.95	438.32	428.81
Mass of H2 in Vessel [g]	1.61	1.81	1.80	1.95
Mass H2 in MOF-5 Bed [g]	0.86	1.01	0.98	1.09
Cryo-Compressed H2 storage system [g]	1.34	1.43	1.45	1.52
Percent change due to adsorbent [%]	17.17	21.21	19.21	22.15

Experiment Name	MOF-5 NC H2 Exp.#5	MOF-5 NC H2 Exp.#6	MOF-5 NC H2 Exp.#7	MOF-5 NC H2 Exp.#8
Charging time to 50 bar [s]	24.25	22.75	25.75	24.25
Charging Pressure [bar]	54.75	55.03	54.66	53.90
Avg. Initial Bed Temperature [K]	110.88	129.33	130.72	131.75
Avg. Bed Temperature Rise [K]	48.22	44.29	42.44	42.04
Avg. Max Bed Temperature [K]	159.09	173.62	173.17	173.79
Avg. Final Bed Temperature [K]	132.09	143.97	143.63	143.21
LN2 Flow Rate [g s^{-1}]	-	-	-	-
Avg. LN2 Temperature [K]	-	-	-	-
Dewar Temperature [K]	130.00	140.50	140.50	140.00
Effective Heat Generation [J]	400.64	303.63	268.51	238.84
Mass of H2 in Vessel [g]	1.97	1.81	1.81	1.75
Mass H2 in MOF-5 Bed [g]	1.09	1.03	1.02	0.97
Cryo-Compressed H2 storage system [g]	1.56	1.38	1.39	1.38
Percent change due to adsorbent [%]	20.91	23.68	22.92	20.94

Non-cooled Hydrogen Adsorption on MOF-5 (Continued)

Experiment Name	MOF-5 NC H2 Exp.#9	MOF-5 NC H2 Exp.#10	MOF-5 NC H2 Exp.#11	MOF-5 NC H2 Exp.#12
Charging time to 50 bar [s]	26.75	34.25	22.75	21.00
Charging Pressure [bar]	52.16	52.00	52.32	52.55
Avg. Initial Bed Temperature [K]	134.57	128.84	124.77	136.06
Avg. Bed Temperature Rise [K]	40.27	40.64	45.52	43.54
Avg. Max Bed Temperature [K]	174.85	169.47	170.29	179.60
Avg. Final Bed Temperature [K]	143.71	140.93	136.27	147.58
LN2 Flow Rate [g s^{-1}]	-	-	-	-
Avg. LN2 Temperature [K]	-	-	-	-
Dewar Temperature [K]	140.50	137.00	133.50	146.00
Effective Heat Generation [J]	192.30	248.26	230.00	246.16
Mass of H2 in Vessel [g]	1.68	0.78	1.79	1.63
Mass H2 in MOF-5 Bed [g]	0.92	0.02	0.98	0.91
Cryo-Compressed H2 storage system [g]	1.33	1.35	1.43	1.29
Percent change due to adsorbent [%]	20.52	-73.11	20.12	21.18

Experiment Name	MOF-5 NC H2 Exp.#13	MOF-5 NC H2 Exp.#14	MOF-5 NC H2 Exp.#15	MOF-5 NC H2 Exp.#16
Charging time to 50 bar [s]	22.75	21.75	21.75	20.75
Charging Pressure [bar]	52.75	52.89	53.05	53.16
Avg. Initial Bed Temperature [K]	127.11	129.49	120.53	128.73
Avg. Bed Temperature Rise [K]	45.54	44.14	47.01	44.67
Avg. Max Bed Temperature [K]	172.65	173.63	167.54	173.39
Avg. Final Bed Temperature [K]	140.03	141.19	133.94	141.31
LN2 Flow Rate [g s^{-1}]	-	-	-	-
Avg. LN2 Temperature [K]	-	-	-	-
Dewar Temperature [K]	137.00	132.50	130.00	137.50
Effective Heat Generation [J]	263.19	240.88	262.81	258.60
Mass of H2 in Vessel [g]	1.73	1.74	1.79	1.74
Mass H2 in MOF-5 Bed [g]	0.97	0.98	0.98	0.97
Cryo-Compressed H2 storage system [g]	1.35	1.34	1.43	1.36
Percent change due to adsorbent [%]	21.75	22.81	20.06	21.86

Appendix B: Mathematical Model Derivation

The mass, momentum, and energy balances derived below are derived using the following general balance

$$Accumulation = IN - OUT + Generation - Consumption$$

Components of the overall balance are derived in sections and summed together using the equation above.

Control volume is defined as

$$dV = dxdydz\left[m^3\right] \tag{B.1}$$

Conservation of Mass

The mass of the solid adsorbent in the packed bed is

$$\frac{\partial\left(m_{SA}\right)}{\partial t} = \frac{\partial\left(\frac{m_{SA}}{V_{SA}}\right)}{\partial t} = \left(1-\varepsilon\right)V\frac{\partial\left(\frac{m_{SA}}{V_{SA}}\right)}{\partial t} = \left(1-\varepsilon\right)V\frac{\partial\rho_{SA}}{\partial t} = 0\left[\frac{kg_g}{s}\right] \tag{B.2}$$

on a per-volume basis

$$\left(1-\varepsilon\right)\frac{\partial\rho_{SA}}{\partial t} = 0\left[\frac{kg_g}{m^3 s}\right] \tag{B.3}$$

If the density of the packed bed is considered to be

$$\rho_b = \frac{m_{SA}+m_g}{V} = \frac{\left(1-\varepsilon\right)V\rho_{SA}+\varepsilon V\rho_g}{V} = \left(1-\varepsilon\right)\rho_{SA}+\varepsilon\rho_g\left[\frac{kg_g}{m^3}\right] \tag{B.4}$$

and assuming that the contribution of the mass of the gas phase is negligible compared to the solid adsorbent mass

$$\rho_b = (1-\varepsilon)\rho_{SA}\left[\frac{kg_g}{m^3}\right] \tag{B.5}$$

The change in density of the adsorbed gas phase is

$$\frac{\partial \rho_a}{\partial t} = \gamma_m \left[\frac{kg_g}{m^3 s}\right] \tag{B.6}$$

The mass source/sink due to the adsorption of gas on the adsorbent surface is expressed as

$$\gamma_m = M_g \rho_b \frac{\partial n_a}{\partial t}\left[\frac{kg_g}{m^3 s}\right] \tag{B.7}$$

The change in hydrogen mass in the packed bed of adsorbing material with time is

$$\frac{\partial m_g}{\partial t} = (\varepsilon dV)\frac{\partial\left(\frac{m}{V}\right)_g}{\partial t} = (\varepsilon dV)\frac{\partial \rho_g}{\partial t}\left[\frac{kg_g}{s}\right] \tag{B.8}$$

The convective transfer of hydrogen through the control volume is

$$\begin{aligned}
&(\varepsilon u_x \rho_g)\,dydz - \left(\varepsilon u_x \rho_g + \frac{\partial(\varepsilon u_x \rho_g)}{\partial x}dx\right)dydz \\
&+(\varepsilon u_y \rho_g)\,dxdz - \left(\varepsilon u_y \rho_g + \frac{\partial(\varepsilon u_y \rho_g)}{\partial y}dy\right)dxdz \\
&+(\varepsilon u_z \rho_g)\,dxdy - \left(\varepsilon u_z \rho_g + \frac{\partial(\varepsilon u_z \rho_g)}{\partial z}dz\right)dxdy\left[\frac{kg_g}{s}\right]
\end{aligned} \tag{B.9}$$

The hydrogen adsorption source/sink is defined as

$$\gamma_m dV = \gamma_m dV \left[\frac{kg_g}{mol_g}\right]\left[\frac{kg_{SA}}{m^3}\right]\left[\frac{mol_g}{kg_{SA}s}\right]\left[m^3\right] \therefore \left[\frac{kg_g}{s}\right] \tag{B.10}$$

Summing all together, using (B.1) produces

$$\begin{aligned}(\varepsilon dV)\frac{\partial \rho_g}{\partial t} &= -\frac{\partial\left(\varepsilon u_x \rho_g\right)}{\partial x}dxdydz - \frac{\partial\left(\varepsilon u_y \rho_g\right)}{\partial y}dxdydz \\ &- \frac{\partial\left(\varepsilon u_z \rho_g\right)}{\partial z}dxdzdy - \gamma_m V\left[\frac{kg_g}{s}\right]\end{aligned} \tag{B.11}$$

and dividing by the control volume, $dV = dxdydz$

$$\varepsilon\frac{\partial \rho_g}{\partial t} = -\frac{\partial\left(\varepsilon u_x \rho_g\right)}{\partial x} - \frac{\partial\left(\varepsilon u_y \rho_g\right)}{\partial y} - \frac{\partial\left(\varepsilon u_z \rho_g\right)}{\partial z} - \gamma_m\left[\frac{kg_g}{m^3 s}\right] \tag{B.12}$$

By defining the superficial velocity in the porous material as, $u_{i,A} = \varepsilon u_i$, the final form of the material balance for the adsorbent material is

$$\varepsilon\frac{\partial \rho_g}{\partial t} + \frac{\partial\left(u_{x,A}\rho_g\right)}{\partial x} + \frac{\partial\left(u_{y,A}\rho_g\right)}{\partial y} + \frac{\partial\left(u_{z,A}\rho_g\right)}{\partial z} = -\gamma_m\left[\frac{kg_g}{m^3 s}\right] \tag{B.13}$$

and can be represented in the vector notation as

$$\varepsilon\frac{\partial \rho_g}{\partial t} + \nabla\cdot\left(\overrightarrow{u_A}\rho_g\right) = -\gamma_m\left[\frac{kg_g}{m^3 s}\right] \tag{B.14}$$

Now, the mass balance of hydrogen in the free flow area (non-porous region)

$$\frac{\partial m_g}{\partial t} = dV\frac{\partial\left(\frac{m}{V}\right)_g}{\partial t} = dV\frac{\partial \rho_g}{\partial t}\left[\frac{kg_g}{s}\right] \tag{B.15}$$

Convective transfer of hydrogen through the control volume is

$$\left(u_x\rho_g\right)dydz-\left(u_x\rho_g+\frac{\partial\left(u_x\rho_g\right)}{\partial x}dx\right)dydz+\left(u_y\rho_g\right)dxdz-$$
$$\left(u_y\rho_g+\frac{\partial\left(u_y\rho_g\right)}{\partial y}dy\right)dxdz+\left(u_z\rho_g\right)dxdy-\left(u_z\rho_g+\frac{\partial\left(u_z\rho_g\right)}{\partial z}dz\right)dxdy\left[\frac{kg_g}{s}\right] \quad \text{(B.16)}$$

and summing all together

$$dV\frac{\partial\rho_g}{\partial t}=-\frac{\partial\left(u_x\rho_g\right)}{\partial x}dxdydz-\frac{\partial\left(u_y\rho_g\right)}{\partial y}dxdydz-\frac{\partial\left(u_z\rho_g\right)}{\partial z}dxdzdy\left[\frac{kg_g}{s}\right] \quad \text{(B.17)}$$

dividing by the control volume, $dV=dxdydz$, produces

$$\frac{\partial\rho_g}{\partial t}+\frac{\partial\left(u_x\rho_g\right)}{\partial x}+\frac{\partial\left(u_y\rho_g\right)}{\partial y}+\frac{\partial\left(u_z\rho_g\right)}{\partial z}=0\left[\frac{kg_g}{m^3s}\right] \quad \text{(B.18)}$$

It should be pointed out that the mass balance in the free flow region may be obtained from the porous media balance by setting the porosity of the system, ε, to unity and the mass sink to zero.

Conservation of Momentum

X – Momentum

The change in x-momentum with time is

$$\frac{\partial(m_gu_i)}{\partial t}=\frac{\partial\left(\varepsilon dV\left(\frac{m}{V}\right)_g u_x\right)}{\partial t}=dV\frac{\partial\left(\varepsilon\rho_g u_x\right)}{\partial t}\left[m^3_{bed}\left(\frac{kg_g}{m_g^2s^2}\right)\right] \quad \text{(B.19)}$$

x-momentum in to the control volume

$$\varepsilon\phi_{xx}dydz + \varepsilon\phi_{yx}dxdz + \varepsilon\phi_{zx}dxdy\left[m_{bed}^2\left(\frac{kg_g}{m_g^2 s^2}\right)\right] \tag{B.20}$$

x-Momentum out of the control volume

$$\left(\varepsilon\phi_{xx} + \frac{\partial(\varepsilon\phi_{xx})}{\partial x}dx\right)dydz + \left(\varepsilon\phi_{yx} + \frac{\partial(\varepsilon\phi_{yx})}{\partial y}dy\right)dxdz$$
$$+\left(\varepsilon\phi_{zx} + \frac{\partial(\varepsilon\phi_{zx})}{\partial z}dz\right)dxdy\left[m_{bed}^3\left(\frac{kg_g}{m_g^2 s^2}\right)\right] \tag{B.21}$$

summing the previous equations together, yields

$$-\frac{\partial(\varepsilon\phi_{xx})}{\partial x}dxdydz - \frac{\partial(\varepsilon\phi_{yx})}{\partial y}dxdydz - \frac{\partial(\varepsilon\phi_{zx})}{\partial z}dxdydz\left[m_{bed}^3\left(\frac{kg_g}{m_g^2 s^2}\right)\right] \tag{B.22}$$

The combined momentum flux ϕ_{ij} is [86]

$$\phi_{ij} = p + \tau_{ij} + \rho_g u_i u_j \qquad i = j$$
$$\phi_{ij} = \tau_{ij} + \rho_g u_i u_j \qquad i \neq j \tag{B.23}$$

Substituting (B.23) into (B.22) yields

$$-\left(\frac{\partial(\varepsilon p)}{\partial x} + \frac{\partial(\varepsilon\tau_{xx})}{\partial x} + \frac{\partial(\varepsilon\rho_g u_x u_x)}{\partial x}\right)dxdydz$$
$$-\left(\frac{\partial(\varepsilon\tau_{yx})}{\partial y} + \frac{\partial(\varepsilon\rho_g u_x u_y)}{\partial y}\right)dxdydz$$
$$-\left(\frac{\partial(\varepsilon\tau_{zx})}{\partial z} + \frac{\partial(\varepsilon\rho_g u_x u_z)}{\partial z}\right)dxdydz\left[m_{bed}^3\left(\frac{kg_g}{m_g^2 s^2}\right)\right] \tag{B.24}$$

.

Combining the above with the change in x momentum with time

$$dV\frac{\partial\left(\varepsilon\rho_g u_x\right)}{\partial t}=-\left(\frac{\partial(\varepsilon p)}{\partial x}+\frac{\partial(\varepsilon\tau_{xx})}{\partial x}+\frac{\partial(\varepsilon\rho_g u_x u_x)}{\partial x}\right)dxdydz$$
$$-\left(\frac{\partial(\varepsilon\tau_{yx})}{\partial y}+\frac{\partial(\varepsilon\rho_g u_x u_y)}{\partial y}\right)dxdydz$$
$$-\left(\frac{\partial(\varepsilon\tau_{zx})}{\partial z}+\frac{\partial(\varepsilon\rho_g u_x u_z)}{\partial z}\right)dxdydz\left[m_{bed}^3\left(\frac{kg_g}{m_g^2 s^2}\right)\right] \tag{B.25}$$

and diving by the control volume and some rearranging

$$\frac{\partial\left(\varepsilon\rho_g u_x\right)}{\partial t}+\frac{\partial(\varepsilon\rho_g u_x u_x)}{\partial x}+\frac{\partial(\varepsilon\rho_g u_x u_y)}{\partial y}+\frac{\partial(\varepsilon\rho_g u_x u_z)}{\partial z}=-\frac{\partial(\varepsilon p)}{\partial x}$$
$$-\frac{\partial(\varepsilon\tau_{xx})}{\partial x}-\frac{\partial(\varepsilon\tau_{yx})}{\partial y}-\frac{\partial(\varepsilon\tau_{zx})}{\partial z}\left[\frac{kg_g}{m_g^2 s^2}\right] \tag{B.26}$$

Taking the partial differentials of the right hand side with respect to the velocity terms gives

$$\left[\rho_g\frac{\partial\left(\varepsilon u_x\right)}{\partial t}+u_x\frac{\partial(\varepsilon\rho_g u_x)}{\partial x}+u_y\frac{\partial(\varepsilon\rho_g u_x)}{\partial y}+u_z\frac{\partial(\varepsilon\rho_g u_x)}{\partial z}\right]$$
$$+\left[u_x\frac{\partial\left(\varepsilon\rho_g\right)}{\partial t}+u_x\frac{\partial(\varepsilon\rho_g u_x)}{\partial x}+u_x\frac{\partial(\varepsilon\rho_g u_y)}{\partial y}+u_x\frac{\partial(\varepsilon\rho_g u_z)}{\partial z}\right]=$$
$$-\frac{\partial(\varepsilon p)}{\partial x}-\frac{\partial(\varepsilon\tau_{xx})}{\partial x}-\frac{\partial(\varepsilon\tau_{yx})}{\partial y}-\frac{\partial(\varepsilon\tau_{zx})}{\partial z}\left[\frac{kg_g}{m_g^2 s^2}\right] \tag{B.27}$$

The second term on the left hand side is equal to the right hand side of the material balance multiplied by the *x* component velocity, therefore, giving

$$\left[\rho_g\frac{\partial\left(\varepsilon u_x\right)}{\partial t}+u_x\frac{\partial(\varepsilon\rho_g u_x)}{\partial x}+u_y\frac{\partial(\varepsilon\rho_g u_x)}{\partial y}+u_z\frac{\partial(\varepsilon\rho_g u_x)}{\partial z}\right]$$
$$-u_x\left(M_{Wg}\rho_{SA}\frac{\partial n_a}{\partial t}\right)=-\frac{\partial(\varepsilon p)}{\partial x}-\frac{\partial(\varepsilon\tau_{xx})}{\partial x}-\frac{\partial(\varepsilon\tau_{yx})}{\partial y}-\frac{\partial(\varepsilon\tau_{zx})}{\partial z}\left[\frac{kg_g}{m_g^2 s^2}\right] \tag{B.28}$$

Next, the viscous stresses, τ_{ij}, can be expanded according to the following [86]

$$\tau_{ij} = -2\mu\frac{\partial u_j}{\partial j} + \frac{2}{3}(\mu-\eta)\left[\frac{\partial u_x}{\partial x} + \frac{\partial u_y}{\partial y} + \frac{\partial u_z}{\partial z}\right] \qquad i = j$$
$$\tau_{ij} = \tau_{ji} = -\mu\left[\frac{\partial u_i}{\partial j} + \frac{\partial u_j}{\partial i}\right] \qquad i \neq j \tag{B.29}$$

The contribution of the dilatational viscosity term, η, can be neglected for the case under investigation [70], thus transforming the x-momentum equation into

$$\left[\rho_g\frac{\partial(\varepsilon u_x)}{\partial t} + u_x\frac{\partial(\varepsilon\rho_g u_x)}{\partial x} + u_y\frac{\partial(\varepsilon\rho_g u_x)}{\partial y} + u_z\frac{\partial(\varepsilon\rho_g u_x)}{\partial z}\right] - u_x\gamma_m =$$
$$-\frac{\partial(\varepsilon p)}{\partial x} - \frac{\partial}{\partial x}\left[-2\varepsilon\mu\frac{\partial u_x}{\partial x} + \frac{2\varepsilon\mu}{3}\left[\frac{\partial u_x}{\partial x} + \frac{\partial u_y}{\partial y} + \frac{\partial u_z}{\partial z}\right]\right]$$
$$-\frac{\partial}{\partial y}\left[-\varepsilon\mu\left[\frac{\partial u_x}{\partial y} + \frac{\partial u_y}{\partial x}\right]\right] - \frac{\partial}{\partial z}\left[-\varepsilon\mu\left[\frac{\partial u_x}{\partial z} + \frac{\partial u_z}{\partial x}\right]\right]\left[\frac{kg_g}{m_g^2 s^2}\right] \tag{B.30}$$

This can be separated to yield

$$\left[\rho_g\frac{\partial(\varepsilon u_x)}{\partial t} + u_x\frac{\partial(\varepsilon\rho_g u_x)}{\partial x} + u_y\frac{\partial(\varepsilon\rho_g u_x)}{\partial y} + u_z\frac{\partial(\varepsilon\rho_g u_x)}{\partial z}\right] - u_x\gamma_m =$$
$$-\frac{\partial(\varepsilon p)}{\partial x} + \frac{\partial}{\partial x}\left[\frac{4\varepsilon\mu}{3}\frac{\partial u_x}{\partial x}\right] - \frac{\partial}{\partial x}\left[\frac{2\varepsilon\mu}{3}\frac{\partial u_y}{\partial y}\right] - \frac{\partial}{\partial x}\left[\frac{2\varepsilon\mu}{3}\frac{\partial u_z}{\partial z}\right]$$
$$+\frac{\partial}{\partial y}\left[\varepsilon\mu\frac{\partial u_x}{\partial y}\right] + \frac{\partial}{\partial y}\left[\varepsilon\mu\frac{\partial u_y}{\partial x}\right] + \frac{\partial}{\partial z}\left[\varepsilon\mu\frac{\partial u_x}{\partial z}\right] + \frac{\partial}{\partial z}\left[\varepsilon\mu\frac{\partial u_z}{\partial x}\right]\left[\frac{kg_g}{m_g^2 s^2}\right] \tag{B.31}$$

The x-momentum sink in a packed bed may be represented as [70]

$$\varepsilon^2\frac{\mu}{\kappa}u_x\left[\frac{kg_g}{m_g^2 s^2}\right] \tag{B.32}$$

where the permeability of the material is given by Blake-Kozeny equation [86]

$$\frac{1}{\kappa} = 150\frac{(1-\varepsilon)^2}{D_p^2\varepsilon^3}\left[\frac{1}{m^2}\right] \tag{B.33}$$

The gravitational force acting on the gas inside the adsorbent bed, or open space, will be neglected for all momentums in this investigation, thus yielding the x-momentum balance

$$\begin{aligned}
&\left[\rho_g\frac{\partial(\varepsilon u_x)}{\partial t} + u_x\frac{\partial(\varepsilon\rho_g u_x)}{\partial x} + u_y\frac{\partial(\varepsilon\rho_g u_x)}{\partial y} + u_z\frac{\partial(\varepsilon\rho_g u_x)}{\partial z}\right] - u_x\gamma_m = \\
&-\frac{\partial(\varepsilon p)}{\partial x} + \frac{\partial}{\partial x}\left[\frac{4\varepsilon\mu}{3}\frac{\partial u_x}{\partial x}\right] - \frac{\partial}{\partial x}\left[\frac{2\varepsilon\mu}{3}\frac{\partial u_y}{\partial y}\right] - \frac{\partial}{\partial x}\left[\frac{2\varepsilon\mu}{3}\frac{\partial u_z}{\partial z}\right] \\
&+\frac{\partial}{\partial y}\left[\varepsilon\mu\frac{\partial u_x}{\partial y}\right] + \frac{\partial}{\partial y}\left[\varepsilon\mu\frac{\partial u_y}{\partial x}\right] + \frac{\partial}{\partial z}\left[\varepsilon\mu\frac{\partial u_x}{\partial z}\right] + \frac{\partial}{\partial z}\left[\varepsilon\mu\frac{\partial u_z}{\partial x}\right] - \varepsilon^2\frac{\mu}{\kappa}u_x\left[\frac{kg_g}{m_g^2 s^2}\right]
\end{aligned} \tag{B.34}$$

Recalling that the superficial velocity in the adsorbent bed is $u_{i,A} = \varepsilon u_i$ the x-momentum balance takes on the form

$$\begin{aligned}
&\left[\frac{\rho_g}{\varepsilon}\frac{\partial(u_{x,A})}{\partial t} + \frac{u_{x,A}}{\varepsilon^2}\frac{\partial(\rho_g u_{x,A})}{\partial x} + \frac{u_{y,A}}{\varepsilon^2}\frac{\partial(\rho_g u_{x,A})}{\partial y} + \frac{u_{z,A}}{\varepsilon^2}\frac{\partial(\rho_g u_{x,A})}{\partial z}\right] \\
&+\left(\frac{\mu}{\kappa}\right)u_{x,A} - \frac{1}{\varepsilon^2}\gamma_m u_{x,A} = -\frac{\partial(p)}{\partial x} \\
&+\left(\frac{1}{\varepsilon}\right)\left[\frac{\partial}{\partial x}\left[\frac{4\mu}{3}\frac{\partial u_{x,A}}{\partial x}\right] + \frac{\partial}{\partial y}\left[\mu\frac{\partial u_{x,A}}{\partial y}\right] + \frac{\partial}{\partial z}\left[\mu\frac{\partial u_{x,A}}{\partial z}\right]\right] \\
&+\left[\frac{\partial}{\partial y}\left[\mu\frac{\partial u_{y,A}}{\partial x}\right] - \frac{\partial}{\partial x}\left[\frac{2\mu}{3}\frac{\partial u_{y,A}}{\partial y}\right]\right] \\
&+\left(\frac{1}{\varepsilon}\right)\left[\frac{\partial}{\partial z}\left[\mu\frac{\partial u_{z,A}}{\partial x}\right] - \frac{\partial}{\partial x}\left[\frac{2\mu}{3}\frac{\partial u_{z,A}}{\partial z}\right]\right]\left[\frac{kg_g}{m_g^2 s^2}\right]
\end{aligned} \tag{B.35}$$

The same procedure as above is followed to develop the y-momentum and z-momentum equations, respectively,

$$\left[\frac{\rho_g}{\varepsilon}\frac{\partial\left(u_{y,A}\right)}{\partial t}+\frac{u_{x,A}}{\varepsilon^2}\frac{\partial(\rho_g u_{y,A})}{\partial x}+\frac{u_{y,A}}{\varepsilon^2}\frac{\partial(\rho_g u_{y,A})}{\partial y}+\frac{u_{z,A}}{\varepsilon^2}\frac{\partial(\rho_g u_{y,A})}{\partial z}\right]+\left(\frac{\mu}{\kappa}\right)u_{y,A}$$
$$-\frac{1}{\varepsilon^2}\gamma_m u_{y,A}=-\frac{\partial(p)}{\partial y}+\left(\frac{1}{\varepsilon}\right)\left[\frac{\partial}{\partial x}\left[\mu\frac{\partial u_{x,A}}{\partial y}\right]-\frac{\partial}{\partial y}\left[\frac{2\mu}{3}\frac{\partial u_{x,A}}{\partial x}\right]\right]$$
$$+\left(\frac{1}{\varepsilon}\right)\left[\frac{\partial}{\partial x}\left[\mu\frac{\partial u_{y,A}}{\partial x}\right]+\frac{\partial}{\partial y}\left[\frac{4\mu}{3}\frac{\partial u_{y,A}}{\partial y}\right]+\frac{\partial}{\partial z}\left[\mu\frac{\partial u_{y,A}}{\partial z}\right]\right]$$
$$+\left(\frac{1}{\varepsilon}\right)\left[\frac{\partial}{\partial z}\left[\mu\frac{\partial u_{z,A}}{\partial y}\right]-\frac{\partial}{\partial y}\left[\frac{2\mu}{3}\frac{\partial u_{z,A}}{\partial z}\right]\right] \tag{B.36}$$

$$\left[\frac{\rho_g}{\varepsilon}\frac{\partial\left(u_{z,A}\right)}{\partial t}+\frac{u_{x,A}}{\varepsilon^2}\frac{\partial(\rho_g u_{z,A})}{\partial x}+\frac{u_{y,A}}{\varepsilon^2}\frac{\partial(\rho_g u_{z,A})}{\partial y}+\frac{u_{z,A}}{\varepsilon^2}\frac{\partial(\rho_g u_{z,A})}{\partial z}\right]+\left(\frac{\mu}{\kappa}\right)u_{z,A}$$
$$-\frac{1}{\varepsilon^2}\gamma_m u_{z,A}=-\frac{\partial(p)}{\partial z}+\left(\frac{1}{\varepsilon}\right)\left[\frac{\partial}{\partial x}\left[\mu\frac{\partial u_{x,A}}{\partial z}\right]-\frac{\partial}{\partial z}\left[\frac{2\mu}{3}\frac{\partial u_{x,A}}{\partial x}\right]\right]$$
$$+\left(\frac{1}{\varepsilon}\right)\left[\frac{\partial}{\partial y}\left[\mu\frac{\partial u_{y,A}}{\partial z}\right]-\frac{\partial}{\partial z}\left[\frac{2\mu}{3}\frac{\partial u_{y,A}}{\partial y}\right]\right]$$
$$+\left(\frac{1}{\varepsilon}\right)\left[\frac{\partial}{\partial x}\left[\mu\frac{\partial u_{z,A}}{\partial x}\right]+\frac{\partial}{\partial y}\left[\mu\frac{\partial u_{z,A}}{\partial y}\right]+\frac{\partial}{\partial z}\left[\frac{4\mu}{3}\frac{\partial u_{z,A}}{\partial z}\right]\right] \tag{B.37}$$

This can be written in the vector form as

$$\frac{\rho_g}{\varepsilon}\frac{\partial\overrightarrow{u_A}}{\partial t}+\frac{\overrightarrow{u_A}}{\varepsilon^2}\nabla\left(\rho_g\overrightarrow{u_A}\right)+\left[\frac{\mu}{\kappa}-\frac{1}{\varepsilon^2}\gamma_m\right]\overrightarrow{u_A}=-\nabla p+$$
$$\nabla\cdot\left[\frac{\mu}{\varepsilon}\left(\nabla\overrightarrow{u_A}+\nabla\overrightarrow{u_A}^T\right)\right]-\nabla\cdot\left[\frac{2\mu}{3\varepsilon}\nabla\cdot\overrightarrow{u_A}I\right] \tag{B.38}$$

The momentum balance in the free flow area is derived the same as it is for the adsorbent bed, with the following modifications

1. Porosity of the open space, ε, is 1
2. There are no mass sinks present in the open space, therefore, the convective term derived from the mass balance is zero

3. The presence of additional sources or sinks from the adsorbent bed are not present and are zero
4. Gravitational effects acting on the gas phase are still neglected

The vector form of the momentum balance in free flow regions is

$$\rho_g \frac{\partial \vec{u}}{\partial t} + \vec{u}\nabla\left(\rho_g \vec{u}\right) = -\nabla p + \nabla \cdot \left[\mu\left(\nabla\vec{u} + \nabla\vec{u}^T\right)\right] - \nabla \cdot \left[\frac{2\mu}{3}\nabla \cdot \vec{u}I\right] \tag{B.39}$$

Conservation of Energy

Due to the number of components in the energy balance, terms will be derived individually and presented in the most concise form possible, it is assumed that each term is developed for the control volume and subsequently divided by the control volume in the end. It is also assumed that a local thermal equilibrium exists between the solid adsorbent, the gas phase, and adsorbed phase allowing a single temperature *T* is capable of describing the entire adsorbent volume.

The change in internal energy of the gas is

$$\frac{\partial m_g U_g}{\partial t} = \frac{\partial\left(\varepsilon dV\left(\frac{m_g}{V_g}\right)U_g\right)}{\partial t} = dV\frac{\partial\left(\varepsilon\rho_g U_g\right)}{\partial t}\left[\frac{J}{s}\right] \tag{B.40}$$

Dividing by the control volume

$$\frac{\partial\left(\varepsilon\rho_g U_g\right)}{\partial t}\left[\frac{J}{m^3 s}\right] \tag{B.41}$$

The energy entering the control volume by conduction through gas phase

$$\varepsilon q_{gx} dydz + \varepsilon q_{gy} dxdz + \varepsilon q_{gz} dxdy\left[\frac{J}{s}\right] \tag{B.42}$$

The conductive energy transport exiting the control volume is

$$\left(\varepsilon q_{gx}+\frac{\partial \varepsilon q_{gx}}{\partial x}dx\right)dydz+\left(\varepsilon q_{gy}+\frac{\partial \varepsilon q_{gy}}{\partial y}dy\right)dxdz+\left(\varepsilon q_{gz}+\frac{\partial \varepsilon q_{gz}}{\partial z}dz\right)dxdy\left[\frac{J}{s}\right] \tag{B.43}$$

Thus, the net conductive energy transport is

$$-\left[\frac{\partial \varepsilon q_x}{\partial x}+\frac{\partial \varepsilon q_y}{\partial y}+\frac{\partial \varepsilon q_z}{\partial z}\right]\left[\frac{J}{m^3 s}\right] \tag{B.44}$$

Substituting Fourier's Law of conduction

$$-\left[\frac{\partial}{\partial x}\left(-\varepsilon k_g\frac{\partial T}{\partial x}\right)+\frac{\partial}{\partial y}\left(-\varepsilon k_g\frac{\partial T}{\partial y}\right)+\frac{\partial}{\partial z}\left(-\varepsilon k_g\frac{\partial T}{\partial y}\right)\right]\left[\frac{J}{m^3 s}\right] \tag{B.45}$$

$$\left[\frac{\partial}{\partial x}\left(\varepsilon k_g\frac{\partial T}{\partial x}\right)+\frac{\partial}{\partial y}\left(\varepsilon k_g\frac{\partial T}{\partial y}\right)+\frac{\partial}{\partial z}\left(\varepsilon k_g\frac{\partial T}{\partial y}\right)\right]\left[\frac{J}{m^3 s}\right] \tag{B.46}$$

Finally this can be represented as

$$\nabla \varepsilon k_g \nabla T \tag{B.47}$$

The convective transport of internal energy into the system

$$\left(\varepsilon \rho_g U_g u_x\right)dydz+\left(\varepsilon \rho U_g u_y\right)dxdz+\left(\varepsilon \rho U_g u_z\right)dxdy\left[\frac{J}{s}\right] \tag{B.48}$$

Convective transport out of the system

$$\left(\varepsilon \rho_g U_g u_x+u_x\frac{\partial\left(\varepsilon \rho_g U_g\right)}{\partial x}dx\right)dydz+\left(\varepsilon \rho U_g u_y+u_y\frac{\partial\left(\varepsilon \rho_g U_g\right)}{\partial y}dy\right)dxdz$$
$$+\left(\varepsilon \rho U_g u_z+u_z\frac{\partial\left(\varepsilon \rho_g U_g\right)}{\partial z}dz\right)dxdy\left[\frac{J}{s}\right] \tag{B.49}$$

Therefore, the net convective transport through the system, after diving by the control volume, is

$$-\left[\frac{\partial\left(\varepsilon\rho_g U_g u_x\right)}{\partial x}+\frac{\partial\left(\varepsilon\rho_g U_g u_y\right)}{\partial y}+\frac{\partial\left(\varepsilon\rho_g U_g u_z\right)}{\partial z}\right]\left[\frac{J}{m^3 s}\right] \tag{B.50}$$

this can be simplified to

$$-\nabla\left(\varepsilon\rho_g U_g \vec{u}\right) \tag{B.51}$$

Defining the molecular momentum flux as

$$\begin{aligned}\pi_{ij} &= p+\tau_{ij} \qquad i=j\\ \pi_{ij} &= \tau_{ij} \qquad i\neq j\end{aligned} \tag{B.52}$$

The energy transfer by the gas in the control volume to the environment is

$$\begin{aligned}&-\left(\frac{\partial(\varepsilon u_x\pi_{xx})}{\partial x}+\frac{\partial(\varepsilon u_x\pi_{yx})}{\partial y}+\frac{\partial(\varepsilon u_x\pi_{zx})}{\partial z}\right)-\left(\frac{\partial(\varepsilon u_y\pi_{xy})}{\partial x}+\frac{\partial(\varepsilon u_y\pi_{yy})}{\partial y}+\frac{\partial(\varepsilon u_y\pi_{zy})}{\partial z}\right)\\ &-\left(\frac{\partial(\varepsilon u_z\pi_{xz})}{\partial x}+\frac{\partial(\varepsilon u_z\pi_{yz})}{\partial y}+\frac{\partial(\varepsilon u_z\pi_{zz})}{\partial z}\right)\left[\frac{J}{m^3 s}\right]\end{aligned} \tag{B.53}$$

the expression above can be decoupled to yield

$$\begin{aligned}&-u_x\left(\frac{\partial(\varepsilon\pi_{xx})}{\partial x}+\frac{\partial(\varepsilon\pi_{yx})}{\partial y}+\frac{\partial(\varepsilon\pi_{zx})}{\partial z}\right)-u_y\left(\frac{\partial(\varepsilon\pi_{xy})}{\partial x}+\frac{\partial(\varepsilon\pi_{yy})}{\partial y}+\frac{\partial(\varepsilon\pi_{zy})}{\partial z}\right)\\ &-u_z\left(\frac{\partial(\varepsilon\pi_{xz})}{\partial x}+\frac{\partial(\varepsilon\pi_{yz})}{\partial y}+\frac{\partial(\varepsilon\pi_{zz})}{\partial z}\right)\left[\frac{J}{m^3 s}\right]\end{aligned} \tag{B.54}$$

and

$$-\left(\pi_{xx}\frac{\partial(\varepsilon u_x)}{\partial x}+\pi_{yx}\frac{\partial(\varepsilon u_x)}{\partial y}+\pi_{zx}\frac{\partial(\varepsilon u_x)}{\partial z}\right)$$
$$-\left(\pi_{xy}\frac{\partial(\varepsilon u_y)}{\partial x}+\pi_{yy}\frac{\partial(\varepsilon u_y)}{\partial y}+\pi_{zy}\frac{\partial(\varepsilon u_y)}{\partial z}\right)$$
$$-\left(\pi_{xz}\frac{\partial(\varepsilon u_z)}{\partial x}+\pi_{yz}\frac{\partial(\varepsilon u_z)}{\partial y}+\pi_{zz}\frac{\partial(\varepsilon u_z)}{\partial z}\right)\left[\frac{J}{m^3 s}\right] \tag{B.55}$$

The first term has described by Bejan (1984) as the change in kinetic energy of the fluid in the control volume, which may be considered negligible [94], leaving

$$-p\left(\frac{\partial(\varepsilon u_x)}{\partial x}+\frac{\partial(\varepsilon u_y)}{\partial y}+\frac{\partial(\varepsilon u_z)}{\partial z}\right)-\left(\tau_{xx}\frac{\partial(\varepsilon u_x)}{\partial x}+\tau_{yx}\frac{\partial(\varepsilon u_x)}{\partial y}+\tau_{zx}\frac{\partial(\varepsilon u_x)}{\partial z}\right)$$
$$-\left(\tau_{xy}\frac{\partial(\varepsilon u_y)}{\partial x}+\tau_{yy}\frac{\partial(\varepsilon u_y)}{\partial y}+\tau_{zy}\frac{\partial(\varepsilon u_y)}{\partial z}\right)$$
$$-\left(\tau_{xz}\frac{\partial(\varepsilon u_z)}{\partial x}+\tau_{yz}\frac{\partial(\varepsilon u_z)}{\partial y}+\tau_{zz}\frac{\partial(\varepsilon u_z)}{\partial z}\right)\left[\frac{J}{m^3 s}\right] \tag{B.56}$$

and can be written in vector notation as

$$-p\nabla\left(\varepsilon\vec{u}\right)+\left[\nabla\cdot\left[\mu\left(\nabla\vec{u}+\nabla\vec{u}^{T}\right)\right]-\nabla\cdot\left[\frac{2\mu}{3}\nabla\cdot\vec{u}I\right]\right]\nabla\varepsilon\vec{u} \tag{B.57}$$

The second term in the above expression is the viscous dissipation within the system such that

$$\left[\nabla\cdot\left[\mu\left(\nabla\vec{u}+\nabla\vec{u}^{T}\right)\right]-\nabla\cdot\left[\frac{2\mu}{3}\nabla\cdot\vec{u}I\right]\right]\nabla\varepsilon\vec{u}=\varepsilon\Phi_g \tag{B.58}$$

Summing the energy transport by flow, pressure, and conduction to the transient change gives

$$\frac{\partial\left(\varepsilon\rho_g U_g\right)}{\partial t}+\nabla\left(\varepsilon\rho_g U_g\vec{u}\right)=\nabla\varepsilon k_g\nabla T-p\nabla\left(\varepsilon\vec{u}\right)+\varepsilon\Phi_g \tag{B.59}$$

The equation above is rearranged to yield

$$\rho_g\left[\frac{\partial\left(\varepsilon U_g\right)}{\partial t}+\vec{u}\nabla\left(\varepsilon U_g\right)\right]+U_g\left[\frac{\partial\left(\varepsilon\rho_g\right)}{\partial t}+\nabla\left(\varepsilon\rho_g\vec{u}\right)\right]=\nabla\varepsilon k_g\nabla T-p\nabla\left(\varepsilon\vec{u}\right)+\varepsilon\Phi_g \tag{B.60}$$

The second term on the left hand side of the equation above, is equal to the internal energy of the gas times the left hand side of the mass balance derived earlier, therefore, the mass sink can be substituted into the above equation to give

$$\rho_g\left[\frac{\partial\left(\varepsilon U_g\right)}{\partial t}+\vec{u}\nabla\left(\varepsilon U_g\right)\right]-U_g\gamma_m=\nabla\varepsilon k_g\nabla T-p\nabla\left(\varepsilon\vec{u}\right)+\varepsilon\Phi_g \tag{B.61}$$

Now, using thermodynamic relationship for the internal energy of the gas

$$U=H-\frac{p}{\rho} \tag{B.62}$$

And substituting into the previous equation

$$\rho_g\left[\frac{\partial\left(\varepsilon\left(H_g-\frac{p}{\rho_g}\right)\right)}{\partial t}+\vec{u}\nabla\left(\varepsilon\left(H_g-\frac{p}{\rho_g}\right)\right)\right]-\left(H_g-\frac{p}{\rho_g}\right)\gamma_m$$
$$=\nabla\varepsilon k_g\nabla T-p\nabla\left(\varepsilon\vec{u}\right)+\varepsilon\Phi_g \quad . \tag{B.63}$$

which can be split and rearranged into

$$\left[\rho_g\left(\frac{\partial\left(\varepsilon H_g\right)}{\partial t}+\vec{u}\nabla\left(\varepsilon H_g\right)\right)-\left(\frac{\partial\left(\varepsilon p\right)}{\partial t}+\vec{u}\nabla\left(\varepsilon p\right)\right)+\frac{p}{\rho_g}\left(\frac{\partial\left(\varepsilon\rho_g\right)}{\partial t}+\vec{u}\nabla\left(\varepsilon\rho_g\right)\right)\right]$$
$$-\left(H_g-\frac{p}{\rho_g}\right)\gamma_m=\nabla\varepsilon k_g\nabla T-p\nabla\left(\varepsilon\vec{u}\right)+\varepsilon\Phi_g \tag{B.64}$$

The last term in the brackets on the left hand side of the previous equation can be compared to the mass balance derived earlier

$$\varepsilon\frac{\partial\rho_g}{\partial t}+\nabla\cdot\left(\varepsilon\vec{u}\rho_g\right)=-\gamma_m=\varepsilon\frac{\partial\rho_g}{\partial t}+\vec{u}\nabla\cdot\left(\varepsilon\rho_g\right)+\rho_g\nabla\cdot\left(\varepsilon\vec{u}\right) \tag{B.65}$$

Therefore,

$$\varepsilon\frac{\partial\rho_g}{\partial t}+\vec{u}\nabla\cdot\left(\varepsilon\rho_g\right)=-\gamma_m-\rho_g\nabla\cdot\left(\varepsilon\vec{u}\right) \tag{B.66}$$

this can be substituted into (B.64) to give

$$\left[\rho_g\frac{\partial\varepsilon H_g}{\partial t}+\rho_g\vec{u}\nabla\left(\varepsilon H_g\right)-\left(\frac{\partial\varepsilon p}{\partial t}+\vec{u}\nabla\left(\varepsilon p\right)\right)-\frac{p}{\rho_g}\left(M_{Wg}\rho_b\frac{\partial n_a}{\partial t}+\rho_g\nabla\cdot\left(\varepsilon\vec{u}\right)\right)\right]$$
$$-\left(H_g-\frac{p}{\rho_g}\right)\gamma_m=\nabla\varepsilon k_g\nabla T-p\nabla\left(\varepsilon\vec{u}\right)+\varepsilon\Phi_g \tag{B.67}$$

this can then be simplified to

$$\left[\rho_g\frac{\partial\varepsilon H_g}{\partial t}+\rho_g\vec{u}\nabla\left(\varepsilon H_g\right)-\left(\frac{\partial\varepsilon p}{\partial t}+\vec{u}\nabla\left(\varepsilon p\right)\right)\right]$$
$$-\left(H_g\right)\gamma_m=\nabla\varepsilon k_g\nabla T+\varepsilon\Phi_g \tag{B.68}$$

Using an additional thermodynamic relationship

$$dH_g=C_{pg}dT+\left[\frac{1}{\rho_g}+\frac{T}{\rho_g^2}\left(\frac{\partial\rho_g}{\partial T}\right)_p\right]dp \tag{B.69}$$

The partial derivative in the brackets above is equal to the coefficient of thermal expansion

$$\left(\frac{\partial \rho_g}{\partial T}\right)_p = -\delta\rho_g \tag{B.70}$$

yielding

$$dH_g = C_{pg}dT + \left[\frac{1}{\rho_g} - \frac{\delta T}{\rho_g}\right]dp \tag{B.71}$$

and (B.71) can be substituted into the gas phase energy to give

$$\begin{aligned}&\left[\rho_g C_{pg}\left(\frac{\partial \varepsilon T}{\partial t} + \vec{u}\nabla(\varepsilon T)\right) - \delta T\left(\frac{\partial \varepsilon p}{\partial t} + \vec{u}\nabla(\varepsilon p)\right)\right]\\ &= \left(H_g\right)\gamma_m + \nabla\varepsilon k_g \nabla T + \varepsilon\Phi_g\end{aligned} \tag{B.72}$$

The gas phase equation can be rearranged and transformed into superficial velocities to yield

$$\rho_g C_{pg}\left(\varepsilon\frac{\partial T}{\partial t} + \overrightarrow{u_A}\nabla(T)\right) = \left(H_g\right)\gamma_m + \nabla\varepsilon k_g\nabla T + \delta T\left(\varepsilon\frac{\partial p}{\partial t} + \overrightarrow{u_A}\nabla(p)\right) + \Phi_{Ag} \tag{B.73}$$

Similarly, the energy change in the solid phase, solid adsorbent and adsorbed phase can be described as

$$\left(\rho_b C_{p,SA} + M_{Wg}\rho_b n_a C_{p,a}\right)\frac{\partial T}{\partial t} = \nabla(1-\varepsilon)k_{SA}\nabla T - \gamma_m H_a \tag{B.74}$$

this can be combined with the gas phase energy balance to give

$$\begin{aligned}&\left(\rho_g C_{pg}\varepsilon + M_{Wg}\rho_b n_a C_{p,a} + \rho_b C_{p,SA}\right)\frac{\partial T}{\partial t} + \rho_g C_{pg}\overrightarrow{u_A}\nabla T = \left(H_g - H_a\right)\gamma_m\\ &+\nabla\varepsilon k_g\nabla T + \nabla(1-\varepsilon)k_{SA}\nabla T + \delta T\left(\varepsilon\frac{\partial p}{\partial t} + \overrightarrow{u_A}\nabla(p)\right) + \Phi_{Ag}\end{aligned} \tag{B.75}$$

In the first term on the right hand side of the equation above, the difference between the gas phase and adsorbed phase enthalpies is assumed to be the change of enthalpy due to the adsorption process, heat of adsorption, given by [82]

$$\Delta H_{ads} = \frac{\alpha}{M_{Wg}} \sqrt{\ln\left(\frac{n_{\max}}{n_a}\right)} \tag{B.76}$$

Which α is the enthalpic factor of the modified D-A parameters. Thus yielding

$$\begin{aligned} &\left(\rho_g C_{pg}\varepsilon + M_{Wg}\rho_b n_a C_{p,a} + \rho_b C_{p,SA}\right)\frac{\partial T}{\partial t} + \rho_g C_{pg}\overrightarrow{u_A}\nabla T = \Delta H_{ads}\gamma_m \\ &+\nabla\varepsilon k_g \nabla T + \nabla\left(1-\varepsilon\right)k_{SA}\nabla T + \delta T\left(\varepsilon\frac{\partial p}{\partial t} + \overrightarrow{u_A}\nabla\left(p\right)\right) + \Phi_{Ag} \end{aligned} \tag{B.77}$$

and

$$\begin{aligned} &\left(\rho_g C_{pg}\varepsilon + M_{Wg}\rho_b n_a C_{p,a} + \rho_b C_{p,SA}\right)\frac{\partial T}{\partial t} + \rho_g C_{pg}\overrightarrow{u_A}\nabla T = \frac{\alpha}{M_{Wg}}\sqrt{\ln\left(\frac{n_{\max}}{n_a}\right)}\gamma_m \\ &+\nabla\varepsilon k_g \nabla T + \nabla\left(1-\varepsilon\right)k_{SA}\nabla T + \delta T\left(\varepsilon\frac{\partial p}{\partial t} + \overrightarrow{u_A}\nabla\left(p\right)\right) + \Phi_{Ag} \end{aligned} \tag{B.78}$$

and now, defining an effective conductivity of the adsorbent media as

$$k_{eff} = \varepsilon k_g + \left(1-\varepsilon\right)k_{SA} \tag{B.79}$$

thus, the energy balance takes the form of

$$\begin{aligned} &\left(\rho_g C_{pg}\varepsilon + M_{Wg}\rho_b n_a C_{p,a} + \rho_b C_{p,SA}\right)\frac{\partial T}{\partial t} + \rho_g C_{pg}\overrightarrow{u_A}\nabla T = \frac{\alpha}{M_{Wg}}\sqrt{\ln\left(\frac{n_{\max}}{n_a}\right)}\gamma_m \\ &\nabla k_{eff}\nabla T + \delta T\left(\varepsilon\frac{\partial p}{\partial t} + \overrightarrow{u_A}\nabla\left(p\right)\right) + \Phi_{Ag} \end{aligned}$$

The energy balance in free space can be obtained by the previous expression by setting the heat generation due to adsorption, amount of adsorbed gas, n_a, and bulk

density of the adsorbent to zero, setting the porosity to unity and replacing the superficial velocity with a standard velocity to give

$$\rho_g C_{pg}\left[\frac{\partial T}{\partial t}+\vec{u}\nabla T\right]=\nabla k_g \nabla T+\delta T\left(\frac{\partial p}{\partial t}+\vec{u}\nabla\left(p\right)\right)+\Phi_g \tag{B.80}$$

Derivation of Characteristic Times of Energy Transport

The following derivation may be applied to the stainless steel pressure vessel, stack of stainless steel shims, PTFE insulation, and PTFE plugs used in the experimental system. It is assumed that heat transfer by conduction is the dominant form of transport for the materials mentioned above. The following derivation assumes the thermal conductivity does not change in *x*, *y*, or *z*, and for simplicity is constant.

The conservation of energy is expressed as

$$\rho C_p \frac{\partial T}{\partial t}=k\left[\frac{\partial^2 T}{\partial x^2}+\frac{\partial^2 T}{\partial y^2}+\frac{\partial^2 T}{\partial z^2}\right] \tag{B.81}$$

and there exists three characteristic lengths such that

$$\overline{x}=\frac{x}{L_x};\overline{y}=\frac{y}{L_y};\overline{z}=\frac{z}{L_z} \tag{B.82}$$

Substituting (2) into (1) and rearranging yields

$$\frac{\partial T}{\partial t}=\frac{k}{\rho C_p L_x^2}\frac{\partial^2 T}{\partial \overline{x}^2}+\frac{k}{\rho C_p L_y^2}\frac{\partial^2 T}{\partial \overline{y}^2}+\frac{k}{\rho C_p L_z^2}\frac{\partial^2 T}{\partial \overline{z}^2} \tag{B.83}$$

and performing a unit analysis on the terms preceding the partial derivatives on the right hand side of (3), it can be demonstrated that

$$\frac{k}{\rho C_p L^2} = \left[\frac{\left[\frac{J}{s \cdot m \cdot K} \right]}{\left[\frac{kg}{m^3} \right] \left[\frac{J}{kg \cdot K} \right] \left[m^2 \right]} \right] = \left[\frac{1}{s} \right] \tag{B.84}$$

Therefore, the characteristic time constants of conductive heat transfer through the material are

$$\tau_{xcond} = \frac{\rho C_p L_x^2}{k}; \tau_{ycond} = \frac{\rho C_p L_y^2}{k}; \tau_{zcond} = \frac{\rho C_p L_z^2}{k} \tag{B.85}$$

If $L_x \approx L_y \approx L_z \approx L$, there characteristic time constant of conductive heat transfer is

$$\tau_{cond} = \frac{\rho C_p L^2}{k} \tag{B.86}$$

Beginning from the total energy balance for the adsorbent bed

$$\left(\rho_g C_{pg} \varepsilon + M_g \rho_b n_a C_{p,a} + \rho_b C_{p,SA} \right) \frac{\partial T}{\partial t} + \rho_g C_{pg} \overrightarrow{u_A} \nabla T = \nabla k_{eff} \nabla T + \delta T \left(\varepsilon \frac{\partial p}{\partial t} + \overrightarrow{u_A} \nabla \left(p \right) \right) + \Phi_{Ag} + \gamma_T \tag{B.87}$$

The characteristic times for conduction, convection, and generation by adsorption are derived using a simplified energy balance

$$\left(\rho_g C_{pg} \varepsilon + M_g \rho_b n_a C_{p,a} + \rho_b C_{p,SA} \right) \frac{\partial T}{\partial t} + \rho_g C_{pg} \overrightarrow{u_A} \nabla T = k_{eff} \nabla^2 T + \gamma_T \tag{B.88}$$

Note: the following derivation will be completed with the assumption of a single characteristic length, $L_x \approx L_y \approx L_z \approx L$, however, as demonstrated above three separate time constants may be calculated in the event that different characteristic lengths are required in any or all directions. Thus, for simplicity, the characteristic time constant

will be derived for only a single directional component, *x*, and the same procedure as outlined above can be followed to derive all others.

Defining,

$$\overline{x} = \frac{x}{L}; \Theta = \frac{T}{T_R} \tag{B.89}$$

where L is the characteristic length, Θ is the dimensionless temperature, and T_R is the reference temperature of the system. Substituting (9) into (8) yields

$$\left(\rho_g C_{pg}\varepsilon + M_g \rho_b n_a C_{p,a} + \rho_b C_{p,SA}\right) T_R \frac{\partial \Theta}{\partial t} + \rho_g C_{pg} \overrightarrow{u_A} \frac{T_R}{L} \nabla\Theta = k_{eff} \frac{T_R}{L^2} \nabla^2\Theta + \gamma_T \tag{B.90}$$

Dividing (B.90) by the term preceding the partial derivative on the left hand side of (B.90) gives

$$\frac{\partial \Theta}{\partial t} + \frac{\rho_g C_{pg} \overrightarrow{u_A}}{\left(\rho_g C_{pg}\varepsilon + M_g \rho_b n_a C_{p,a} + \rho_b C_{p,SA}\right) L} \nabla\Theta = \frac{k_{eff}}{\left(\rho_g C_{pg}\varepsilon + M_g \rho_b n_a C_{p,a} + \rho_b C_{p,SA}\right) L^2} \nabla^2\Theta + \frac{\gamma_T}{\left(\rho_g C_{pg}\varepsilon + M_g \rho_b n_a C_{p,a} + \rho_b C_{p,SA}\right) T_R} \tag{B.91}$$

First, a unit analysis will be performed on the term in parenthesis in the denominator of (B.91), subject to the assumption that $C_{p,a} \approx C_{pg}$

$$\left(\rho_g C_{pg}\varepsilon + M_g \rho_b n_a C_{p,a} + \rho_b C_{p,SA}\right) \Rightarrow$$

$$\left[\left[\frac{\cancel{kg_g}}{\cancel{m_g^3}}\right]\left[\frac{J}{\cancel{kg_g} K}\right]\left[\frac{\cancel{m_g^3}}{m^3}\right] + \left[\frac{\cancel{kg_g}}{\cancel{mol_g}}\right]\left[\frac{\cancel{kg_{SA}}}{m^3}\right]\left[\frac{\cancel{mol_g}}{\cancel{kg_{SA}}}\right]\left[\frac{J}{\cancel{kg_g} K}\right] + \left[\frac{\cancel{kg_{SA}}}{m^3}\right]\left[\frac{J}{\cancel{kg_{SA}} K}\right]\right] = \left[\left[\frac{J}{m^3 K}\right]\right] \tag{B.92}$$

With the unit analysis complete, the term in (B.92) will be abbreviated as

$$\left(\rho_g C_{pg}\varepsilon + M_g \rho_b n_a C_{p,a} + \rho_b C_{p,SA}\right) = \sum\left(\rho C_p\right) \tag{B.93}$$

the abbreviation of (B.93) transforms (B.91) into

$$\frac{\partial\Theta}{\partial t} + \frac{\rho_g C_{pg}\overrightarrow{u_A}}{\sum\left(\rho C_p\right)L}\nabla\Theta = \frac{k_{eff}}{\sum\left(\rho C_p\right)L^2}\nabla^2\Theta + \frac{\gamma_T}{\sum\left(\rho C_p\right)T_R} \tag{B.94}$$

From (B.94) the characteristic times of convective and conductive heat transfer through the adsorbent system are

$$\tau_{cv,ad} = \frac{\sum\left(\rho C_p\right)L}{\rho_g C_{pg}\overrightarrow{u_A}} \tag{B.95}$$

$$\tau_{cond,ad} = \frac{\sum\left(\rho C_p\right)L^2}{k_{eff}} \tag{B.96}$$

The characteristic time for the generation of heat due to adsorption is:

$$\tau_{ah,ad} = \frac{\sum\left(\rho C_p\right)T_R}{\gamma_T} = \frac{\sum\left(\rho C_p\right)T_R}{\Delta H_{ads}\gamma_m} = \frac{\sum\left(\rho C_p\right)T_R}{\Delta H_{ads}M_{Wg}\rho_b\dfrac{\partial n_a}{\partial t}} \tag{B.97}$$

Appendix C: Comparison of Experimental and Simulated Results Liquid Cooled Simulations

Name	MOF-5 LN2 H2 Exp. #1							
	Absolute Error [K]				Relative Error [%]			
	Max Error Value	Min. Error Value	Average of Absolute Values	RMS	Max Error Value	Min. Error Value	Average of Absolute Values	RMS
TC9	19.89	-4.89	4.21	5.83	12.84	-3.73	2.86	3.85
TC10	12.94	-4.49	4.30	5.19	8.02	-3.08	2.59	3.10
TC11	15.65	0.93	5.04	5.80	9.63	0.64	3.10	3.54
TC12	13.88	-2.27	4.37	4.87	9.86	-1.90	3.11	3.45
TC13	17.78	-1.31	7.74	8.49	10.51	-0.89	4.49	4.89
TC14	12.65	-7.02	5.56	5.94	9.08	-5.85	4.31	4.61

H_2 Mass [g]	Experimental	Simulation	Absolute Error [g]	Relative Error [%]
Vessel Mass	1.73	1.91	-0.18	-10.15
Bed Mass	1.03	1.14	-0.11	-10.91
Void Mass	0.70	0.76	-0.06	-9.04

Name	MOF-5 LN2 H2 Exp. #2							
	Absolute Error [K]				Relative Error [%]			
	Max Error Value	Min. Error Value	Average of Absolute Values	RMS	Max Error Value	Min. Error Value	Average of Absolute Values	RMS
TC9	20.02	-2.30	2.64	4.43	13.21	-1.75	1.82	2.92
TC10	11.11	-2.90	2.82	3.69	7.26	-2.26	1.74	2.25
TC11	14.24	1.34	5.37	5.67	9.24	1.01	3.52	3.71
TC12	12.12	-2.66	3.24	3.66	8.80	-2.33	2.42	2.70
TC13	17.90	-0.31	6.64	7.13	11.00	-0.23	4.05	4.31
TC14	16.97	-7.38	6.36	6.72	12.16	-5.81	5.04	5.26

H_2 Mass [g]	Experimental	Simulation	Absolute Error [g]	Relative Error [%]
Vessel Mass	1.78	1.97	-0.19	-10.44
Bed Mass	1.00	1.24	-0.23	-23.04
Void Mass	0.78	0.73	0.05	5.81

Liquid Cooled Simulations (Continued)

Name	MOF-5 LN2 H2 Exp. #4							
	Absolute Error [K]				Relative Error [%]			
	Max Error Value	Min. Error Value	Average of Absolute Values	RMS	Max Error Value	Min. Error Value	Average of Absolute Values	RMS
TC9	17.97	-6.66	4.80	5.56	13.15	-5.47	3.68	4.28
TC10	7.09	-4.41	3.34	3.87	4.21	-3.34	2.20	2.51
TC11	7.90	-2.27	1.19	1.60	5.80	-1.40	0.83	1.13
TC12	0.07	-0.05	4.51	4.79	6.96	-4.64	3.65	3.90
TC13	11.99	0.66	5.28	5.88	8.35	0.53	3.38	3.71
TC14	15.87	-13.84	11.65	12.11	12.44	-11.84	9.94	10.40

H_2 Mass [g]	Experimental	Simulation	Absolute Error [kg]	Relative Error [%]
Vessel Mass	1.73	2.18	-0.46	-26.36
Bed Mass	0.85	1.26	-0.40	-47.21
Void Mass	0.87	0.93	-0.05	-5.98

Name	MOF-5 LN2 H2 Exp. #5							
	Absolute Error [K]				Relative Error [%]			
	Max Error Value	Min. Error Value	Average of Absolute Values	RMS	Max Error Value	Min. Error Value	Average of Absolute Values	RMS
TC9	16.42	-4.15	3.31	4.01	12.16	-3.32	2.56	3.08
TC10	6.35	-6.48	3.65	4.24	4.85	-5.01	2.61	3.10
TC11	8.10	-4.99	2.44	2.60	6.07	-3.10	1.72	1.83
TC12	8.07	-2.66	1.75	2.00	6.67	-2.10	1.42	1.61
TC13	11.92	-2.30	1.67	2.33	8.63	-1.72	1.15	1.64
TC14	14.84	-10.42	8.41	8.68	11.78	-8.74	7.19	7.44

H_2 Mass [g]	Experimental	Simulation	Absolute Error [kg]	Relative Error [%]
Vessel Mass	2.05	2.28	-0.24	-11.56
Bed Mass	1.15	1.35	-0.20	-17.60
Void Mass	0.90	0.94	-0.04	-3.88

Liquid Cooled Simulations (Continued)

Name	MOF-5 LN2 H2 Exp. #6							
	Absolute Error [K]				Relative Error [%]			
	Max Error Value	Min. Error Value	Average of Absolute Values	RMS	Max Error Value	Min. Error Value	Average of Absolute Values	RMS
TC9	12.07	-4.44	3.15	3.59	9.69	-3.67	2.52	2.91
TC10	5.01	-7.34	3.39	3.80	3.41	-4.92	2.38	2.69
TC11	5.61	-7.27	1.06	1.76	4.48	-4.80	0.77	1.23
TC12	6.10	-6.74	2.82	3.00	5.28	-5.00	2.32	2.46
TC13	8.35	-1.89	2.70	3.49	6.45	-1.21	1.76	2.24
TC14	9.53	-11.10	8.85	9.18	8.16	-9.44	7.69	8.02

H_2 Mass [g]	Experimental	Simulation	Absolute Error [kg]	Relative Error [%]
Vessel Mass	2.17	2.31	-0.14	-6.32
Bed Mass	1.24	1.37	-0.13	-10.80
Void Mass	0.94	0.94	0.00	-0.40

Name	MOF-5 LN2 H2 Exp. #8							
	Absolute Error [K]				Relative Error [%]			
	Max Error Value	Min. Error Value	Average of Absolute Values	RMS	Max Error Value	Min. Error Value	Average of Absolute Values	RMS
TC9	14.65	-5.16	3.61	4.23	9.68	-4.32	2.69	3.13
TC10	8.07	-8.98	4.94	5.72	5.47	-6.78	3.42	4.05
TC11	8.31	-6.91	3.88	4.00	5.70	-4.07	2.66	2.72
TC12	8.08	-3.71	3.10	3.28	5.65	-3.17	2.43	2.58
TC13	13.94	-4.83	3.12	3.82	9.21	-3.55	2.11	2.60
TC14	12.01	-11.59	10.00	10.26	8.27	-9.54	8.20	8.47

H_2 Mass [g]	Experimental	Simulation	Absolute Error [kg]	Relative Error [%]
Vessel Mass	1.96	2.16	-0.20	-10.24
Bed Mass	1.09	1.28	-0.19	-17.55
Void Mass	0.87	0.88	-0.01	-1.06

Liquid Cooled Simulations (Continued)

Name	MOF-5 LN2 H2 Exp. #10							
	Absolute Error [K]				Relative Error [%]			
	Max Error Value	Min. Error Value	Average of Absolute Values	RMS	Max Error Value	Min. Error Value	Average of Absolute Values	RMS
TC9	15.86	-5.65	4.02	4.81	10.03	-4.65	2.93	3.43
TC10	12.59	-7.83	4.37	5.24	7.96	-5.86	2.98	3.62
TC11	11.44	-3.80	2.68	3.08	7.27	-2.26	1.81	2.05
TC12	11.60	-4.41	3.31	3.63	7.65	-3.79	2.55	2.79
TC13	16.59	-3.27	2.25	3.71	10.42	-2.39	1.46	2.35
TC14	13.04	-11.36	9.98	10.28	8.51	-10.27	8.15	8.48

H_2 Mass [g]	Experimental	Simulation	Absolute Error [kg]	Relative Error [%]
Vessel Mass	1.92	2.12	-0.20	-10.29
Bed Mass	1.09	1.25	-0.15	-13.78
Void Mass	0.82	0.87	-0.05	-5.65

Name	MOF-5 LN2 H2 Exp. #5 - Original Base Case							
	Absolute Error [K]				Relative Error [%]			
	Max Error Value	Min. Error Value	Average of Absolute Values	RMS	Max Error Value	Min. Error Value	Average of Absolute Values	RMS
TC9	16.99	-18.05	14.89	15.45	12.56	-14.79	11.47	12.07
TC10	7.00	-18.12	12.08	13.21	5.31	-14.03	8.52	9.50
TC11	9.00	-15.30	13.19	13.53	6.71	-11.29	9.53	9.85
TC12	8.71	-12.57	10.84	11.13	7.16	-10.87	8.87	9.19
TC13	12.54	-11.91	9.37	9.72	9.01	-8.91	6.43	6.76
TC14	15.34	-20.21	17.77	18.21	12.12	-18.00	15.28	15.79

H_2 Mass [g]	Experimental	Simulation	Absolute Error [kg]	Relative Error [%]
Vessel Mass	2.05	2.23	-0.18	-8.80
Bed Mass	1.15	1.28	-0.14	-11.99
Void Mass	0.90	0.94	-0.04	-4.75

Non-cooled Simulations

Name	MOF-5 NC H2 Exp.#3							
	Absolute Error [K]				Relative Error [%]			
	Max Error Value	Min. Error Value	Average of Absolute Values	RMS	Max Error Value	Min. Error Value	Average of Absolute Values	RMS
TC9	10.64	-2.01	2.14	2.73	8.08	-1.47	1.45	1.84
TC10	3.99	-5.69	2.48	2.72	3.03	-3.57	1.65	1.81
TC11	4.48	-5.09	0.47	1.03	3.43	-3.19	0.31	0.68
TC12	6.57	-4.94	3.68	3.90	5.34	-3.68	2.72	2.90
TC13	6.20	-4.21	1.80	2.26	4.68	-2.61	1.16	1.44
TC14	10.65	-6.24	4.58	4.90	8.49	-4.66	3.40	3.66

H_2 Mass [g]	Experimental	Simulation	Absolute Error [kg]	Relative Error [%]
Vessel Mass	1.80	1.90	-0.10	-5.51
Bed Mass	0.98	1.06	-0.09	-8.75
Void Mass	0.82	0.84	-0.01	-1.66

Name	MOF-5 NC H2 Exp.#4							
	Absolute Error [K]				Relative Error [%]			
	Max Error Value	Min. Error Value	Average of Absolute Values	RMS	Max Error Value	Min. Error Value	Average of Absolute Values	RMS
TC9	11.34	-0.61	1.94	2.96	8.68	-1.31	1.31	1.77
TC10	7.38	-3.72	2.19	2.73	5.78	-2.85	1.60	1.87
TC11	8.29	-3.77	0.68	1.34	6.47	-2.82	1.04	1.29
TC12	8.65	-3.69	2.78	2.98	6.88	-3.50	2.52	2.70
TC13	9.30	-3.21	1.41	1.85	7.25	-2.91	2.06	2.30
TC14	10.27	-6.59	4.03	4.49	8.21	-5.75	3.68	4.00

H_2 Mass [g]	Experimental	Simulation	Absolute Error [kg]	Relative Error [%]
Vessel Mass	1.95	1.99	-0.04	-1.95
Bed Mass	1.09	1.12	-0.03	-2.43
Void Mass	0.86	0.87	-0.01	-1.33

Non-cooled Simulations (Continued)

Name	MOF-5 NC H2 Exp.#8							
	Absolute Error [K]				Relative Error [%]			
	Max Error Value	Min. Error Value	Average of Absolute Values	RMS	Max Error Value	Min. Error Value	Average of Absolute Values	RMS
TC9	12.58	-1.60	2.40	3.13	8.21	-0.91	1.59	2.07
TC10	13.41	-6.97	5.85	6.09	8.92	-4.50	3.69	3.87
TC11	12.29	-10.42	6.70	7.22	8.23	-6.36	4.30	4.58
TC12	12.74	0.96	5.40	5.71	8.32	0.56	3.59	3.82
TC13	12.77	-8.47	7.44	7.57	8.55	-5.35	4.74	4.83
TC14	9.63	-2.94	3.28	3.71	6.44	-1.76	2.25	2.56

H_2 Mass [g]	Experimental	Simulation	Absolute Error [kg]	Relative Error [%]
Vessel Mass	1.75	1.84	-0.10	-5.69
Bed Mass	0.97	1.04	-0.07	-7.43
Void Mass	0.78	0.81	-0.03	-3.54

Name	MOF-5 NC H2 Exp.#13							
	Absolute Error [K]				Relative Error [%]			
	Max Error Value	Min. Error Value	Average of Absolute Values	RMS	Max Error Value	Min. Error Value	Average of Absolute Values	RMS
TC9	15.58	0.40	2.95	3.91	10.09	0.31	1.87	2.44
TC10	15.89	-6.78	5.06	5.76	10.46	-4.56	3.29	3.77
TC11	13.77	-8.34	6.13	6.42	9.22	-5.22	4.04	4.20
TC12	13.38	0.33	6.85	7.08	8.84	0.25	4.52	4.65
TC13	12.98	-8.23	7.12	7.29	8.76	-5.58	4.69	4.83
TC14	11.57	-0.07	3.08	3.53	7.88	-0.04	2.12	2.42

H_2 Mass [g]	Experimental	Simulation	Absolute Error [kg]	Relative Error [%]
Vessel Mass	1.73	1.81	-0.08	-4.70
Bed Mass	0.97	1.04	-0.08	-7.95
Void Mass	0.77	0.77	0.00	-0.59

Non-cooled Simulations (Continued)

Name	MOF-5 NC H2 Exp.#15							
	Absolute Error [K]				Relative Error [%]			
	Max Error Value	Min. Error Value	Average of Absolute Values	RMS	Max Error Value	Min. Error Value	Average of Absolute Values	RMS
TC9	17.38	-0.70	1.48	3.36	11.63	-0.58	0.96	2.17
TC10	18.75	-8.01	6.37	6.98	12.86	-5.57	4.26	4.71
TC11	16.17	-10.53	7.67	8.02	11.27	-6.84	5.25	5.44
TC12	15.18	-0.11	5.33	5.64	10.37	-0.09	3.64	3.83
TC13	16.14	-7.91	7.02	7.24	11.42	-5.62	4.79	4.98
TC14	11.60	-2.81	1.54	2.18	8.18	-1.74	1.08	1.52

H_2 Mass [g]	Experimental	Simulation	Absolute Error [kg]	Relative Error [%]
Vessel Mass	1.79	1.89	-0.10	-5.82
Bed Mass	0.98	1.10	-0.12	-12.06
Void Mass	0.81	0.79	0.01	1.75

Name	MOF-5 NC H2 Exp.#4 – NC Base Case							
	Absolute Error [K]				Relative Error [%]			
	Max Error Value	Min. Error Value	Average of Absolute Values	RMS	Max Error Value	Min. Error Value	Average of Absolute Values	RMS
TC9	11.36	-11.26	8.90	9.26	8.65	-7.91	6.24	6.53
TC10	7.61	-15.45	11.46	12.15	5.82	-10.80	7.73	8.29
TC11	8.60	-17.09	13.80	14.20	6.60	-11.72	9.57	9.87
TC12	8.84	-11.20	7.86	8.16	6.97	-8.10	5.73	5.95
TC13	9.64	-14.53	11.96	12.32	7.33	-10.14	8.11	8.41
TC14	10.39	-15.49	10.87	11.25	8.25	-11.33	8.01	8.30

H_2 Mass [g]	Experimental	Simulation	Absolute Error [kg]	Relative Error [%]
Vessel Mass	1.95	1.89	0.06	3.18
Bed Mass	1.09	1.06	0.04	3.34
Void Mass	0.86	0.83	0.03	2.97